

Topics in Gravitational Wave Physics: Quantum Theory for Detector Improvement and High-Precision Modeling of Binary Black Hole Ringdown Waveform

Thesis by
Xiang Li

In Partial Fulfillment of the Requirements for the
Degree of
Doctor of Philosophy

The logo for the California Institute of Technology (Caltech), featuring the word "Caltech" in a bold, orange, sans-serif font.

CALIFORNIA INSTITUTE OF TECHNOLOGY
Pasadena, California

2023
Defended October 4, 2022

© 2023

Xiang Li

ORCID: 0000-0002-3780-7735

All rights reserved

ACKNOWLEDGEMENTS

First of all, I would like to express my deep and sincere gratitude to my advisor, Professor Yanbei Chen. He led me into the field of quantum precision measurement and gravitational wave physics and supervised me throughout my research. He always has a great passion for physics and a unique insight into nature and society. He is an exceptionally talented physicist and is well trained to dig deeply but explain concisely the complicated problems. Whenever I got lost in the vast sea of details, his sharp physical insights and clear vision always lit me up and motivated me to move forward. It is among the most correct choices in my life to take him as my PhD advisor. Moreover, I am deeply impressed by his natural and humorous attitude toward life, and it is a great honor to let him be one of the witnesses of my wedding.

My candidacy and thesis committee members, Professor Alan Weinstein, Professor Rana Adhikari, Professor Nick Hutzler, Professor Katerina Chatziioannou, and Professor Lee McCuller, were extremely supportive. I am grateful for the collaboration and research support from Professor Alan Weinstein, Professor Rana Adhikari, Professor Katerina Chatziioannou, and their groups. I thank all of them for their interest in my work, their valuable suggestions, and their investment of time.

I am very thankful to Professor Yiqiu Ma, who was my postdoc mentor at the beginning year of my PhD. He is a scientifically serious person and has the spirit of questioning everything. He guided me in the field of quantum optomechanics and measurement, and how to think and study as a researcher. In life, he has an interesting personality and a great taste in art and history. That made him a strict mentor at the start, but a nice friend in the long term.

I am indebted to Professor Ling Sun, who was my postdoc collaborator in gravitational wave analysis. She is a well-organized person and would insist on digging out coherent stories of physics from massive research. This helped me introspect and improve my research and presentation style. Apart from that, her personal story is legendary, switching from a software engineer to a gravitational wave physicist after she recognized her true dream. Her experience greatly inspired me to step out of my comfort zone and explore new directions.

I would like to thank my collaborators, Professor Haixing Miao, Professor Farid Khalili, Dr. Mikhail Korobko, Dr. Joe Bentley, Jiri Smetana, Amit Singh Ubhi, and Dr. Luca Dellantonio, for discussions on quantum optomechanics and measurement.

Especially, I would thank Professor Haixing Miao for initiating collaborations among multiple institutes, and I thank Dr. Mikhail Korobko for organizing the Macroscopic Quantum Mechanics (MQM) discussion group, where I obtained a broader view of this field. I thank my group mate, Dr. Belinda Pang, for discussion on atomic interferometry. I thank Professor Chunrong Zhao at The University of Western Australia (UWA) for inviting me to give the remote talk at the ARC Centre of Excellence for Gravitational Wave Discovery (OzGrav). I thank Professor Selim Shahriar at Northwestern University for inviting me to present remotely at SPIE Photonics West 2021 Session: Optical and Quantum Sensing and Precision Metrology.

I thank my collaborators and colleagues Sizheng Ma, Rico Lo, Ethan Payne, Keefe Mitman, and Dr. Max Isi, for discussions on ringdown gravitational wave physics. I thank Professor Leo Stein at University of Mississippi (UMiss), and Professor Huan Yang at Perimeter Institute (PI) for inviting me to give talks remotely at their institutes. I also thank Professor Will Farr, Dr. Max Isi and the Simons Foundation for inviting to participate in the the Black-hole Ringdowns Workshop at Center for Computational Astrophysics (CCA).

In addition to the above, I would like to thank all my friends for the enjoyable time shared together to make my PhD life colorful. Specifically, I would thank Dr. Yunxuan Li, Dr. Jian Xu, Dr. Baoyi Chen, and Dr. Hao Xie, for career suggestions and help, and Xiuqi Ma for delicious food. I also thank JoAnn Boyd and Sofia Leon from PMA, Laura Flower Kim and Daniel Yoder from ISP, for their assistance on administrative issues and support on campus life, especially when I first arrived in the US.

I would like to thank my family, specifically my mother Mingying Gao and father Zhongnan Li, for raising me up and loving me. I am greatly indebted to my husband and soulmate, Shan Zhong, for all the love, care, and support along our way across the Pacific Ocean. Love Never Fails.

ABSTRACT

This thesis covers topics in gravitational wave physics, including optomechanical measurement theory, novel detection schemes (\mathcal{PT} -symmetric interferometer, matter-wave interferometer), and modeling of binary black hole ringdown waveform.

Measurements are accomplished through the interaction between signal and measurement devices. Identifying the nature of couplings is an important step in designing setups for specific applications. In Chapter II, we develop a general framework based on the system Hamiltonian to unambiguously classify optomechanical couplings. We add the new type, “coherent coupling”, where the mechanical oscillation couples several non-degenerate optical modes supported in the cavity. We give examples of different couplings, discuss in detail one particular case of the coherent coupling, and demonstrate its benefits in optomechanical experiments. Our general framework allows the design of optomechanical systems in a methodological way, to precisely exploit the strengths of some particular optomechanical couplings.

Conventional resonant detectors are subject to bandwidth-peak sensitivity trade-off, which can be traced back to the quantum Cramer-Rao Bound. Chapters III and IV in this thesis are devoted to the study of \mathcal{PT} -symmetric amplifier, which is a stable quantum amplification scheme enabled by two-mode non-degenerate parametric amplification. In Chapter III, we study stability and sensitivity improvements for laser-interferometric gravitational-wave detectors and microwave cavity axion detectors, under Hamiltonian formalism adopting single-mode and resolved-sideband approximations. In Chapter IV, we go beyond these approximations and consider realistic parameters in the optomechanical realization of \mathcal{PT} -symmetric interferometer for gravitational detection. We show that the main conclusion concerning stability remains intact using Nyquist analysis and a detailed time-domain simulation.

The detection method of gravitational waves is developed with linear quantum measurement theory. In Chapter V, we extend the usage of this theory to another kind of measurement device — matter-wave interferometers, which have been widely discussed as an important platform for many high-precision measurements. This theory allows us to consider fluctuations from both atoms and light and leads to a detailed analysis of back-action (of light back onto the atoms) and its effect on dynamics and measurement noise in atom interferometry. From this analysis, we

obtain a Standard Quantum Limit for matter-wave interferometry. We also give a comparison between the LIGO detector and matter-wave interferometer from the perspective of quantum measurement.

In Chapter VI, we switch focus from measurement to gravitational wave sources. Specifically, we study high-frequency gravitational radiation from the ringdown of a binary black hole merger. We study the high-precision modeling on both temporal and spatial features of ringdown wave to propose a more complete test of General Relativity. We show that spin-weighted spheroidal harmonics, rather than spin-weighted spherical harmonics, better represent ringdown angular patterns. We also study the correlation between progenitor binary properties and the excitation of quasinormal modes, including higher-order angular modes, overtones, prograde and retrograde modes. This chapter seeks to provide an analytical strategy and inspire the future development of ringdown tests using data from real gravitational wave events.

PUBLISHED CONTENT AND CONTRIBUTIONS

- [1] Xiang Li, Mikhail Korobko, Yiqiu Ma, Roman Schnabel, and Yanbei Chen. Coherent coupling completing an unambiguous optomechanical classification framework. *Phys. Rev. A*, 100(5):053855, 2019.
<https://link.aps.org/doi/10.1103/PhysRevA.100.053855>
X.L. participated in the conception of the project, formulated the optomechanical classification framework, analyzed and solved the ring cavity, and wrote the manuscript.
- [2] Yiqiu Ma, Xiang Li, Shengjun Yang, and Yanbei Chen. Linear quantum measurement theory of matter-wave interferometry. 11 2019.
<https://doi.org/10.48550/arXiv.1911.08697>
X.L. participated in the conception of the project, analyzed matter-wave interferometry in the framework of linear quantum measurement theory, and participated in the writing of the manuscript.
- [3] Xiang Li, Maxim Goryachev, Yiqiu Ma, Michael E. Tobar, Chunnong Zhao, Rana X. Adhikari, and Yanbei Chen. Broadband sensitivity improvement via coherent quantum feedback with PT symmetry. 12 2020.
<https://doi.org/10.48550/arXiv.2012.00836>
X.L. was involved in developing the idea, formulated and analyzed the PT-symmetric interferometer, and wrote the manuscript.
- [4] Xiang Li, Jiri Smetana, Amit Singh Ubhi, Joe Bentley, Yanbei Chen, Yiqiu Ma, Haixing Miao, and Denis Martynov. Enhancing interferometer sensitivity without sacrificing bandwidth and stability: Beyond single-mode and resolved-sideband approximation. *Phys. Rev. D*, 103(12):122001, 2021.
<https://link.aps.org/doi/10.1103/PhysRevD.103.122001>
X.L. developed the idea, did the frequency domain numerical analysis, and led the writing of the manuscript.
- [5] Xiang Li, Ling Sun, Rico Ka Lok Lo, Ethan Payne, and Yanbei Chen. Angular emission patterns of remnant black holes. *Phys. Rev. D*, 105(2):024016, 2022.
<https://link.aps.org/doi/10.1103/PhysRevD.105.024016>
X.L. developed the idea, did the numerical fitting, and led the writing of the manuscript.

TABLE OF CONTENTS

Acknowledgements	iii
Abstract	v
Published Content and Contributions	vii
Bibliography	vii
Table of Contents	vii
List of Illustrations	x
List of Tables	xiii
Chapter I: Introduction	1
1.1 Preface	1
1.2 Linear quantum measurement device for gravitational wave detection	1
1.3 Modeling of BBH ringdown gravitational waves	5
Bibliography	7
Chapter II: Classification of optomechanical interaction and the discovery of coherent coupling	21
2.1 Introduction	21
2.2 Classification of optomechanical couplings	24
2.3 Example of different couplings	27
2.4 Purely coherent coupling in a ring cavity system	32
2.5 Discussion	42
2.6 Appendix: Dispersive Hamiltonian	43
2.7 Appendix: Optoacoustic Hamiltonian	43
2.8 Appendix: Hamiltonian derivation of ring cavity system	44
2.9 Appendix: Optomechanical cooling limit in the ring cavity system	51
Bibliography	57
Chapter III: PT-symmetric amplifier: Broadband sensitivity improvement via coherent quantum feedback	64
3.1 Introduction	64
3.2 PT-symmetric amplifier	66
3.3 Comparison with the unstable amplifier	71
3.4 Application to laser interferometer GW detectors	75
3.5 Application to microwave axion detectors	77
3.6 Discussion	81
Bibliography	83
Chapter IV: Optomechanical realization of PT-symmetric interferometer	89
4.1 Introduction	89
4.2 From single-mode approximation to full analysis	91
4.3 Frequency-domain analysis	97
4.4 Time-domain analysis	106
4.5 Optimal readout scheme	112

4.6 Discussion	115
Bibliography	115
Chapter V: Atom interferometry: Linear quantum measurement theory and the precision limit	119
5.1 Introduction	119
5.2 Effective Hamiltonian of an atom interferometer	121
5.3 Interferometry solution	127
5.4 Back-action in atom interferometer pair	132
5.5 Dynamics of the effective operators: A more exact treatment	134
5.6 Conceptual comparison with the laser interferometer GW detector	140
5.7 Discussion	141
5.8 Appendix: Field formalism for atom interferometer	143
5.9 Appendix: Field quantization	148
5.10 Appendix: Mean field solutions	151
Bibliography	152
Chapter VI: High-precision modeling for gravitational waves of BBH remnants	157
6.1 Introduction	157
6.2 Ringdown models	159
6.3 Fit memory-free NR waveforms with QNM expansions	170
6.4 Fitting the benchmark GW150921-like binary	172
6.5 Nonspinning binaries with different mass ratios	179
6.6 Spinning binaries and retrograde excitation	184
6.7 Discussion	191
6.8 Appendix: QNM expansion conventions	192
6.9 Appendix: Limitation of single-direction fittings	195
6.10 Appendix: Numerical implementation for optimizing $\{B_{lmn}^{(\pm)}\}$	196
6.11 Appendix: Full fitting results for N1–N9	198
6.12 Appendix: Numerical error in SXS waveforms	198
Bibliography	210

LIST OF ILLUSTRATIONS

<i>Number</i>	<i>Page</i>
1.1 Block diagram of a linear quantum measurement device.	5
2.1 The comparison between coherent coupling and dispersive coupling.	26
2.2 Single cavity with a movable end mirror.	27
2.3 On-chip optomechanical coupling between the curved input waveguide and the optical racetrack cavity.	29
2.4 Mapping from three-mode optoacoustic system to a power and signal-recycled interferometer.	30
2.5 The coupled cavity configuration.	31
2.6 Ring cavity configuration and field labeling.	33
2.7 Cavity modes splitting caused by different membrane reflectivity r . .	34
2.8 Illustrating plot of \hat{c}_{\pm} wavefunction $P_{\pm}(z; x)$ in Eq. (2.81)	36
2.9 Pumping regime of sideband cooling.	40
3.1 Coherent quantum feedback for laser interferometer GW detectors. . .	65
3.2 Mode interaction and stability analysis.	67
3.3 Coherent amplification of sensitivity by sWLC and uWLC.	69
3.4 The comparison between sWLC and uWLC.	73
3.5 Nyquist Plot for the open-loop gain of sWLC and uWLC.	74
3.6 Example of GW noise spectra for sWLC and uWLC.	76
3.7 Illustration of the axion search.	78
3.8 Microwave axion detector and the Bode plots for signal transfer functions.	80
3.9 Sensitivity improvement for axion detection.	82
4.1 A schematics of the interferometer configuration with the signal-recycling cavity (SRC) as the optomechanical filter.	91
4.2 Idealized mode interaction structure of the optomechanical system illustrated in Fig. 4.1.	93
4.3 The signal-referred shot noise spectral density for different optomechanical interaction strengths G	94
4.4 The fields involved in the complete analysis of the scheme shown in Fig. 4.1.	96

4.5	Coupling between the optical modes and the mechanical modes represented in frequency domain.	98
4.6	The signal-referred shot-noise spectral densities from the full analysis in comparison with the one obtained from idealized Hamiltonian.	103
4.7	The noise spectral density for the idler channel.	103
4.8	The plots for the determinant of the open-loop transfer matrix, with vs. without optical spring compensation.	105
4.9	The plots for the determinant of the open-loop transfer matrix with different G/ω_s values, with optical spring compensated.	105
4.10	Field interactions at a mirror.	107
4.11	Logical flowchart of the time-domain simulation.	109
4.12	In-loop step-response of the position of the undamped mechanical oscillator.	111
4.13	Transfer functions for optical gain with optical-spring compensated.	112
4.14	Optical gain transfer functions for the signal and idler channels in the undamped, optical-spring-compensated system.	113
4.15	The normalized noise spectrum for the signal and idler channels.	114
5.1	Block diagram of a linear quantum measurement device.	121
5.2	A four-boson Raman interaction kernel and its corresponding WKB trajectory.	122
5.3	Comparison between atom interferometer and optical Mach-Zender interferometer.	129
5.4	Atom interferometer gravitational wave detector configuration.	133
5.5	Atom-light interaction kernel.	136
6.1	Convention of coordinate continuation from positive to negative values of the final spin.	160
6.2	Examples of complex QMN frequencies.	164
6.3	Polarization contents ($h_+(t)$, $h_\times(t)$) of the template ringdown waveform indexed with $(l, m) = (2, 2), (2, -2)$	167
6.4	The relative importance \mathcal{A}_{lm} as defined in Eq. (6.16).	173
6.5	Fitting results for the benchmark binary G0.	176
6.6	Fitting results for G0 using SXS data with different numerical levels.	177
6.7	The minimum distance χ_{\min}^2 obtained for binaries G0 and N1–N9 with different numbers of overtones.	180
6.8	The S model transition time t_{trans} for binaries G0 and N1–N9.	182

6.9	Example S model distances χ^2 for binaries G0 and N9, with respect to t_{offset}	183
6.10	The relative importance \mathcal{A}_{lm} of binaries A0–A3.	185
6.11	Polarization contents $(h_+(t), h_\times(t))$ of the ringdown waveform of binaries A0–A3.	187
6.12	Fitting results for binaries A0–A3 using the S model.	188
6.13	Fitting results for the binary waveforms A0–A3 using SXS data with different numerical levels.	189
6.14	Fitting results for binary waveform N1.	199
6.15	Fitting results for binary waveform N2.	200
6.16	Fitting results for binary waveform N3.	201
6.17	Fitting results for binary waveform N4.	202
6.18	Fitting results for binary waveform N5.	203
6.19	Fitting results for binary waveform N6.	204
6.20	Fitting results for binary waveform N7.	205
6.21	Fitting results for binary waveform N8.	206
6.22	Fitting results for binary waveform N9.	207
6.23	Fitting results for N1–N4 using SXS data with different numerical levels.	208
6.24	Fitting results for N5–N8 using SXS data with different numerical levels.	209
6.25	Fitting results for N9 using SXS data with different numerical levels.	210

LIST OF TABLES

<i>Number</i>	<i>Page</i>
4.1 A list of parameters and nominal values	95
6.1 Notations and terminology used in this chapter.	163
6.2 Conventions and notations for writing the QNM expansion.	165
6.3 SXS BBH waveforms used in Secs. 6.4–6.5.	173
6.4 The values of χ_{\min}^2 when fitting G0 with different (l, m) modes.	178
6.5 SXS BBH waveforms used in Sec. 6.6.	185
6.6 The values of χ_{\min}^2 when fitting with prograde modes only, vs. fitting with both prograde and retrograde modes.	189

Chapter 1

INTRODUCTION

1.1 Preface

Gravitational waves (GW) are *the ripples of space-time* predicted by Einstein's theory of General Relativity (GR). The detection of gravitational waves from a Binary Black Hole (BBH) merger in 2015 [1] opened a new window of astronomy observation.

Embedded in perturbation of space-time curvature, GWs can be treated as weak classical signals in experimental measurements. Oscillators are often used to measure weak signals, for which the quantum uncertainty and the measurement-induced back-action play important roles. Therefore, the analysis of such precision measurement processes must be carried out in a linear quantum measurement framework.

Many new methods and technology have been developed to enhance the detection sensitivity spectrum, together with the science case discussion on astrophysical sources for different frequency ranges. This thesis covers topics in these two aspects: on the detection side, it involves the development of quantum theory for detector improvement; on the source side, it involves modeling of BBH ringdown waveform.

1.2 Linear quantum measurement device for gravitational wave detection

In the early days of GW detection, excitations of mechanical oscillators (resonant bars) were read out by inductive, capacitive [2], or parametric [3] transducers and via a superconducting quantum interference device (SQUID) amplifier [2–4]. A more sensitive technique is to read out the phase fluctuations in a light beam (Michelson and Fabry-Perot type interferometers) [1, 5, 6] using photodetection. Signal recycling [7] and Resonant Sideband Extraction (RSE) [8] techniques were designed to optimize GW sensitivity by tailoring the optical frequency response.

1.2.1 Optomechanics and the interaction classification

Cavity optomechanics [9–12] studies the interaction between light and mechanical systems embedded into optical resonators. The precision at which modern optomechanical experiments operate allows us to study the quantum properties of light and matter, including the cooling of macroscopic oscillators to their quantum ground

state [13–15], optomechanical squeezing of quantum fluctuations in light [16–19], quantum entanglement between optical and mechanical degrees of freedom [20–23] as well as between space-like separated mechanical oscillators [21, 24–27] and non-classical states of mechanical oscillators [20, 27–30]. Optomechanics has become an experimental platform for testing quantum mechanics in the macroscopic world [21, 24, 31, 32] and looking for potential paths towards quantum gravity [27, 33–35]. Optomechanics has also been established as a toolbox for computational and metrological tasks, such as: frequency-converting microwaves to optical light [36–39], on-chip signal modulation and processing [40], nanoscale torque detection [41] and the detection of gravitational waves [1, 42, 43] with kilometer-scale detectors (Advanced LIGO [44, 45], Advanced Virgo [46, 47], GEO600 [48, 49], KAGRA [50, 51]).

While optomechanical systems vary in scale, frequency, and complexity, their theoretical description on a fundamental level can be reduced to simple Hamiltonians. Conventionally the coupling between the optical and mechanical degrees of freedom is classified based on intuitive physical picture of the setup. Most common are the systems with *dispersive* coupling, where the mechanical oscillation modulates the cavity’s resonance frequency [9]. The simplest case of such systems is a Fabry-Pérot cavity with a movable end mirror [52]. Another type of coupling is *dissipative* [53]: the oscillation modulates the coupling between the system and the environment. Any system with a movable mirror that simultaneously couples with the cavity modes and the pumping field can be viewed as having dissipative coupling, and the simplest example is a Fabry-Pérot cavity with a movable front mirror [54]. There exists another type of interaction where the mechanical oscillation modulates the coupling between two or more cavity modes [55]. In practice, a complex optomechanical system might not fit into one single type of interaction presented above, or might be misclassified. Therefore, we want a *mutually exclusive and collectively exhaustive* way of classification. Exploring such a problem defines the theme of Chapter II. Our classification strategy will help physicists approach the experimental design in a systematic way and choose the system that would perform optimally.

1.2.2 Novel schemes to bypass bandwidth-sensitivity trade-off

Since the first detection in 2015 [1], BBH systems have so far been the most commonly measured GW sources [56, 57]. The demand for extracting richer properties of the ringdown stage [58–62], as well as other astrophysical processes that produce

pronounced gravitational waves at high frequencies, calls for the broadband and high-frequency sensitivity of gravitational wave detectors.

In the canonical interferometer configuration [63], resonant arm cavities are used to increase the relative signal strength by effectively extending the length of the detector via repeated reflections of the optical field. However, the positive dispersion of the arm cavity makes the signal at higher frequencies no longer resonant. This leads to an inverse relationship between the peak sensitivity and bandwidth of the detector, known as the Mizuno limit [64]. This can be traced back to the energetic quantum limit [65, 66], which is also called the quantum Cramer-Rao Bound (QCRB) [67], and is therefore limited by the quantum fluctuation of the intracavity light field [68].

Bandwidth-sensitivity trade-off. – Early in 1990s, Mizuno noticed a trade-off between bandwidth and peak sensitivity [64] — analogous to the gain-bandwidth product in electronic amplifiers [69]. Braginsky et al. [65, 66] showed, using the energy-phase uncertainty relation, that the power spectral density of equivalent spacetime strain noise is $S_h(\Omega) \geq 4\hbar^2/S_{\mathcal{E}}(\Omega)$ where $S_{\mathcal{E}}$ is the spectral density of energy in the cavity, and

$$\int_0^{+\infty} d\Omega/(2\pi)S_h^{-1}(\Omega) \leq \Delta\mathcal{E}^2/(4\hbar^2). \quad (1.1)$$

This was also obtained by Tsang, et al. using Quantum Fisher Information [67], and further elaborated in Refs. [68, 70–72]. For coherent states, $\Delta\mathcal{E}^2 = \hbar\omega_0\mathcal{E}$, and in this case, Eq. (3.1) is also referred to as the *Energetic Quantum Limit* (EQL) for GW detection. The EQL trade-off applies to all quantum metrology experiments that use oscillators at coherent states. Specifically, GW detectors (of the laser interferometer type [1]) use optical resonators to increase the interaction between the spacetime strain and the laser light field. Axion detectors [73] (of the Sikivie Haloscope type [74]) use microwave resonators and a powerful permanent magnet to increase the interaction with the axion field and the microwave field. In both cases, the emphasis is on increasing the quality factor [75] of the resonance to maximize the transduction coefficient between the physical signal and an electrical readout variable. However, the EQL limits the useful bandwidth of the detector according to the gain-bandwidth trade-off.

In GW detection, the EQL can be surpassed when non-classical states of light are created for the arm cavity, with $\Delta\mathcal{E}^2 > \mathcal{E}^2/\bar{N}$ [76–79]. This can be implemented via squeezing injection [63, 80], or internal ponderomotive squeezing achieved by

optical springs [68, 81, 82]. To directly address the EQL, the concept of White-Light Cavity (WLC), which resonates with a broader spectrum of frequencies without sacrificing sensitivity, has been proposed [76–79, 83–87]. In the unstable WLC (uWLC) design of Miao et al. [77], a negative-dispersion optomechanical filter cavity is attached to the arm cavity [77], which can compensate for the phase gained in the arm cavity. However, this scheme is dynamically unstable and an additional stabilizing controller must be implemented, which makes the setup rather complex. In a later study [88], it was found that converting the signal-recycling cavity (SRC) into the optomechanical filter can lead to bandwidth broadening with a simpler optical layout, while the parameter regime considered still leads to an unstable system.

In Chapters III and IV, we introduce and model a parity-time (\mathcal{PT})-symmetric coherent quantum control strategy [88–91] that not only leads to a stable spectrum enhancement but also applies to a wide range of other quantum systems.

1.2.3 Matter-wave interferometer

Parallel to LIGO detector where the underlying principle is the interference of the electromagnetic waves, other concepts of GW detectors have also been proposed, even before the first detection event [1]. One particular attractive concept is the atom-interferometer GW detector, first raised by Dimopoulos et al. [92, 93] and later enriched by many further discussions [94–102]. Different from the LIGO, the physical principles under the atom-interferometer GW detector is the interference of the matter waves, rather than the light waves.

The advantage of the proposed application of atom interferometer in GW detection is mostly at low frequency (below 10 Hz), which can be understood as follows. Since the test masses are connected to the ground through suspension system, the sensitivity of a laser interferometer GW detector is seriously contaminated at low frequencies partly through the coupling of the test masses with the seismic oscillations, although the multi-stage vibration isolation technique has been applied [98]. For space-borne optical GW detector such as Laser Interferometer Space Antenna (LISA), the test masses are also connected to the satellite platforms, thereby the random motion of the satellites will be transferred onto the test masses and contaminate the GW signal. However, for the atom interferometer, since the atoms are free-falling during the interferometry process, they are less sensitive to the seismic perturbation (or the satellite motion in the space case). The laser noise can be re-

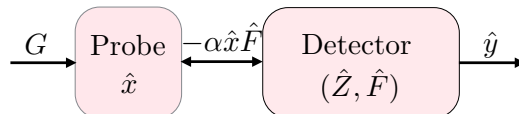


Figure 1.1: Block diagram of a linear quantum measurement device.

moved by designing the detector configuration with common mode rejection. More sophisticated designs such as implementing the large momentum transfer technique or optical cavities have been also discussed [103–107].

Typically, experimental devices such as GW detectors that targeted on measuring extremely weak signals are affected by the quantum mechanics. The theory of quantum measurement developed from the 1960s is a framework to analyze how quantum mechanics affects the sensitivity of an experimental device [108]. As shown in Fig. 1.1, in this framework, a quantum measurement device is divided into probe and detector, where the probe dynamical quantity \hat{x} is linearly coupled to G — the information to be measured. The probe and detector are coupled through linear Hamiltonian $\hat{H}_{\text{int}} = -\alpha \hat{x} \hat{F}$. The information of G will flow into the detector through probe-detector interaction \hat{H}_{int} and then be read out as $\hat{y}(t)$. The early resonant bar GW detectors and the current laser interferometer GW detectors have been extensively studied and understood using this quantum measurement theory framework [108–110].

For atom interferometry, although the effect of quantum noise has been discussed by various authors [111–114], a complete analysis under quantum measurement theory has not been discussed in the current literature. Establishing such a theory provides important insights in understanding the atom interferometer. In Chapter V, we set up a quantum measurement theory framework for analyzing the physics of atom interferometer based on the interaction between atom cloud and two optical fields. A comparison between the LIGO detector and matter-wave interferometer is also given from the perspective of quantum measurement.

1.3 Modeling of BBH ringdown gravitational waves

In gravitational wave observations, the prospective searches for ringdown waveforms [115, 116] would enable the tests of GR [117–120] from different aspects. With the rapidly increasing number of binary coalescences observed [121–124] by ground-based detectors like Advanced LIGO [125] and Advanced Virgo [126], events with detectable higher-order modes [127–129] are observed, e.g., GW190412 [130]

and GW190814 [131]. The detectability of higher-order modes not only impacts the parameter estimation [120, 132–136], but can be used to study angular emission as well. Currently, in the ringdown stage, a high signal-to-noise ratio (SNR) is difficult to achieve due to the lack of post-merger cycles and the degraded detector sensitivity at high frequency range. However, the sensitivity of the proposed next-generation detectors, including Einstein Telescope [137, 138], Cosmic Explorer [139, 140], and NEMO [141], will be significantly improved [142], especially at the high frequencies, opening more possibilities in the BBH post-merger studies [143].

The gravitational waves emitted at the final stage of a BBH merger, the ringdown stage, consist of a series of quasinormal modes (QNMs) [144–148]. QNMs are solutions to the homogeneous Teukolsky equation [149–152], i.e., the linearized Einstein’s equations in the background of a Kerr black hole, as described by numerous work since the 1970s [153–157]. The foundation for doing so follows models that describe stellar collapses [153–156] — the strong-field region “falls down” toward the future horizon of the final black hole, revealing a spacetime region in which perturbations satisfy the homogeneous Teukolsky equation with ingoing condition near the horizon, and outgoing condition near infinity.

The homogeneous Teukolsky equation predicts the *temporal* dependence of the ringdown waves, in terms of their *complex* spectra, as well as their *spatial* distributions, in terms of angular emission patterns. There have been many studies on black hole ringdown spectroscopy involving multiple angular frequencies by modeling it as the superposition of exponentially damped sinusoids [132, 134, 158–161], or using other methods of frequency extraction [162, 163]. Recently, it has been shown that the inclusion of overtones [147, 164] can improve the fitting of numerical relativity (NR) waveforms and lead to better estimation of ringdown model parameters [143, 161, 165], because of the better characterization of the post-merger signal from an earlier time.

Although a single event could provide limited information about angular dependence, combining multiple events and extracting angular-dependent features will become possible with the expected large number of events in the future. That calls for strategic studies of temporal-spatial emission patterns before more events with high ringdown SNR are observed. Many phenomenological fitting studies based on NR waveforms have been done [166–168], while most previous work focused on the ringdown temporal properties. As the temporal-spatial consistency check of ringdown emission can provide more complete tests of GR, exploring such a

problem defines the theme of Chapter VI.

References

- [1] Benjamin P Abbott et al. Observation of gravitational waves from a binary black hole merger. *Physical Review Letters*, 116(6):061102, 2016.
- [2] N Solomonson, WO Hamilton, W Johnson, and B Xu. Construction and performance of a low noise inductive transducer for the louisiana state university gravitational wave detector. *Review of scientific instruments*, 65(1):174–181, 1994.
- [3] D. G. Blair, E. N. Ivanov, M. E. Tobar, P. J. Turner, F. van Kann, and I. S. Heng. High sensitivity gravitational wave antenna with parametric transducer readout. *Phys. Rev. Lett.*, 74:1908–1911, Mar 1995.
- [4] E. Mauceli, Z. K. Geng, W. O. Hamilton, W. W. Johnson, S. Merkwitz, A. Morse, B. Price, and N. Solomonson. The allegro gravitational wave detector: Data acquisition and analysis. *Phys. Rev. D*, 54:1264–1275, Jul 1996.
- [5] B Abbott, R Abbott, R Adhikari, A Ageev, Bruce Allen, R Amin, SB Anderson, WG Anderson, M Araya, H Armandula, et al. Detector description and performance for the first coincidence observations between ligo and geo. *Nuclear Instruments and Methods in Physics Research Section A: Accelerators, Spectrometers, Detectors and Associated Equipment*, 517(1-3):154–179, 2004.
- [6] Rana X Adhikari. Gravitational radiation detection with laser interferometry. *Reviews of Modern Physics*, 86(1):121, 2014.
- [7] Brian J Meers. Recycling in laser-interferometric gravitational-wave detectors. *Physical Review D*, 38(8):2317, 1988.
- [8] Jun Mizuno, Kenneth A Strain, PG Nelson, JM Chen, Roland Schilling, Albrecht Rüdiger, Walter Winkler, and Karsten Danzmann. Resonant side-band extraction: a new configuration for interferometric gravitational wave detectors. *Physics Letters A*, 175(5):273–276, 1993.
- [9] Tobias J Kippenberg and Kerry J Vahala. Cavity optomechanics: back-action at the mesoscale. *Science*, 321(5893):1172–1176, 2008.
- [10] Ivan Favero and Khaled Karrai. Optomechanics of deformable optical cavities. *Nature Photonics*, 3(4):201, 2009.
- [11] Markus Aspelmeyer, Tobias J Kippenberg, and Florian Marquardt. Cavity optomechanics. *Reviews of Modern Physics*, 86(4):1391, 2014.

- [12] Warwick P Bowen and Gerard J Milburn. *Quantum optomechanics*. CRC press, 2015.
- [13] M Bhattacharya and Pierre Meystre. Trapping and cooling a mirror to its quantum mechanical ground state. *Physical Review Letters*, 99(7):073601, 2007.
- [14] Liu Yong-Chun, Hu Yu-Wen, Wong Chee Wei, and Xiao Yun-Feng. Review of cavity optomechanical cooling. *Chinese Physics B*, 22(11):114213, 2013.
- [15] Andreas Sawadsky, Henning Kaufer, Ramon Moghadas Nia, Sergey P Tarabrin, Farid Ya Khalili, Klemens Hammerer, and Roman Schnabel. Observation of generalized optomechanical coupling and cooling on cavity resonance. *Physical Review Letters*, 114(4):043601, 2015.
- [16] Thomas P Purdy, P L Yu, R W Peterson, N S Kampel, and C A Regal. Strong optomechanical squeezing of light. *Physical Review X*, 3(3):031012, 2013.
- [17] Andreas Kronwald, Florian Marquardt, and Aashish A Clerk. Dissipative optomechanical squeezing of light. *New Journal of Physics*, 16(6):063058, 2014.
- [18] Nancy Aggarwal, Torrey Cullen, Jonathan Cripe, Garrett D Cole, Robert Lanza, Adam Libson, David Follman, Paula Heu, Thomas Corbitt, and Nergis Mavalvala. Room temperature optomechanical squeezing. *arXiv preprint arXiv:1812.09942*, 2018.
- [19] Roman Schnabel. Squeezed states of light and their applications in laser interferometers, sec. 5.6. *Physics Reports*, 684:1–51, 2017.
- [20] S Bose, K Jacobs, and P L Knight. Preparation of nonclassical states in cavities with a moving mirror. *Physical Review A*, 56(5):4175, 1997.
- [21] Sougato Bose, Kurt Jacobs, and Peter L Knight. Scheme to probe the decoherence of a macroscopic object. *Physical Review A*, 59(5):3204, 1999.
- [22] David Vitali, Sylvain Gigan, Anderson Ferreira, H R Böhm, Paolo Tombesi, Ariel Guerreiro, Vlatko Vedral, Anton Zeilinger, and Markus Aspelmeyer. Optomechanical entanglement between a movable mirror and a cavity field. *Physical Review Letters*, 98(3):030405, 2007.
- [23] Haixing Miao, Stefan Danilishin, and Yanbei Chen. Universal quantum entanglement between an oscillator and continuous fields. *Physical Review A*, 81(5):052307, 2010.
- [24] Stefano Mancini, Vittorio Giovannetti, David Vitali, and Paolo Tombesi. Entangling macroscopic oscillators exploiting radiation pressure. *Physical Review Letters*, 88(12):120401, 2002.

- [25] M Bhattacharya, P-L Giscard, and Pierre Meystre. Entangling the rovibrational modes of a macroscopic mirror using radiation pressure. *Physical Review A*, 77(3):030303(R), 2008.
- [26] Michael J Hartmann and Martin B Plenio. Steady state entanglement in the mechanical vibrations of two dielectric membranes. *Physical Review Letters*, 101(20):200503, 2008.
- [27] Roman Schnabel. Einstein-podolsky-rosen–entangled motion of two massive objects. *Physical Review A*, 92(1):012126, 2015.
- [28] P D Nation. Nonclassical mechanical states in an optomechanical micromaser analog. *Physical Review A*, 88(5):053828, 2013.
- [29] Matteo Brunelli, Oussama Houhou, Darren W Moore, Andreas Nunnenkamp, Mauro Paternostro, and Alessandro Ferraro. Unconditional preparation of nonclassical states via linear-and-quadratic optomechanics. *Physical Review A*, 98(6):063801, 2018.
- [30] Emily J Davis, Zhaoyou Wang, Amir H Safavi-Naeini, and Monika H Schleier-Smith. Painting nonclassical states of spin or motion with shaped single photons. *Physical Review Letters*, 121(12):123602, 2018.
- [31] Yanbei Chen. Macroscopic quantum mechanics: theory and experimental concepts of optomechanics. *Journal of Physics B: Atomic, Molecular and Optical Physics*, 46(10):104001, 2013.
- [32] Tom P Purdy, Robert W Peterson, and C.A. Regal. Observation of radiation pressure shot noise on a macroscopic object. *Science*, 339(6121):801–804, 2013.
- [33] Mateusz Bawaj, Ciro Biancofiore, Michele Bonaldi, Federica Bonfigli, Antonio Borrielli, Giovanni Di Giuseppe, Lorenzo Marconi, Francesco Marino, Riccardo Natali, Antonio Pontin, et al. Probing deformed commutators with macroscopic harmonic oscillators. *Nature Communications*, 6:7503, 2015.
- [34] Jie Li, Stefano Zippilli, Jing Zhang, and David Vitali. Discriminating the effects of collapse models from environmental diffusion with levitated nanospheres. *Physical Review A*, 93(5):050102(R), 2016.
- [35] Alessio Belenchia, Dionigi M T Benincasa, Stefano Liberati, Francesco Marin, Francesco Marino, and Antonello Ortolan. Tests of quantum-gravity-induced nonlocality via optomechanical experiments. *Physical Review D*, 95(2):026012, 2017.
- [36] Lin Tian and Hailin Wang. Optical wavelength conversion of quantum states with optomechanics. *Physical Review A*, 82(5):053806, 2010.

- [37] Jeff T Hill, Amir H Safavi-Naeini, Jasper Chan, and Oskar Painter. Coherent optical wavelength conversion via cavity optomechanics. *Nature Communications*, 3:1196, 2012.
- [38] C F Ockeloen-Korppi, Erno Damskäg, J M Pirkkalainen, T T Heikkilä, Francesco Massel, and M A Sillanpää. Low-noise amplification and frequency conversion with a multiport microwave optomechanical device. *Physical Review X*, 6(4):041024, 2016.
- [39] F Lecocq, J B Clark, R W Simmonds, J Aumentado, and J D Teufel. Mechanically mediated microwave frequency conversion in the quantum regime. *Physical Review Letters*, 116(4):043601, 2016.
- [40] JG Huang, Y Li, Lip Ket Chin, H Cai, YD Gu, Muhammad Faeyz Karim, JH Wu, TN Chen, ZC Yang, YL Hao, et al. A dissipative self-sustained optomechanical resonator on a silicon chip. *Applied Physics Letters*, 112(5):051104, 2018.
- [41] Marcelo Wu, Aaron C Hryciw, Chris Healey, David P Lake, Harishankar Jayakumar, Mark R Freeman, John P Davis, and Paul E Barclay. Dissipative and dispersive optomechanics in a nanocavity torque sensor. *Physical Review X*, 4(2):021052, 2014.
- [42] David E McClelland, Nergis Mavalvala, Yanbei Chen, and Roman Schnabel. Advanced interferometry, quantum optics and optomechanics in gravitational wave detectors. *Laser & Photonics Reviews*, 5(5):677–696, 2011.
- [43] Benjamin P Abbott et al. Prospects for observing and localizing gravitational-wave transients with advanced ligo, advanced virgo and kagra. *Living Reviews in Relativity*, 21(1):3, 2018.
- [44] Gregory M Harry. Advanced ligo: the next generation of gravitational wave detectors. *Classical and Quantum Gravity*, 27(8):084006, 2010.
- [45] J Aasi et al. Advanced ligo. *Classical and quantum gravity*, 32(7):074001, 2015.
- [46] F Acernese et al. Advanced virgo: a second-generation interferometric gravitational wave detector. *Classical and Quantum Gravity*, 32(2):024001, 2014.
- [47] F Acernese et al. The advanced virgo detector. In *Journal of Physics: Conference Series*, volume 610, page 012014. IOP Publishing, 2015.
- [48] Harald Lück and the GEO600 Team. The geo600 project. *Classical and quantum gravity*, 14(6):1471, 1997.
- [49] C Affeldt, K Danzmann, KL Dooley, H Grote, M Hewitson, S Hild, J Hough, J Leong, H Lück, M Prijatelj, et al. Advanced techniques in geo 600. *Classical and quantum gravity*, 31(22):224002, 2014.

- [50] Yoichi Aso, Yuta Michimura, Kentaro Somiya, Masaki Ando, Osamu Miyakawa, Takanori Sekiguchi, Daisuke Tatsumi, and Hiroaki Yamamoto. Interferometer design of the kagra gravitational wave detector. *Physical Review D*, 88(4):043007, 2013.
- [51] Kentaro Somiya. Detector configuration of kagra—the japanese cryogenic gravitational-wave detector. *Classical and Quantum Gravity*, 29(12):124007, 2012.
- [52] Dustin Kleckner, William Marshall, Michiel J A de Dood, Khodadad Nima Dinyari, Bart-Jan Pors, William T M Irvine, and Dirk Bouwmeester. High finesse opto-mechanical cavity with a movable thirty-micron-size mirror. *Physical Review Letters*, 96(17):173901, 2006.
- [53] André Xuereb, Roman Schnabel, and Klemens Hammerer. Dissipative optomechanics in a michelson-sagnac interferometer. *Physical Review Letters*, 107(21):213604, 2011.
- [54] Sergey P Vyatchanin and Andrey B Matsko. Quantum speed meter based on dissipative coupling. *Physical Review A*, 93(6):063817, 2016.
- [55] Farid Ya Khalili, Sergey P Tarabrin, Klemens Hammerer, and Roman Schnabel. Generalized analysis of quantum noise and dynamic backaction in signal-recycled michelson-type laser interferometers. *Physical Review A*, 94(1):013844, 2016.
- [56] B. P. Abbott, R. Abbott, T. D. Abbott, S. Abraham, and et. al. Gwtc-1: A gravitational-wave transient catalog of compact binary mergers observed by ligo and virgo during the first and second observing runs. *Phys. Rev. X*, 9:031040, Sep 2019.
- [57] R. Abbott, T. D. Abbott, S. Abraham, F. Acernese, and et. al. Gwtc-2: Compact binary coalescences observed by ligo and virgo during the first half of the third observing run, 2020.
- [58] Ioannis Kamaretsos, Mark Hannam, Sascha Husa, and B. S. Sathyaprakash. Black-hole hair loss: Learning about binary progenitors from ringdown signals. *Phys. Rev. D*, 85:024018, Jan 2012.
- [59] Ioannis Kamaretsos, Mark Hannam, and B. S. Sathyaprakash. Is black-hole ringdown a memory of its progenitor? *Phys. Rev. Lett.*, 109:141102, Oct 2012.
- [60] Andrea Taracchini, Alessandra Buonanno, Gaurav Khanna, and Scott A. Hughes. Small mass plunging into a kerr black hole: Anatomy of the inspiral-merger-ringdown waveforms. *Phys. Rev. D*, 90:084025, Oct 2014.

- [61] B. P. Abbott, R. Abbott, T. D. Abbott, M. R. Abernathy, F. Acernese, K. Ackley, C. Adams, T. Adams, P. Addesso, R. X. Adhikari, V. B. Adya, C. Affeldt, M. Agathos, K. Agatsuma, N. Aggarwal, and et al Aguiar, O. D. First targeted search for gravitational-wave bursts from core-collapse supernovae in data of first-generation laser interferometer detectors. *Phys. Rev. D*, 94:102001, Nov 2016.
- [62] Scott A. Hughes, Anuj Apte, Gaurav Khanna, and Halston Lim. Learning about black hole binaries from their ringdown spectra. *Phys. Rev. Lett.*, 123:161101, Oct 2019.
- [63] H. J. Kimble, Yuri Levin, Andrey B. Matsko, Kip S. Thorne, and Sergey P. Vyatchanin. Conversion of conventional gravitational-wave interferometers into quantum nondemolition interferometers by modifying their input and/or output optics. *Phys. Rev. D*, 65:022002, Dec 2001.
- [64] Jun Mizuno. *Comparison of optical configurations for laser-interferometric gravitational-wave detectors*. PhD thesis, AEI-Hannover, MPI for Gravitational Physics, Max Planck Society, 1995.
- [65] Vladimir Braginsky and Farid Ya Khalili. *Quantum measurement*. Cambridge University Press, 1995.
- [66] Vladimir B Braginsky, Mikhail L Gorodetsky, Farid Ya Khalili, and Kip S Thorne. Energetic quantum limit in large-scale interferometers. In *AIP Conference Proceedings*, volume 523, pages 180–190. AIP, 2000.
- [67] Mankei Tsang, Howard M. Wiseman, and Carlton M. Caves. Fundamental quantum limit to waveform estimation. *Phys. Rev. Lett.*, 106:090401, Mar 2011.
- [68] Haixing Miao, Rana X Adhikari, Yiqiu Ma, Belinda Pang, and Yanbei Chen. Towards the fundamental quantum limit of linear measurements of classical signals. *Phys. Rev. Lett.*, 119:050801, Aug 2017.
- [69] E. A. Faulkner and J. B. Grimpleby. Active filters and gain-bandwidth product. *Electronics Letters*, 6(17):549–550, 1970.
- [70] Belinda Pang and Yanbei Chen. Quantum interactions between a laser interferometer and gravitational waves. *Physical Review D*, 98(12):124006, 2018.
- [71] Belinda Pang and Yanbei Chen. Fundamental relations between measurement, radiation, and decoherence in gravitational wave laser interferometer detectors. *Physical Review D*, 99(12):124016, 2019.
- [72] Haixing Miao, Nicolas D Smith, and Matthew Evans. Quantum limit for laser interferometric gravitational-wave detectors from optical dissipation. *Physical Review X*, 9(1):011053, 2019.

- [73] T. Braine, R. Cervantes, N. Crisosto, N. Du, S. Kimes, L. J. Rosenberg, G. Rybka, J. Yang, D. Bowering, A. S. Chou, R. Khatriwada, A. Sonnenschein, W. Wester, G. Carosi, N. Woollett, L. D. Duffy, R. Bradley, C. Boutan, M. Jones, B. H. LaRoque, N. S. Oblath, M. S. Taubman, J. Clarke, A. Dove, A. Eddins, S. R. O’Kelley, S. Nawaz, I. Siddiqi, N. Stevenson, A. Agrawal, A. V. Dixit, J. R. Gleason, S. Jois, P. Sikivie, J. A. Solomon, N. S. Sullivan, D. B. Tanner, E. Lentz, E. J. Daw, J. H. Buckley, P. M. Harrington, E. A. Henriksen, and K. W. Murch. Extended search for the invisible axion with the axion dark matter experiment. *Phys. Rev. Lett.*, 124:101303, Mar 2020.
- [74] P. Sikivie. Experimental tests of the "invisible" axion. *Phys. Rev. Lett.*, 51:1415–1417, Oct 1983.
- [75] I Stern, A A Chisholm, J Hoskins, P Sikivie, N S Sullivan, D B Tanner, G Carosi, and K van Bibber. Cavity design for high-frequency axion dark matter detectors. *Review of Scientific Instruments*, 86(12):123305, December 2015.
- [76] Minchuan Zhou, Zifan Zhou, and Selim M Shahriar. Quantum noise limits in white-light-cavity-enhanced gravitational wave detectors. *Physical Review D*, 92(8):082002, 2015.
- [77] Haixing Miao, Yiqiu Ma, Chunnong Zhao, and Yanbei Chen. Enhancing the bandwidth of gravitational-wave detectors with unstable optomechanical filters. *Physical review letters*, 115(21):211104, 2015.
- [78] Mikhail Korobko, Lisa Kleybolte, Stefan Ast, Haixing Miao, Yanbei Chen, and Roman Schnabel. Beating the standard sensitivity-bandwidth limit of cavity-enhanced interferometers with internal squeezed-light generation. *Physical review letters*, 118(14):143601, 2017.
- [79] Mikhail Korobko, Yiqiu Ma, Yanbei Chen, and Roman Schnabel. Quantum expander for gravitational-wave observatories. *arXiv preprint arXiv:1903.05930*, 2019.
- [80] Carlton M Caves. Quantum-mechanical noise in an interferometer. *Physical Review D*, 23(8):1693, 1981.
- [81] Alessandra Buonanno and Yanbei Chen. Quantum noise in second generation, signal-recycled laser interferometric gravitational-wave detectors. *Physical Review D*, 64(4):042006, 2001.
- [82] Alessandra Buonanno and Yanbei Chen. Signal recycled laser-interferometer gravitational-wave detectors as optical springs. *Physical Review D*, 65(4):042001, 2002.
- [83] A Wicht, Karsten Danzmann, M Fleischhauer, M Scully, G Müller, and R-H Rinkelf. White-light cavities, atomic phase coherence, and gravitational wave detectors. *Optics Communications*, 134(1-6):431–439, 1997.

- [84] Stacy Wise, G Mueller, D Reitze, DB Tanner, and Bernard F Whiting. Linewidth-broadened fabry–perot cavities within future gravitational wave detectors. *Classical and Quantum Gravity*, 21(5):S1031, 2004.
- [85] Stacy Wise, V Quetschke, AJ Deshpande, G Mueller, DH Reitze, DB Tanner, BF Whiting, Y Chen, A Tünnermann, E Kley, et al. Phase effects in the diffraction of light: beyond the grating equation. *Physical review letters*, 95(1):013901, 2005.
- [86] GS Pati, M Salit, K Salit, and MS Shahriar. Demonstration of a tunable-bandwidth white-light interferometer using anomalous dispersion in atomic vapor. *Physical review letters*, 99(13):133601, 2007.
- [87] Yiqiu Ma, Haixing Miao, Chunnong Zhao, and Yanbei Chen. Quantum noise of a white-light cavity using a double-pumped gain medium. *Physical Review A*, 92(2):023807, 2015.
- [88] Joe Bentley, Philip Jones, Denis Martynov, Andreas Freise, and Haixing Miao. Converting the signal-recycling cavity into an unstable optomechanical filter to enhance the detection bandwidth of gravitational-wave detectors. *Phys. Rev. D*, 99:102001, May 2019.
- [89] A. Metelmann and A. A. Clerk. Quantum-limited amplification via reservoir engineering. *Phys. Rev. Lett.*, 112:133904, Apr 2014.
- [90] Zhong-Peng Liu, Jing Zhang, Şahin Kaya Özdemir, Bo Peng, Hui Jing, Xin-You Lü, Chun-Wen Li, Lan Yang, Franco Nori, and Yu-xi Liu. Metrology with pt-symmetric cavities: enhanced sensitivity near the pt-phase transition. *Physical review letters*, 117(11):110802, 2016.
- [91] Yu-Xin Wang and A. A. Clerk. Non-hermitian dynamics without dissipation in quantum systems. *Phys. Rev. A*, 99:063834, Jun 2019.
- [92] S. Dimopoulos, P. W. Graham, J. M. Hogan, M. A. Kasevich, and S. Rajendran. Gravitational wave detection with atom interferometry. *Physics Letter B*, 678:37–40, jul 2009.
- [93] Savas Dimopoulos, Peter W. Graham, Jason M. Hogan, Mark A. Kasevich, and Surjeet Rajendran. Atomic gravitational wave interferometric sensor. *Phys. Rev. D*, 78:122002, Dec 2008.
- [94] G M Tino and F Vetrano. Is it possible to detect gravitational waves with atom interferometers? *Classical and Quantum Gravity*, 24(9):2167–2178, apr 2007.
- [95] N. Yu and M. Tinto. Gravitational wave detection with single-laser atom interferometers. *Gen. Rel. Grav.*, 43:1943–1952, jul 2011.

- [96] P. L. Bender. Limitations of atom interferometry for gravitational wave observations in space. *Gen. Relativ. Gravit.*, 44(711), Nov 2012.
- [97] Peter W. Graham, Jason M. Hogan, Mark A. Kasevich, and Surjeet Rajendran. New method for gravitational wave detection with atomic sensors. *Phys. Rev. Lett.*, 110:171102, apr 2013.
- [98] Jan Harms, Bram J. J. Slagmolen, Rana X. Adhikari, M. Coleman Miller, Matthew Evans, Yanbei Chen, Holger Mueller, and Masaki Ando. Low-frequency terrestrial gravitational-wave detectors. *Phys. Rev. D*, 88:122003, Dec 2013.
- [99] Remi Geiger. Future gravitational wave detectors based on atom interferometry. In Gerard Auger and Eric Plagnol, editors, *An Overview of Gravitational Waves: Theory, Sources and Detection*, pages 285–313. World Scientific, 2017.
- [100] Peter W. Graham and Sunghoon Jung. Localizing gravitational wave sources with single-baseline atom interferometers. *Phys. Rev. D*, 97:024052, Jan 2018.
- [101] J. Junca, A. Bertoldi, D. O. Sabulsky, G. Lefevre, X. Zou, J.-B. Decitre, R. Geiger, A. Landragin, S. Gaffet, P. Bouyer, and B. Canuel. Characterizing earth gravity field fluctuations with the miga antenna for future gravitational wave detectors. *Phys. Rev. D*, 99:104026, may 2019.
- [102] Ming-Sheng Zhan, Jin Wang, Wei-Tou Ni, Dong-Feng Gao, Gang Wang, Ling-Xiang He, Run-Bing Li, Lin Zhou, Xi Chen, Jia-Qi Zhong, Biao Tang, Zhan-Wei Yao, Lei Zhu, Zong-Yuan Xiong, Si-Bin Lu, Geng-Hua Yu, Qun-Feng Cheng, Min Liu, Yu-Rong Liang, Peng Xu, Xiao-Dong He, Min Ke, Zheng Tan, and Jun Luo. ZAIGA: Zhaoshan Long-baseline Atom Interferometer Gravitation Antenna. *arXiv e-prints*, page arXiv:1903.09288, Mar 2019.
- [103] Holger Mueller, Sheng-wei Chiow, Quan Long, Sven Herrmann, and Steven Chu. Atom interferometry with up to 24-photon-momentum-transfer beam splitters. *Phys. Rev. Lett.*, 100:180405, May 2008.
- [104] Pierre Clade, Saidada Guellati-Khelifa, Francois Nez, and Francois Biraben. Large momentum beam splitter using bloch oscillations. *Phys. Rev. Lett.*, 102:240402, Jun 2009.
- [105] Onur Hosten, Nils J. Engelsen, Rajiv Krishnakumar, and Mark A. Kasevich. Measurement noise 100 times lower than the quantum-projection limit using entangled atoms. *Nature*, 529:505 EP –, 01 2016.
- [106] Paul Hamilton, Matt Jaffe, Justin M. Brown, Lothar Maisenbacher, Brian Estey, and Holger Mueller. Atom interferometry in an optical cavity. *Phys. Rev. Lett.*, 114:100405, Mar 2015.

- [107] B. Canuel, A. Bertoldi, L. Amand, E. Pozzo di Borgo, T. Chantrait, C. Danquigny, M. Dovale Álvarez, B. Fang, A. Freise, R. Geiger, J. Gillot, S. Henry, J. Hinderer, D. Holleville, J. Junca, G. Lefèvre, M. Merzougui, N. Mielec, T. Monfret, S. Pelisson, M. Prevedelli, S. Reynaud, I. Riou, Y. Rogister, S. Rosat, E. Cormier, A. Landragin, W. Chaibi, S. Gaffet, and P. Bouyer. Exploring gravity with the miga large scale atom interferometer. *Scientific Reports*, 8(1):14064, 2018.
- [108] V. B. Braginsky, F. Y. Khalili, and K. S. Thorne. *Quantum Measurement*. Cambridge University Press, sep 1992.
- [109] H. J. Kimble, Yuri Levin, Andrey B. Matsko, Kip S. Thorne, and Sergey P. Vyatchanin. Conversion of conventional gravitational-wave interferometers into quantum nondemolition interferometers by modifying their input and/or output optics. *Phys. Rev. D*, 65:022002, Dec 2001.
- [110] Alessandra Buonanno and Yanbei Chen. Signal recycled laser-interferometer gravitational-wave detectors as optical springs. *Phys. Rev. D*, 65:042001, Jan 2002.
- [111] W. M. Itano, J. C. Bergquist, J. J. Bollinger, J. M. Gilligan, D. J. Heinzen, F. L. Moore, M. G. Raizen, and D. J. Wineland. Quantum projection noise: Population fluctuations in two-level systems. *Phys. Rev. A*, 47:3554–3570, May 1993.
- [112] J. Jacobson, G. Bjork, and Y. Yamamoto. Quantum limit for the atom-light interferometer. *Applied Physics B: Lasers and Optics*, 60:187–191, feb 1995.
- [113] Jonathan P. Dowling. Correlated input-port, matter-wave interferometer: Quantum-noise limits to the atom-laser gyroscope. *Phys. Rev. A*, 57:4736–4746, jun 1998.
- [114] Marlan O. Scully and Jonathan P. Dowling. Quantum-noise limits to matter-wave interferometry. *Phys. Rev. A*, 48:3186–3190, Oct 1993.
- [115] Emanuele Berti, Jaime Cardoso, Vitor Cardoso, and Marco Cavaglia. Matched-filtering and parameter estimation of ringdown waveforms. *Phys. Rev. D*, 76:104044, 2007.
- [116] Andrea Maselli, Kostas Kokkotas, and Pablo Laguna. Observing binary black hole ringdowns by advanced gravitational wave detectors. *Phys. Rev. D*, 95(10):104026, 2017.
- [117] Vitor Cardoso and Leonardo Gualtieri. Testing the black hole ‘no-hair’ hypothesis. *Class. Quant. Grav.*, 33(17):174001, 2016.
- [118] Maximiliano Isi, Matthew Giesler, Will M. Farr, Mark A. Scheel, and Saul A. Teukolsky. Testing the no-hair theorem with GW150914. *Phys. Rev. Lett.*, 123:111102, Sep 2019.

- [119] B. P. Abbott et al. Tests of General Relativity with the Binary Black Hole Signals from the LIGO-Virgo Catalog GWTC-1. *Phys. Rev. D*, 100(10):104036, 2019.
- [120] R. Abbott et al. Tests of General Relativity with Binary Black Holes from the second LIGO-Virgo Gravitational-Wave Transient Catalog, 10 2020.
- [121] B. P. Abbott et al. Binary Black Hole Mergers in the first Advanced LIGO Observing Run. *Phys. Rev. X*, 6(4):041015, 2016. [Erratum: <https://journals.aps.org/prx/abstract/10.1103/PhysRevX.8.039903> *Phys. Rev. X* 8, 039903 (2018)].
- [122] B. P. Abbott et al. GWTC-1: A Gravitational-Wave Transient Catalog of Compact Binary Mergers Observed by LIGO and Virgo during the First and Second Observing Runs. *Phys. Rev. X*, 9(3):031040, 2019.
- [123] Tejaswi Venumadhav, Barak Zackay, Javier Roulet, Liang Dai, and Matias Zaldarriaga. New binary black hole mergers in the second observing run of advanced ligo and advanced virgo. *Phys. Rev. D*, 101:083030, Apr 2020.
- [124] R. Abbott et al. GWTC-2: Compact Binary Coalescences Observed by LIGO and Virgo During the First Half of the Third Observing Run, 10 2021.
- [125] J. Aasi et al. Advanced LIGO. *Class. Quant. Grav.*, 32:074001, 2015.
- [126] F. Acernese et al. Advanced Virgo: a second-generation interferometric gravitational wave detector. *Class. Quant. Grav.*, 32(2):024001, 2015.
- [127] James Healy, Pablo Laguna, Larne Pekowsky, and Deirdre Shoemaker. Template Mode Hierarchies for Binary Black Hole Mergers. *Phys. Rev. D*, 88(2):024034, 2013.
- [128] Larne Pekowsky, James Healy, Deirdre Shoemaker, and Pablo Laguna. Impact of higher-order modes on the detection of binary black hole coalescences. *Phys. Rev. D*, 87(8):084008, 2013.
- [129] Cameron Mills and Stephen Fairhurst. Measuring gravitational-wave higher-order multipoles. *Phys. Rev. D*, 103:024042, Jan 2021.
- [130] R. Abbott et al. GW190412: Observation of a Binary-Black-Hole Coalescence with Asymmetric Masses. *Phys. Rev. D*, 102(4):043015, 2020.
- [131] R. Abbott et al. GW190814: Gravitational Waves from the Coalescence of a 23 Solar Mass Black Hole with a 2.6 Solar Mass Compact Object. *Astrophys. J. Lett.*, 896(2):L44, 2020.
- [132] Richard Brito, Alessandra Buonanno, and Vivien Raymond. Black-hole spectroscopy by making full use of gravitational-wave modeling. *Phys. Rev. D*, 98:084038, Oct 2018.

- [133] Roberto Cotesta, Alessandra Buonanno, Alejandro Bohé, Andrea Taracchini, Ian Hinder, and Serguei Ossokine. Enriching the symphony of gravitational waves from binary black holes by tuning higher harmonics. *Phys. Rev. D*, 98:084028, Oct 2018.
- [134] Gregorio Carullo, Walter Del Pozzo, and John Veitch. Observational Black Hole Spectroscopy: A time-domain multimode analysis of GW150914. *Phys. Rev. D*, 99(12):123029, 2019. [Erratum: <https://link.aps.org/doi/10.1103/PhysRevD.100.089903>Phys.Rev.D 100, 089903 (2019)].
- [135] Ethan Payne, Colm Talbot, and Eric Thrane. Higher order gravitational-wave modes with likelihood reweighting. *Phys. Rev. D*, 100:123017, Dec 2019.
- [136] Jacob Lange, Richard O’Shaughnessy, and Monica Rizzo. Rapid and accurate parameter inference for coalescing, precessing compact binaries, 2018.
- [137] M. Punturo et al. The Einstein Telescope: A third-generation gravitational wave observatory. *Class. Quant. Grav.*, 27:194002, 2010.
- [138] Michele Maggiore et al. Science Case for the Einstein Telescope. *JCAP*, 03:050, 2020.
- [139] David Reitze et al. Cosmic Explorer: The U.S. Contribution to Gravitational-Wave Astronomy beyond LIGO. *Bull. Am. Astron. Soc.*, 51(7):035, 2019.
- [140] Evan D. Hall et al. Gravitational-wave physics with Cosmic Explorer: limits to low-frequency sensitivity, 12 2020.
- [141] K. Ackley et al. Neutron Star Extreme Matter Observatory: A kilohertz-band gravitational-wave detector in the global network. *Publ. Astron. Soc. Austral.*, 37:e047, 2020.
- [142] Divyajyoti, Preet Baxi, Chandra Kant Mishra, and K. G. Arun. Detectability of gravitational higher order modes in the 3G era, 3 2021.
- [143] Xisco Jiménez Forteza, Swetha Bhagwat, Paolo Pani, and Valeria Ferrari. Spectroscopy of binary black hole ringdown using overtones and angular modes. *Phys. Rev. D*, 102:044053, Aug 2020.
- [144] E. W. Leaver. An Analytic representation for the quasi normal modes of Kerr black holes. *Proc. Roy. Soc. Lond. A*, 402:285–298, 1985.
- [145] Kostas D. Kokkotas and Bernd G. Schmidt. Quasinormal modes of stars and black holes. *Living Rev. Rel.*, 2:2, 1999.
- [146] Hans-Peter Nollert. TOPICAL REVIEW: Quasinormal modes: the characteristic ‘sound’ of black holes and neutron stars. *Class. Quant. Grav.*, 16:R159–R216, 1999.

- [147] Emanuele Berti, Vitor Cardoso, and Andrei O. Starinets. Quasinormal modes of black holes and black branes. *Class. Quant. Grav.*, 26:163001, 2009.
- [148] Maximiliano Isi and Will M. Farr. Analyzing black-hole ringdowns, 7 2021.
- [149] Saul A. Teukolsky. Rotating black holes: Separable wave equations for gravitational and electromagnetic perturbations. *Phys. Rev. Lett.*, 29:1114–1118, Oct 1972.
- [150] Saul A. Teukolsky. Perturbations of a Rotating Black Hole. I. Fundamental Equations for Gravitational, Electromagnetic, and Neutrino-Field Perturbations. *Astrophys. J.*, 185:635–648, October 1973.
- [151] William H. Press and Saul A. Teukolsky. Perturbations of a Rotating Black Hole. II. Dynamical Stability of the Kerr Metric. *Astrophys. J.*, 185:649–674, October 1973.
- [152] Gregory B. Cook and Maxim Zaltskiy. Gravitational perturbations of the Kerr geometry: High-accuracy study. *Phys. Rev. D*, 90(12):124021, 2014.
- [153] Richard H. Price. Nonspherical Perturbations of Relativistic Gravitational Collapse. I. Scalar and Gravitational Perturbations. *Phys. Rev. D*, 5:2419–2438, May 1972.
- [154] Richard H. Price. Nonspherical Perturbations of Relativistic Gravitational Collapse. II. Integer-Spin, Zero-Rest-Mass Fields. *Phys. Rev. D*, 5:2439–2454, May 1972.
- [155] C. T. Cunningham, R. H. Price, and V. Moncrief. Radiation from collapsing relativistic stars. I - Linearized odd-parity radiation. *Astrophys. J.*, 224:643, 1978.
- [156] C. T. Cunningham, R. H. Price, and V. Moncrief. Radiation from collapsing relativistic stars. II. Linearized even-parity radiation. *Astrophys. J.*, 230:870–892, 1979.
- [157] Saul A Teukolsky. The kerr metric. *Classical and Quantum Gravity*, 32(12):124006, jun 2015.
- [158] Thibault Damour and Alessandro Nagar. New analytic representation of the ringdown waveform of coalescing spinning black hole binaries. *Phys. Rev. D*, 90:024054, Jul 2014.
- [159] B. P. Abbott et al. Tests of general relativity with GW150914. *Phys. Rev. Lett.*, 116(22):221101, 2016. [Erratum: <https://journals.aps.org/prl/abstract/10.1103/PhysRevLett.121.129902>Phys. Rev. Lett. 121, 129902 (2018)].
- [160] Walter Del Pozzo and Alessandro Nagar. Analytic family of post-merger template waveforms. *Phys. Rev. D*, 95:124034, Jun 2017.

- [161] Gregory B. Cook. Aspects of multimode Kerr ringdown fitting. *Phys. Rev. D*, 102:024027, Jul 2020.
- [162] Emanuele Berti, Vitor Cardoso, Jose A. Gonzalez, and Ulrich Sperhake. Mining information from binary black hole mergers: A Comparison of estimation methods for complex exponentials in noise. *Phys. Rev. D*, 75:124017, 2007.
- [163] Hiroyuki Nakano, Tatsuya Narikawa, Ken-ichi Oohara, Kazuki Sakai, Hisaaki Shinkai, Hirotaka Takahashi, Takahiro Tanaka, Nami Uchikata, Shun Yamamoto, and Takahiro S. Yamamoto. Comparison of various methods to extract ringdown frequency from gravitational wave data. *Phys. Rev. D*, 99(12):124032, 2019.
- [164] Emanuele Berti and Vitor Cardoso. Quasinormal ringing of Kerr black holes. I. The Excitation factors. *Phys. Rev. D*, 74:104020, 2006.
- [165] Matthew Giesler, Maximiliano Isi, Mark A. Scheel, and Saul A. Teukolsky. Black hole ringdown: The importance of overtones. *Phys. Rev. X*, 9:041060, Dec 2019.
- [166] Lionel London, Deirdre Shoemaker, and James Healy. Modeling ringdown: Beyond the fundamental quasinormal modes. *Phys. Rev. D*, 90(12):124032, 2014. [Erratum: *Phys.Rev.D* 94, 069902 (2016)].
- [167] Xisco Jiménez-Forteza, David Keitel, Sascha Husa, Mark Hannam, Sebastian Khan, and Michael Pürrer. Hierarchical data-driven approach to fitting numerical relativity data for nonprecessing binary black holes with an application to final spin and radiated energy. *Phys. Rev. D*, 95(6):064024, 2017.
- [168] L. T. London. Modeling ringdown. II. Aligned-spin binary black holes, implications for data analysis and fundamental theory. *Phys. Rev. D*, 102(8):084052, 2020.

*Chapter 2***CLASSIFICATION OF OPTOMECHANICAL INTERACTION
AND THE DISCOVERY OF COHERENT COUPLING**

In most optomechanical systems, a movable mirror is a part of an optical cavity, and its oscillation modulates either the resonance frequency of the cavity or its coupling to the environment. There exists the third option — which we call “coherent coupling” — when the mechanical oscillation couples several non-degenerate optical modes supported by the cavity. Identifying the nature of the coupling can be an important step in designing the setup for a specific application. In order to unambiguously distinguish between different optomechanical couplings, we develop a general framework based on the Hamiltonian of the system. Using this framework, we give examples of different couplings and discuss in detail one particular case of a purely coherent coupling in a ring cavity with a movable mirror inside. We demonstrate that in certain cases coherent coupling can be beneficial for cooling the motion of the mechanical oscillator. Our general framework allows us to approach the design of optomechanical experiments in a methodological way, for precise exploitation of the strengths of particular optomechanical couplings.

2.1 Introduction

Cavity optomechanics [1–4] studies the interaction between light and mechanical systems embedded into optical resonators. The precision at which modern optomechanical experiments operate allows us to study the quantum properties of light and matter, including the cooling of macroscopic oscillators to their quantum ground state [5–7], optomechanical squeezing of quantum fluctuations in light [8–11], quantum entanglement between optical and mechanical degrees of freedom [12–15], as well as between space-like separated mechanical oscillators [13, 16–19] and non-classical states of mechanical oscillators [12, 19–22]. Optomechanics has become an experimental platform for testing quantum mechanics in the macroscopic world [13, 16, 23, 24] and looking for potential paths towards quantum gravity [19, 25–27]. Optomechanics has also been established as a toolbox for computational and metrological tasks, such as: frequency-converting microwaves to optical light [28–31], on-chip signal modulation and processing [32], nanoscale torque detection [33], and the detection of gravitational waves [34–36] with kilometer-scale

detectors (Advanced LIGO [37, 38], Advanced Virgo [39, 40], GEO600 [41, 42], KAGRA [43, 44]).

While optomechanical systems vary in scale, frequency, and complexity, their theoretical description on a fundamental level can be reduced to simple Hamiltonians. Conventionally the coupling between the optical and mechanical degrees of freedom is classified based on intuitive physical picture of the setup. Most common are the systems with *dispersive* coupling, where the mechanical oscillation modulates the cavity's resonance frequency [1]. The simplest case of such systems is a Fabry-Pérot cavity with a movable end mirror [45]. Another type of coupling is *dissipative* [46]: the oscillation modulates the coupling between the system and the environment. Any system with a movable mirror that simultaneously couples with the cavity modes and the pumping field can be viewed as having dissipative coupling, and the simplest example is a Fabry-Pérot cavity with a movable front mirror [47]. There exists another type of interaction where the mechanical oscillation modulates the coupling between two or more cavity modes [48]. In practice, a complex optomechanical system might not fit into one single type of interaction presented above, or might be misclassified. Therefore, we want a *mutually exclusive and collectively exhaustive* way of classification.

To illustrate the necessity for such a classification, we show how the coupling could be identified ambiguously when the description of one optomechanical system has different forms depending on the choice of cavity basis modes. We consider two optical modes \hat{a}_1, \hat{a}_2 with frequencies ω_1, ω_2 coupled via the mechanical oscillation x . Such system is described by the following intuitive Hamiltonian:

$$\hat{H}_{\text{cav}} = \hbar\omega_1\hat{a}_1^\dagger\hat{a}_1 + \hbar\omega_2\hat{a}_2^\dagger\hat{a}_2 + \hbar g_{12}x(\hat{a}_1^\dagger\hat{a}_2 + \text{h.c.}). \quad (2.1)$$

If the system is classified simply based on this Hamiltonian, it could fall into the category of "optical modes coupled by mechanical oscillation." However, this Hamiltonian would have two different forms based on the parameters of the system. The first case is when the frequencies of the modes \hat{a}_1, \hat{a}_2 are equal ($\omega_1 = \omega_2$). Then Eq. (2.1) can be presented in another form:

$$\hat{H}'_{\text{cav}} = \hbar(\omega_1 - g_{12}x)\hat{a}'_1{}^\dagger\hat{a}'_1 + \hbar(\omega_1 + g_{12}x)\hat{a}'_2{}^\dagger\hat{a}'_2, \quad (2.2)$$

with the following choice of basis modes:

$$\hat{a}'_1 = \frac{\hat{a}_1 - \hat{a}_2}{\sqrt{2}}, \quad \hat{a}'_2 = \frac{\hat{a}_1 + \hat{a}_2}{\sqrt{2}}. \quad (2.3)$$

Such Hamiltonian is a dispersive one: the resonant frequencies of the modes are modulated by the mechanical oscillation. The second case is when the eigenfrequencies of the modes $\hat{a}_{1,2}$ are separated by $\Delta\omega \equiv (\omega_2 - \omega_1)/2$. Then we can define a new basis of x -dependent modes $\hat{a}''_{1,2}(x)$:

$$\hat{a}''_1(x) = \hat{a}_1 - \frac{g_{12}}{2\Delta\omega}x\hat{a}_2, \quad \hat{a}''_2(x) = \hat{a}_2 + \frac{g_{12}}{2\Delta\omega}x\hat{a}_1, \quad (2.4)$$

where we assume mechanical oscillation to be small ($g_{12}x \ll |\Delta\omega|$) and keep only the terms linear in x . Under this basis the Hamiltonian in Eq. (2.1) takes another form:

$$\hat{H}''_{\text{cav}} = \hbar\omega_1\hat{a}''_1{}^\dagger(x)\hat{a}''_1(x) + \hbar\omega_2\hat{a}''_2{}^\dagger(x)\hat{a}''_2(x), \quad (2.5)$$

where the modes themselves have x -dependence. Such a form of the optomechanical coupling is distinct from either the dispersive or the dissipative coupling. We call it *coherent* coupling and will define rigorously in the next section. These three different forms of the Hamiltonian illustrate the ambiguity: Eq. (2.1) describes the coupling between the two modes via the mechanical oscillation, but in different regimes depending on $\Delta\omega$, it could also be either classified as dispersive coupling in Eq. (2.2), or have some new form in Eq. (2.5). However, one system should have a unique classification, which is determined by the physical properties, not by the choice of basis. Identifying the coupling correctly and uniquely is important for optimizing the design of the experiment. Thus, an unambiguous classification framework is necessary.

In this work, we establish a general framework for the unambiguous classification of the optomechanical systems. The chapter is organized as follows: Sec. 2.2 provides a step-by-step strategy for expressing the Hamiltonian in a canonical form and discriminating between different x -dependence. We make emphasis in this section on the coherent coupling, which has not been widely recognized as a separate type of optomechanical coupling. Sec. 2.3 gives some examples from the literature, including possible ambiguities that could arise in identifying couplings and how our approach helps to resolve them. We provide a further focus on the purely coherent coupling in Sec. 2.4, where we investigate an optomechanical ring cavity system [49–51]. We provide an application example where in certain cases this coupling is beneficial for laser cooling of the mechanical oscillator to its ground state. Sec. 2.5 includes a summary of the chapter and further discussion.

2.2 Classification of optomechanical couplings

In this section we provide a step-by-step strategy that will lead to a unique classification for each cavity optomechanical system and help to avoid potential ambiguity. We start by expressing the total optical Hamiltonian in a canonical form that can describe any optomechanical system with multiple optical and mechanical degrees of freedom:

$$\hat{H}(\mathbf{x}) = \hbar \hat{\mathbf{a}}^\dagger(\mathbf{x}) \Omega(\mathbf{x}) \hat{\mathbf{a}}(\mathbf{x}) + i\hbar \left(\hat{\mathbf{a}}^\dagger(\mathbf{x}) \mathbb{F}(\mathbf{x}) \hat{\mathbf{b}} - \text{h.c.} \right), \quad (2.6)$$

where $\mathbf{x} = \{x_1, x_2, \dots\}$ are the displacements of mechanical oscillators from their equilibrium positions; $\hat{\mathbf{a}}(\mathbf{x}) = (\hat{a}_1(\mathbf{x}), \hat{a}_2(\mathbf{x}), \dots)^\text{T}$ are the cavity eigenmodes, such that $\Omega(\mathbf{x}) = \text{diag}(\omega_1(\mathbf{x}), \omega_2(\mathbf{x}), \dots)$ is a diagonal matrix with the corresponding eigenfrequencies; $\hat{\mathbf{b}} = (\hat{b}_1, \hat{b}_2, \dots)^\text{T}$ are the external electromagnetic modes, which couple to cavity eigenmodes with coupling rates $\mathbb{F}(\mathbf{x}) = \text{diag}(\sqrt{2\gamma_1(\mathbf{x})}, \sqrt{2\gamma_2(\mathbf{x})}, \dots)$ and the optical linewidths are $\gamma_{1,2,\dots}(\mathbf{x})$. Note that \mathbf{x} can be treated as quasi-stationary parameters here because the time scale for optical relaxation is much smaller than the mechanical one. For practical calculation, the \mathbf{x} -dependence in $\hat{\mathbf{a}}(\mathbf{x})$, $\Omega(\mathbf{x})$, $\mathbb{F}(\mathbf{x})$ can be expanded in series and \mathbf{x} can be upgraded to dynamical variables and quantum operators $\hat{\mathbf{x}}$ following the canonical formulation [52–54]. We further consider a conventional linear regime, where the mechanical oscillation \mathbf{x} is much smaller than the optical wavelength λ , allowing the Hamiltonian to remain only linear \mathbf{x} terms for a good approximation. While this approximation is not necessarily applicable to all optomechanical systems [55–58], it covers most of the popular ones.

One system can be described by different Hamiltonians under different choices of basis, as shown from Eq. (2.1) to Eq. (2.5), but the canonical form in Eq. (2.6) is always *unique*. This serves as the starting point for establishing an unambiguous classification. Position-dependence in $\Omega(\mathbf{x})$ and $\mathbb{F}(\mathbf{x})$ are intuitive and can be directly understood as dispersive and dissipative couplings separately. We construct a mutually exclusive and collectively exhaustive way of classification by considering the last possible \mathbf{x} -dependence: $\hat{\mathbf{a}}(\mathbf{x})$, which we call coherent coupling. Such \mathbf{x} -dependent modes $\hat{\mathbf{a}}(\mathbf{x})$ can be presented as linear combinations of unperturbed modes $\hat{\mathbf{a}}(\mathbf{0})$ coupled via the mechanical oscillation \mathbf{x} , as follows from the linearity of the optical system:

$$\hat{a}_i(\mathbf{x}) = \sum_l f_{il}(\mathbf{x}) \hat{a}_l(\mathbf{0}), \quad (2.7)$$

where $f_{il}(\mathbf{x})$ are the coupling coefficients and $f_{ii}(\mathbf{x}) \equiv 1$ (no summation for the repetitive i).

In order to classify an optomechanical system without any ambiguity, we formulate the following steps:

1. Write the total Hamiltonian of the optomechanical system including all the optical and mechanical degrees of freedom and the coupling among them in any convenient basis.
2. Transform the Hamiltonian to the canonical form shown by Eq. (2.6), where $\Omega(\mathbf{x})$ and $\Gamma(\mathbf{x})$ are diagonal and $\hat{\mathbf{a}}(\mathbf{x})$ is the set of cavity eigenmodes. Environmental modes $\hat{\mathbf{b}}$ can be chosen correspondingly.
3. Classify the type of optomechanical interaction by the \mathbf{x} -dependence feature in $\hat{\mathbf{a}}(\mathbf{x})$, $\Omega(\mathbf{x})$, and $\Gamma(\mathbf{x})$.

We can follow these steps to illustrate the classification of the optomechanical couplings into three types mentioned in the Introduction. We consider a specific example with two cavity modes \hat{a}_1, \hat{a}_2 and one mechanical degree of freedom x , and expand the x -dependence up to a linear order in x , where $g_{1,2}$ and $g_{\gamma 1, \gamma 2}$ are the expansion coefficients of diagonal terms in $\Omega(x)$ and $\Gamma(x)$ matrices:

1. *Dispersive coupling*, where the eigenfrequencies depend on the mechanical oscillation: $\Omega(\mathbf{x})$, the example reads:

$$\Omega(x) = \begin{pmatrix} \omega_1 - g_1 x & 0 \\ 0 & \omega_2 - g_2 x \end{pmatrix}. \quad (2.8)$$

2. *Dissipative coupling*, where the rates of coupling to the external modes depend on the mechanical oscillation: $\Gamma(\mathbf{x})$, the example reads:

$$\Gamma(x) = \begin{pmatrix} \sqrt{2\gamma_1} + g_{\gamma 1} x & 0 \\ 0 & \sqrt{2\gamma_2} + g_{\gamma 2} x \end{pmatrix}. \quad (2.9)$$

3. *Coherent coupling*, where the eigenmodes depend on the mechanical oscillation: $\hat{\mathbf{a}}(\mathbf{x})$, and the derivative of any optical mode \hat{a}_i with respect to any mechanical displacement x_j includes only the other optical modes (see Eq. (2.7)):

$$\left. \frac{\partial \hat{a}_i(\mathbf{x})}{\partial x_j} \right|_{\mathbf{x}=\mathbf{0}} = \sum_{l \neq i} \left. \frac{\partial f_{il}(\mathbf{x})}{\partial x_j} \right|_{\mathbf{x}=\mathbf{0}} \hat{a}_l(\mathbf{0}). \quad (2.10)$$

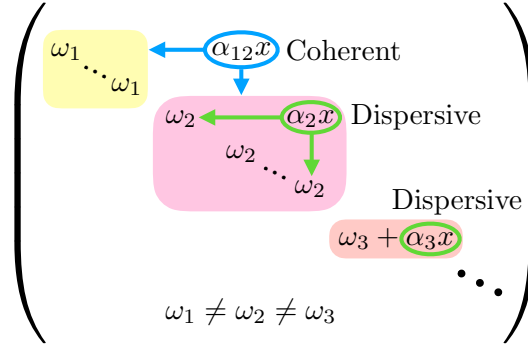


Figure 2.1: The comparison between coherent coupling and dispersive coupling: the $\Omega(\mathbf{x})$ matrix under the basis of $\hat{\mathbf{a}}(\mathbf{0})$. Each color block represents a frequency degenerate subspace, which can have one or more modes. Different blocks have different frequencies, e.g., $\omega_1 \neq \omega_2 \neq \omega_3$. The influence of mechanical oscillation shows up as \mathbf{x} -dependent perturbation, which will either directly add on to diagonal terms as dispersive coupling, e.g., the $\alpha_3 x$ term, or will show up in off-diagonal terms to couple different modes. The off-diagonal coupling within one color block, e.g., the $\alpha_2 x$ term, will open the degeneracy and also cause dispersive coupling. While the coupling between blocks, e.g., the $\alpha_{12} x$ term, won't change the eigenfrequencies $\omega_{1,2}$ and will cause coherent coupling. See main text for detailed discussion.

The simple example can be taken from Eq. (2.5) where the original modes $\hat{a}_{1,2}$ become mixed by x (see Eq. (2.4)) and the corresponding eigenfrequency matrix:

$$\Omega''(x) = \begin{pmatrix} \omega_1 & 0 \\ 0 & \omega_2 \end{pmatrix}, \quad (2.11)$$

doesn't depend on x : $d\Omega''(x)/dx = 0$.

Following our classification strategy, one can clearly distinguish among the different types of interactions, even in cases where several couplings coexist.

In addition to the definition above, a physical picture of coherent coupling also helps to understand this new concept. The difference between dispersive coupling and coherent coupling can sometimes be not obvious: both of them can be expressed as coupling of optical modes by mechanical motion under some specific cavity basis, as showed the example in Eq. (2.1). The distinction between them is illustrated in Fig. 2.1: when mechanical motion couples different optical modes, these modes are either frequency-degenerate or have different frequencies. When the unperturbed modes are frequency-degenerate, the coupling via the mechanical motion breaks the degeneracy and leads to new \mathbf{x} -dependent eigenfrequencies, which are the sign

of dispersive coupling. On the other hand, when the unperturbed modes have different frequencies, the mechanical displacement leads to a coherent energy transfer between these modes, and such coupling is coherent. Expressed in the canonical Hamiltonian, up to linear order in \mathbf{x} , the eigenfrequencies remain unchanged, but the eigenmodes are the original ones mixed in a \mathbf{x} -dependent way.

2.3 Example of different couplings

In this section, we provide some detailed examples of optomechanical coupling of the above three categories. We also cover cases with coexisting couplings.

2.3.1 Dispersive coupling

Dispersive coupling is the most well-studied type of optomechanical interactions [1]. The physical origin of dispersive coupling is the dependence of cavity resonant frequencies on the mechanical oscillation x . The Hamiltonian of a single cavity, shown in Fig. 2.2, reads:

$$\hat{H}_{\text{cav}} = \hbar(\omega_a - g_\omega x)\hat{a}^\dagger\hat{a}, \quad (2.12)$$

where ω_a is the resonant frequency not affected by the mechanical oscillation, $g_\omega = \omega_a/L$ is the dispersive coupling strength, x is the end mirror displacement from its equilibrium position (see detailed derivation in App. 2.6).

In this section, we discuss a metrological system that features the dispersive coupling: the Laser Interferometer Gravitational-Wave Observatory (LIGO) [38, 48]. This detector takes advantage of two Fabry-Pérot cavities in the arms of the Michelson interferometer (arm cavities), which sense the gravitational-wave-induced displacement of the test masses. The two arm-cavity modes are represented by \hat{a} , \hat{b} and their resonance frequencies are by ω_0 . These two modes have the same dispersive coupling strength g , but they couple to two different displacements x_1, x_2 .

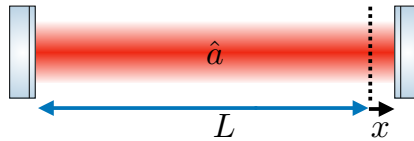


Figure 2.2: Single cavity with a movable end mirror. L is the original cavity length, x is the end mirror displacement from its equilibrium position, \hat{a} is the cavity optical mode.

The cavity Hamiltonian can be expressed as:

$$\hat{H}_{\text{cav}} = \hbar(\omega_0 - gx_1)\hat{a}^\dagger\hat{a} + \hbar(\omega_0 - gx_2)\hat{b}^\dagger\hat{b}. \quad (2.13)$$

Defining the common and differential mechanical and optical modes as $x_+ = (x_1 + x_2)/\sqrt{2}$, $x_- = (x_1 - x_2)/\sqrt{2}$; $\hat{c}_+ = (\hat{a} + \hat{b})/\sqrt{2}$, $\hat{c}_- = (\hat{a} - \hat{b})/\sqrt{2}$, the transformed Hamiltonian takes the form:

$$\hat{H}_{\text{cav}} = \hbar(\omega_0 - gx_+)\hat{\mathbf{c}}^\dagger\hat{\mathbf{c}} + \hbar gx_-\hat{\mathbf{c}}^\dagger\hat{\sigma}_x\hat{\mathbf{c}}, \quad (2.14)$$

where $\hat{\mathbf{c}} = (\hat{c}_+, \hat{c}_-)^T$ and σ_x is the x -component of Pauli matrix. Only the differential motion x_- carries the gravitational wave strain signal, so we don't consider the common motion x_+ . After this operation the transformation from \hat{c}_+, \hat{c}_- to \hat{a}, \hat{b} is equivalent to the transformation from \hat{a}_1, \hat{a}_2 to \hat{a}'_1, \hat{a}'_2 in Eq. (2.3). Even though the Hamiltonian can be expressed in different forms in Eqs. (2.13) and (2.14), in our classification strategy, the coupling will *always* be classified as dispersive with eigenmodes \hat{a}, \hat{b} and x_- -dependent eigenfrequencies: $\omega_\pm(x_-) = \omega_0 \pm gx_-$.

2.3.2 Dissipative coupling

Dissipative coupling happens when the coupling of cavity modes to external modes depends on x . For example, for a single cavity mode \hat{a} :

$$\hat{H}_\gamma = i\hbar \left(\sqrt{2\gamma} + g_\gamma x \right) \left(\hat{a}^\dagger \hat{b} - \text{h.c.} \right), \quad (2.15)$$

where \hat{b} is the external mode and $\sqrt{2\gamma} + g_\gamma x$ is the coupling rate, which gives rise to the finite cavity linewidth. The $g_\gamma x$ term describes the dependence of the dissipation rate on the mechanical oscillation x . The form of dissipative coupling strength g_γ depends on the specific physical realization.

One recent example is the on-chip dissipative optomechanical resonator [32]. As schematically shown in Fig. 2.3, this system consists of a racetrack optical cavity, which is also a mechanical resonator with out-of-plane vibrations, and a curved input waveguide. Except for the material refractive indices, the optical coupling rate between the racetrack cavity and the input waveguide is determined by the distance between them. The racetrack cavity supports optical mode \hat{a} and the out-of-plane oscillation expressed by x , while the input waveguide carries optical mode \hat{b} . The mechanical oscillation x changes the distance between the racetrack cavity and the input waveguide and thus changes the optical coupling rate between modes \hat{a} and \hat{b} . The Hamiltonian describing the optical modes reads:

$$\hat{H} = \hbar\omega_a\hat{a}^\dagger\hat{a} + i\hbar \left(\sqrt{2\gamma} + g_\gamma x \right) \left(\hat{a}^\dagger \hat{b} - \text{h.c.} \right), \quad (2.16)$$

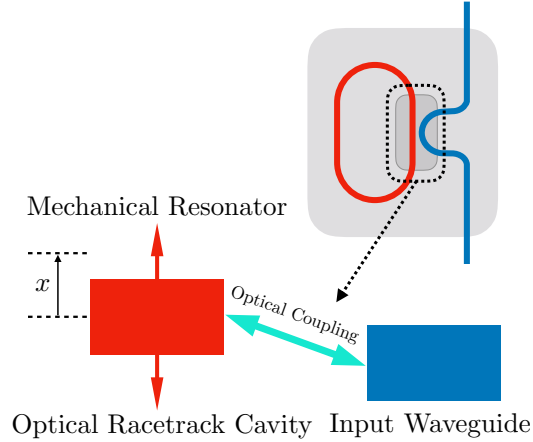


Figure 2.3: On-chip optomechanical coupling between the curved input waveguide and the optical racetrack cavity, adapted from FIG. 1 in Ref. [32]. The upper right is the top view of the chip, where blue line represents the input waveguide and the red one represents that optical racetrack cavity which is also a mechanical resonator that can have out-of-plane vibrations. The lower left is the schematic of the cross-section inside the dashed area of the upper right. See the main context for discussion.

where neither the cavity mode \hat{a} nor its resonance frequency ω_a depends on x . There exists only one cavity eigenmode and it already satisfies the canonical form of Eq. (2.6). Thus, the x -dependence in \hat{a}, \hat{b} coupling rate shows the feature of dissipative coupling.

2.3.3 Coherent coupling

The last interaction category to be discussed is coherent coupling where the x -dependence appears in the eigenmodes themselves rather than the eigenfrequencies of the optical modes.

One notable example of coherent coupling is the three-modes optoacoustic interaction [59]. It can give rise to important non-linear optomechanical effects such as parametric instability [60, 61], which complicates the operation of gravitational-wave detectors. In a simplified model [59] as shown on the left side in Fig. 2.4, there are two orthogonal transverse optical-cavity modes \hat{a} and \hat{b} with *different* resonant frequencies ω_1 and ω_2 . The acoustic mode has a torsional mode profile and x is its generalized coordinate. The cavity Hamiltonian in this case has the form (see App. 2.7 for detailed derivation):

$$\hat{H}_{\text{cav}} = \hbar\omega_1\hat{a}^\dagger\hat{a} + \hbar\omega_2\hat{b}^\dagger\hat{b} + \hbar G_0x \left(\hat{a}^\dagger\hat{b} + \text{h.c.} \right). \quad (2.17)$$

Note that Eq. (2.17) has the same structure as Eq. (2.1) and thus follows the same

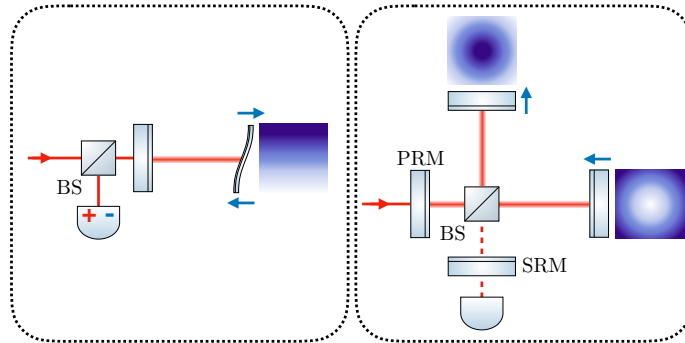


Figure 2.4: Mapping from three-mode optoacoustic system to a power and signal-recycled interferometer, adapted from FIG.2 in Ref. [59]. Although they share a similar three-mode scheme, their physical origins and classification results are different. See the main text in Sec. 2.3.1 and Sec. 2.3.3 for detailed discussion.

transformation process as in Eq. (2.4). Up to linear order in x , the eigenfrequencies remain the same and the new eigenmodes are the original ones mixed by mechanical oscillation x :

$$\hat{a}(x) = \hat{a} - \frac{G_0}{2\Delta\omega}x\hat{b}, \quad \hat{b}(x) = \hat{b} + \frac{G_0}{2\Delta\omega}x\hat{a}, \quad (2.18)$$

where $\Delta\omega \equiv (\omega_2 - \omega_1)/2$ is the frequency difference. The x -dependence in eigenmodes shows the feature of coherent coupling.

Note that Ref. [62] was aware of the x -dependence that only happens in eigenmodes, but didn't notice the new coherent coupling category in optomechanics. In Sec. 2.4 we will investigate a ring cavity system, where the coherent coupling is mediated by the longitudinal oscillation of the mechanical center-of-mass degree of freedom.

2.3.4 Coexisting coupling

In many cases, different types of optomechanical couplings can coexist. Some optomechanical systems might show different coupling features depending on the parameter regimes that they work in. Following our classification strategy, each type in the coexisting couplings can be clearly distinguished.

One notable example is the Michelson-Sagnac interferometer [7, 46] with coexisting dispersive and dissipative couplings. With careful tuning [7], it can become either pure dissipative coupling or pure dispersive coupling.

Another example of a system with coexisting couplings is the system of two coupled cavities separated by a movable mirror, as shown in Fig. 2.5. The coupling

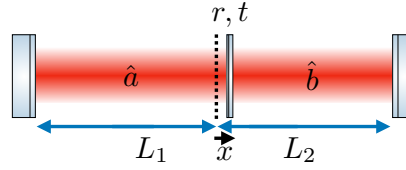


Figure 2.5: The coupled cavity configuration. $L_{1,2}$ are the length of two subcavities, r and t are the amplitude reflectivity and transmittance of the mirror inside, and x is membrane oscillation around its equilibrium position. In the main text we consider membrane with low transmittance $t \ll 1$. It is then reasonable to claim that the left and right subcavities can support \hat{a} and \hat{b} modes separately. The bare optical frequencies of the two modes are $\omega_{1,2}$ and the optomechanical coupling constants are $g_{1,2} = \omega_{1,2}/L_{1,2}$. Different parameter regime can lead to different classification results. See main text for details.

in such a system can be classified as dispersive, or coherent, or coexisting, depending on the position and optical properties of the central mirror [5, 62, 63]. In the following contents, we give a theoretical description of this system and classify it using our strategy.

When the transmittance of the central mirror is relatively low, $t \ll 1$, we can define two optical modes \hat{a}, \hat{b} for the left and the right subcavities respectively, which are coupled at a characteristic sloshing frequency ω_s . In terms of these modes the cavity Hamiltonian can be expressed as:

$$\hat{H}_{\text{cav}} = \hbar(\omega_1 - g_1 x) \hat{a}^\dagger \hat{a} + \hbar(\omega_2 + g_2 x) \hat{b}^\dagger \hat{b} + \hbar\omega_s (\hat{a}^\dagger \hat{b} + \text{h.c.}). \quad (2.19)$$

For convenience, we define the average frequency $\omega_0 \equiv (\omega_1 + \omega_2)/2$ and the frequency difference $\Delta\omega \equiv (\omega_2 - \omega_1)/2$. We then convert the Hamiltonian in Eq.(2.19) into the canonical form in Eq.(2.6) as required by our classification procedure.

When the central mirror is perfectly reflective [5], the sloshing frequency becomes zero ($\omega_s = 0$) and Eq. (2.19) is already in the canonical form. No optical coupling can happen between \hat{a}, \hat{b} modes and they remain to be cavity eigenmodes. The corresponding eigenfrequencies $\omega_1 - g_1 x, \omega_2 + g_2 x$ are x -dependent. In this case, the system has pure dispersive coupling.

When $\omega_s \neq 0$, Eq. (2.19) needs to be transformed to the canonical form. The interaction with the mechanical oscillation x couples the original optical eigenmodes

$$\hat{c}_\pm(0) = (-\Delta\omega \pm \sqrt{\Delta\omega^2 + \omega_s^2}) \hat{a} + \omega_s \hat{b}, \quad (2.20)$$

and they become:

$$\hat{c}_{\pm}(x) = \hat{c}_{\pm}(0) \pm \frac{g_1 + g_2}{4\sqrt{\Delta\omega^2 + \omega_s^2}} x \hat{c}_{\mp}(0), \quad (2.21)$$

with the corresponding eigenfrequencies:

$$\omega_{\pm}(x) = \omega_0 \pm \sqrt{\Delta\omega^2 + \omega_s^2} + \left(\frac{g_2 - g_1}{2} \mp \frac{(g_1 + g_2)\Delta\omega}{2\sqrt{\Delta\omega^2 + \omega_s^2}} \right) x + \mathcal{O}(x^2). \quad (2.22)$$

Both the eigenmodes and eigenfrequencies depend on x , which reveals the coexisting coherent and dispersive couplings.

The system can have a purely coherent coupling if the central mirror has low transmittance and the two subcavities have the same length $L_1 = L_2$ [62, 63]. In this case, the sub cavity frequencies and the corresponding coupling rates in Eq. (2.19) become equal: $\omega_1 = \omega_2 = \omega_0$, $\Delta\omega = 0$, $g_1 = g_2$. The original eigenmodes are $\hat{c}_{\pm}(0) \propto \hat{b} \pm \hat{a}$ and the dispersive feature is absent as the eigenfrequencies of Eq. (2.22) no longer have x -dependence: $\omega_{\pm} = \omega_0 \pm \omega_s$.

The purely coherent coupling in this coupled cavity example only happens in some specific parameter regimes. In the following section, we will discuss a ring cavity system which always has a purely coherent coupling.

2.4 Purely coherent coupling in a ring cavity system

In this section we discuss an example of purely coherent coupling in an optomechanical ring cavity system where two resonant modes are coupled via the oscillation of a partially reflective mirror, see Fig. 2.6. Similar ring cavity systems with one or multiple scattering objects inside have been studied, including some cases with membranes or mirrors [64–66] and some other cases with cold atom clouds [67–74]. However, no systematic Hamiltonian construction with a clear definition of optical modes has been done. That motivates our derivation in this section. We also analyze how the coherent coupling helps the laser cooling of mechanical oscillation and compare it with the single cavity dispersive coupling case [6].

2.4.1 Cavity modes and the Hamiltonian

The detailed derivation of the total Hamiltonian of the ring cavity system can be found in App. 2.8. Here we only sketch the key steps of the derivation.

Without the membrane, the ring cavity can support degenerate clockwise and counterclockwise modes that propagate independently. The membrane reflection

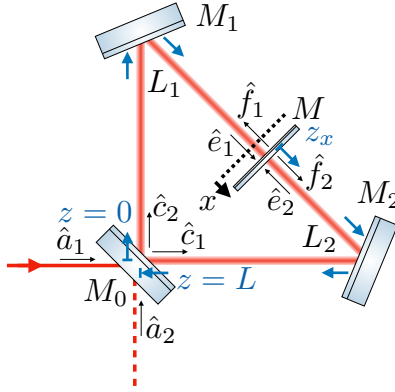


Figure 2.6: Ring cavity configuration and field labeling. Here M_0 is the front mirror with amplitude reflectivity r_0 and transmittance t_0 , $M_{1,2}$ are two fixed totally reflective end mirror, M is the movable membrane with amplitude reflectivity r and transmittance it . L is the total cavity length, $L_1 = L_2 = L/2$ are the distances from the M_0 to the equilibrium position of M in clockwise and counterclockwise directions, x is the microscopic displacement of M from its equilibrium. For fields, $\hat{c}_{1,2}$ are the counterclockwise, clockwise propagating field directly coupled from outside continuum $\hat{a}_{1,2}$. Defined at the instantaneous position of the membrane, $\hat{e}_{2,1}$ ($\hat{f}_{1,2}$) are the propagating fields towards (away from) the membrane in counterclockwise, clockwise direction separately.

couples the two circulating waves and opens the mode degeneracy, as shown in Fig. 2.7. We first consider resonant cavity modes assuming a perfectly reflective front mirror M_0 . In this case no outside field can couple into the cavity and the field operator vector $\hat{\mathbf{e}}(k) = (\hat{e}_1(k), \hat{e}_2(k))^T$ obeys the following matrix formula:

$$\mathbb{T}_c(k)\hat{\mathbf{e}}(k) = \hat{\mathbf{0}}, \quad (2.23)$$

where $\mathbb{T}_c(k)$ is the closed form transfer matrix:

$$\mathbb{T}_c(k) = \begin{pmatrix} 1 - ite^{ikL} & -re^{ikL} \\ -re^{ikL} & 1 - ite^{ikL} \end{pmatrix}. \quad (2.24)$$

Solving this equation allows us to find wave numbers k_{\pm} of the resonant fields:

$$k_{\pm} = \frac{1}{iL} \log(\pm r - it). \quad (2.25)$$

The two corresponding resonant frequencies $\omega_{\pm} = ck_{\pm}$ within one free spectral range (FSR) $\Delta\omega_{\text{FSR}} = 2\pi c/L$ are separated by:

$$\omega_s = \frac{c \arcsin r}{L}. \quad (2.26)$$

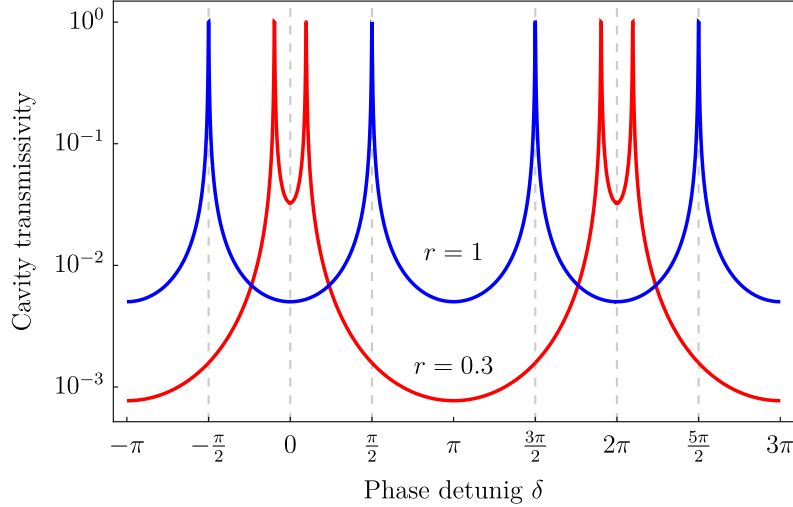


Figure 2.7: Cavity modes splitting caused by different membrane reflectivity r . The horizontal axis is a relative phase defined as $\delta \equiv (k_p L + \pi/2) - N2\pi$ and the vertical axis is the ratio of the field amplitude in and out of the system from the input port. The red and blue line correspond to $r = 0.3, 1$ respectively. As analyzed in the main context, the cavity resonant frequencies do not depend on x while the electromagnetic mode profiles depend on that. This optomechanical interaction is called coherent coupling. The cavity free spectral range (FSR) is $\Delta\omega_{\text{FSR}} = 2\pi c/L$ and the linewidth is $\gamma = ct_0^2/2L$.

The two resonant modes have the following feature (see Eq. (2.72)):

$$\hat{e}_1(k_+) = \hat{e}_2(k_+), \quad (2.27a)$$

$$\hat{e}_1(k_-) = -\hat{e}_2(k_-), \quad (2.27b)$$

and the field operators $\hat{e}_{1,2}(k_{\pm})$ are denoted by $\hat{e}_{1,2\pm}$ in the following contents for notational convenience.

We assume that the membrane has a low reflectivity ($r \ll 1$), which allows us to work only with two modes that are close to each other within one FSR, i.e., $\omega_s \ll \Delta\omega_{\text{FSR}}$, as shown approximately by the red line in Fig. 2.7. In this case, we do not need to consider the other optical resonances out of one FSR. We then assign \hat{c}_{\pm} to represent the annihilation operator of the two cavity modes with optical frequencies ω_{\pm} . The only nonzero commutators between them are:

$$[\hat{c}_-, \hat{c}_-^\dagger] = 1, \text{ and } [\hat{c}_+, \hat{c}_+^\dagger] = 1. \quad (2.28)$$

According to Eq. (2.27), \hat{c}_+ is named symmetric mode and \hat{c}_- is named antisym-

metric mode. \hat{c}_\pm can be constructed from $\hat{e}_{1,2\pm}$ fields :

$$\hat{c}_+ \equiv \frac{\hat{e}_{2+} + \hat{e}_{1+}}{\sqrt{2}}, \quad (2.29a)$$

$$\hat{c}_- \equiv \frac{\hat{e}_{2-} - \hat{e}_{1-}}{\sqrt{2}}, \quad (2.29b)$$

such that $\hat{e}_{2+} = \hat{c}_+/\sqrt{2}$ and $e_{2-} = \hat{c}_-/\sqrt{2}$.

To quantitatively describe the electric field distribution, we introduce a coordinate system inside the ring cavity, as shown in Fig. 2.6. The origin of this z -coordinate is the front mirror M_0 and it increases clockwise along the optical axis of the ring cavity. It becomes $z_x = L/2 + x$ at the instantaneous position of the membrane and finally becomes $z = L$ when it reaches the front mirror again. The coordinate system here is circular and thus $z = L$ represents the same position as $z = 0$. The electric field inside the ring cavity can be represented by the standing wave distribution of two optical modes (see Eq. (2.80)):

$$\hat{E}^+(z; x) = \mathcal{N}(\omega_-)P_-(z; x)\hat{c}_- + \mathcal{N}(\omega_+)P_+(z; x)\hat{c}_+, \quad (2.30)$$

where $\mathcal{N}(\omega) = \sqrt{\hbar\omega/2\mathcal{A}\epsilon_0 L}$ is the frequency-dependent normalization factor for a beam with cross-sectional area \mathcal{A} inside the ring cavity, and $P_-(z; x), P_+(z; x)$ are the wavefunctions of \hat{c}_-, \hat{c}_+ modes along z axis:

$$P_-(z; x) = \begin{cases} 2i \sin(k_-(z-x)) & z \in (0, z_x), \\ 2i \sin(k_-(z-L-x)) & z \in (z_x, L), \end{cases} \quad (2.31a)$$

$$P_+(z; x) = \begin{cases} 2 \cos(k_+(z-x)) & z \in (0, z_x), \\ 2 \cos(k_+(z-L-x)) & z \in (z_x, L). \end{cases} \quad (2.31b)$$

$P_\pm(z; x)$ also represent the electric field standing wave distribution and are qualitatively shown in Fig. 2.8. The position of the nodes for both symmetric and antisymmetric modes are shifted with the membrane position z_x and $P_\pm(z; x)$ have the following features:

$$P_\pm(z_x - \zeta \bmod L; x) = \pm P_\pm(z_x + \zeta \bmod L; x), \quad (2.32a)$$

$$|P_-(z = x; x)| = 0, \quad (2.32b)$$

$$|P_+(z = x; x)| = \max_{z \in (0, L)} |P_+(z; x)|, \quad (2.32c)$$

where ζ represents the distance from an arbitrary point to the membrane. That is, starting from z_x and going in two directions, the standing wave amplitude of

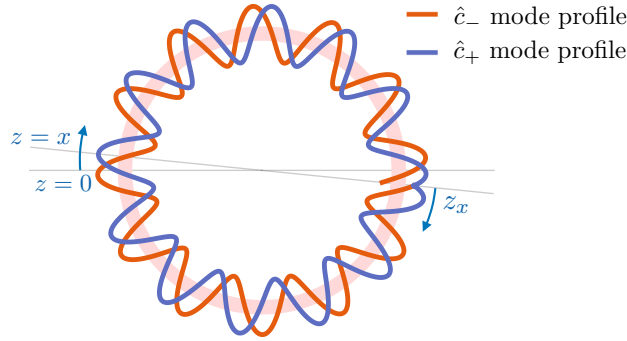


Figure 2.8: Illustrating plot of \hat{c}_{\pm} wavefunction $P_{\pm}(z; x)$ in Eq.(2.81). We use here a circle instead of a triangle to represent the space inside the ring cavity for plotting convenience. The coordinate system is the same as that in Fig. 2.6: $z = 0$ is the position of the front mirror M_0 and z_x is the position of the membrane. The position of the nodes for both symmetric and antisymmetric modes are shifted with the position of the membrane z_x . Starting from z_x and going in two directions, the standing wave amplitude of $\hat{c}_{+(-)}$ mode remains the same (opposite sign), until it reaches maximum (zero) at $z = x$.

$\hat{c}_{+(-)}$ mode remains the same (opposite sign), until it reaches the maximum (zero) at $z = x$, which is $L/2$ away from z_x both clockwise and counterclockwise. The standing wave feature of $\hat{c}_{+(-)}$ mode agrees with the naming of (anti)symmetric mode.

The cavity Hamiltonian can be obtained from the total optical energy inside the ring cavity [75] and it reads:

$$\hat{H}_{\text{cav}} = \hbar\omega_- \hat{c}_-^\dagger \hat{c}_- + \hbar\omega_+ \hat{c}_+^\dagger \hat{c}_+. \quad (2.33)$$

It doesn't have x -dependence because the ring cavity is a closed quantum system until now, as shown by the x -independent equation Eq. (2.23) that we start from.

To obtain the total Hamiltonian and reveal the x -dependence, we consider the coupling of the cavity modes to the outside modes by assuming the front mirror to have low transmittance ($t_0 \ll 1$). The cavity linewidth γ can be obtained from the input-output relation (see Eq. (2.65)):

$$\gamma = \frac{ct_0^2}{2L}, \quad (2.34)$$

and the ring cavity, as an open passive system, only supports the inside field with the pumping frequency $\omega_p = k_p c$. The extent to which \hat{c}_{\pm} modes are excited depends

on the detuning of the pumping frequency to the resonant ones: $\omega_p - \omega_{\pm}$. In the following sections we will use the wavevector k_p of the pumping field instead of the resonant wavevectors k_{\pm} . We use $\hat{c}_{1,2}$ to represent the counterclockwise and clockwise propagating fields that the environment fields $\hat{a}_{1,2}$ directly couples to. Thus the cavity-environment interaction Hamiltonian can be expressed as:

$$\hat{H}_{\gamma} = i\hbar\sqrt{2\gamma}(\hat{c}_1^{\dagger}\hat{a}_1 - \text{h.c.}) + i\hbar\sqrt{2\gamma}(\hat{c}_2^{\dagger}\hat{a}_2 - \text{h.c.}). \quad (2.35)$$

The front mirror position $z = 0$ is a natural choice of phase reference point for modes $\hat{c}_{1,2}$. However, the resonant modes \hat{c}_{\pm} take the membrane position z_x as the phase reference point, as shown in Eq. (2.32a). Thus, the transformation between $\hat{c}_{1,2}$ and \hat{c}_{\pm} depends on x :

$$\hat{c}_{\pm}(x) = \frac{1}{\sqrt{2}}e^{ik_p L/2}(e^{-ik_p x}\hat{c}_1 \pm e^{ik_p x}\hat{c}_2), \quad (2.36)$$

where $\hat{c}_{\pm}(0)$ is the *original* cavity modes that the outside modes $\hat{a}_{1,2}$ directly couple to and they have distribution $P_{\pm}(z; x = 0)$. For the outside modes, $\hat{c}_{\pm}(x)$ are the new resonant modes when the membrane is displaced by x . It is equivalent to saying that the mechanical oscillation x changes the way of interference between $\hat{c}_{1,2}$ that leads to the formation of different resonant modes $\hat{c}_{\pm}(x)$.

The cavity optomechanical Hamiltonian linearized with respect to x (see Eq. (2.89)) reads:

$$\hat{H}_{\text{opt}}(x) = \hat{H}_0 + \hat{H}_{\text{int}}(x), \quad (2.37)$$

where the free part \hat{H}_0 is equivalent to Eq. (2.33) with $\hat{c}_{\pm} \rightarrow \hat{c}_{\pm}(0)$ and the optomechanical interaction part $\hat{H}_{\text{int}}(t)$ reads:

$$\hat{H}_{\text{int}}(x) = 2i\omega_s\hbar k_p x \left(\hat{c}_-^{\dagger}(0)\hat{c}_+(0) - \text{h.c.} \right). \quad (2.38)$$

The feature of coherent coupling is shown in Eq. (2.38) explicitly: the mechanical oscillation x induces the coupling between two original optical modes $\hat{c}_{\pm}(0)$ which have non-degenerate frequencies.

In the derivation until now, x merely works as a parameter. Alternatively, one can start from the total Lagrangian including the mechanical degree of freedom and follow the canonical formulation [52–54], where x can be upgraded to a dynamical variable and further becomes a quantum operator \hat{x} after quantization.

To describe the system in the general framework of Eq. (2.6), we need to express the total Hamiltonian in terms of the new resonant modes $\hat{c}_{\pm}(\hat{x})$. Applying

similar transformation as in Eq. (2.36), we can express the input modes $\hat{a}_{1,2}$ into antisymmetric and symmetric ones:

$$\hat{c}_{\pm\text{in}}(\hat{x}) = \frac{1}{\sqrt{2}} e^{ik_p L/2} (e^{-ik_p \hat{x}} \hat{a}_1 \pm e^{ik_p \hat{x}} \hat{a}_2). \quad (2.39)$$

Up to linear order in \hat{x} , the cavity-environment interaction Hamiltonian in Eq. (2.35) can be transformed to (see Eq. (2.94)):

$$\hat{H}_\gamma(\hat{x}) = i\hbar\sqrt{2\gamma} \left(\hat{c}_-^\dagger(\hat{x}) \hat{c}_{-\text{in}}(\hat{x}) + c_+^\dagger(\hat{0}) \hat{c}_{+\text{in}}(\hat{x}) - \text{h.c.} \right). \quad (2.40)$$

It is clear from Eq. (2.40) that the \hat{x} dependence only lies on optical modes $\hat{c}_{\pm(\text{in})}(\hat{x})$ themselves and the cavity-environment coupling rate γ doesn't depend on \hat{x} . Thus, this optomechanical coupling has no dissipative feature.

To sum up, the total Hamiltonian reads:

$$\hat{H}(x) = \hat{H}_{\text{opt}}(x) + \hat{H}_\gamma + \hat{H}_m, \quad (2.41)$$

where the cavity optomechanical part $\hat{H}_{\text{opt}}(x)$ is given in Eq. (2.37), the cavity-environment interaction part \hat{H}_γ is given in Eq. (2.40) and the free mechanical part is:

$$\hat{H}_m = \frac{\hat{p}^2}{2m} + \frac{1}{2} m \Omega_m^2 \hat{x}^2 - G \hat{x}, \quad (2.42)$$

with G representing any external force exerted on the mechanical oscillator. If we write it in the canonical form of Eq. (2.6), we obtain:

$$\Omega = \begin{pmatrix} \omega_- & 0 \\ 0 & \omega_+ \end{pmatrix}, \quad \Gamma = \begin{pmatrix} i\sqrt{2\gamma} & 0 \\ 0 & i\sqrt{2\gamma} \end{pmatrix}, \quad (2.43)$$

and the mode operators are $\hat{\mathbf{a}}(\hat{x}) = (\hat{c}_-(\hat{x}), \hat{c}_+(\hat{x}))^T$, $\hat{\mathbf{a}}_{\text{in}}(\hat{x}) = (\hat{c}_{-\text{in}}(\hat{x}), \hat{c}_{+\text{in}}(\hat{x}))^T$. There is neither dispersive nor dissipative feature in the Hamiltonian above, and thus the coherent coupling is verified.

In the next section, we will discuss the advantage of coherent coupling in enhanced optomechanical cooling.

2.4.2 Application: Enhanced cooling

Mechanical oscillators can be cooled to their ground states by extracting thermal phonons through laser light with a near-zero effective temperature bath [76]. Such optomechanical cooling contributes to fundamental physics in studying the quantum effects of macroscopic objects [23, 24]. It is also beneficial in the application aspect of frequency conversion [28–31] and quantum information processing [32].

In the Hamiltonian linearized with respect to x , the coherent coupling starts with two non-degenerate optical modes and then couples them by mechanical oscillation. This coupling doesn't change the resonance frequency up to linear order in \hat{x} . Thus, the double resonance structure of coherent coupling systems can potentially provide a more efficient cooling compared with the standard dispersive-coupling-based cooling [6], because of the additional resonant enhancement of the pumping field: When the mechanical frequency matches the frequency distance between the two resonance peaks and the lower frequency is pumped, both the pumping field and the upper mechanical sideband are resonant inside the cavity.

The optoacoustic interaction [59] in Sec. 2.3.3 has similar physics properties with the ring cavity system. Contrary to the cooling described above, when the cavity mode with upper frequency is pumped, both the pumping field and the lower mechanical sideband are resonant and the enhanced heating occurs. That explains the principle of parametric instability [60, 61]. Different from the optoacoustic interaction which influences the transverse mechanical oscillation, the ring cavity system interacts with the longitudinal mechanical oscillation. In this section, we will focus on the cooling of the ring cavity system and compare it with the single cavity dispersive coupling case.

The detailed derivation of optomechanical cooling and mechanical occupation number limit in the ring cavity system can be found in App. 2.9. Here we only list the main results. Under the resolved sideband condition $\Omega_m \gg \gamma$, we obtain the optical damping rate (see Eq. (2.103b)):

$$\gamma_{\text{opt}} = \frac{2|A_{\text{in}}|^2 k_p^2 \hbar \omega_s}{m\gamma^2}, \quad (2.44)$$

such that the equation of motion for mechanical operator \hat{x} becomes:

$$m\ddot{\hat{x}} = \hat{F}_{\text{baff}} - m\Omega_m^2 \hat{x} - m(\gamma + \gamma_{\text{opt}})\dot{\hat{x}}, \quad (2.45)$$

where \hat{F}_{baff} is the x -independent part of fluctuating back-action force (see Eq. (2.102) and the contents below it). The mechanical occupation number can be expressed as:

$$\langle \hat{n} \rangle = \frac{\gamma_{\text{opt}}}{\gamma_m + \gamma_{\text{opt}}} \frac{1}{2} \left[\frac{\gamma^2}{4\Omega_m^2} - \frac{\gamma_m}{\gamma_{\text{opt}}} \right] + \frac{\gamma_m}{\gamma_m + \gamma_{\text{opt}}} \frac{k_B T}{\Omega_m \hbar}. \quad (2.46)$$

Under further condition $\gamma_{\text{opt}} \gg \gamma_m$, we can obtain the ultimate cooling limit:

$$\langle \hat{n} \rangle = \frac{\gamma_m}{\gamma_m + \gamma_{\text{opt}}} n_{\text{th}} + \frac{\gamma_{\text{opt}}}{\gamma_m + \gamma_{\text{opt}}} n_{\text{ba}} \approx n_{\text{ba}}, \quad (2.47)$$

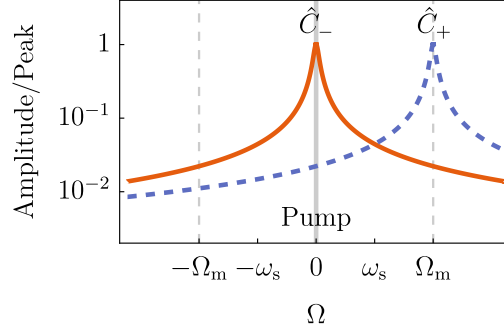


Figure 2.9: Pumping regime of sideband cooling. Coherent coupling has a potential advantage over dispersive coupling in sideband cooling because the pumping frequency is also resonant inside the cavity. Dispersive coupling only has the right resonance peak shown by the blue dashed line.

where $n_{\text{th}} = k_B T / \Omega_m \hbar$ is the thermal occupation number and $n_{\text{ba}} = \gamma^2 / 8\Omega_m^2$ is the back-action limited occupation number.

We then compare the cooling rate in ring cavity (with coherent coupling) and the one in a single cavity (with dispersive coupling). We assume the two systems have the same optical bandwidth γ and similar *round-trip length* L, L_{sc} , and are used to cool a mechanical oscillator with the same resonant frequency Ω_m . Both of the two systems are pumped with frequency ω_p . For the ring cavity case, $\omega_p = \omega_-$ and the pumping is injected from the left port as analyzed above. For the single cavity case, ω_p is red detuned by Ω_m from its resonance. In both cases, $\Omega_m \ll \Delta\omega_{\text{FSR}}$ and thus the two-mode or single-mode approximation is feasible. The ultimate occupation number n_{ba} is determined by the ratio between γ and Ω_m and is the same in the two cases. The advantage of coherent coupling is the simultaneous resonant enhancement of pumping field and the upper sideband, which can support higher intracavity field and thus provide larger optical damping γ_{opt} . The intracavity field amplitudes in two cases are:

$$C_- = \frac{A_{\text{in}}}{\sqrt{\gamma}} \quad \text{in the ring cavity,} \quad (2.48a)$$

$$A_{\text{sc}} = \frac{\sqrt{2\gamma} A_{\text{in}}}{\gamma + i\Omega_m} \approx \frac{\sqrt{2\gamma} A_{\text{in}}}{i\Omega_m} \quad \text{in the single cavity,} \quad (2.48b)$$

which are related as $|C_-| \gg |A_{\text{sc}}|$ for the same input amplitude A_{in} . The optical

damping rates of the ring cavity and the single cavity are:

$$\gamma_{\text{opt,rc}} = \frac{2\omega_s k_p^2 \hbar}{m\gamma} |C_-|^2, \quad (2.49a)$$

$$\gamma_{\text{opt,sc}} = \frac{g_{\text{sc}}^2 \hbar}{m\gamma\Omega_m} |A_{\text{sc}}|^2, \quad (2.49b)$$

where $2\omega_s = \Omega_m$ is the setting of ring cavity resonance and $g_{\text{sc}} = 2\omega_p/L_{\text{sc}}$ is the dispersive coupling strength (see Eq. (2.58)) expressed in cavity round-trip length L_{sc} . According to Eq. (2.38) with coherent coupling strength defined as $g_{\text{rc}} = 2i\omega_s k_p$, the damping rate in Eq. (2.49a) takes the form:

$$\gamma_{\text{opt,rc}} = \frac{|g_{\text{rc}}|^2 \hbar}{m\gamma\Omega_m} |C_-|^2, \quad (2.50)$$

which has the same as Eq. (2.49b). Assuming the same single-photon coupling rates, the advantage of intracavity resonance in the coherent coupling case described in Eq. (2.48) shows up. Substituting Eq. (2.48) in, we obtain the damping rates under the same input amplitude:

$$\gamma_{\text{opt,rc}} = \frac{\Omega_m k_p^2 \hbar}{m\gamma^2} |A_{\text{in}}|^2, \quad (2.51a)$$

$$\gamma_{\text{opt,sc}} = \frac{8\omega_p^2 \hbar}{mL_{\text{sc}}^2 \Omega_m^3} |A_{\text{in}}|^2. \quad (2.51b)$$

The ratio between the damping rates of the two cases is:

$$R_{\text{rc/sc}} = \frac{\Omega_m^4 L_{\text{sc}}^2}{8c^2 \gamma^2}. \quad (2.52)$$

The ring cavity has the advantage in cooling efficiency over a single cavity so long as Ω_m is larger than the geometric mean of $\Delta\omega_{\text{FSR}}$ and γ , i.e., $\Omega_m \gg \sqrt{\Delta\omega_{\text{FSR}}\gamma}$. Because of Eqs. (2.26) and (2.34), the ratio above can also be expressed as:

$$R_{\text{rc/sc}} = \frac{8L_{\text{sc}}^2 (\arcsin r)^4}{L^2 t_0^4} = \frac{L_s^2 L^2 \Omega_m^4}{2t_0^4 c^4}. \quad (2.53)$$

These equations demonstrates that the ring cavity can provide benefit in a larger-scale optomechanical setup with long cavities or with high-frequency mechanical oscillators. For example, if we compare a single and a ring cavity with a mechanical membrane as an oscillator of frequency of 2.5 MHz [77], front mirror transmission of 0.01%, and an equal length of $\sim 40\text{cm}$, we find that the cooling rate in the ring cavity is 2.4 times higher than in a single cavity. The ring cavity thus could be beneficial for long cavities, used, e.g., as optomechanical filters for gravitational-wave detectors [78].

2.5 Discussion

In this work, we build an unambiguous framework for classifying the optomechanical interaction in a unique way. This framework prescribes to express each Hamiltonian in the canonical form and examine the dependence of its terms on the mechanical oscillation. The canonical form of the Hamiltonian is unique for each system, hence the classification based on that is mutually exclusive. No ambiguity in classifying similar systems, as it was illustrated in the Introduction, can occur. There are some limitations in our classification framework: we only consider Hamiltonians linear in x and linear in optical modes. Quadratic optomechanical coupling and nonlinear optical effects, for example, are not covered in our framework and need further consideration.

Based on our framework, we analyze several optomechanical systems, including the newly investigated ring cavity system which exhibits purely coherent coupling. We show that coherent coupling is fundamentally different from either dispersive or dissipative coupling and allows us to complete our classification framework. Our analysis reveals a previously underestimated relevance of coherent coupling in optomechanical systems. It will show up whenever the system has two or more optical modes with non-degenerate frequencies get coupled by mechanical oscillation. We show that although coherent coupling occurs even in some well-studied systems, yet it has never been identified as such. For instance, in the system of two coupled cavities with a movable central mirror, both dispersive and coherent coupling coexist, as we show in the Sec. 2.3.4.

The nature of the optomechanical coupling defines the strengths and weaknesses of the system in one desired application. Our classification strategy will allow us to approach the experimental design in a systematic way and choose the system that would perform optimally. As a concrete result, we show that coherent coupling allows for more effective laser cooling of the mechanical oscillation due to the simultaneous resonant of pumping field and the upper mechanical sideband.

We anticipate our classification framework to serve as a methodological and practical guide in the growing field of optomechanics. We believe the recognition of the highlighted coherent coupling will lead to the development of novel quantum optomechanical systems and new parameter regimes in the existing ones.

2.6 Appendix: Dispersive Hamiltonian

The resonance condition gives wave vector $k_n(x) = n\pi/(L+x)$ and the corresponding resonant frequency $\omega_n(x) = ck_n(x)$. The electric field inside a single cavity is the superposition of modes with multiple resonant frequencies:

$$\hat{E}^+(z) = \sum_n \sqrt{\frac{\hbar\omega_n(x)}{4\mathcal{A}\epsilon_0(L+x)}} 2 \cos(k_n(x)z) \hat{a}_n, \quad (2.54)$$

with z ranging in $(0, L+x)$. The counterintuitive node antinode distribution is because we choose zero reflection phase in two cavity mirrors.

The cavity Hamiltonian can be obtained from the total optical energy [75]:

$$\hat{H}_{\text{cav}}(x) = \int_0^{L+x} 2\mathcal{A}\epsilon_0 \hat{E}^-(z) \hat{E}^+(z) dz, \quad (2.55)$$

where the factor 2 accounts for both electric and magnetic energy. The integration result of Eq. (2.55) is:

$$\hat{H}_{\text{cav}}(x) = \sum_n \hbar\omega_n(x) \hat{a}_n^\dagger \hat{a}_n. \quad (2.56)$$

Under single-mode approximation, only one specific mode n is considered and we obtain the cavity Hamiltonian:

$$\hat{H}_{\text{cav}}(x) = \hbar(\omega_a - g_\omega x) \hat{a}^\dagger \hat{a}, \quad (2.57)$$

by defining $\omega_a = \omega_n(0)$ for mode n . The dispersive coupling strength g_ω can be extracted from the expressions above as:

$$g_\omega = \frac{\omega_a}{L}. \quad (2.58)$$

2.7 Appendix: Optoacoustic Hamiltonian

The Hamiltonian of three-modes optoacoustic interaction [59] in Eq. (2.17) is originated from the following cavity integral:

$$H \propto \int dr_\perp (L+xu_z) \left[\epsilon(E_0 + E_1)^2 + \frac{1}{\mu}(B_0 + B_1)^2 \right], \quad (2.59)$$

where $u_z = u_z(\vec{r}_\perp)$ is the transverse spatial profile of mechanical oscillation and (E_0, H_0) , (E_1, H_1) are two optical modes TEM_{00} , TEM_{01} with orthogonal transverse profile $f_0(\vec{r}_\perp)$, $f_1(\vec{r}_\perp)$. The dispersive coupling and the three-modes coupling in this system appear as:

$$\begin{aligned} H_{\text{disp}} &\propto \sum_{0,1} \int d\vec{r}_\perp x u_z \left[\epsilon E_{0,1}^2 + \frac{1}{\mu} B_{0,1}^2 \right], \\ H_{\text{3-mode}} &\propto \int d\vec{r}_\perp x u_z \left[\epsilon E_0 E_1 + \frac{1}{\mu} B_0 B_1 \right]. \end{aligned} \quad (2.60)$$

Apparently, they contain overlapping function $\Lambda_{0,1} = \int d\vec{r}_\perp u_z f_{0,1}^2$ and $\Lambda_{01} = \int d\vec{r}_\perp u_z f_0 f_1$, respectively. In general, both terms should exist. The reason for the vanishing of dispersive coupling here is simply because of the vanishing of the overlapping function $\Lambda_{0,1}$. In Eq. (2.17) the coupling constant is defined as $G_0 \equiv \sqrt{\Lambda \hbar \omega_0 \omega_1 / (m \Omega_m L^2)}$ with the geometrical overlapping factor $\Lambda \equiv (L \Lambda_{01} / V)^2$.

2.8 Appendix: Hamiltonian derivation of ring cavity system

2.8.1 Input-output relation

We start the rigorous derivation by writing down the input-output relations [23] for the coupling of incoming electromagnetic fields $\hat{a}_{1,2}(k)$ of wavenumber k to all intracavity fields shown in Fig. 2.6. Unless claimed otherwise, we will view x as a parameter in the following contents as the two counterpropagating fields $\hat{e}_{1,2}(k)$ are defined at the instantaneous position of the membrane. The input-output relations can be derived from the frequency space field transfer matrices:

$$\hat{\mathbf{e}}(k) = \mathbb{T}_{ec}(k; x) \hat{\mathbf{c}}(k), \quad (2.61a)$$

$$\hat{\mathbf{c}}(k) = \mathbb{T}_{cf}(k; x) \hat{\mathbf{f}}(k) + \mathbb{T}_{ca} \hat{\mathbf{a}}(k), \quad (2.61b)$$

$$\hat{\mathbf{f}}(k) = \mathbb{M} \hat{\mathbf{e}}(k), \quad (2.61c)$$

where the field vectors are:

$$\begin{aligned} \hat{\mathbf{e}}(k) &= \begin{pmatrix} \hat{e}_1(k) \\ \hat{e}_2(k) \end{pmatrix}, \quad \hat{\mathbf{f}}(k) = \begin{pmatrix} \hat{f}_1(k) \\ \hat{f}_2(k) \end{pmatrix} \\ \hat{\mathbf{c}}(k) &= \begin{pmatrix} \hat{c}_1(k) \\ \hat{c}_2(k) \end{pmatrix}, \quad \hat{\mathbf{a}}(k) = \begin{pmatrix} \hat{a}_1(k) \\ \hat{a}_2(k) \end{pmatrix}, \end{aligned} \quad (2.62)$$

and the transfer matrices read:

$$\begin{aligned} \mathbb{T}_{ec}(k; x) &= \begin{pmatrix} 0 & e^{ik(L/2+x)} \\ e^{ik(L/2-x)} & 0 \end{pmatrix}, \\ \mathbb{T}_{cf}(k; x) &= \begin{pmatrix} r_0 e^{ik(L/2+x)} & 0 \\ 0 & r_0 e^{ik(L/2-x)} \end{pmatrix}, \\ \mathbb{T}_{ca} &= \begin{pmatrix} t_0 & 0 \\ 0 & t_0 \end{pmatrix}, \quad \mathbb{M} = \begin{pmatrix} r & it \\ it & r \end{pmatrix}. \end{aligned} \quad (2.63)$$

The $\hat{e}_{1,2}(k)$ fields thus take the form:

$$\hat{\mathbf{e}}(k) = \mathbb{T}_p(k) \hat{\mathbf{e}}(k) + \mathbb{T}_{in}(k; x) \hat{\mathbf{a}}(k), \quad (2.64)$$

where $\mathbb{T}_p(k) = \mathbb{T}_{ec}(k; x)\mathbb{T}_{cf}(k; x)\mathbb{M}$ is the transfer matrix describing the circulation of $\hat{\mathbf{e}}(k)$ inside the cavity and it no longer has x -dependence; $\mathbb{T}_{in}(k; x) = \mathbb{T}_{ec}(k; x)\mathbb{T}_{ca}$ is the transfer matrix describing the process of $\hat{\mathbf{a}}(k)$ coupling into the cavity and propagating to join $\hat{\mathbf{e}}(k)$. Eq. (2.64) can further be written as:

$$\hat{\mathbf{e}}(k) = \mathbb{T}_c(k)^{-1}\mathbb{T}_{in}(k; x)\hat{\mathbf{a}}(k). \quad (2.65)$$

where $\mathbb{T}_c(k)$ is the closed form transfer matrix defined as:

$$\mathbb{T}_c(k) \equiv \mathbb{1} - \mathbb{T}_p(k) = \begin{pmatrix} 1 - ite^{ikL} & -re^{ikL} \\ -re^{ikL} & 1 - ite^{ikL} \end{pmatrix}, \quad (2.66)$$

and $\mathbb{T}_c(k)^{-1}$ works as the feedback kernel that describes the effect of cavity circulation.

2.8.2 Resonance structure

To derive the Hamiltonian, we first consider resonant cavity modes assuming a perfectly reflective front mirror M_0 . In this case no outside field can couple in, i.e., $\mathbb{T}_{in}(k; x) \equiv \mathbb{0}$, and therefore Eq. (2.64) becomes:

$$\mathbb{T}_c(k)\hat{\mathbf{e}}(k) = \hat{\mathbf{0}}. \quad (2.67)$$

The resonance condition can be obtained from the nontrivial solutions of Eq. (2.67) which requires $\det \mathbb{T}_c = 0$. Within one FSR, the ring cavity can support two resonances with different propagation phases:

$$e^{ik_+L} = r - it, \quad (2.68a)$$

$$e^{ik_-L} = -r - it, \quad (2.68b)$$

where k_{\pm} are the resonant wavenumbers that depend only on the total cavity length L and the optical property r, t of the membrane. The distance between the frequencies $\omega_{\pm} = ck_{\pm}$ of the two modes within one FSR is:

$$\omega_s \equiv \frac{\omega_+ - \omega_-}{2} = \frac{c \arcsin r}{L}. \quad (2.69)$$

To work in a parameter regime which only involves two optical resonances closely separated within one FSR, as shown approximately by the red line in Fig. 2.7, we assume the membrane to have low reflectivity $r \ll 1$ such that $\omega_s \ll \Delta\omega_{\text{FSR}}$. In this case, we don't need to consider the other optical resonances out of one FSR. We

then assign \hat{c}_\pm to represent the annihilation operator of the two cavity modes with optical frequencies ω_\pm . The only nonzero commutators between them are:

$$[\hat{c}_-, \hat{c}_-^\dagger] = 1, \text{ and } [\hat{c}_+, \hat{c}_+^\dagger] = 1. \quad (2.70)$$

The relation between $\hat{e}_{1,2}$ in the two resonant modes \hat{c}_\pm can be obtained by plugging k_\pm into Eq. (2.66) and Eq. (2.67) thus becomes:

$$\begin{pmatrix} 1 & -1 \\ -1 & 1 \end{pmatrix} \begin{pmatrix} \hat{e}_1(k_+) \\ \hat{e}_2(k_+) \end{pmatrix} = \hat{0}, \quad \begin{pmatrix} 1 & 1 \\ 1 & 1 \end{pmatrix} \begin{pmatrix} \hat{e}_1(k_-) \\ \hat{e}_2(k_-) \end{pmatrix} = \hat{0}. \quad (2.71)$$

The two solutions $\hat{e}(k_\pm)$ have the following feature:

$$\hat{e}_1(k_+) = \hat{e}_2(k_+), \quad (2.72a)$$

$$\hat{e}_1(k_-) = -\hat{e}_2(k_-). \quad (2.72b)$$

The operator vector $\hat{\mathbf{f}}(k) = (\hat{f}_1(k), \hat{f}_2(k))^T$ is defined similarly as $\hat{e}(k)$, containing two fields $\hat{f}_{1,2}(k)$ that propagate away from the membrane, as shown in Fig. 2.6. $\hat{\mathbf{f}}(k)$ satisfies $\mathbb{T}_c(k)\hat{\mathbf{f}}(k) = \hat{0}$, the same as $\hat{e}(k)$ in Eq. (2.67), and its two solutions have the same feature as $\hat{e}(k_\pm)$ in Eq. (2.72). These field operators $\hat{e}_{1,2}(k_\pm), \hat{f}_{1,2}(k_\pm)$, represented by $\hat{e}_{1,2\pm}, \hat{f}_{1,2\pm}$ in the following contents for convenience, are related by the propagation phases:

$$\hat{e}_{1\pm} = e^{ik_\pm L} \hat{f}_{2\pm}, \quad (2.73a)$$

$$\hat{e}_{2\pm} = e^{ik_\pm L} \hat{f}_{1\pm}. \quad (2.73b)$$

According to the spatial features mentioned above, \hat{c}_+ is named symmetric mode and \hat{c}_- is named antisymmetric mode. They can be constructed from $\hat{e}_{1,2\pm}$ fields as follow:

$$\hat{c}_+ \equiv \frac{\hat{e}_{2+} + \hat{e}_{1+}}{\sqrt{2}}, \quad (2.74a)$$

$$\hat{c}_- \equiv \frac{\hat{e}_{2-} - \hat{e}_{1-}}{\sqrt{2}}, \quad (2.74b)$$

such that $\hat{e}_{2+} = \hat{c}_+/\sqrt{2}$ and $\hat{e}_{2-} = \hat{c}_-/\sqrt{2}$ because of Eq. (2.72). We will use these expressions above to construct the electric field in the following contents.

2.8.3 Electric field standing wave distribution

To quantitatively describe the electric field distribution, we construct a coordinate system inside the ring cavity, as shown in Fig. 2.6. The origin of this z -coordinate

is the front mirror M_0 and it increases clockwise along the optical axis of the ring cavity. It becomes $z_x = L/2 + x$ at the instantaneous position of the membrane and finally becomes $z = L$ when reaching the front mirror again. The coordinate system here is folded and thus $z = L$ represents the same position as $z = 0$.

For a beam with cross-sectional area \mathcal{A} inside the ring cavity, the frequency-dependent normalization factor is:

$$\mathcal{N}(\omega) = \sqrt{\frac{\hbar\omega}{2\mathcal{A}\epsilon_0 L}}, \quad (2.75)$$

such that the positive frequency part of the electric field at any spatial coordinate z can be written as [46]:

$$\hat{E}^+(z, t; x) = \int_0^{+\infty} d\omega \mathcal{N}(\omega) \tilde{c}(z, \omega/c; x) e^{-i\omega t}, \quad (2.76)$$

where the mode function $\tilde{c}(z, \omega/c; x) \equiv \hat{c}(z, k; x) e^{i\omega t}$ with $k = \omega/c$ can be constructed from $\hat{e}_{1,2}(k)$, $\hat{f}_{1,2}(k)$ fields taking the membrane position z_x as the phase reference point:

$$\hat{c}(z, k; x) = \begin{cases} e^{ik(z-z_x)} \hat{e}_1(k) + e^{-ik(z-z_x)} \hat{f}_1(k) & z \in (0, z_x), \\ e^{ik(z-z_x)} \hat{e}_2(k) + e^{-ik(z-z_x)} \hat{f}_2(k) & z \in (z_x, L), \end{cases} \quad (2.77)$$

because the optical relaxation time is much less than the mechanical one and thus the field distribution can adjust itself simultaneously when z_x changes. The field inside a perfect cavity is rigorously restricted by the resonance structure and thus has a discretized frequency space distribution, as shown in Eq. (2.68). Therefore, instead of an integral over the whole spectrum as in Eq. (2.76), the electric field takes the summation of components with discretized frequencies ω_{\pm} :

$$\hat{E}^+(z; x) = \sqrt{\frac{\hbar}{2\mathcal{A}\epsilon_0 L}} \times \begin{cases} \sum_{\pm} \sqrt{\omega_{\pm}} e^{ik_{\pm}(z-z_x)} \hat{e}_{1\pm} + \sum_{\pm} \sqrt{\omega_{\pm}} e^{-ik_{\pm}(z-z_x)} \hat{f}_{1\pm} & z \in (0, z_x), \\ \sum_{\pm} \sqrt{\omega_{\pm}} e^{ik_{\pm}(z-z_x)} \hat{f}_{2\pm} + \sum_{\pm} \sqrt{\omega_{\pm}} e^{-ik_{\pm}(z-z_x)} \hat{e}_{2\pm} & z \in (z_x, L). \end{cases} \quad (2.78)$$

Considering all Eqs. (2.68)(2.72)(2.73)(2.74) and plugging them into Eq. (2.78), where the process is actually a unitary transformation from $(\hat{e}_{\pm}, \hat{f}_{\pm})$ basis to $(\hat{c}_{+}, \hat{c}_{-})$

basis, the optical standing wave inside the ring cavity can be derived as:

$$\hat{E}^+(z; x) = \sqrt{\frac{\hbar}{4\mathcal{A}\epsilon_0 L}} \times \begin{cases} 2i \sin(k_-(z-x))\sqrt{\omega_-\hat{c}_-} + 2 \cos(k_+(z-x))\sqrt{\omega_+\hat{c}_+} & z \in (0, z_x), \\ 2i \sin(k_-(z-L-x))\sqrt{\omega_-\hat{c}_-} + 2 \cos(k_+(z-L-x))\sqrt{\omega_+\hat{c}_+} & z \in (z_x, L). \end{cases} \quad (2.79)$$

Or equivalently,

$$\hat{E}^+(z; x) = \mathcal{N}(\omega_-)P_-(z; x)\hat{c}_- + \mathcal{N}(\omega_+)P_+(z; x)\hat{c}_+, \quad (2.80)$$

where $P_-(z; x)$ and $P_+(z; x)$ are the wavefunctions of the two modes \hat{c}_- and \hat{c}_+ along z axis:

$$P_-(z; x) = \begin{cases} 2i \sin(k_-(z-x)) & z \in (0, z_x), \\ 2i \sin(k_-(z-L-x)) & z \in (z_x, L), \end{cases} \quad (2.81a)$$

$$P_+(z; x) = \begin{cases} 2 \cos(k_+(z-x)) & z \in (0, z_x), \\ 2 \cos(k_+(z-L-x)) & z \in (z_x, L). \end{cases} \quad (2.81b)$$

$P_{\pm}(z; x)$ represent the electric field standing wave distribution and are qualitatively plotted in Fig. 2.8. The position of the nodes for both symmetric and antisymmetric modes are shifted with the membrane position z_x and $P_{\pm}(z; x)$ has the following features:

$$P_{\pm}(z_x - \zeta \bmod L; x) = \pm P_{\pm}(z_x + \zeta \bmod L; x), \quad (2.82a)$$

$$|P_-(z = x; x)| = 0, \quad (2.82b)$$

$$|P_+(z = x; x)| = \max_{z \in (0, L)} |P_+(z; x)|, \quad (2.82c)$$

where ζ represents the distance from an arbitrary point to the membrane. That is, starting from z_x and going in two directions, the standing wave amplitude of $\hat{c}_{+(-)}$ mode remains the same (opposite sign), until it reaches maximum (zero) at $z = x$, which is $L/2$ away from z_x both clockwise and counterclockwise. The standing wave feature of $\hat{c}_{+(-)}$ mode agrees with the naming of (anti)symmetric mode.

2.8.4 Conservative cavity Hamiltonian

The cavity Hamiltonian can be obtained from the total optical energy inside the ring cavity [75]:

$$\hat{H}_{\text{cav}} = 2\mathcal{A}\epsilon_0 \int_0^L \hat{E}^-(z; x)\hat{E}^+(z; x)dz. \quad (2.83)$$

Substituting Eq. (2.79) in, we can obtain:

$$\hat{H}_{\text{cav}} = \hbar\omega_- \hat{c}_-^\dagger \hat{c}_- + \hbar\omega_+ \hat{c}_+^\dagger \hat{c}_+. \quad (2.84)$$

The cavity Hamiltonian doesn't have x -dependence because the ring cavity is a closed quantum system until now, as shown by the x -independent equation Eq. (2.67) that we start from. Explicitly illustrated in Eq. (2.82a), the field distribution relative to the position of the membrane remains the same regardless of the value of x . As the coordinate system is a folded one, the integration in Eq. (2.83) doesn't contain x .

2.8.5 Interaction with the environment

To complete the total Hamiltonian derivation and reveal the x -dependence, we consider the coupling of the cavity modes to the outside continuum by assuming the front mirror to have low transmittance $t_0 \ll 1$. The cavity linewidth γ can be obtained from the imaginary part of the pole of Eq. (2.65) and it only depends on L and front mirror transmittance t_0 :

$$\gamma = \frac{ct_0^2}{2L}. \quad (2.85)$$

Also according to Eq. (2.65), as an open passive system when $\mathbb{T}_{\text{in}}(k; x) \neq 0$, the ring cavity actually only carries the pumping frequency $\omega_p = k_p c$. The extent to which \hat{c}_\pm modes are excited depends on the detuning of the pumping frequency to the resonant ones: $\omega_p - \omega_\pm$. In the following contents we will use the wavevector k_p of the pumping field instead of the resonant wavevectors k_\pm . We use $\hat{c}_{1,2}$ to represent the counterclockwise and clockwise propagating fields that the environment fields $\hat{a}_{1,2}$ directly couple to. According to $\mathbb{T}_{ec}(k; x)$ in Eq. (2.63), the field operators $\hat{c}_{1,2}$ and $\hat{e}_{1,2}$ are related by the propagation phases:

$$\hat{e}_1 = e^{ik_p z_x} \hat{c}_2, \quad (2.86a)$$

$$\hat{e}_2 = e^{ik_p(L-z_x)} \hat{c}_1. \quad (2.86b)$$

The cavity-environment interaction Hamiltonian can be expressed as:

$$\hat{H}_\gamma = i\hbar\sqrt{2\gamma}(\hat{c}_1^\dagger \hat{a}_1 - \text{h.c.}) + i\hbar\sqrt{2\gamma}(\hat{c}_2^\dagger \hat{a}_2 - \text{h.c.}). \quad (2.87)$$

For $\hat{c}_{1,2}$ as well as the fields leaking out from the ring cavity towards the detector, the front mirror position is a natural choice of the phase reference point. However, the resonant modes \hat{c}_\pm take the membrane position z_x as the phase reference point, as shown in Eqs. (2.77), (2.78), and (2.79). The x -dependent way that $\hat{c}_{1,2}$ get

superimposed to form \hat{c}_\pm is revealed by Eqs. (2.74) and (2.86). The transformation between $\hat{c}_{1,2}$ and \hat{c}_\pm thus depends on x :

$$\hat{c}_\pm(x) = \frac{1}{\sqrt{2}} e^{ik_p L/2} (e^{-ik_p x} \hat{c}_1 \pm e^{ik_p x} \hat{c}_2). \quad (2.88)$$

Note that $\hat{c}_\pm(0)$ can be seen as the *original* optical modes that the outside modes directly couple to and they have the specific distribution when the membrane stays on its equilibrium $x = 0$. For the outside modes, $\hat{c}_\pm(x)$ are the new resonant modes when the membrane is displaced by x . It is equivalent to say that the mechanical oscillation x changes the way of interference between $\hat{c}_{1,2}$ that leads to the formation of different resonant modes $\hat{c}_\pm(x)$.

To show the feature of optomechanical coupling, we linearize Eq. (2.88) with respect to x :

$$\hat{c}_-(x) = \hat{c}_-(0) - ik_p x \hat{c}_+(0), \quad (2.89a)$$

$$\hat{c}_+(x) = \hat{c}_+(0) - ik_p x \hat{c}_-(0). \quad (2.89b)$$

Thus, the optomechanical Hamiltonian can be expressed as:

$$\begin{aligned} \hat{H}_{\text{opt}}(x) &= \hbar\omega_- \hat{c}_-^\dagger(x) \hat{c}_-(x) + \hbar\omega_+ \hat{c}_+^\dagger(x) \hat{c}_+(x) \\ &\equiv \hat{H}_0 + \hat{H}_{\text{int}}(x), \end{aligned} \quad (2.90)$$

where the free part \hat{H}_0 is equivalent to Eq. (2.84) and the optomechanical interaction part $\hat{H}_{\text{int}}(t)$ reads:

$$\hat{H}_{\text{int}}(x) = 2i\omega_s \hbar k_p x \left(\hat{c}_-^\dagger(0) \hat{c}_+(0) - \text{h.c.} \right). \quad (2.91)$$

The interaction Hamiltonian in Eq. (2.91) explicitly shows the feature of coherent coupling: the mechanical oscillation x induces the coupling between two original optical modes $\hat{c}_\pm(0)$ which have non-degenerate frequencies. Note that in the previous derivation x merely works as a parameter. Alternatively, one can start with the total Lagrangian including the mechanical degree of freedom and follow the canonical formulation [52–54], x can thus be upgraded to be a dynamical variable and further becomes a quantum operator \hat{x} after quantization. To describe the system under the general framework of Eq. (2.6), we need to express the total Hamiltonian with the new resonant modes $\hat{c}_\pm(\hat{x})$. Applying the same transformation as in Eq. (2.88), we can express the input modes $\hat{a}_{1,2}$ into antisymmetric and symmetric ones:

$$\hat{c}_{\pm\text{in}}(\hat{x}) = \frac{1}{\sqrt{2}} e^{ik_p L/2} (e^{-ik_p \hat{x}} \hat{a}_1 \pm e^{ik_p \hat{x}} \hat{a}_2). \quad (2.92)$$

Thus, the cavity-environment interaction Hamiltonian in Eq. (2.87) can be transformed to:

$$\hat{H}_\gamma = i\hbar\sqrt{2\gamma}\left(\hat{c}_-^\dagger(0)\hat{c}_{-\text{in}}(0) + c_+^\dagger(0)\hat{c}_{+\text{in}}(0) - \text{h.c.}\right), \quad (2.93)$$

which is equivalent to the generalized expression up to linear order in \hat{x} :

$$\begin{aligned} \hat{H}_\gamma(x) &= \sum_{\pm} i\hbar\sqrt{2\gamma}\left(\hat{c}_{\pm}^\dagger(\hat{x})\hat{c}_{\pm\text{in}}(\hat{x}) - \text{h.c.}\right) \\ &\approx \sum_{\pm} i\hbar\sqrt{2\gamma}\left((1 - 2k_p^2\hat{x}^2)\hat{c}_{\pm}^\dagger(0)\hat{c}_{\pm\text{in}}(0) - \text{h.c.}\right) \\ &= \hat{H}_\gamma + O(\hat{x}^2). \end{aligned} \quad (2.94)$$

It is clear from Eq. (2.94) that, even expressed in $\hat{c}_{\pm\text{in}}(\hat{x})$ for consistency under the framework, the coupling rate with the environment doesn't depend on \hat{x} . Thus, the optomechanical coupling has no dissipative feature.

2.9 Appendix: Optomechanical cooling limit in the ring cavity system

2.9.1 Coupled optical and mechanical equations of motion

For notational convenience, in the following contents, all expressions without explicit arguments are by default in time domain with temporal argument t ; all derivatives represented by dot are with respect to t , i.e., $\dot{\hat{c}}_{\pm} \equiv \partial\hat{c}_{\pm}/\partial t$; $\hat{c}_{\pm(\text{in})}$ are used to represent $\hat{c}_{\pm(\text{in})}(0)$; $C_{\pm} \equiv \langle\hat{c}_{\pm}\rangle$ are used to represent the expectation value of optical modes, i.e., the classical amplitude. We assume single-port pumping from \hat{a}_1 with frequency ω_- and amplitude A_1 . According to Eq. (2.92), the pumping amplitude of cavity modes are $C_{\pm\text{in}} = A_1/\sqrt{2}$. We work in the rotating frame with pumping frequency ω_- . Based on the Hamiltonian in Eq. (2.41), the equations of motion for \hat{c}_{\pm} modes read:

$$\dot{\hat{c}}_- = 2\omega_s k_p \hat{x} \hat{c}_+ - \gamma \hat{c}_- + \sqrt{2\gamma} \hat{c}_{-\text{in}}, \quad (2.95a)$$

$$\dot{\hat{c}}_+ = -2i\omega_s \hat{c}_+ - 2\omega_s k_p \hat{x} \hat{c}_- - \gamma \hat{c}_+ + \sqrt{2\gamma} \hat{c}_{+\text{in}}. \quad (2.95b)$$

The intracavity amplitudes of the two modes are given by the static solutions of Eq. (2.95) with $\hat{x} = 0$:

$$C_- = \frac{C_{-\text{in}}\sqrt{2\gamma}}{\gamma} = \frac{A_1}{\sqrt{\gamma}}, \quad (2.96a)$$

$$C_+ = \frac{C_{+\text{in}}\sqrt{2\gamma}}{\gamma + 2i\omega_s} = \frac{A_1\sqrt{\gamma}}{\gamma + 2i\omega_s}. \quad (2.96b)$$

It can be seen from Eq. (2.96) that \hat{c}_- mode is on resonance while \hat{c}_+ mode is off resonance.

Each optical field can be divided into static amplitude and quantum fluctuation $\hat{c}_\pm \rightarrow C_\pm + \hat{c}_\pm$ and Eq. (2.95) can thus be linearized as:

$$\dot{\hat{c}}_- = 2\omega_s k_p \hat{x} C_+ - \gamma \hat{c}_- + \sqrt{2\gamma} \hat{c}_{-\text{in}}, \quad (2.97a)$$

$$\dot{\hat{c}}_+ = -2i\omega_s \hat{c}_+ - 2\omega_s k_p \hat{x} C_- - \gamma \hat{c}_+ + \sqrt{2\gamma} \hat{c}_{+\text{in}}. \quad (2.97b)$$

The mechanical equations of motion are:

$$\dot{\hat{x}} = \frac{\hat{p}}{m} \quad (2.98a)$$

$$\begin{aligned} \dot{\hat{p}} = & 2i\omega_s k_p \hbar (\hat{c}_+^\dagger \hat{c}_- - \hat{c}_-^\dagger \hat{c}_+) \\ & - 4\omega_s k_p^2 \hbar \hat{x} (\hat{c}_-^\dagger \hat{c}_- - \hat{c}_+^\dagger \hat{c}_+) \\ & + G - m\Omega_m^2 \hat{x} - m\gamma_m \dot{\hat{x}}. \end{aligned} \quad (2.98b)$$

The linearization of Eq. (2.98b) gives:

$$\begin{aligned} \dot{\hat{p}} = & 2i\omega_s k_p \hbar (C_+^* C_- - C_-^* C_+), \\ & + 2i\omega_s k_p \hbar (\hat{c}_+^\dagger C_- - \hat{c}_-^\dagger C_+ - \hat{c}_+ C_-^* + \hat{c}_- C_+^*) \\ & - 4\omega_s k_p^2 \hbar \hat{x} (C_-^* C_- - C_+^* C_+) \\ & + G - m\Omega_m^2 \hat{x} - m\gamma_m \dot{\hat{x}}, \end{aligned} \quad (2.99)$$

where the first line represents the static radiation pressure, the second line is fluctuating radiation pressure and the third line represents optical trapping due to standing wave energy distribution.

2.9.2 Sideband feature and optical damping

To solve the coupled optical and mechanical EOMs in Eqs. (2.97), (2.98a), and (2.99), we transfer them into frequency domain [3]. The \hat{x} -dependence in sidebands of each mode \hat{c}_\pm is obtained by scattering from the other mode amplitude C_\mp and can be expressed as:

$$\hat{c}_-^{(\hat{x})}(+\Omega) = C_+ \times \frac{2\omega_s k_p \hat{x}}{\gamma - i\Omega}, \quad (2.100a)$$

$$\hat{c}_-^{\dagger(\hat{x})}(-\Omega) = C_+^* \times \frac{2\omega_s k_p \hat{x}}{\gamma - i\Omega}, \quad (2.100b)$$

$$\hat{c}_+^{(\hat{x})}(+\Omega) = C_- \times \frac{-2\omega_s k_p \hat{x}}{\gamma - i(\Omega - 2\omega_s)}, \quad (2.100c)$$

$$\hat{c}_+^{\dagger(\hat{x})}(-\Omega) = C_-^* \times \frac{-2\omega_s k_p \hat{x}}{\gamma - i(\Omega + 2\omega_s)}. \quad (2.100d)$$

Note that $\hat{c}_-^{(\hat{x})}$ is gained by scattering from C_+ which is off-resonance in cavity and the two sidebands $\hat{c}_-^{(\hat{x})}(+\Omega)$ and $\hat{c}_-^{\dagger(\hat{x})}(-\Omega)$ are symmetric. Similarly, $\hat{c}_+^{(\hat{x})}$ is

gained by scattering from the resonant mode C_- . However, as \hat{c}_+ is peaked at a higher frequency from pumping, the two sidebands $\hat{c}_+^{(\hat{x})}(+\Omega)$ and $\hat{c}_+^{(\hat{x})}(-\Omega)$ are extremely unbalanced. See Fig.2.9 for illustration. Based on sideband expressions in Eq. (2.100), we derive the \hat{x} -dependent part in $(\hat{c}_+^\dagger C_- - \hat{c}_-^\dagger C_+ - \hat{c}_+ C_-^* + \hat{c}_- C_+^*)$ as below:

$$\begin{aligned}
& (\hat{c}_+^\dagger C_- - \hat{c}_-^\dagger C_+ - \hat{c}_+ C_-^* + \hat{c}_- C_+^*)^{(\hat{x})} \\
&= 2\omega_s k_p \hat{x} |C_-|^2 \left(\frac{1}{\gamma - i(\Omega - 2\omega_s)} - \frac{1}{\gamma - i(\Omega + 2\omega_s)} \right) \\
&+ 2\omega_s k_p \hat{x} |C_+|^2 \left(\frac{1}{\gamma - i\Omega} - \frac{1}{\gamma - i\Omega} \right) \\
&\approx 2\omega_s k_p \hat{x} \frac{|A_{\text{in}}|^2}{\gamma} \frac{-4i\omega_s}{(\gamma - i\Omega)^2 + 4\omega_s^2},
\end{aligned} \tag{2.101}$$

The beating between C_- and two highly unbalanced sidebands in \hat{c}_+ mode provides strong optical rigidity and damping to the mechanical oscillator. Note that strong average field in each mode only beats with quantum fluctuation in the other mode. This scattering-like interaction between non-degenerate optical modes is the essential feature of coherent optomechanical couplings. Because the two optical resonance is splitted by $2\omega_s$, the two sidebands will have maximum difference when $\Omega \approx 2\omega_s$. As a result, optical cooling happens when we pump the antisymmetric mode with frequency ω_- and will be the strongest when $\Omega_m \approx 2\omega_s$.

We will focus on parameter regime $\Omega \approx \Omega_m \approx 2\omega_s$ in the following contents of this section. The momentum equation of motion near that frequency is:

$$\mathcal{F}[\hat{p}] = \hat{F}_{\text{baff}}(\Omega) + G_{\text{eff}} - m\Omega_{\text{eff}}^2 \hat{x}(\Omega) + im\gamma_{\text{eff}} \Omega \hat{x}(\Omega), \tag{2.102}$$

where \hat{F}_{baff} is the x -independent part of radiation pressure force $2i\omega_s k_p \hbar (\hat{c}_+^\dagger C_- - \hat{c}_-^\dagger C_+ - \hat{c}_+ C_-^* + \hat{c}_- C_+^*)$, $G_{\text{eff}} = G - 2|A_{\text{in}}|^2 k_p \hbar$ is the offsetted external force, $\Omega_{\text{eff}}^2 = \Omega_m^2 + 3|A_{\text{in}}|^2 k_p^2 \hbar \omega_s / m\gamma$ is the mechanical resonance together with optical rigidity, $\gamma_{\text{eff}} = \gamma_m + 2|A_{\text{in}}|^2 k_p^2 \hbar \omega_s / m\gamma^2$ is effective mechanical damping rate including optical cooling. All expressions above are obtained under approximation condition $\Omega_m \gg \gamma$. We can extract the optical spring and optical damping terms from the approximated formulas above:

$$\text{Optical spring:} \quad \Omega_{\text{opt}}^2 = \frac{3|A_{\text{in}}|^2 k_p^2 \hbar \omega_s}{m\gamma}, \tag{2.103a}$$

$$\text{Optical damping:} \quad \gamma_{\text{opt}} = \frac{2|A_{\text{in}}|^2 k_p^2 \hbar \omega_s}{m\gamma^2}. \tag{2.103b}$$

Compared with original mechanical properties, optical spring is always negligible within reachable input power ($P_{\text{in}} < 1\text{W}$) while optical damping is comparable with mechanical damping when $P_{\text{in}} \approx 0.04\text{W}$ and is much bigger with higher input power.

2.9.3 Quantum limit of mechanical occupation number

We then calculate the occupation number limit. In the case where the mechanical object is a high-Q-oscillator, we represent the mechanical oscillation in terms of mechanical creation and annihilation operators \tilde{m}^\dagger and \tilde{m} in the rotating frame of mechanical resonant frequency Ω_m :

$$\hat{x} = x_{\text{ZPF}}(\tilde{m}e^{-i\Omega_m t} + \tilde{m}^\dagger e^{i\Omega_m t}), \quad (2.104)$$

where $x_{\text{ZPF}} = \sqrt{\hbar/2m\Omega_m}$ is the zero-point fluctuation of the mechanical oscillator. Using ω to represent the sideband frequency of mechanical oscillator around Ω_m , the Fourier components of \tilde{m} and \tilde{m}^\dagger read:

$$\tilde{m}(t) = \int_{-\Omega_m}^{+\infty} \frac{d\omega}{2\pi} \tilde{m}(\omega) e^{-i\omega t}, \quad (2.105a)$$

$$\tilde{m}^\dagger(t) = \int_{-\infty}^{\Omega_m} \frac{d\omega}{2\pi} \tilde{m}^\dagger(-\omega) e^{-i\omega t}. \quad (2.105b)$$

Although the upper and lower limits for both integrals in Eq. (2.105) can be extended to infinity under condition $\omega \ll \Omega_m$, we keep this rigorous form for clearer future reference. The average mechanical occupation number is defined as [79]:

$$\langle n(t) \rangle \equiv \frac{\langle \tilde{m}(t)\tilde{m}^\dagger(t) + \tilde{m}^\dagger(t)\tilde{m}(t) \rangle - 1}{2}. \quad (2.106)$$

According to Eq. (2.105) $\tilde{m}(t)\tilde{m}^\dagger(t)$ and $\tilde{m}^\dagger(t)\tilde{m}(t)$ can be expressed as:

$$\tilde{m}(t)\tilde{m}^\dagger(t) = \iint_{-\Omega_m}^{+\infty} \frac{d\omega d\omega'}{(2\pi)^2} \tilde{m}(\omega)\tilde{m}^\dagger(\omega') e^{i(\omega'-\omega)t}, \quad (2.107a)$$

$$\tilde{m}^\dagger(t)\tilde{m}(t) = \iint_{-\Omega_m}^{+\infty} \frac{d\omega d\omega'}{(2\pi)^2} \tilde{m}^\dagger(\omega')\tilde{m}(\omega) e^{i(\omega'-\omega)t}. \quad (2.107b)$$

To obtain the mechanical occupation number, we need to calculate the second-order correlation function of mechanical operators $\langle \tilde{m}(\omega)\tilde{m}^\dagger(\omega') \rangle$ and $\langle \tilde{m}^\dagger(\omega')\tilde{m}(\omega) \rangle$. Therefore, we need to obtain equations of motion of \tilde{m} , \tilde{m}^\dagger by rephrasing those of \hat{x} , \hat{p} in Sec. 2.9.1 and Sec. 2.9.2.

Quoting Eq. (2.102) and ignoring the static force by letting $G_{\text{eff}} = 0$, we obtain the second-order equation of motion of \hat{x} :

$$m\ddot{\hat{x}} = \hat{F}_{\text{baff}} - m\Omega_m^2\hat{x} - m\gamma_{\text{eff}}\dot{\hat{x}}. \quad (2.108)$$

Transferred into frequency domain, Eq. (2.108) becomes:

$$m(\Omega_m^2 - \Omega^2 - i\Omega\gamma_{\text{eff}})\hat{x}(\Omega) = \hat{F}_{\text{baff}}(\Omega), \quad (2.109)$$

which can be factorized under condition $\gamma_{\text{eff}} \ll \Omega_m$ as:

$$\left[\frac{\gamma_{\text{eff}}}{2} - i(\Omega - \Omega_m) \right] \left[\frac{\gamma_{\text{eff}}}{2} - i(\Omega + \Omega_m) \right] \hat{x}(\Omega) = \frac{\hat{F}_{\text{baff}}(\Omega)}{m}. \quad (2.110)$$

According to Eqs. (2.104) and (2.105), the Fourier Transformation of \hat{x} reads:

$$\begin{aligned} \hat{x}(\Omega) &\equiv \int_{-\infty}^{+\infty} dt \hat{x}(t) e^{i\Omega t} \\ &= x_{\text{ZPF}} \int_{-\infty}^{+\infty} dt \left[e^{i(\Omega - \Omega_m)t} \int_{-\Omega_m}^{+\infty} \frac{d\omega}{2\pi} \tilde{m}(\omega) e^{-i\omega t} + e^{i(\Omega + \Omega_m)t} \int_{-\infty}^{\Omega_m} \frac{d\omega}{2\pi} \tilde{m}^\dagger(-\omega) e^{-i\omega t} \right] \\ &= x_{\text{ZPF}} \left[\tilde{m}(\Omega - \Omega_m) \theta(\Omega) + m^\dagger(-\Omega - \Omega_m) \theta(-\Omega) \right], \end{aligned} \quad (2.111)$$

where $\theta(\Omega)$ is the Heaviside step function and $\delta(\Omega)$ is the Dirac delta function. Plugging Eq. (2.111) into Eq. (2.110) and considering the thermal force \hat{F}_{th} , we obtain the equations of motion for $\tilde{m}^\dagger, \tilde{m}$ in their frequency domain:

$$\left[\frac{\gamma_m + \gamma_{\text{opt}}}{2} - i\omega \right] \tilde{m}(\omega) = \frac{ix_{\text{ZPF}}}{\hbar} \left[\hat{F}_{\text{baff}}(\Omega_m + \omega) + \hat{F}_{\text{th}}(\Omega_m + \omega) \right], \quad (2.112a)$$

$$\left[\frac{\gamma_m + \gamma_{\text{opt}}}{2} + i\omega \right] \tilde{m}^\dagger(\omega) = -\frac{ix_{\text{ZPF}}}{\hbar} \left[\hat{F}_{\text{baff}}(-(\Omega_m + \omega)) + \hat{F}_{\text{th}}(-(\Omega_m + \omega)) \right]. \quad (2.112b)$$

The fluctuating back-action force on the mechanical oscillator in the frequency domain reads:

$$\hat{F}_{\text{baff}}(\Omega) = 2i\omega_s \hbar k_p \left(C_+^* \hat{c}_-(\Omega) - C_+ \hat{c}_+^\dagger(-\Omega) - C_-^* \hat{c}_+(\Omega) + C_- \hat{c}_+^\dagger(-\Omega) \right), \quad (2.113)$$

and satisfies the relation $\hat{F}_{\text{baff}}^\dagger(\Omega) = \hat{F}_{\text{baff}}(-\Omega)$. The spectrum $S_F(\Omega)$ of the back-action force $\hat{F}_{\text{baff}}(\Omega)$ is defined as:

$$\langle \hat{F}_{\text{baff}}(\Omega) \hat{F}_{\text{baff}}(\Omega') \rangle = 2\pi \delta(\Omega' + \Omega) S_F(\Omega) \quad (2.114)$$

and takes the following expression:

$$S_F(\Omega) = 8A_{\text{in}}^2 \omega_s^2 \hbar^2 k_p^2 \gamma^2 \left[\frac{1}{\gamma^2(\gamma^2 + (\Omega - 2\omega_s)^2)} + \frac{1}{(\gamma^2 + \Omega^2)(\gamma^2 + 4\omega_s^2)} \right]. \quad (2.115)$$

Also, the thermal force \hat{F}_{th} has white spectrum:

$$\langle \hat{F}_{\text{th}}(\Omega) \hat{F}_{\text{th}}(\Omega') \rangle = 2\pi \delta(\Omega' + \Omega) 2mk_B T \gamma_m. \quad (2.116)$$

Thus, the second-order correlation function of mechanical operators can be calculated by:

$$\langle \tilde{m}(\omega) \tilde{m}^\dagger(\omega') \rangle = 2\pi \delta(\omega - \omega') S_+(\omega), \quad (2.117a)$$

$$\langle \tilde{m}^\dagger(\omega') \tilde{m}(\omega) \rangle = 2\pi \delta(\omega - \omega') S_-(\omega), \quad (2.117b)$$

with $S_+(\omega)$ and $S_-(\omega)$ defined as:

$$S_+(\omega) \equiv \frac{x_{\text{ZPF}}^2 / \hbar^2 [S_F(\Omega_m + \omega) + 2mk_B T \gamma_m]}{\left(\frac{\gamma_m + \gamma_{\text{opt}}}{2}\right)^2 + \omega^2}, \quad (2.118a)$$

$$S_-(\omega) \equiv \frac{x_{\text{ZPF}}^2 / \hbar^2 [S_F(-(\Omega_m + \omega)) + 2mk_B T \gamma_m]}{\left(\frac{\gamma_m + \gamma_{\text{opt}}}{2}\right)^2 + \omega^2}. \quad (2.118b)$$

According to Eq. (2.107), the time-domain mechanical correlation functions can be calculated as follows:

$$\begin{aligned} \langle \tilde{m}(t) \tilde{m}^\dagger(t) \rangle &= \int_{-\Omega_m}^{+\infty} S_+(\omega) \frac{d\omega}{2\pi} \\ &= \frac{4A_{\text{in}}^2 \gamma^2 k_p^2 \hbar \omega_s^2}{m \Omega_m (\gamma_m + \gamma_{\text{opt}})} \left[\frac{1}{\gamma^2 (\gamma^2 + (\Omega_m - 2\omega_s)^2)} + \frac{1}{4\Omega_m^2 \omega_s^2} \right] + \frac{\gamma_m}{\gamma_m + \gamma_{\text{opt}}} \frac{k_B T}{\Omega_m \hbar}, \end{aligned} \quad (2.119a)$$

$$\begin{aligned} \langle \tilde{m}^\dagger(t) \tilde{m}(t) \rangle &= \int_{-\Omega_m}^{+\infty} S_-(\omega) \frac{d\omega}{2\pi} \\ &= \frac{4A_{\text{in}}^2 \gamma^2 k_p^2 \hbar \omega_s^2}{m \Omega_m (\gamma_m + \gamma_{\text{opt}})} \left[\frac{1}{\gamma^2 (\Omega_m + 2\omega_s)^2} + \frac{1}{4\Omega_m^2 \omega_s^2} \right] + \frac{\gamma_m}{\gamma_m + \gamma_{\text{opt}}} \frac{k_B T}{\Omega_m \hbar}. \end{aligned} \quad (2.119b)$$

Based on all derivation above, under condition $\Omega_m \gg \gamma$, the mechanical occupation number defined in Eq. (2.106) can be expressed as:

$$\langle \hat{n} \rangle = \frac{\gamma_{\text{opt}}}{\gamma_m + \gamma_{\text{opt}}} \frac{1}{2} \left[\frac{\gamma^2}{4\Omega_m^2} - \frac{\gamma_m}{\gamma_{\text{opt}}} \right] + \frac{\gamma_m}{\gamma_m + \gamma_{\text{opt}}} \frac{k_B T}{\Omega_m \hbar}. \quad (2.120)$$

Under further condition $\gamma_{\text{opt}} \gg \gamma_m$, we can rewrite the expression above to get the ultimate cooling limit:

$$\langle \hat{n} \rangle = \frac{\gamma_m}{\gamma_m + \gamma_{\text{opt}}} n_{\text{th}} + \frac{\gamma_{\text{opt}}}{\gamma_m + \gamma_{\text{opt}}} n_{\text{ba}} \approx n_{\text{ba}}, \quad (2.121)$$

where $n_{\text{th}} = k_B T / \Omega_m \hbar$ is the thermal occupation number and $n_{\text{ba}} = \gamma^2 / 8\Omega_m^2$ is the back-action limited occupation number.

References

- [1] Tobias J Kippenberg and Kerry J Vahala. Cavity optomechanics: back-action at the mesoscale. *Science*, 321(5893):1172–1176, 2008.
- [2] Ivan Favero and Khaled Karrai. Optomechanics of deformable optical cavities. *Nature Photonics*, 3(4):201, 2009.
- [3] Markus Aspelmeyer, Tobias J Kippenberg, and Florian Marquardt. Cavity optomechanics. *Reviews of Modern Physics*, 86(4):1391, 2014.
- [4] Warwick P Bowen and Gerard J Milburn. *Quantum optomechanics*. CRC press, 2015.
- [5] M Bhattacharya and Pierre Meystre. Trapping and cooling a mirror to its quantum mechanical ground state. *Physical Review Letters*, 99(7):073601, 2007.
- [6] Liu Yong-Chun, Hu Yu-Wen, Wong Chee Wei, and Xiao Yun-Feng. Review of cavity optomechanical cooling. *Chinese Physics B*, 22(11):114213, 2013.
- [7] Andreas Sawadsky, Henning Kaufer, Ramon Moghadas Nia, Sergey P Tarabrin, Farid Ya Khalili, Klemens Hammerer, and Roman Schnabel. Observation of generalized optomechanical coupling and cooling on cavity resonance. *Physical Review Letters*, 114(4):043601, 2015.
- [8] Thomas P Purdy, P L Yu, R W Peterson, N S Kampel, and C A Regal. Strong optomechanical squeezing of light. *Physical Review X*, 3(3):031012, 2013.
- [9] Andreas Kronwald, Florian Marquardt, and Aashish A Clerk. Dissipative optomechanical squeezing of light. *New Journal of Physics*, 16(6):063058, 2014.
- [10] Nancy Aggarwal, Torrey Cullen, Jonathan Cripe, Garrett D Cole, Robert Lanza, Adam Libson, David Follman, Paula Heu, Thomas Corbitt, and Nergis Mavalvala. Room temperature optomechanical squeezing. *arXiv preprint arXiv:1812.09942*, 2018.
- [11] Roman Schnabel. Squeezed states of light and their applications in laser interferometers, sec. 5.6. *Physics Reports*, 684:1–51, 2017.
- [12] S Bose, K Jacobs, and P L Knight. Preparation of nonclassical states in cavities with a moving mirror. *Physical Review A*, 56(5):4175, 1997.
- [13] Sougato Bose, Kurt Jacobs, and Peter L Knight. Scheme to probe the decoherence of a macroscopic object. *Physical Review A*, 59(5):3204, 1999.

- [14] David Vitali, Sylvain Gigan, Anderson Ferreira, H R Böhm, Paolo Tombesi, Ariel Guerreiro, Vlatko Vedral, Anton Zeilinger, and Markus Aspelmeyer. Optomechanical entanglement between a movable mirror and a cavity field. *Physical Review Letters*, 98(3):030405, 2007.
- [15] Haixing Miao, Stefan Danilishin, and Yanbei Chen. Universal quantum entanglement between an oscillator and continuous fields. *Physical Review A*, 81(5):052307, 2010.
- [16] Stefano Mancini, Vittorio Giovannetti, David Vitali, and Paolo Tombesi. Entangling macroscopic oscillators exploiting radiation pressure. *Physical Review Letters*, 88(12):120401, 2002.
- [17] M Bhattacharya, P-L Giscard, and Pierre Meystre. Entangling the rovibrational modes of a macroscopic mirror using radiation pressure. *Physical Review A*, 77(3):030303(R), 2008.
- [18] Michael J Hartmann and Martin B Plenio. Steady state entanglement in the mechanical vibrations of two dielectric membranes. *Physical Review Letters*, 101(20):200503, 2008.
- [19] Roman Schnabel. Einstein-podolsky-rosen–entangled motion of two massive objects. *Physical Review A*, 92(1):012126, 2015.
- [20] P D Nation. Nonclassical mechanical states in an optomechanical micromaser analog. *Physical Review A*, 88(5):053828, 2013.
- [21] Matteo Brunelli, Oussama Houhou, Darren W Moore, Andreas Nunnenkamp, Mauro Paternostro, and Alessandro Ferraro. Unconditional preparation of nonclassical states via linear-and-quadratic optomechanics. *Physical Review A*, 98(6):063801, 2018.
- [22] Emily J Davis, Zhaoyou Wang, Amir H Safavi-Naeini, and Monika H Schleier-Smith. Painting nonclassical states of spin or motion with shaped single photons. *Physical Review Letters*, 121(12):123602, 2018.
- [23] Yanbei Chen. Macroscopic quantum mechanics: theory and experimental concepts of optomechanics. *Journal of Physics B: Atomic, Molecular and Optical Physics*, 46(10):104001, 2013.
- [24] Tom P Purdy, Robert W Peterson, and C.A. Regal. Observation of radiation pressure shot noise on a macroscopic object. *Science*, 339(6121):801–804, 2013.
- [25] Mateusz Bawaj, Ciro Biancofiore, Michele Bonaldi, Federica Bonfigli, Antonio Borrielli, Giovanni Di Giuseppe, Lorenzo Marconi, Francesco Marino, Riccardo Natali, Antonio Pontin, et al. Probing deformed commutators with macroscopic harmonic oscillators. *Nature Communications*, 6:7503, 2015.

- [26] Jie Li, Stefano Zippilli, Jing Zhang, and David Vitali. Discriminating the effects of collapse models from environmental diffusion with levitated nanospheres. *Physical Review A*, 93(5):050102(R), 2016.
- [27] Alessio Belenchia, Dionigi M T Benincasa, Stefano Liberati, Francesco Marin, Francesco Marino, and Antonello Ortolan. Tests of quantum-gravity-induced nonlocality via optomechanical experiments. *Physical Review D*, 95(2):026012, 2017.
- [28] Lin Tian and Hailin Wang. Optical wavelength conversion of quantum states with optomechanics. *Physical Review A*, 82(5):053806, 2010.
- [29] Jeff T Hill, Amir H Safavi-Naeini, Jasper Chan, and Oskar Painter. Coherent optical wavelength conversion via cavity optomechanics. *Nature Communications*, 3:1196, 2012.
- [30] C F Ockeloen-Korppi, Erno Damskäg, J M Pirkkalainen, T T Heikkilä, Francesco Massel, and M A Sillanpää. Low-noise amplification and frequency conversion with a multiport microwave optomechanical device. *Physical Review X*, 6(4):041024, 2016.
- [31] F Lecocq, J B Clark, R W Simmonds, J Aumentado, and J D Teufel. Mechanically mediated microwave frequency conversion in the quantum regime. *Physical Review Letters*, 116(4):043601, 2016.
- [32] JG Huang, Y Li, Lip Ket Chin, H Cai, YD Gu, Muhammad Faeyz Karim, JH Wu, TN Chen, ZC Yang, YL Hao, et al. A dissipative self-sustained optomechanical resonator on a silicon chip. *Applied Physics Letters*, 112(5):051104, 2018.
- [33] Marcelo Wu, Aaron C Hryciw, Chris Healey, David P Lake, Harishankar Jayakumar, Mark R Freeman, John P Davis, and Paul E Barclay. Dissipative and dispersive optomechanics in a nanocavity torque sensor. *Physical Review X*, 4(2):021052, 2014.
- [34] David E McClelland, Nergis Mavalvala, Yanbei Chen, and Roman Schnabel. Advanced interferometry, quantum optics and optomechanics in gravitational wave detectors. *Laser & Photonics Reviews*, 5(5):677–696, 2011.
- [35] Benjamin P Abbott et al. Observation of gravitational waves from a binary black hole merger. *Physical Review Letters*, 116(6):061102, 2016.
- [36] Benjamin P Abbott et al. Prospects for observing and localizing gravitational-wave transients with advanced ligo, advanced virgo and kagra. *Living Reviews in Relativity*, 21(1):3, 2018.
- [37] Gregory M Harry. Advanced ligo: the next generation of gravitational wave detectors. *Classical and Quantum Gravity*, 27(8):084006, 2010.

- [38] J Aasi et al. Advanced ligo. *Classical and quantum gravity*, 32(7):074001, 2015.
- [39] F Acernese et al. Advanced virgo: a second-generation interferometric gravitational wave detector. *Classical and Quantum Gravity*, 32(2):024001, 2014.
- [40] F Acernese et al. The advanced virgo detector. In *Journal of Physics: Conference Series*, volume 610, page 012014. IOP Publishing, 2015.
- [41] Harald Lück and the GEO600 Team. The geo600 project. *Classical and quantum gravity*, 14(6):1471, 1997.
- [42] C Affeldt, K Danzmann, KL Dooley, H Grote, M Hewitson, S Hild, J Hough, J Leong, H Lück, M Prijatelj, et al. Advanced techniques in geo 600. *Classical and quantum gravity*, 31(22):224002, 2014.
- [43] Yoichi Aso, Yuta Michimura, Kentaro Somiya, Masaki Ando, Osamu Miyakawa, Takanori Sekiguchi, Daisuke Tatsumi, and Hiroaki Yamamoto. Interferometer design of the kagra gravitational wave detector. *Physical Review D*, 88(4):043007, 2013.
- [44] Kentaro Somiya. Detector configuration of kagra—the japanese cryogenic gravitational-wave detector. *Classical and Quantum Gravity*, 29(12):124007, 2012.
- [45] Dustin Kleckner, William Marshall, Michiel J A de Dood, Khodadad Nima Dinyari, Bart-Jan Pors, William T M Irvine, and Dirk Bouwmeester. High finesse opto-mechanical cavity with a movable thirty-micron-size mirror. *Physical Review Letters*, 96(17):173901, 2006.
- [46] André Xuereb, Roman Schnabel, and Klemens Hammerer. Dissipative optomechanics in a michelson-sagnac interferometer. *Physical Review Letters*, 107(21):213604, 2011.
- [47] Sergey P Vyatchanin and Andrey B Matsko. Quantum speed meter based on dissipative coupling. *Physical Review A*, 93(6):063817, 2016.
- [48] Farid Ya Khalili, Sergey P Tarabrin, Klemens Hammerer, and Roman Schnabel. Generalized analysis of quantum noise and dynamic backaction in signal-recycled michelson-type laser interferometers. *Physical Review A*, 94(1):013844, 2016.
- [49] André Xuereb, Peter Horak, and Tim Freegerde. Amplified optomechanics in a unidirectional ring cavity. *Journal of Modern Optics*, 58(15):1342–1348, 2011.
- [50] Stefano Chesi, Ying-Dan Wang, and Jason Twamley. Diabolical points in multi-scatterer optomechanical systems. *Scientific Reports*, 5:7816 EP –, 01 2015.

- [51] Arzu Yilmaz, Simon Schuster, Philip Wolf, Dag Schmidt, Max Eisele, Claus Zimmermann, and Sebastian Slama. Optomechanical damping of a nanomembrane inside an optical ring cavity. *New Journal of Physics*, 19(1):013038, jan 2017.
- [52] CK Law. Interaction between a moving mirror and radiation pressure: A hamiltonian formulation. *Physical Review A*, 51(3):2537, 1995.
- [53] Sina Khorasani. Higher-order interactions in quantum optomechanics: Revisiting theoretical foundations. *Applied Sciences*, 7(7):656, 2017.
- [54] Belinda Heyun Pang. *Theoretical Foundations for Quantum Measurement in a General Relativistic Framework*. PhD thesis, California Institute of Technology, 2018.
- [55] JD Thompson, BM Zwickl, AM Jayich, Florian Marquardt, SM Girvin, and JGE Harris. Strong dispersive coupling of a high-finesse cavity to a micromechanical membrane. *Nature*, 452(7183):72, 2008.
- [56] M Karuza, M Galassi, C Biancofiore, C Molinelli, R Natali, P Tombesi, G Di Giuseppe, and D Vitali. Tunable linear and quadratic optomechanical coupling for a tilted membrane within an optical cavity: theory and experiment. *Journal of Optics*, 15(2):025704, 2012.
- [57] Hong Xie, Chang-Geng Liao, Xiao Shang, Ming-Yong Ye, and Xiu-Min Lin. Phonon blockade in a quadratically coupled optomechanical system. *Physical Review A*, 96(1):013861, 2017.
- [58] JDP Machado, RJ Slooter, and Ya M Blanter. Quantum signatures in quadratic optomechanics. *Physical Review A*, 99(5):053801, 2019.
- [59] Haixing Miao, Chunnong Zhao, L Ju, and David G Blair. Quantum ground-state cooling and tripartite entanglement with three-mode optoacoustic interactions. *Physical Review A*, 79(6):063801, 2009.
- [60] VB Braginsky, SE Strigin, and S Pr Vyatchanin. Parametric oscillatory instability in fabry–perot interferometer. *Physics Letters A*, 287(5-6):331–338, 2001.
- [61] Matthew Evans, Slawek Gras, Peter Fritschel, John Miller, Lisa Barsotti, Denis Martynov, Aidan Brooks, Dennis Coyne, Rich Abbott, Rana X Adhikari, et al. Observation of parametric instability in advanced ligo. *Physical Review Letters*, 114(16):161102, 2015.
- [62] Haixing Miao, Stefan Danilishin, Thomas Corbitt, and Yanbei Chen. Standard quantum limit for probing mechanical energy quantization. *Physical Review Letters*, 103(10):100402, 2009.

- [63] Yiqiu Ma, Shtefan L Danilishin, Chunrong Zhao, Haixing Miao, W Zach Korth, Yanbei Chen, Robert L Ward, and David G Blair. Narrowing the filter-cavity bandwidth in gravitational-wave detectors via optomechanical interaction. *Physical Review Letters*, 113(15):151102, 2014.
- [64] André Xuereb, Peter Horak, and Tim Freearge. Amplified optomechanics in a unidirectional ring cavity. *Journal of Modern Optics*, 58(15):1342–1348, 2011.
- [65] Stefano Chesi, Ying-Dan Wang, and Jason Twamley. Diabolical points in multi-scatterer optomechanical systems. *Scientific reports*, 5:7816, 2015.
- [66] Arzu Yilmaz, Simon Schuster, Philip Wolf, Dag Schmidt, Max Eisele, Claus Zimmermann, and Sebastian Slama. Optomechanical damping of a nanomembrane inside an optical ring cavity. *New Journal of Physics*, 19(1):013038, 2017.
- [67] Boris Nagorny, Th Elsässer, and A Hemmerich. Collective atomic motion in an optical lattice formed inside a high finesse cavity. *Physical Review Letters*, 91(15):153003, 2003.
- [68] D Kruse, Ch von Cube, C Zimmermann, and Ph W Courteille. Observation of lasing mediated by collective atomic recoil. *Physical Review Letters*, 91(18):183601, 2003.
- [69] Th Elsässer, B Nagorny, and A Hemmerich. Optical bistability and collective behavior of atoms trapped in a high-q ring cavity. *Physical Review A*, 69(3):033403, 2004.
- [70] Julian Klinner, Malik Lindholdt, Boris Nagorny, and Andreas Hemmerich. Normal mode splitting and mechanical effects of an optical lattice in a ring cavity. *Physical Review Letters*, 96(2):023002, 2006.
- [71] S Slama, S Bux, G Krenz, C Zimmermann, and Ph W Courteille. Superradiant rayleigh scattering and collective atomic recoil lasing in a ring cavity. *Physical Review Letters*, 98(5):053603, 2007.
- [72] Helmut Ritsch, Peter Domokos, Ferdinand Brennecke, and Tilman Esslinger. Cold atoms in cavity-generated dynamical optical potentials. *Reviews of Modern Physics*, 85(2):553, 2013.
- [73] D Schmidt, H Tomczyk, S Slama, and C Zimmermann. Dynamical instability of a bose-einstein condensate in an optical ring resonator. *Physical Review Letters*, 112(11):115302, 2014.
- [74] Farokh Mivehvar, Stefan Ostermann, Francesco Piazza, and Helmut Ritsch. Driven-dissipative supersolid in a ring cavity. *Physical Review Letters*, 120(12):123601, 2018.

- [75] H K Cheung and C K Law. Nonadiabatic optomechanical hamiltonian of a moving dielectric membrane in a cavity. *Physical Review A*, 84(2):023812, 2011.
- [76] Marlan O. Scully and M. Suhail Zubairy. *Quantum Optics*. Cambridge University Press, 1997.
- [77] William Hvidtfelt Padkær Nielsen, Yeghishe Tsaturyan, Christoffer Bo Møller, Eugene S Polzik, and Albert Schliesser. Multimode optomechanical system in the quantum regime. *Proceedings of the National Academy of Sciences*, 114(1):62–66, 2017.
- [78] Haixing Miao, Yiqiu Ma, Chunnong Zhao, and Yanbei Chen. Enhancing the bandwidth of gravitational-wave detectors with unstable optomechanical filters. *Physical review letters*, 115(21):211104, 2015.
- [79] Jun John Sakurai and Jim Napolitano. *Modern quantum mechanics; 2nd ed.* Addison-Wesley, San Francisco, CA, 2011.

PT-SYMMETRIC AMPLIFIER: BROADBAND SENSITIVITY IMPROVEMENT VIA COHERENT QUANTUM FEEDBACK

Conventional resonant detectors are subject to bandwidth-peak sensitivity trade-off, which can be traced back to the quantum Cramer-Rao Bound. Anomalous dispersion has been shown to improve it by signal amplification while leading to instability. We propose a stable quantum amplifier enabled by two-mode non-degenerate parametric amplification. Operated at the threshold, one amplifier mode is \mathcal{PT} -symmetric to the original detector mode. Our scheme is applicable to all linear systems operating at fundamental limits. Sensitivity improvements are shown for laser-interferometric gravitational-wave detectors and microwave cavity axion detectors.

3.1 Introduction

Oscillators are often used to measure weak classical signals. In the early days of gravitational-wave (GW) detection, excitations of mechanical oscillators (resonant bars) were read out by inductive, capacitive [1], or parametric [2] transducers and via a superconducting quantum interference device (SQUID) amplifier [1–3]. A more sensitive technique is to read out the phase fluctuations in a light beam (Michelson and Fabry-Perot type interferometers) [4–6] using photodetection. Signal recycling [7] and Resonant Sideband Extraction (RSE) [8] techniques were designed to optimize GW sensitivity by tailoring the optical frequency response. In this process, Mizuno noticed a trade-off between bandwidth and peak sensitivity [9] — analogous to the gain-bandwidth product in electronic amplifiers [10]. Braginsky et al. [11, 12] showed, using the energy-phase uncertainty relation, that the power spectral density of equivalent spacetime strain noise is $S_h(\Omega) \geq 4\hbar^2/S_{\mathcal{E}}(\Omega)$ where $S_{\mathcal{E}}$ is the spectral density of energy in the cavity, and

$$\int_0^{+\infty} d\Omega/(2\pi)S_h^{-1}(\Omega) \leq \Delta\mathcal{E}^2/(4\hbar^2). \quad (3.1)$$

This was also obtained by Tsang, et al. using Quantum Fisher Information [13], and further elaborated in Refs. [14–17]. For coherent states, $\Delta\mathcal{E}^2 = \hbar\omega_0\mathcal{E}$, and in this case Eq. (3.1) is also referred to as the *Energetic Quantum Limit* (EQL) for GW detection. The EQL trade-off applies to all quantum metrology experiments that use oscillators at coherent states. Specifically, GW detectors (of the laser

interferometer type [6]) use optical resonators to increase the interaction between the spacetime strain and the laser light field. Axion detectors [18] (of the Sikivie Haloscope type [19]) use microwave resonators and a powerful permanent magnet to increase the interaction with the axion field and the microwave field. In both cases, the emphasis is on increasing the quality factor [20] of the resonance to maximize the transduction coefficient between the physical signal and an electrical readout variable. However, the EQL limits the useful bandwidth of the detector according to the gain-bandwidth trade-off in Eq. (3.1).

In GW detection, the EQL can be surpassed when non-classical states of light are created for the arm cavity, with $\Delta\mathcal{E}^2 > \mathcal{E}^2/\bar{N}$ [21–24]. This can be implemented via squeezing injection [25, 26], or internal ponderomotive squeezing achieved by optical springs [14, 27, 28]. To directly address the EQL, the concept of White-Light Cavity (WLC), which resonates with a broader spectrum of frequencies without sacrificing sensitivity, has been proposed [21–24, 29–33]. In the unstable WLC (uWLC) design of Miao et al. [22] (Fig. 3.1), an additional *coherent quantum feedback controller* [34, 35] (enabled by an *unstable* optomechanical oscillator) is attached to a laser interferometer to provide an “anomalous dispersion” whose *negative group time delay* cancels the positive group time delay in the interferometer, achieving broadband signal amplification without increasing noise. The instability of this quantum system can, in principle, be stabilized by a classical controller without adding quantum noise [27, 28].

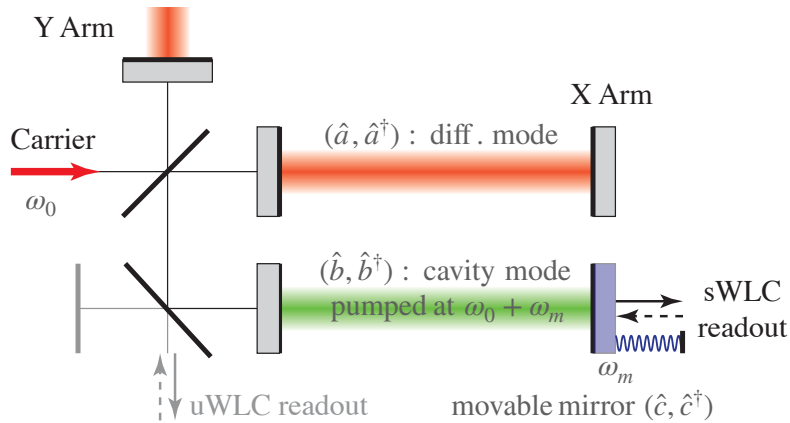


Figure 3.1: Coherent quantum feedback for laser interferometer GW detectors. The feedback controller (parametric amplifier) is achieved by the filter cavity pumped at $\omega_0 + \omega_m$ and the movable mirror with oscillation frequency ω_m . The uWLC scheme (shown in gray) extracts signals from the arm cavity, while the sWLC scheme extracts signals at the end of the filter cavity (shown in black).

In this chapter we introduce a parity-time (\mathcal{PT})-symmetric coherent quantum control strategy [36–39] that not only leads to a stable WLC (sWLC), but also applies to a wide range of quantum systems. We first consider the simplest sWLC, showing that it approaches an *Exceptional Point* (EP) [40–42] as the feedback gain reaches the threshold, where the theoretical gain in sensitivity is infinite. We then show the generality of this design strategy, since the controller’s Hamiltonian always corresponds to the time reversal of that of the plant. We finally discuss applications to GW detection and axion detection. Specifically, for the optomechanical GW detection, we further introduce a more complete \mathcal{PT} -symmetric structure with a fictitious “negative mass” to evade the measurement-induced back-action.

3.2 PT-symmetric amplifier

3.2.1 Theoretical model

Suppose the mode of a weak-signal sensor has annihilation/creation operators $(\hat{a}, \hat{a}^\dagger)$, which can be reorganized into quadrature operators $\hat{a}_1 = (\hat{a} + \hat{a}^\dagger)/\sqrt{2}$, $\hat{a}_2 = (\hat{a} - \hat{a}^\dagger)/(\sqrt{2}i)$, and the detector is coupled to a signal h via $\hat{V}_s = -\alpha\hat{a}_1h$. For a GW detector, \hat{a} is the cavity mode, h is GW strain, while α is achieved by strong carrier field in the cavity (ignoring the radiation-pressure effects [26]).

As shown in Fig. 3.2, \hat{a} and \hat{b} are coupled with rate κ , while \hat{b} and \hat{c} are amplified by a non-degenerate amplifier with rate χ , the Hamiltonian reads (Sec. 2 of Ref. [43]):

$$\hat{V} = i\hbar\kappa(\hat{a}\hat{b}^\dagger - \hat{a}^\dagger\hat{b}) + i\hbar\chi(\hat{b}^\dagger\hat{c}^\dagger - \hat{b}\hat{c}). \quad (3.2)$$

The mode \hat{b} is read out from \hat{v} , which in turn gives input quantum noise \hat{u} . The resulting Heisenberg equations reads:

$$\dot{\hat{a}} = i\alpha h - \kappa\hat{b}, \quad \dot{\hat{c}}^\dagger = \chi\hat{b}, \quad \dot{\hat{b}} = -\gamma_R\hat{b} + \kappa\hat{a} + \chi\hat{c}^\dagger + \sqrt{2\gamma_R}\hat{u}, \quad (3.3)$$

and $\hat{v} = \hat{u} - \sqrt{2\gamma_R}\hat{b}$. The combination

$$\chi\hat{a} + \kappa\hat{c}^\dagger \quad (3.4)$$

forms an *internal mode* that responds purely to the signal, i.e., $d(\chi\hat{a} + \kappa\hat{c}^\dagger)/dt = i\chi\alpha h$, with the vacuum noise coherently canceled out. When $\chi = \kappa$, this internal mode coincides with the *extraction mode*

$$\kappa\hat{a} + \chi\hat{c}^\dagger \quad (3.5)$$

that directly couples to mode \hat{b} , as shown in last equation in Eqs. (3.2). A similar system was analyzed in Ref. [36] as an amplifier to manipulate the injected signal,

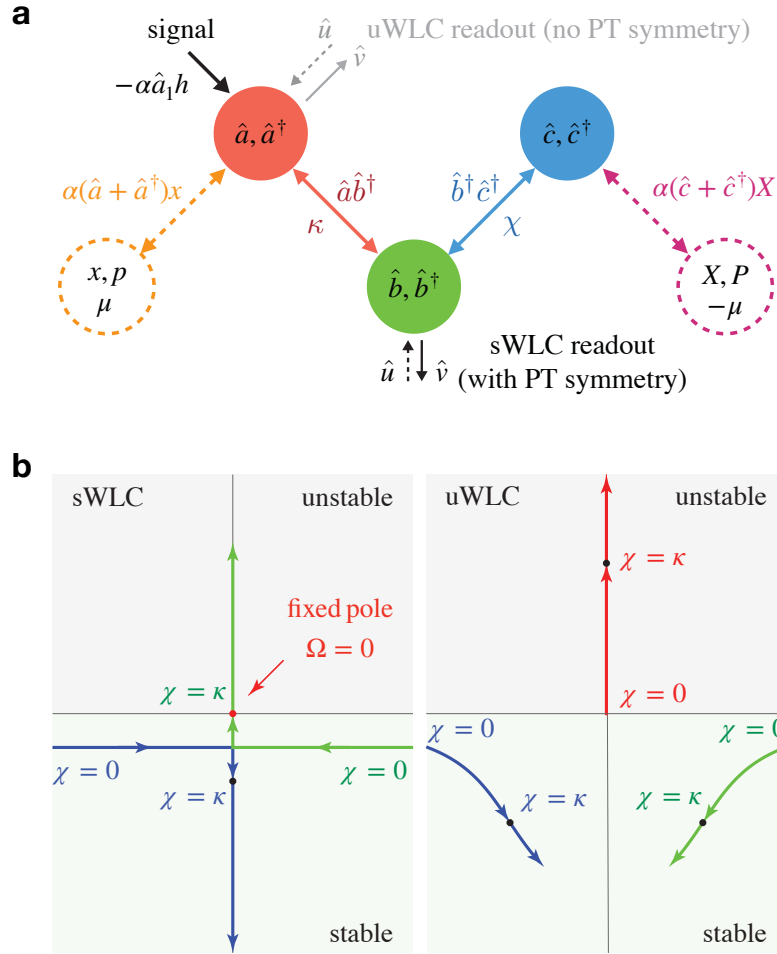


Figure 3.2: Mode interaction and stability analysis. **a**, A weak signal sensor [mode $(\hat{a}, \hat{a}^\dagger)$, plus (x, p) for the test mass in case of GW detectors] plus coherent quantum feedback with modes $(\hat{b}, \hat{b}^\dagger)$, $(\hat{c}, \hat{c}^\dagger)$. For the “sWLC readout”, the mode \hat{a} couples to \hat{b} (via $\hat{a}^\dagger \hat{b}$), which in turn couples to \hat{c} (via $\hat{b}^\dagger \hat{c}^\dagger$). The mode \hat{b} is coupled to an external continuum. The system is \mathcal{PT} -symmetric when $\kappa = \chi$. Mode \hat{c} may also couple to (X, P) with negative mass to evade the back-action noise caused by \hat{a} ’s coupling to (x, p) (see Fig. 3.6). The uWLC scheme (in gray) is recovered when \hat{a} directly couples to continuum; further setting $\kappa \rightarrow 0$ reduces it to a conventional detector. **b**, Poles trajectories of the two WLC dynamics in the complex plane, where arrows show the directions for increasing χ with κ fixed. Left: the sWLC has a fixed pole at $\Omega = 0$, invisible to the input-output relation in Eq. (3.6); the other two poles move up and down along the imaginary axis after meeting each other, until one reaches 0 at $\chi = \kappa$. For $\chi > \kappa$, the system becomes unstable. Right: the uWLC is unstable when $\chi \neq 0$.

while our system was used to surpass the EQL that limits the sensitivity for weak classical signal detection. The phase quadrature of the output field reads:

$$\hat{v}_2 = \frac{\Omega^2 - i\gamma_R\Omega + \chi^2 - \kappa^2}{\Omega^2 + i\gamma_R\Omega + \chi^2 - \kappa^2} \hat{u}_2 + \frac{2\sqrt{\gamma_R}\kappa\alpha}{\Omega^2 + i\gamma_R\Omega + \chi^2 - \kappa^2} h. \quad (3.6)$$

As shown by pole trajectories in Fig. 3.2(b), for sWLC, increasing the χ tends to destabilize the system, while increasing κ tends to stabilize it; the entire system is stable when $\chi \leq \kappa$. While for sWLC, the dynamics is always unstable.

In the single-cavity (conventional) detector where \hat{a} is read out directly, without adding \hat{b} and \hat{c} , the output field has: $\hat{v}_2 = (\Omega - i\gamma_R)/(\Omega + i\gamma_R)\hat{u}_2 - 2i\sqrt{\gamma_R}\alpha h/(\Omega + i\gamma_R)$. For vacuum fluctuations, we have the spectrum $S_{\hat{u}_i\hat{u}_j} = \delta_{ij}$, and thus

$$S_h^{\text{con}} = \frac{\Omega^2 + \gamma_R^2}{2\gamma_R\alpha^2}, \quad S_h^{\text{amp}} = \frac{(\Omega^2 - \kappa^2 + \chi^2)^2 + \gamma_R^2\Omega^2}{2\gamma_R\kappa^2\alpha^2}. \quad (3.7)$$

The gain in integrated sensitivity by amplification reads

$$\Lambda \equiv \frac{\int_0^{+\infty} d\Omega/(2\pi)[S_h^{\text{amp}}]^{-1}}{\int_0^{+\infty} d\Omega/(2\pi)[S_h^{\text{con}}]^{-1}} = (1 - \chi^2/\kappa^2)^{-1}, \quad (3.8)$$

which $\Lambda \rightarrow +\infty$ as $\chi \rightarrow \kappa^-$. Both configurations have the same noise level in \hat{v}_2 , while the amplifier has higher signal amplitude, especially as $\chi \rightarrow \kappa^-$. The broadband improvement for an example case of $\kappa = 10\gamma_R$ is shown in Fig. 3.3.

3.2.2 Connection to EP, PT-symmetry, and multi-mode generalization

On threshold at $\chi = \kappa$, poles of the output field \hat{v}_2 are at $\Omega = 0, -i\gamma_R$, making $\Omega = 0$ a double pole (see Fig. 3.2). At this point, the internal mode (Eq.(3.4)) will be parallel to the signal extraction mode (Eq.(3.5)), and the system only has two independent eigenmodes, making it an Exceptional Point (EP) [40–42].

The system is also \mathcal{PT} -symmetric: the Hamiltonian is invariant if exchanging $\hat{a} \rightarrow \hat{c}^\dagger$ and $\hat{c} \rightarrow \hat{a}^\dagger$. Specifically, the \mathcal{P} (parity) transformation swaps the $(\hat{a}, \hat{a}^\dagger)$ -mode and the $(\hat{c}, \hat{c}^\dagger)$ -mode, the \mathcal{T} (time-reversal) transformation swaps creation and annihilation operators; combination of \mathcal{PT} transformation leaves \hat{b} invariant.

For a multi-mode device with modes $\{\hat{a}_j\}$ coupled to signal h with coefficients $\{\alpha_j\}$ and with $\sum \beta_j \hat{a}_j$ originally coupled to the external continuum, let us bring in systems \hat{b} and $\{\hat{c}_j\}$, with $\{\hat{c}_j^\dagger\}$ having the same equations of motion as $\{\hat{a}_j\}$, and \hat{b} coupled to $\{\hat{a}_j\}, \{\hat{c}_j^\dagger\}$ symmetrically:

$$\dot{\hat{a}}_j = \mathcal{M}_{jk}\hat{a}_k + i\alpha_j h - \kappa\beta_j\hat{b}, \quad \dot{\hat{c}}_j^\dagger = \mathcal{M}_{jk}\hat{c}_k^\dagger + \chi\beta_j\hat{b}, \quad (3.9)$$

$$\dot{\hat{b}} = -\gamma_R\hat{b} + \kappa\beta_j\hat{a}_j + \chi\beta_j\hat{c}_j^\dagger + \sqrt{2\gamma_R}\hat{u}, \quad \hat{v} = \hat{u} - \sqrt{2\gamma_R}\hat{b}. \quad (3.10)$$

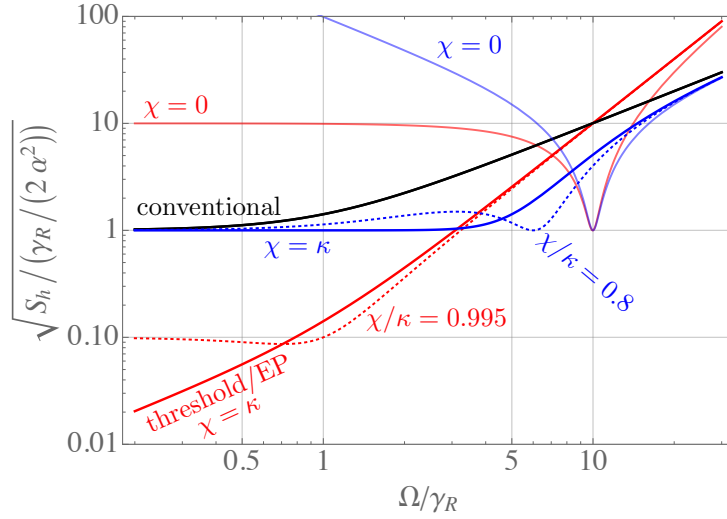


Figure 3.3: Coherent amplification of sensitivity by sWLC (red) and uWLC (blue) when $\kappa = 10\gamma_R$, compared with the conventional detector (black), all lossless. For the same choice of γ_R and χ , uWLC tends to improve higher frequency sensitivity, while sWLC tends to improve lower frequency sensitivity.

These equations can be solved in a matrix form and lead to:

$$\hat{v} = \left(\frac{\Omega - i\gamma_R - i\Delta}{\Omega + i\gamma_R - i\Delta} \right) \hat{u} - i\sqrt{2\gamma_R\kappa} \left(\frac{\sum_{k,l} \beta_k G_{kl} \alpha_l}{-i\Omega + \gamma_R - \Delta} \right) h, \quad (3.11)$$

where

$$\Delta = (\chi^2 - \kappa^2) \sum_{k,l} \beta_k G_{kl} \beta_l, \quad \mathbf{G} = (-i\Omega \mathbf{I} - \mathcal{M})^{-1}. \quad (3.12)$$

Similar to the single-mode case, \mathcal{PT} -symmetry at $\chi = \kappa$ allows $\Delta = 0$, hence the cancellation of response delay exists for $\{\hat{a}_j\}$, and leads to a broadband amplification of signal — noise remains white, while signal transfer function is proportional to κ .

Previous studies of \mathcal{PT} -symmetric systems [44, 45] highlighted the feature of gain-loss balance, usually in the context of non-Hermitian Hamiltonians constructed by eliminating the external degrees of freedom. In our case, if the \hat{b} mode is adiabatically eliminated, the $(\{\hat{a}_j\})$ and $(\{\hat{c}_j\})$ modes would have balanced effective loss and gain, respectively [36, 39].

3.2.3 Effect of Decoherence

Suppose the $(\hat{a}, \hat{b}, \hat{c})$ modes have dissipation rates γ_a, γ_b and γ_c , to their baths respectively, and have noises $\hat{n}_a^L, \hat{n}_b^L, \hat{n}_c^L$ entering in return. The effect of decoherence can be modeled by adding dissipation terms $-\gamma_Y \hat{Y}$ and noise terms $\sqrt{2\gamma_Y} \hat{n}_Y^L$ ($Y =$

a, b, c) to Eq. (3.3):

$$\dot{\hat{a}} = i\alpha h - \kappa \hat{b} - \gamma_a \hat{a} + \sqrt{2\gamma_a} \hat{n}_a^L, \quad (3.13a)$$

$$\dot{\hat{c}}^\dagger = \chi \hat{b} - \gamma_c \hat{c}^\dagger + \sqrt{2\gamma_c} \hat{n}_c^{\dagger L}, \quad (3.13b)$$

$$\dot{\hat{b}} = -(\gamma_R + \gamma_b) \hat{b} + \kappa \hat{a} + \chi \hat{c}^\dagger + \sqrt{2\gamma_R} \hat{u} + \sqrt{2\gamma_b} \hat{n}_b^L, \quad (3.13c)$$

where the noise operators $\hat{n}_{a,b,c}^L$ in the baths are associated with spectrum $S_{a,b,c}^L$, respectively.

Depending on the different nature of noise sources, the decay rate and noise spectrum vary. For the laser interferometer type GW detectors, the arm cavity mode \hat{a} and filter cavity mode \hat{b} decay to optical baths with vacuum fluctuation noise, while the mechanical mode \hat{c} decays to a thermal bath. For the Sikivie Haloscope type axion detectors [19], all modes decay to thermal baths. There are two thermal noise sources: Nyquist noise from the resonator (narrowband), and amplifier noise characterized by noise temperature (broadband). If the quality factor Q of the axion field is greater than that of the resonators, both noise sources may appear broadband. In this sense, the noise temperature is approximately the ambient temperature at the resonant frequency before tuning.

The thermal fluctuation of a mechanical oscillator is driven by thermal noise from the bath attached to it [22, 46], and therefore the occupation number for \hat{c}_2 needs to be $k_B T_{\text{env}} / (\hbar \omega_m)$, with T_{env} being the bath temperature and ω_m being the mechanical resonant frequency. Noting that

$$\frac{c_1^2 + c_2^2}{2} = c^\dagger c + \frac{1}{2}, \quad (3.14)$$

at thermal equilibrium, for $j = 1, 2$ we have

$$\int_0^{+\infty} \frac{d\Omega}{2\pi} S_{c_j} = \langle \hat{c}_j^2 \rangle = \langle N \rangle + 1/2 \approx \frac{k_B T_{\text{env}}}{\hbar \omega_m}. \quad (3.15)$$

Meanwhile, without optomechanical coupling,

$$S_{c_j} = \frac{2\gamma_m}{\gamma_m^2 + \Omega^2} S^{\text{bath}}, \quad (3.16)$$

where S^{bath} is the spectrum of the thermal bath attached to mechanical \hat{c} mode, which is supposed to have white noise. Thus, the single-sided thermal noise spectrum reads:

$$S_c^{\text{th}} = \frac{2k_B T_{\text{env}}}{\hbar \omega_m}. \quad (3.17)$$

It can also be derived from first-principles using Bose-Einstein distribution under the high-temperature limit $k_B T_{\text{env}} \gg \hbar \omega_m$.

In the scenario of GW detectors, we can assume the decoherence rates to be low compared with the readout rate γ_R [4–6], and only consider the noise effect. Different noise sources are uncorrelated with each other, and thus the effect of decoherence-induced noise to the h -normalized spectrum is given by:

$$S_h^L = [2\gamma_a S_a^L + 2\gamma_b (\Omega/\kappa)^2 S_b^L + 2\gamma_c (\chi/\kappa)^2 S_c^L] / \alpha^2, \quad (3.18)$$

where $S_{a,b,c}^L$ are the spectrum of $\hat{n}_{a,b,c}^L$ baths. If \hat{c} is a mechanical mode with eigenfrequency ω_m , quality factor Q_m , and is kept at temperature T_{env} , we have $\gamma_c = \omega_m / (2Q_m)$ and S_c^{th} is given by Eq. (3.17). Even though S_c^{th} is much greater than unity, γ_c can be much lower than optical relaxation rates.

3.3 Comparison with the unstable amplifier

In this section, we will carry out a more detailed comparison between uWLC and sWLC. Specifically, we will analyze the problem from the perspective of control theory [47].

In sWLC, the mode \hat{b} is read out by being coupled to a continuum \hat{w}_ξ of incoming ($\xi < 0$) and outgoing ($\xi > 0$) fields at $\xi = 0$, with $\hat{V}_b = i\sqrt{2\gamma_R} \hat{b} \hat{w}_{\xi=0}^\dagger + \int_{-\infty}^{+\infty} d\xi \left[i\hat{w}_\xi^\dagger \partial_\xi \hat{w}_\xi + \text{h.c.} \right]$. In uWLC, instead of \hat{b} , the original detector mode \hat{a} is coupled to the continuum, as shown in Fig. 3.2 a. We shall use \hat{u} and \hat{v} to denote \hat{w}_{0-} and \hat{w}_{0+} , the field right before entering and right after leaving. Thus, different from sWLC having Eq.(3.3), uWLC has the following equations of motion in phase quadrature:

$$\dot{\hat{a}}_2 = \alpha h - \kappa \hat{b}_2 - \gamma_R \hat{a}_2 + \sqrt{2\gamma_R} \hat{u}_2, \quad (3.19)$$

$$\dot{\hat{b}}_2 = \kappa \hat{a}_2 - \chi \hat{c}_2, \quad (3.20)$$

$$\dot{\hat{c}}_2 = -\gamma_m \hat{c}_2 - \chi \hat{b}_2 + \sqrt{2\gamma_m} \hat{w}_2, \quad (3.21)$$

where \hat{u}_2 and \hat{w}_2 represent the phase quadrature of optical vacuum and thermal noise respectively. As in Sec. 3.2.3, we ignore the mechanical loss rate and only consider the thermal noise, the solution reads:

$$\hat{v}_2 = \frac{\Omega^3 - i\gamma_R \Omega^2 + (\chi^2 - \kappa^2)\Omega - i\chi^2 \gamma_R}{\Omega^3 + i\gamma_R \Omega^2 + (\chi^2 - \kappa^2)\Omega + i\chi^2 \gamma_R} \hat{u}_2 - \frac{2i\sqrt{\gamma_R} [(\chi^2 + \Omega^2)\alpha h + \kappa\chi\sqrt{\gamma_m} \hat{w}_2]}{\Omega^3 + i\gamma_R \Omega^2 + (\chi^2 - \kappa^2)\Omega + i\chi^2 \gamma_R}. \quad (3.22)$$

Here we have the h -normalized shot noise given by

$$S_{\text{shot}}(\Omega) = \frac{\gamma_R^2 + \Omega^2 \left(\frac{\Omega^2 + \chi^2 - \kappa^2}{\Omega^2 + \chi^2} \right)^2}{2\alpha^2 \gamma_R}, \quad (3.23)$$

and the h -normalized thermal noise by

$$S_{\text{thermal}}(\Omega) = \frac{2\kappa^2 \chi^2}{\alpha^2 (\chi^2 + \Omega^2)^2} \frac{k_B T_{\text{env}}}{\hbar Q_m}. \quad (3.24)$$

The regime which we proposed before is to have $\gamma_R/\kappa \ll 1$, and then κ close to χ , and both much larger than Ω , so that the bandwidth is broadened. We have, approximately,

$$S_{\text{shot}}(\Omega) \approx \gamma_R / (2\alpha^2), \quad (3.25)$$

within the bandwidth of roughly

$$\Gamma = \frac{\gamma_R}{|1 - \kappa^2/\chi^2|}. \quad (3.26)$$

From the viewpoint of control theory [47], the sWLC and uWLC have different feedback loops because of their readouts, as shown in Fig. 3.4 **b**. For sWLC, the $\hat{a} - \hat{b}$ interaction forms the open-loop signal transfer (the *plant*) and the \hat{c} mode contributes to the feedback gain (the *controller*) through the interaction with \hat{b} , which is proportional to χ^2 . While in the uWLC case, the \hat{a} mode itself forms the plant, which is the same as the conventional detector, and the $\hat{b} - \hat{c}$ together composes the feedback controller. If we formally represent the plant transfer function as P and the controller transfer function as C , the open-loop gain will be expressed as

$$G_o = CP, \quad (3.27)$$

and the closed-loop gain can be represented as

$$G_c = \frac{P}{1 - G_o}. \quad (3.28)$$

The stability of the system is determined jointly by the stability of open-loop gain G_o and the condition when $G_o = 1$ ¹.

The C, P transfer functions of sWLC and uWLC are shown inside the colored box labeled by *plant* and *controller* in Fig. 3.4 **b**, and the open-loop gains can be

¹In the convention of $G_c = 1/(1 + G_o)$, the gain margin should be $G_o = -1$.

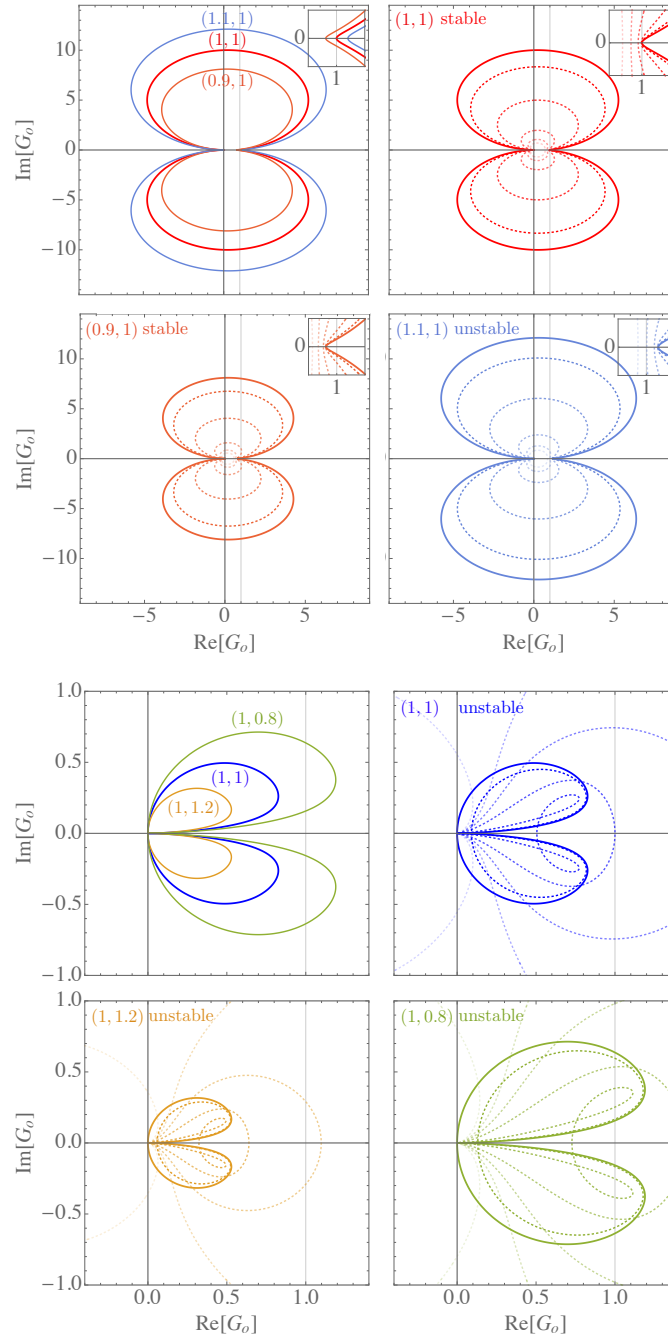


Figure 3.5: Nyquist Plot for the open-loop gain of sWLC (upper) and uWLC (lower) based on Eqs.(3.29) and (3.30). The numbers shown near the solid lines with different colors are $(\chi/(10\gamma_R), \kappa/(10\gamma_R))$ for sWLC or uWLC. The solid lines represent gains with Ω taking real values from $-\infty$ to $+\infty$. The dotted lines with decreasing opacity are Ω taking real values from $-\infty$ to $+\infty$ plus some increasing values of the imaginary part, i.e., they represent the grid image of mapping from the upper half of the Ω complex plane. The system will become unstable if the grid image encloses the $1 + 0i$ point. The right-top inserts of four subplots on the left are the zoom-in near $1 + 0i$. See the main text for more details.

expressed as:

$$G_o^{(\text{sWLC})} = \frac{-\chi^2}{\Omega^2 + i\gamma_R\Omega - \kappa^2}, \quad (3.29)$$

$$G_o^{(\text{uWLC})} = \frac{1}{\gamma_R - i\Omega} \frac{-i\Omega\kappa^2}{\chi^2 + \Omega^2}. \quad (3.30)$$

The feedback gain of uWLC is intrinsically unstable and the instability will be inherited by the whole system; while for sWLC, the stability depends on the relation between feedback gain and the open-loop transfer function, i.e., the condition of reaching $G_o = 1$, which is determined by the value of χ/κ . The open-loop gain maps the complex plane of Ω to the image complex plane. If the image of any point in the upper half of Ω complex plane touches the $1 + 0i$ point, instability will show up in the closed-loop gain. Nyquist plots for the open-loop gains of sWLC and uWLC with different χ/κ values are shown in Fig. 3.5. In our case, it is indicated that uWLC is always unstable, while sWLC becomes unstable only when $\chi/\kappa > 1$.

The connection to feedback control provides another viewpoint on system dynamics and it agrees with the pole trajectory analysis in Fig. 3.2 in terms of stability.

3.4 Application to laser interferometer GW detectors

3.4.1 PT-symmetric amplifier for GW detection

The sWLC can be implemented in a GW detector by making a simple modification of the uWLC: changing the location of signal extraction, as shown in Fig. 3.1. To incorporate motions of mirrors under radiation pressure, we need to modify the interaction Hamiltonian to include \hat{x} and \hat{p} of the differential mode of mirror motion [26]:

$$\hat{V}_{\text{GW}} = -\alpha_{\text{GW}}(\hat{x} - Lh)\hat{a}_1 + \hat{p}^2/(2\mu). \quad (3.31)$$

Here $\alpha_{\text{GW}} = \sqrt{2P_c\hbar\omega_0/(Lc)} = \sqrt{\mathcal{E}\hbar\omega_0}$, P_c is the circulating power in the arm (\mathcal{E} is the energy stored in each arm), ω_0 is the carrier angular frequency, L is the arm length, and $\mu = M/4$ is the reduced mass of the differential mode (M is the mass of each mirror). In Fig. 3.6, we plot quantum noise spectrum (including radiation-pressure noise) for sWLC and uWLC configurations with $\gamma_R/(2\pi) = 500$ Hz, $(\kappa, \chi)/\gamma_R = (10, 9.86)$. We use the LIGO Voyager [48] parameters $M = 200$ kg, $L = 4$ km, circulating power of 3 MW and a 2- μm laser wavelength. We did not include the effect of optical losses, but did consider thermal noise of the \hat{c} oscillator mode, with $Q_m \sim 8 \times 10^9$ and $T = 4$ K [22, 46], which is the most serious source of decoherence in our scheme.

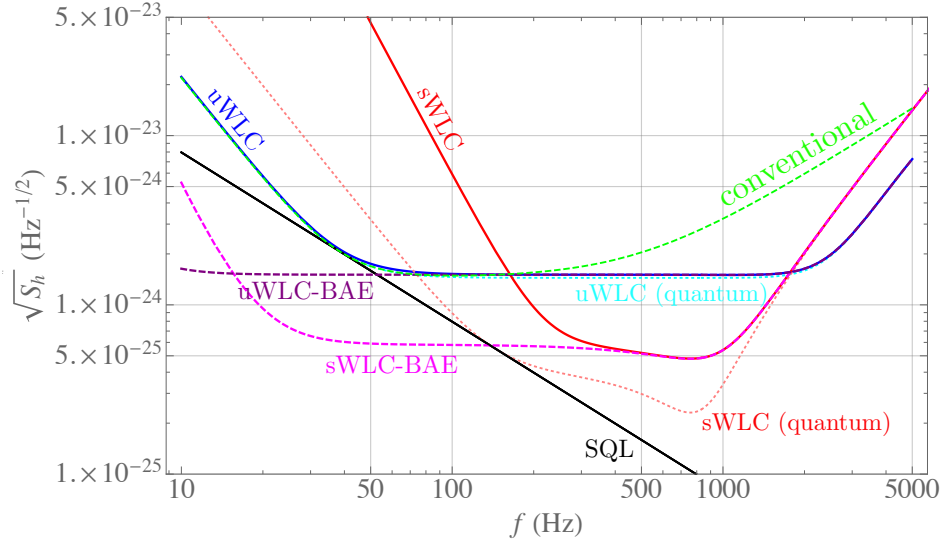


Figure 3.6: Example of GW noise spectra for sWLC and uWLC (both with $\kappa/(2\pi) = 5$ kHz, $\chi/(2\pi) = 4.93$ kHz) configurations, *only* accounting for quantum noise and thermal noise from the mechanical oscillator \hat{c} . The solid red (blue) curve represents sWLC (uWLC), with the dotted pink (cyan) curve showing the quantum noise contribution, while dashed magenta (purple) curve shows the BAE configuration that requires additional nonlinear elements. The quantum noise spectrum for conventional detector without optical loss is shown in green for comparison. All plotted cases have the same carrier wavelength, arm cavity power, WLC \hat{c} -mode mechanical loss, thermal bath condition, and readout rate $\gamma_R/(2\pi) = 500$ Hz.

Our proposal may also be realizable by inserting a nonlinear crystal into the signal recycling cavity, and pump with the sum frequency of the carrier frequency and another cavity mode [24, 49].

3.4.2 BAE with effective negative mass

Furthermore, a full \mathcal{PT} -symmetry can be designed to achieve back-action evasion (BAE) by coupling mode \hat{c} to an ancillary mode (\hat{X}, \hat{P}) that has an *effective negative mass* [50–52] $-\mu$, with Hamiltonian $\hat{V}_{\text{BAE}} = -\alpha_{\text{GW}}\hat{X}\hat{c}_1 - \hat{P}^2/(2\mu)$. Viewed more broadly in the context of coherent quantum control theory [47]: we are attaching a *controller* that consists of a time reversal of the *plant*, which, by canceling the inertia of the plant, helps drive up the *closed-loop* signal gain [53]. We shall leave the details of this for future work, but show their potentially achievable sensitivity in Fig. 3.6, in magenta and purple curves; aside from quantum noise, we have only included \hat{c} -oscillator thermal noise. This significant potential improvement motivates further studies in this direction [54, 55].

3.5 Application to microwave axion detectors

3.5.1 Introduction of microwave axion detector

The Sikivie Haloscope type axion detectors [19] we considered are designed to detect the weak conversion of dark matter axions into microwave photons in the presence of a strong magnetic field. For an axion detector consisting a stationary magnetic field \mathbf{B}_0 and a single mode $\hat{\mathbf{E}}_m$ of a microwave resonator, it can be characterized by the following interaction Hamiltonian:

$$\hat{V}_{\text{axion}} = g_{a\gamma\gamma} \mathcal{A} \int d^3\mathbf{x} \hat{\mathbf{E}}_m(\mathbf{x}) \cdot \mathbf{B}_0(\mathbf{x}), \quad (3.32)$$

where $g_{a\gamma\gamma}$ is axion-photon-photon coupling constant, \mathcal{A} is the axion field (with negligible spatial variation), and $\hat{\mathbf{E}}_m(\mathbf{x}) = \mathbf{E}_m(\mathbf{x})(\hat{a} + \hat{a}^\dagger)/\sqrt{2}$ is the electric field operator of the microwave mode, with $(\hat{a}, \hat{a}^\dagger)$ being the annihilation and creation operators, and the mode function $\mathbf{E}_m(\mathbf{x})$ satisfying $\int \mathbf{E}_m^2(\mathbf{x}) d^3\mathbf{x} = 4\pi\hbar\omega_0$, with ω_0 being eigenfrequency of the mode.

Using ω_0 as carrier frequency, we can rewrite Eq. (3.32) as:

$$\hat{V}_{\text{axion}} = \alpha_{\text{axion}}(\Psi_1 \hat{a}_1 + \Psi_2 \hat{a}_2). \quad (3.33)$$

Here $\hat{a}_{1,2}$ are the mode quadratures of the electric field, $\Psi_1 = (\Psi + \Psi^*)/\sqrt{2}$, $\Psi_2 = (\Psi - \Psi^*)/(\sqrt{2}i)$ are two quadratures of the oscillations of the axion field, $\mathcal{A}(t) = \Psi(t)e^{-i\omega_0 t} + \Psi^*(t)e^{i\omega_0 t}$. The coupling coefficient are defined as:

$$\alpha_{\text{axion}} \equiv 4\pi\eta g_{a\gamma\gamma} \sqrt{\hbar\omega_0 \mathcal{E}_B}, \quad (3.34)$$

where \mathcal{E}_B is the energy of magnetic field, and η is the overlap between the static magnetic field and the cavity mode:

$$\eta = \int \mathbf{E}_m(\mathbf{x}) \cdot \mathbf{B}_0(\mathbf{x}) d^3\mathbf{x} / \left[\int |\mathbf{E}_m|^2 d^3\mathbf{x} \cdot \int |\mathbf{B}_0|^2 d^3\mathbf{x} \right]^{1/2}. \quad (3.35)$$

Note that ω_0 is the central frequency at which the device operates, and it needs to be scanned over different values to search for the yet unknown Compton frequency of axion.

We then discuss the figure of merit for axion searches [56, 57] — the effective scan rate. As shown in Fig. 3.7, the broadband search for axion's Compton frequency requires many different such data stretches with duration $T = \Gamma_A^{-1}$, possibly using different detector configurations. Let us divide the entire bandwidth of Γ into

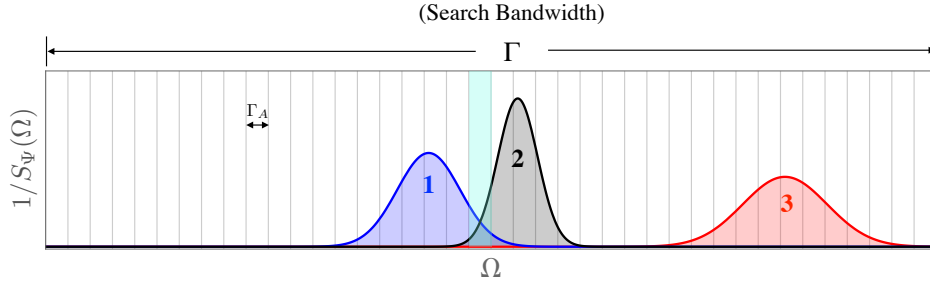


Figure 3.7: Illustration of the axion search. The entire bandwidth Γ is divided into bins with width Γ_A , and to be covered by a (large) number of detectors (three shown in the figure, in terms of their $1/S_\Psi(\Omega)$). Each bin can get contribution from multiple detectors; for example, the highlighted bin is covered by both detectors 1 and 2.

discrete angular frequencies separated by Γ_A , which we label as Δ_j , $j = 1, 2, \dots, n$, with

$$n = \Gamma/\Gamma_A. \quad (3.36)$$

We shall approximately view the search as to be carried out independently for each of these bins.

Our requirement is that for the same fiducial axion amplitude A_0 (eventually the minimum detectable axion-field amplitude), we can cumulate at least ρ_{th}^2 for each axion frequency bin. Note that to achieve the same statistical significance, ρ_{th}^2 should increase as the number of bins (hence the independent trials) increase, but rather mildly. Let us make a very crude estimation. Regarding our problem as having $n = \Gamma/\Gamma_A$ independent trials, an overall false-alarm probability of ϵ requires each bin to have

$$p_{\text{FA}} = \epsilon/N = \epsilon\gamma_a/\Gamma. \quad (3.37)$$

In absence of axion field, in the ideal situation, each ρ satisfies an exponential distribution, which means

$$\rho_{\text{th}}^2 \sim |\log(\epsilon\gamma_a/\Gamma)|, \quad (3.38)$$

which indeed depends very mildly on the number of bins.

For each run, let us assume that we have a noise spectrum of $S_J(\Omega)$. For bin j , we perform

$$Z_J^{(j)} = \left| \int_0^T z_J^{(j)}(t) \cos \Delta_j t dt \right|^2 + \left| \int_0^T z_J^{(j)}(t) \sin \Delta_j t dt \right|^2. \quad (3.39)$$

Here $z_J^{(j)}(t) = n_J(t) + A_0 \cos(\Delta_j t + \phi_0)$ where the second term is a fiducial axion term with amplitude A_0 and unknown phase ϕ_0 . Thus we have (up to numerical factors):

$$\langle Z_J^{(j)} \rangle = A_0^2 T^2 + S_J(\Delta_j) T, \quad \text{Var} Z_J^{(j)} = S_J^2(\Delta_j) T^2. \quad (3.40)$$

It is the A_0 contribution to the expectation of $Z_J^{(j)}$ that we are aiming to detect. We do this by combining multiple observations. If we assign coefficient $c_J^{(j)}$ for the J observation, we will obtain

$$c_J^{(j)} \propto \frac{1}{S_J^2(\Delta_j)}, \quad (3.41)$$

and the total SNR squared we get for the j -th bin is given by

$$[\rho^{(j)}]^2 = \sum_J \frac{A_0^4 T^2}{S_J^2(\Delta_j)}. \quad (3.42)$$

If we focus on each detector J , the figure of merit for axion detection should be counted by the integral of total SNR squared:

$$\int \frac{1}{S^2(\Omega)} d\Omega, \quad (3.43)$$

which is called the *effective scan rate*. We will use that to optimize the amplifier for axion detection in the following section.

3.5.2 PT-symmetric amplifier for axion detection

The circuit diagram that can realize Hamiltonian (3.2) for axion detection is shown in Fig. 3.8 a. The parametric amplification can be realized by a 3-wave mixing device [58–60]; sWLC corresponds to having \hat{b} mode coupled to the external continuum (“sWLC readout” in the figure), while uWLC corresponds to having \hat{a} mode coupled to the external continuum (“conventional/uWLC readout” in the figure). For conventional readout with $\kappa = 0$, the circuit is reduced to be a conventional detector.

Bode plots of the signal transfer function, i.e., from Ψ to \hat{v} , in sWLC and conventional schemes are shown in Fig. 3.8 b. From the feedback control viewpoint discussed in Sec. 3.3 and in Fig. 3.4, the $\chi = 0$ lines represent the open-loop signal transfer function of sWLC, while the $\chi/\kappa = 0.995, 1, 1.005$ lines represent the closed-loop ones. Note that the system is unstable for $\chi/\kappa = 1.005 > 1$, shown by the light blue lines, where the phase of signal transfer function decreases with frequency around the resonance near DC, which is different from the red lines with monotonically increasing phases.

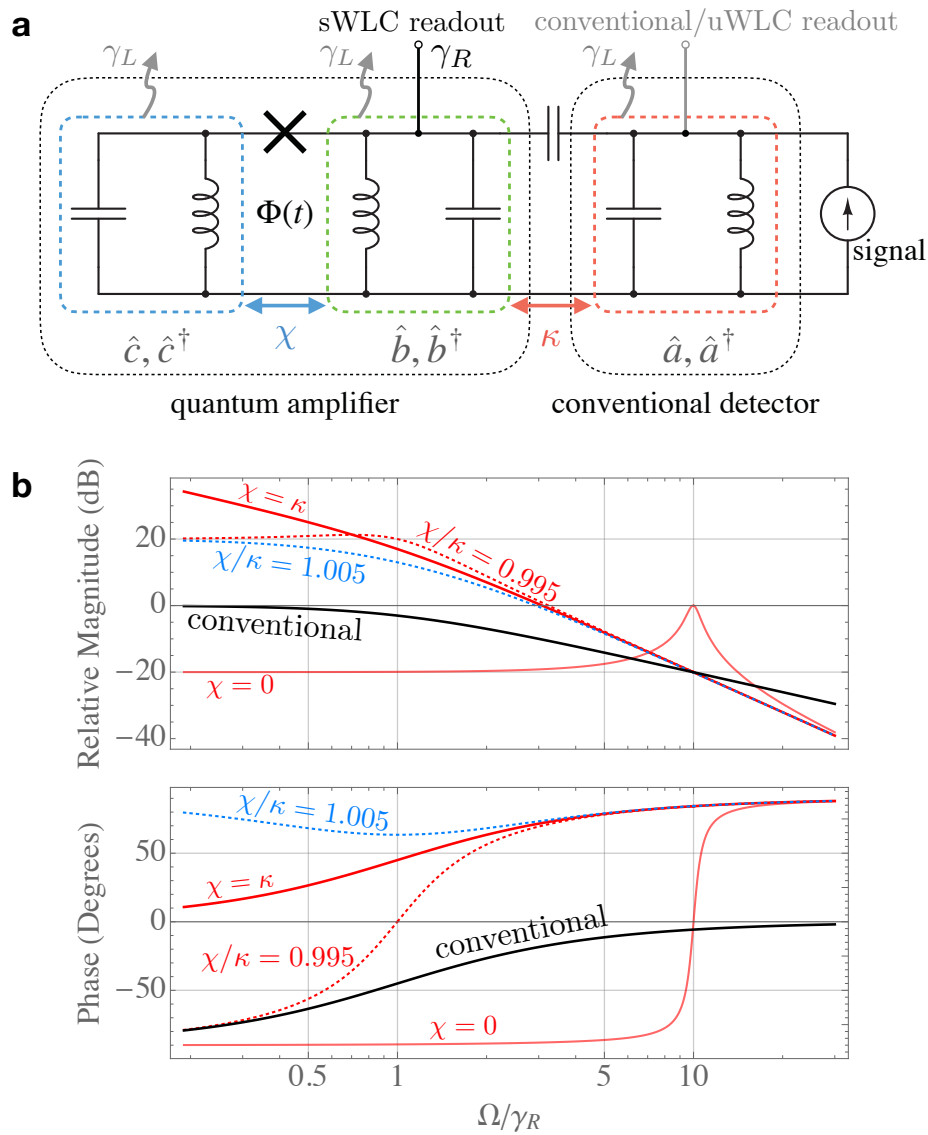


Figure 3.8: **Microwave axion detector and the Bode plots for signal transfer functions.** **a**, Circuit diagram of an axion detector (dashed box on the right) attached to a quantum amplifier (dashed box on the left). The parametric amplifier is achieved by Josephson 3-wave mixer indicated by the \times symbol in the figure, with $\Phi(t)$ indicating time-dependent external flux that act as parametric pumping (see Figure 9 of Ref. [59]). Coupling “sWLC readout” to a continuum results in a sWLC, while keeping “conventional/uWLC readout” coupling to a continuum results in uWLC, and for comparison, using “conventional/uWLC readout” without coupling to “quantum amplifier” results in a conventional detector. **b**, Bode plot of the transfer function from “signal” to “sWLC readout” with $\kappa = 10\gamma_R$ and $\gamma_L = 0$ (lossless), with the black lines representing signal transfer function of conventional detector for comparison. Note that the light blue lines represent an unstable parameter setting in sWLC scheme.

We will consider one axion field quadrature Ψ_1 and account for squeezed vacuum injection with spectral density $S_{\hat{u}_2\hat{u}_2} = e^{-2r}$. We also assume the same loss rate γ_L for \hat{a} , \hat{b} , and \hat{c} modes, assuming vacuum noise from each bath, and propagate these noise contributions to the output by applying Eq. (3.13) to Eqs. (3.3) (with h replaced by Ψ_1), leading to the Ψ_1 -referred noise spectrum $S_\Psi(\Omega)$. For the figure of merit of axion detection, we shall use the effective scan rate [56, 57] as discussed in Sec. 3.5.1:

$$\mathcal{R}_a \equiv \int_0^{+\infty} d\Omega / (2\pi) S_\Psi^{-2}(\Omega), \quad (3.44)$$

which is inversely proportional to the search time, assuming the axion field's coherence time to be very short compared with observation time, and no additional time cost when switching between configurations centered at different frequencies. In comparison with the EQL in Eq. (3.1), the effective scan rate favors peak sensitivity more than bandwidth.

Considering the losses, numerical optimization is carried out on \mathcal{R}_a : for values of χ/γ_L and squeezing factor e^{-2r} , search over κ/γ_L and γ_R/γ_L to achieve an optimal \mathcal{R}_a , and compare it with that of a single-cavity detector with the same γ_L (for which the optimal γ_R/γ_L is 2 [56]). As shown in Fig. 3.9, χ improves \mathcal{R}_a substantially, and in a way compatible with squeezing. The uWLC cases optimized with the same procedure but showing less improvements are plotted for comparison. We also plot the noise spectra of several configurations, which improve the scan rate \mathcal{R}_a (3.44) by substantially broadening the detector bandwidth, thereby requiring *far* less switches between different central frequencies.

3.6 Discussion

We proposed a quantum amplifier that can be attached to an existing sensor as a coherent quantum feedback device, and improve its sensitivity-bandwidth product. The improvement is achieved via signal amplification, and therefore, is robust against readout losses. The sensitivity gain has an interesting connection to \mathcal{PT} -symmetry: a mode \hat{b} is coupled to the original sensor modes $\{\hat{a}_j\}$, as well as auxiliary modes $\{\hat{c}_j\}$, which is time reversal to $\{\hat{a}_j\}$; furthermore, the readout is carried out from mode \hat{b} which is the only one that couples to the continuum, and thus, coherent noise cancellation is achieved when the couplings to original and auxiliary modes match. Such a strategy can be used to substantially improve the sensitivity of laser interferometer gravitational-wave detectors and microwave axion detectors. We analyzed different figures of merit, Eqs. (3.8) and (3.44), for the two detector schemes

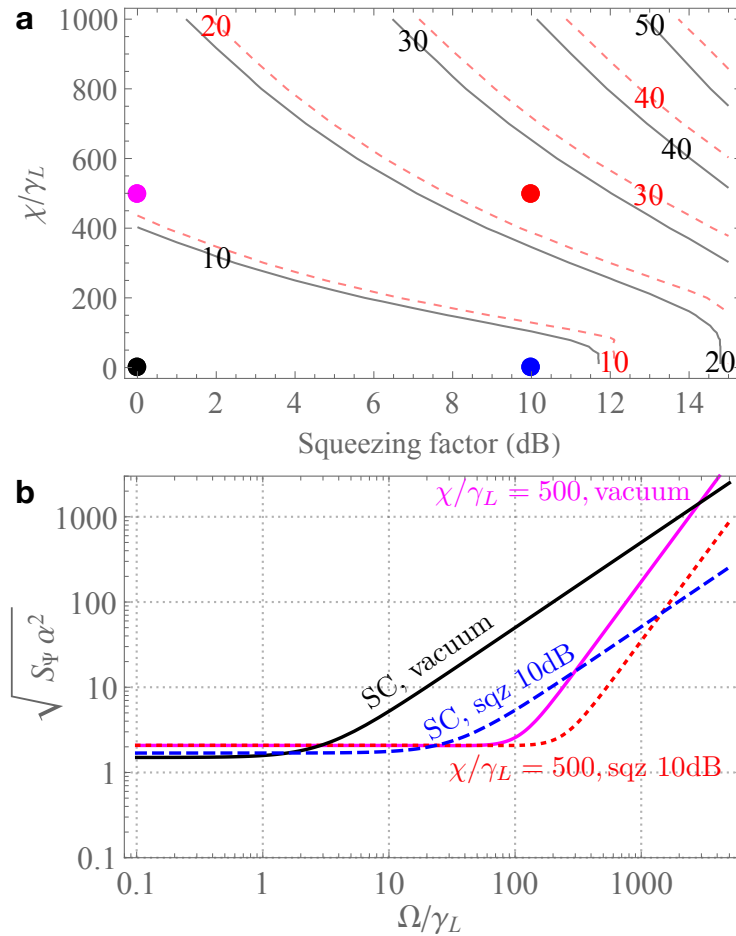


Figure 3.9: **Sensitivity improvement for axion detection.** **a**, The enhancement of effective scan rate \mathcal{R}_a achievable by sWLC (black solid lines) and uWLC (red dashed lines) axion detectors over the single-cavity one, as a function of the amplifier gain χ and squeezing factor e^{-2r} , optimized over the rate of \hat{a} - \hat{b} coupling κ and readout coupling γ_R . **b**, Examples of single-cavity (SC) and sWLC noise spectrum with \mathcal{R}_a -optimized κ , γ_R for different χ and input squeezing levels (sqz) e^{-2r} shown by color dots in **a**. Note that all couplings are shown in the unit of the generic loss rate γ_L .

respectively. Furthermore, in optomechanical GW detection, a more complete \mathcal{PT} -symmetric structure for back-action evasion is proposed using fictitious negative resonance. We leave the more detailed study to future work.

References

- [1] N Solomonson, WO Hamilton, W Johnson, and B Xu. Construction and performance of a low noise inductive transducer for the louisiana state university gravitational wave detector. *Review of scientific instruments*, 65(1):174–181, 1994.
- [2] D. G. Blair, E. N. Ivanov, M. E. Tobar, P. J. Turner, F. van Kann, and I. S. Heng. High sensitivity gravitational wave antenna with parametric transducer readout. *Phys. Rev. Lett.*, 74:1908–1911, Mar 1995.
- [3] E. Mauceli, Z. K. Geng, W. O. Hamilton, W. W. Johnson, S. Merkwowitz, A. Morse, B. Price, and N. Solomonson. The allegro gravitational wave detector: Data acquisition and analysis. *Phys. Rev. D*, 54:1264–1275, Jul 1996.
- [4] B Abbott, R Abbott, R Adhikari, A Ageev, Bruce Allen, R Amin, SB Anderson, WG Anderson, M Araya, H Armandula, et al. Detector description and performance for the first coincidence observations between ligo and geo. *Nuclear Instruments and Methods in Physics Research Section A: Accelerators, Spectrometers, Detectors and Associated Equipment*, 517(1-3):154–179, 2004.
- [5] Rana X Adhikari. Gravitational radiation detection with laser interferometry. *Reviews of Modern Physics*, 86(1):121, 2014.
- [6] B. P. Abbott, R. Abbott, T. D. Abbott, M. R. Abernathy, and et. al. Observation of gravitational waves from a binary black hole merger. *Phys. Rev. Lett.*, 116:061102, Feb 2016.
- [7] Brian J Meers. Recycling in laser-interferometric gravitational-wave detectors. *Physical Review D*, 38(8):2317, 1988.
- [8] Jun Mizuno, Kenneth A Strain, PG Nelson, JM Chen, Roland Schilling, Albrecht Rüdiger, Walter Winkler, and Karsten Danzmann. Resonant sideband extraction: a new configuration for interferometric gravitational wave detectors. *Physics Letters A*, 175(5):273–276, 1993.
- [9] Jun Mizuno. *Comparison of optical configurations for laser-interferometric gravitational-wave detectors*. PhD thesis, AEI-Hannover, MPI for Gravitational Physics, Max Planck Society, 1995.
- [10] E. A. Faulkner and J. B. Grimbleby. Active filters and gain-bandwidth product. *Electronics Letters*, 6(17):549–550, 1970.

- [11] Vladimir Braginsky and Farid Ya Khalili. *Quantum measurement*. Cambridge University Press, 1995.
- [12] Vladimir B Braginsky, Mikhail L Gorodetsky, Farid Ya Khalili, and Kip S Thorne. Energetic quantum limit in large-scale interferometers. In *AIP Conference Proceedings*, volume 523, pages 180–190. AIP, 2000.
- [13] Mankei Tsang, Howard M Wiseman, and Carlton M Caves. Fundamental quantum limit to waveform estimation. *Physical review letters*, 106(9):090401, 2011.
- [14] Haixing Miao, Rana X Adhikari, Yiqiu Ma, Belinda Pang, and Yanbei Chen. Towards the fundamental quantum limit of linear measurements of classical signals. *Physical review letters*, 119(5):050801, 2017.
- [15] Belinda Pang and Yanbei Chen. Quantum interactions between a laser interferometer and gravitational waves. *Physical Review D*, 98(12):124006, 2018.
- [16] Belinda Pang and Yanbei Chen. Fundamental relations between measurement, radiation, and decoherence in gravitational wave laser interferometer detectors. *Physical Review D*, 99(12):124016, 2019.
- [17] Haixing Miao, Nicolas D Smith, and Matthew Evans. Quantum limit for laser interferometric gravitational-wave detectors from optical dissipation. *Physical Review X*, 9(1):011053, 2019.
- [18] T. Braine, R. Cervantes, N. Crisosto, N. Du, S. Kimes, L. J. Rosenberg, G. Rybka, J. Yang, D. Bowering, A. S. Chou, R. Khatriwada, A. Sonnenschein, W. Wester, G. Carosi, N. Woollett, L. D. Duffy, R. Bradley, C. Boutan, M. Jones, B. H. LaRoque, N. S. Oblath, M. S. Taubman, J. Clarke, A. Dove, A. Eddins, S. R. O’Kelley, S. Nawaz, I. Siddiqi, N. Stevenson, A. Agrawal, A. V. Dixit, J. R. Gleason, S. Jois, P. Sikivie, J. A. Solomon, N. S. Sullivan, D. B. Tanner, E. Lentz, E. J. Daw, J. H. Buckley, P. M. Harrington, E. A. Henriksen, and K. W. Murch. Extended search for the invisible axion with the axion dark matter experiment. *Phys. Rev. Lett.*, 124:101303, Mar 2020.
- [19] P. Sikivie. Experimental tests of the "invisible" axion. *Phys. Rev. Lett.*, 51:1415–1417, Oct 1983.
- [20] I Stern, A A Chisholm, J Hoskins, P Sikivie, N S Sullivan, D B Tanner, G Carosi, and K van Bibber. Cavity design for high-frequency axion dark matter detectors. *Review of Scientific Instruments*, 86(12):123305, December 2015.
- [21] Minchuan Zhou, Zifan Zhou, and Selim M Shahriar. Quantum noise limits in white-light-cavity-enhanced gravitational wave detectors. *Physical Review D*, 92(8):082002, 2015.

- [22] Haixing Miao, Yiqiu Ma, Chunnong Zhao, and Yanbei Chen. Enhancing the bandwidth of gravitational-wave detectors with unstable optomechanical filters. *Physical review letters*, 115(21):211104, 2015.
- [23] Mikhail Korobko, Lisa Kleybolte, Stefan Ast, Haixing Miao, Yanbei Chen, and Roman Schnabel. Beating the standard sensitivity-bandwidth limit of cavity-enhanced interferometers with internal squeezed-light generation. *Physical review letters*, 118(14):143601, 2017.
- [24] Mikhail Korobko, Yiqiu Ma, Yanbei Chen, and Roman Schnabel. Quantum expander for gravitational-wave observatories. *Light: Science & Applications*, 8(1):118, dec 2019.
- [25] Carlton M Caves. Quantum-mechanical noise in an interferometer. *Physical Review D*, 23(8):1693, 1981.
- [26] H Jeff Kimble, Yuri Levin, Andrey B Matsko, Kip S Thorne, and Sergey P Vyatchanin. Conversion of conventional gravitational-wave interferometers into quantum nondemolition interferometers by modifying their input and/or output optics. *Physical Review D*, 65(2):022002, 2001.
- [27] Alessandra Buonanno and Yanbei Chen. Quantum noise in second generation, signal-recycled laser interferometric gravitational-wave detectors. *Physical Review D*, 64(4):042006, 2001.
- [28] Alessandra Buonanno and Yanbei Chen. Signal recycled laser-interferometer gravitational-wave detectors as optical springs. *Physical Review D*, 65(4):042001, 2002.
- [29] A Wicht, Karsten Danzmann, M Fleischhauer, M Scully, G Müller, and R-H Rinkleff. White-light cavities, atomic phase coherence, and gravitational wave detectors. *Optics Communications*, 134(1-6):431–439, 1997.
- [30] Stacy Wise, G Mueller, D Reitze, DB Tanner, and Bernard F Whiting. Linewidth-broadened fabry–perot cavities within future gravitational wave detectors. *Classical and Quantum Gravity*, 21(5):S1031, 2004.
- [31] Stacy Wise, V Quetschke, AJ Deshpande, G Mueller, DH Reitze, DB Tanner, BF Whiting, Y Chen, A Tünnermann, E Kley, et al. Phase effects in the diffraction of light: beyond the grating equation. *Physical review letters*, 95(1):013901, 2005.
- [32] GS Pati, M Salit, K Salit, and MS Shahriar. Demonstration of a tunable-bandwidth white-light interferometer using anomalous dispersion in atomic vapor. *Physical review letters*, 99(13):133601, 2007.
- [33] Yiqiu Ma, Haixing Miao, Chunnong Zhao, and Yanbei Chen. Quantum noise of a white-light cavity using a double-pumped gain medium. *Physical Review A*, 92(2):023807, 2015.

- [34] Hideo Mabuchi and Navin Khaneja. Principles and applications of control in quantum systems. *International Journal of Robust and Nonlinear Control: IFAC-Affiliated Journal*, 15(15):647–667, 2005.
- [35] Hendra I Nurdin, Matthew R James, and Ian R Petersen. Coherent quantum lqg control. *Automatica*, 45(8):1837–1846, 2009.
- [36] A. Metelmann and A. A. Clerk. Quantum-limited amplification via reservoir engineering. *Phys. Rev. Lett.*, 112:133904, Apr 2014.
- [37] Zhong-Peng Liu, Jing Zhang, Şahin Kaya Özdemir, Bo Peng, Hui Jing, Xin-You Lü, Chun-Wen Li, Lan Yang, Franco Nori, and Yu-xi Liu. Metrology with pt-symmetric cavities: enhanced sensitivity near the pt-phase transition. *Physical review letters*, 117(11):110802, 2016.
- [38] Joe Bentley, Philip Jones, Denis Martynov, Andreas Freise, and Haixing Miao. Converting the signal-recycling cavity into an unstable optomechanical filter to enhance the detection bandwidth of gravitational-wave detectors. *Phys. Rev. D*, 99:102001, May 2019.
- [39] Yu-Xin Wang and A. A. Clerk. Non-hermitian dynamics without dissipation in quantum systems. *Phys. Rev. A*, 99:063834, Jun 2019.
- [40] Jan Wiersig. Sensors operating at exceptional points: General theory. *Phys. Rev. A*, 93:033809, Mar 2016.
- [41] Hoi-Kwan Lau and Aashish A. Clerk. Fundamental limits and non-reciprocal approaches in non-hermitian quantum sensing. *Nature Communications*, 9(1):4320, 2018.
- [42] Mengzhen Zhang, William Sweeney, Chia Wei Hsu, Lan Yang, A. D. Stone, and Liang Jiang. Quantum noise theory of exceptional point amplifying sensors. *Phys. Rev. Lett.*, 123:180501, Oct 2019.
- [43] Yanbei Chen. Macroscopic quantum mechanics: theory and experimental concepts of optomechanics. *Journal of Physics B: Atomic, Molecular and Optical Physics*, 46(10):104001, 2013.
- [44] Christian E Rüter, Konstantinos G Makris, Ramy El-Ganainy, Demetrios N Christodoulides, Mordechai Segev, and Detlef Kip. Observation of parity–time symmetry in optics. *Nature physics*, 6(3):192–195, 2010.
- [45] Bo Peng, Şahin Kaya Özdemir, Fuchuan Lei, Faraz Monifi, Mariagiovanna Gianfreda, Gui Lu Long, Shanhui Fan, Franco Nori, Carl M Bender, and Lan Yang. Parity–time-symmetric whispering-gallery microcavities. *Nature Physics*, 10(5):394–398, 2014.

- [46] Yiqiu Ma, Shtefan L. Danilishin, Chunnong Zhao, Haixing Miao, W. Zach Korth, Yanbei Chen, Robert L. Ward, and D. G. Blair. Narrowing the filter-cavity bandwidth in gravitational-wave detectors via optomechanical interaction. *Phys. Rev. Lett.*, 113:151102, Oct 2014.
- [47] O.L.R. Jacobs. *Introduction to control theory*. Oxford University Press, 1993.
- [48] R X Adhikari, K Arai, A F Brooks, C Wipf, O Aguiar, P Altin, B Barr, L Barsotti, R Bassiri, A Bell, G Billingsley, R Birney, D Blair, E Bonilla, and et. al. A cryogenic silicon interferometer for gravitational-wave detection. *Classical and Quantum Gravity*, 37(16):165003, jul 2020.
- [49] Vaishali Badrishi Adya, Min Jet Yap, Daniel Toyra, Terry G McRae, Paul A Altin, Lauren K Sarre, Mart Meijerink, Nutsinee Kijbunchoo, Bram JJ Slagmolen, Robert Ward, et al. Quantum enhanced khz gravitational wave detector with internal squeezing. *Classical and Quantum Gravity*, 2020.
- [50] Mankei Tsang and Carlton M Caves. Coherent quantum-noise cancellation for optomechanical sensors. *Physical review letters*, 105(12):123601, 2010.
- [51] F. Ya. Khalili and E. S. Polzik. Overcoming the standard quantum limit in gravitational wave detectors using spin systems with a negative effective mass. *Phys. Rev. Lett.*, 121:031101, Jul 2018.
- [52] Jiashun Yan and Jun Jing. Coherent noise cancellation in optomechanical system with double optical modes, 2020.
- [53] Supplementary material for broadband sensitivity improvement by via coherent quantum feedback with pt symmetry. *Supplementary Material (link to be updated after publication)*.
- [54] Joe Bentley, Hendra Nurdin, Yanbei Chen, and Haixing Miao. A systematic approach to realising quantum filters for high-precision measurements using network synthesis theory. *arXiv preprint arXiv:2002.07644*, 2020.
- [55] Rion Shimazu and Naoki Yamamoto. Quantum functionalities via feedback amplification. *arXiv preprint arXiv:1909.12822*, 2019.
- [56] M Malnou, DA Palken, BM Brubaker, Leila R Vale, Gene C Hilton, and KW Lehnert. Squeezed vacuum used to accelerate the search for a weak classical signal. *Physical Review X*, 9(2):021023, 2019.
- [57] D. A. Palken, B. M. Brubaker, M. Malnou, S. Al Kenany, K. M. Backes, S. B. Cahn, Y. V. Gurevich, S. K. Lamoreaux, S. M. Lewis, R. H. Maruyama, N. M. Rapidis, J. R. Root, M. Simanovskaia, T. M. Shokair, Sukhman Singh, D. H. Speller, I. Urdinaran, K. van Bibber, L. Zhong, and K. W. Lehnert. Improved analysis framework for axion dark matter searches. *Phys. Rev. D*, 101:123011, Jun 2020.

- [58] Baleegh Abdo, Archana Kamal, and Michel Devoret. Nondegenerate three-wave mixing with the josephson ring modulator. *Physical Review B*, 87(1):014508, 2013.
- [59] Ananda Roy and Michel Devoret. Introduction to parametric amplification of quantum signals with josephson circuits. *Comptes Rendus Physique*, 17(7):740–755, 2016.
- [60] Ananda Roy and Michel Devoret. Quantum-limited parametric amplification with josephson circuits in the regime of pump depletion. *Phys. Rev. B*, 98:045405, Jul 2018.

Chapter 4

OPTOMECHANICAL REALIZATION OF PT-SYMMETRIC INTERFEROMETER

Quantum noise limits the sensitivity of precision measurement devices, such as laser interferometer gravitational-wave observatories and axion detectors. In the shot-noise-limited regime, these resonant detectors are subject to a trade-off between the peak sensitivity and bandwidth. One approach to circumvent this limitation in gravitational-wave detectors is to embed an anomalous-dispersion optomechanical filter to broaden the bandwidth. The original filter cavity design, however, makes the entire system unstable. Recently, we proposed the coherent feedback between the arm cavity and the optomechanical filter to eliminate the instability via PT-symmetry [1]. The original analysis based upon the Hamiltonian formalism adopted the single-mode and resolved-sideband approximations. In this study, we go beyond these approximations and consider realistic parameters. We show that the main conclusion concerning stability remains intact, with both Nyquist analysis and a detailed time-domain simulation.

4.1 Introduction

The detection of gravitational waves (GW) from a binary black hole merger in 2015 [2] opened a new window of astronomy observation. Binary black hole systems have so far been the most commonly measured GW sources [3, 4]. The demand for extracting richer properties of the ringdown stage [5–9], as well as other astrophysical processes that produce pronounced gravitational waves at high frequencies, e.g., the binary neutron star mergers [10–12] and core collapse supernovae [13–15], calls for the broadband and high-frequency sensitivity of gravitational wave detectors. For current advanced detectors and even future detectors including Einstein Telescope [16, 17] and Cosmic Explorer [18], the quantum shot noise limits the detector sensitivity from a few hundred Hz to kilo Hz [19]. Similarly, recently proposed detectors of axion-like-particles in the galactic halo suffer from the photon shot noise across their sensitivity bands [20–23].

In the canonical interferometer configuration [24], resonant arm cavities are used to increase the relative signal strength by effectively extending the length of the detector via repeated reflections of the optical field. However, the positive dispersion

of the arm cavity makes the signal at higher frequencies no longer resonant. This leads to an inverse relationship between the peak sensitivity and bandwidth of the detector, known as the Mizuno limit [25]. This can be traced back to the energetic quantum limit [26, 27], which is also called the quantum Cramer-Rao Bound (QCRB) [28], and is therefore limited by the quantum fluctuation of the intracavity light field [29].

One approach to broaden the bandwidth without sacrificing peak sensitivity is to attach a negative-dispersion optomechanical filter cavity to the arm cavity [30], which can compensate for the phase gained in the arm cavity and thus resulting in a *white light cavity* effect. However, such a scheme is dynamically unstable and thus an additional stabilizing controller must be implemented. We will call this unstable white light cavity scheme as *uWLC* for short. In the original proposal [30], in addition to the filter cavity, there are several auxiliary optics, either for impedance match with the input mirror of the arm cavity or for steering the field to the filter, which leads to a rather complex setup.

In a later study [31], it was found that converting the signal-recycling cavity (SRC) into the optomechanical filter can lead to bandwidth broadening with a much simpler optical layout, as illustrated in Fig. 4.1. The parameter regime considered [31], however, still leads to an unstable system. We recently realized that, when the optomechanical interaction strength is smaller than or equal to the coupling frequency between the arm cavity and the filter cavity, the system will be self-stabilized [1]. More interestingly, the peak sensitivity is improved together with the bandwidth, not due to squeezing but a significant enhancement of the signal response. We shall call this stably operated white light cavity scheme as *sWLC* for short. So far, the *sWLC* scheme has only been analyzed using the Hamiltonian in the single-mode and the resolved-sideband approximation [1, 31], which treats the arm cavity signal field, the mechanical oscillator, and the field in the filter cavity as single modes, separately. The stability issue of the system is based on the poles of the resulting input-output relation [1]. One natural question to ask is, whether the stability and sensitivity improvement remain valid when these approximations are removed by considering realistic parameters. Answering such a question defines the theme of this work.

Note that in the low-frequency band (below 40Hz), quantum back-action in the main interferometer will further restrict the sensitivity, because the radiation pressure force from the strong field would interact with the test mass. Throughout the chapter,

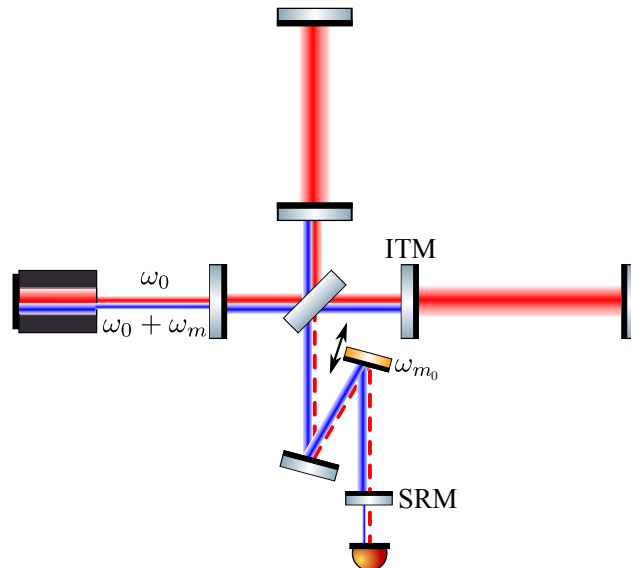


Figure 4.1: A schematics of the interferometer configuration with the signal-recycling cavity (SRC) as the optomechanical filter. Both the main arm cavities and the SRC resonant at ω_0 , but they have different free spectral ranges due to the different cavity lengths. One of the mirrors in the SRC acts as the mechanical degree of freedom that resonant at ω_{m_0} . It couples to the signal sidebands around ω_0 via the radiation pressure due to the blue detuned SRC pumping field at $\omega_0 + \omega_m$. Note that $\omega_{m_0}/\omega_m \approx 1$, with slight difference caused by the optical spring effect due to the blue-detuned pumping (will be explained later near Eq. (4.17)). ITM: input test mass, SRM: signal-recycling mirror.

we will be focusing on the shot-noise-limited sensitivity, leaving the consideration and cancellation of back-action noise for future studies [1].

The outline of this chapter goes as follows: in Sec. 4.2 we revisit the idealized Hamiltonian dynamics and stability requirement, and introduce the full analysis method beyond the single-mode and resolved-sideband approximations. In Sec. 4.3, we solve the system dynamics in the frequency domain. We also analyze the stability using the Nyquist criterion and show the resulting sensitivity. In Sec. 4.4, we carry out a detailed time-domain simulation, and show the agreement with the frequency-domain analysis. Finally, in Sec. 4.6, we summarize our results and discuss further possibilities.

4.2 From single-mode approximation to full analysis

In this section, we will first recap the idealized Hamiltonian dynamics under the single-mode approximation as analyzed in Refs. [1, 31] for the sWLC, and also

revisit the stability requirement. We will then introduce the analyzing framework considering the realistic setup, by abandoning the approximations applied in the previous treatment. The detailed analysis in the frequency and time domain will be carried in Sec. 4.3 and 4.4, respectively.

The idealized sWLC mode interaction in the rotating frame of frequency ω_0 , as illustrated in Fig. 4.2, can be described by the following Hamiltonian:

$$\hat{H}_{\text{int}} = i \hbar \omega_s (\hat{a} \hat{b}^\dagger - \hat{a}^\dagger \hat{b}) + i \hbar G (\hat{b}^\dagger \hat{c}^\dagger - \hat{b} \hat{c}), \quad (4.1)$$

with \hat{a} , \hat{b} , \hat{c} being the quantum operators of the differential optical mode of the arm cavity, the SRC (i.e., the filter cavity) optical mode, and the mechanical mode, respectively. Here ω_s is the beam-splitter-type interaction strength between mode \hat{a} and \hat{b} , and G describes the optomechanical interaction strength between mode \hat{b} and mode \hat{c} .

Considering the GW strain signal input h with coupling strength α , as well as the coupling to the external bath \hat{b}_{in} with rate γ [32], we obtain the Heisenberg equations of motion for the three modes:

$$\begin{aligned} \dot{\hat{a}}(t) &= -\omega_s \hat{b}(t) + i\alpha h(t), \\ \dot{\hat{c}}^\dagger(t) &= G \hat{b}(t), \\ \dot{\hat{b}}(t) &= -\gamma \hat{b}(t) + \omega_s \hat{a}(t) + G \hat{c}^\dagger(t) + \sqrt{2\gamma} \hat{b}_{\text{in}}(t), \end{aligned} \quad (4.2)$$

with outgoing field given by $\hat{b}_{\text{out}}(t) = -\hat{b}_{\text{in}}(t) + \sqrt{2\gamma} \hat{b}(t)$. The above equations can be solved in frequency domain via Fourier transform:

$$\hat{\delta}(\Omega) = \mathcal{F}[\hat{\delta}(t)] \equiv \int_{-\infty}^{\infty} dt e^{i\Omega t} \hat{\delta}(t), \quad (4.3)$$

where Ω is the sideband frequency in the rotating frame of frequency ω_0 , and $\hat{\delta}$ represents \hat{a} , \hat{b} , \hat{c} , or $\hat{b}_{\text{in,out}}$. The resulting solution for the outgoing field is:

$$\begin{aligned} \hat{b}_{\text{out}}(\Omega) &= \frac{i\Omega(\gamma + i\Omega) - G^2 + \omega_s^2}{i\Omega(\gamma - i\Omega) + G^2 - \omega_s^2} \hat{b}_{\text{in}}(\Omega) \\ &\quad + \frac{i\sqrt{2\gamma} \omega_s \alpha}{i\Omega(\gamma - i\Omega) + G^2 - \omega_s^2} h(\Omega). \end{aligned} \quad (4.4)$$

Interestingly, regardless of the value of G and ω_s , the outgoing field is not squeezed, as the modulus of input-to-output transfer function remains equal to unity. The signal is contained entirely in the phase quadrature [33, 34] defined as $\hat{Y} = (\hat{b}_{\text{out}} -$

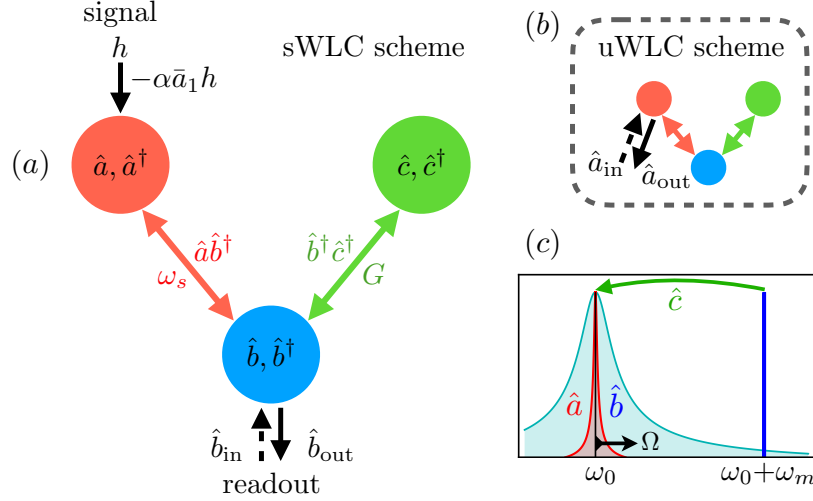


Figure 4.2: Idealized mode interaction structure of the optomechanical system illustrated in Fig. 4.1. (a) The sWLC scheme. Here \hat{a} represents the differential mode of the arm cavity which couples to the GW strain h , \hat{b} represents the SRC (filter) mode, and \hat{c} represents the mechanical mode of the suspended mirror. The coupling between \hat{a} and \hat{b} (\hat{b} and \hat{c}) is characterized by ω_s (G). Mode \hat{b} is coupled to the external ingoing field \hat{b}_{in} , which carries the vacuum noise, and the outgoing field \hat{b}_{out} , which carries the signal and will be read out. (b) The uWLC scheme for comparison. In the intracavity readout scheme presented in Ref. [30], the external fields couple to the arm cavity mode \hat{a} , rather than the filter cavity mode \hat{b} . (c) The frequency-domain mode structure under single-mode (for both \hat{a} and \hat{b}) and resolved sideband (for \hat{b}) approximations. The parametric interaction $\hat{b}^\dagger \hat{c}^\dagger$ is realized by the optomechanical coupling under blue-detuned pumping by the mechanical resonant frequency. Note that all mode operators are defined in the rotating frame of frequency ω_0 , and Ω is the sideband frequency with respect to it.

$\hat{b}_{\text{out}}^\dagger)/(\sqrt{2}i)$. The resulting signal-referred shot noise spectral density when measuring the phase quadrature is given by

$$S_{hh}(\Omega) = \frac{\Omega^2 \gamma^2 + (G^2 - \omega_s^2 + \Omega^2)^2}{4\gamma \omega_s^2 \alpha^2}. \quad (4.5)$$

The sensitivity given different relations between G and ω_s is plotted in Fig. 4.3. One interesting case is when $G = \omega_s$ where the noise spectral density vanishes at DC as the signal response diverges:

$$S_{hh}(\Omega)|_{G=\omega_s} = \frac{\Omega^2(\Omega^2 + \gamma^2)}{4\gamma \omega_s^2 \alpha^2}. \quad (4.6)$$

The system stability, as analyzed in Ref. [1], is determined by the poles of the transfer function in Eq. (4.4), i.e., the roots of

$$i\Omega(\gamma - i\Omega) + G^2 - \omega_s^2 = 0. \quad (4.7)$$

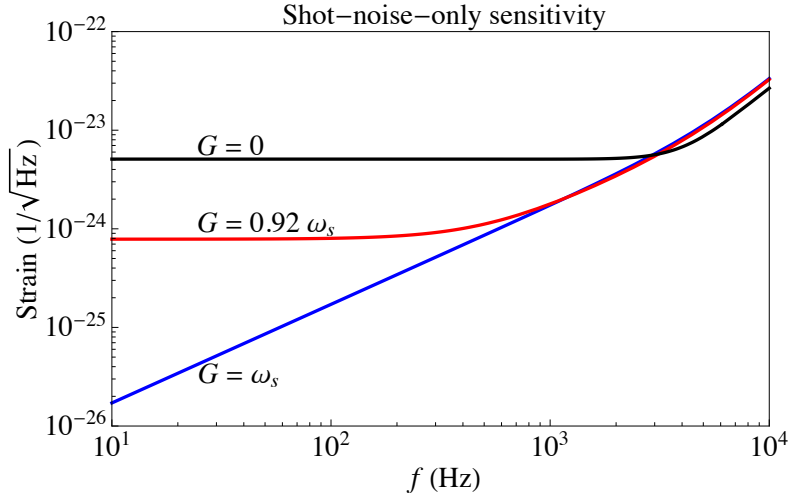


Figure 4.3: The signal-referred shot noise spectral density for different optomechanical interaction strengths G . Different curves are plotted based on Eq. (4.5) with the relation between G and ω_s shown near each line.

When the imaginary part of any root becomes positive, the system becomes unstable. The locations of roots are determined by the relation between G and ω_s . It can be proven [1] that whenever G is equal to or less than ω_s , there is no unstable root. The critical point happens when $G = \omega_s$, and there is a pole at DC, which is consistent with the resulting signal response being infinite at DC, as can be seen in Eqs. (4.4) and (4.6). To summarize, under the idealized Hamiltonian, the system is stable with $G \leq \omega_s$ and at the same time, the shot-noise-limited sensitivity will be improved. In the following content, we will show that these features will remain intact even after we relax the approximations applied in deriving the idealized Hamiltonian.

In terms of the physical parameters described in Table 4.1, the two approximations to produce the idealized Hamiltonian in Eq. (4.1) are: (i) the single-mode approximations, i.e., $\Omega L_{\text{arm}}/c \ll 1$ and $2\omega_{m_0} L_{\text{SRC}}/c \ll 1$, which treats the arm cavity and the filter cavity as single modes each described by an annihilation operators \hat{a} and \hat{b} , and (ii) the resolved-sideband approximation, i.e., $\omega_{m_0} L_{\text{SRC}}/c \gg \gamma$, which treats the mechanical sidebands around ω_0 as a single operator \hat{c} , ignoring the higher sidebands around $\omega_0 + 2\omega_{m_0}$ that should be involved in the interaction between the blue detuned filter cavity and the mechanical oscillator. Note that all the parameters ω_s , G , α , γ used in Eqs. (4.1)–(4.7) above are effective parameters, that can be approximately expressed in terms of the physical parameters. Under the single-mode and resolved-sideband approximations, the mode interaction strength

Table 4.1: A list of parameters and nominal values

Parameters	Description	Value
L_{arm}	arm cavity length	4 km
P_{arm}	arm cavity power	800 kW
T_{ITM}	ITM power transmissivity	0.5%
L_{SRC}	SRC length	40 m
T_{SRM}	SRM power transmissivity	0.02
P_b	filter cavity power	6.4 kW
λ	laser wavelength	1064 nm
m	oscillator mass	10 mg
$\omega_{m_0}/(2\pi)$	mechanical frequency	10^5 Hz
Q_m	mechanical quality factor	∞ ¹

ω_s and G can be expressed as:

$$\omega_s = \frac{c \sqrt{T_{\text{ITM}}}}{2\sqrt{L_{\text{arm}}L_{\text{SRC}}}}, \quad G = \sqrt{\frac{8\pi P_b}{m \lambda \omega_{m_0} L_{\text{SRC}}}}, \quad (4.8)$$

where P_b is the power of the filter cavity pumping field that impinges on the mechanical oscillator. Also, the signal coupling strength α and the SRC cavity half-bandwidth (i.e., the decay rate, or bath coupling rate) γ are defined as:

$$\alpha = \sqrt{\frac{P_{\text{arm}}L_{\text{arm}}\omega_0}{c\hbar}}, \quad \gamma = \frac{c T_{\text{SRM}}}{4L_{\text{SRC}}}. \quad (4.9)$$

For the full analysis, we adopt the approach in Ref. [24] by propagating the fields through the interferometer and taking into account their interactions with the mechanical degree of freedom via the radiation pressure. As all optical elements are axisymmetric, for simplicity, the optical fields can be treated as 1D propagating ones along the optical axis. At each location, the optical field is represented as:

$$\hat{E}(t) = \hat{\delta}(t)e^{-i\omega_0 t} + \hat{\delta}^\dagger(t)e^{i\omega_0 t}, \quad (4.10)$$

where $\hat{\delta}(t)$ can represent $\hat{a}(t)$ and $\hat{b}(t)$, the slowly-varying field operators in the rotating frame of ω_0 for the light inside the arm cavity and filter cavity respectively. We can define sideband operators $\hat{a}(\omega)$ and $\hat{b}(\omega)$ via Fourier transform as in Eq. (4.3), but for a large sideband frequency ω up to the order of ω_{m_0} . Note that so long as $\omega \ll \omega_0$, the slowly-varying operators in time domain and sideband operators in frequency domain will be well-defined.

¹We effectively remove the mechanical damping to highlight that the system can be self-stabilized without additional damping mechanism.

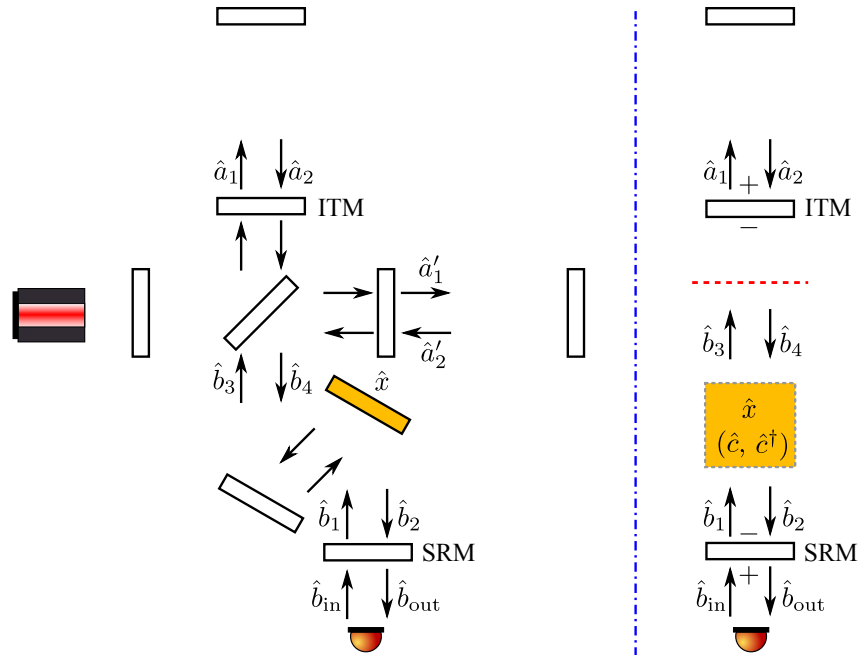


Figure 4.4: The fields involved in the complete analysis of the scheme shown in Fig. 4.1. The right figure is a simplified version of the left one when only looking at the differential mode of the two arms, which is adopted in the analysis in the main text. In the right figure, the sign convention for the mirror reflectivity is also shown. The arm cavity and the SRC length are both tuned to be integer numbers times the wavelength of the carrier at frequency ω_0 .

The relevant fields fully describing the scheme in Fig. 4.1 are illustrated in Fig. 4.4. We will focus on the differential mode of the two arm cavities, and the right panel of Fig. 4.4 shows the simplified representation considered here. We assume both the arm cavity and the SRC are tuned such that the cavity lengths are integer numbers times the wavelength of the carrier at frequency ω_0 . Since we are looking at the linear dynamics, the equations of motion will only involve linear terms of the sideband operators. The Heisenberg equation of motion is formally identical to the classical Maxwell equation. The field operators are described by the following set

of equations:

$$\hat{a}_1(t) = \sqrt{T_{\text{ITM}}} \hat{b}_3(t) + \sqrt{R_{\text{ITM}}} \hat{a}_2(t), \quad (4.11a)$$

$$\hat{a}_2(t) = \hat{a}_1(t - \tau_{\text{arm}}) + 2ik_0 A_{\text{arm}} L_{\text{arm}} h(t), \quad (4.11b)$$

$$\hat{b}_4(t) = \sqrt{T_{\text{ITM}}} \hat{a}_2(t) - \sqrt{R_{\text{ITM}}} \hat{b}_3(t), \quad (4.11c)$$

$$\hat{b}_2(t) = \hat{b}_4(t - \tau_{\text{SRC}}/2) + 2ik_b A_b e^{-i\omega_{m_0} t} \hat{x}(t), \quad (4.11d)$$

$$\hat{b}_3(t) = \hat{b}_1(t - \tau_{\text{SRC}}/2) + 2ik_b A_b e^{-i\omega_{m_0} t} \hat{x}(t), \quad (4.11e)$$

$$\hat{b}_1(t) = \sqrt{T_{\text{SRM}}} \hat{b}_{\text{in}}(t) - \sqrt{R_{\text{SRM}}} \hat{b}_2(t), \quad (4.11f)$$

$$\hat{b}_{\text{out}}(t) = \sqrt{T_{\text{SRM}}} \hat{b}_2(t) + \sqrt{R_{\text{SRM}}} \hat{b}_{\text{in}}(t). \quad (4.11g)$$

Here the round-trip delay times are defined as $\tau_{\text{arm}} = 2L_{\text{arm}}/c$ and $\tau_{\text{SRC}} = 2L_{\text{SRC}}/c$, for the arm cavity and SRC respectively. The two cavities are pumped with frequency ω_0 and $\omega_0 + \omega_{m_0}$, with wave vectors being $k_0 = \omega_0/c$ and $k_b = (\omega_0 + \omega_{m_0})/c \approx k_0$ ($\omega_0 \gg \omega_{m_0}$) respectively. The steady-state field amplitudes A_{arm} and A_b are given by $A_{\text{arm}} = \sqrt{P_{\text{arm}}/(2\hbar\omega_0)}$ and $A_b = \sqrt{P_b/(2\hbar\omega_0)}$. The mechanical motion is driven by the radiation pressure in the presence of the blue-detuned pump field:

$$\ddot{\hat{x}}(t) + \gamma_m \dot{\hat{x}}(t) + \omega_{m_0}^2 \hat{x}(t) = \frac{\hat{F}_{\text{rad}}(t)}{m}, \quad (4.12)$$

where the radiation pressure \hat{F}_{rad} reads:

$$\hat{F}_{\text{rad}}(t) = \frac{2\hbar\omega_0 A_c^*}{c} e^{i\omega_{m_0} t} [\hat{b}_1(t) + \hat{b}_4(t)] + \text{h.c.} \quad (4.13)$$

The displacement operator \hat{x} is related to the mechanical mode operator \hat{c} by:

$$\hat{x}(t) = \sqrt{\frac{\hbar}{2m\omega_{m_0}}} [\hat{c}(t)e^{-i\omega_{m_0} t} + \hat{c}^\dagger(t)e^{i\omega_{m_0} t}]. \quad (4.14)$$

4.3 Frequency-domain analysis

In this section, we will solve the system dynamics in the frequency domain, and analyze the stability using the Nyquist criterion [35].

4.3.1 Formalism

In the frequency domain, Eqs. (4.11a)–(4.11g) can be converted into algebra equations in the matrix representation. For the slowly-varying field operators defined in Eq. (4.10), we apply the time-shifting relation in the Fourier transform of optical modes, i.e.

$$\mathcal{F}[\hat{o}(t - \tau)] = \hat{o}(\omega)e^{i\omega\tau} \text{ for } \hat{o} = \hat{a} \text{ and } \hat{b}, \quad (4.15)$$

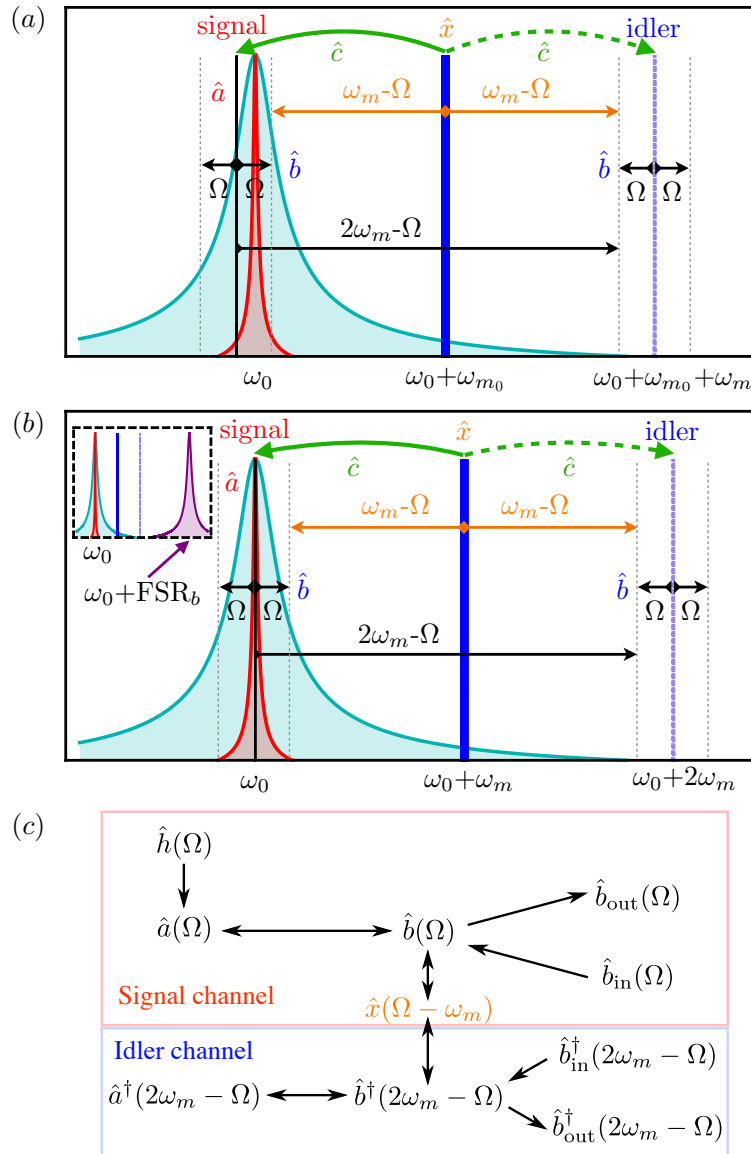


Figure 4.5: Coupling between the optical modes and the mechanical modes represented in frequency domain. (a) Without optical spring compensation, the parametric interaction will be shifted by a small frequency (not to scale) which will greatly ruin the designed filter response. (b) With optical spring compensation, the correct sidebands are coupled. It is achieved by making the value of blue-detuning to be slightly larger than the bare mechanical resonant frequency, as described in Eq. (4.17). Insert: the best scenario for resolved-sideband is to set $2\omega_m$ around half FSR_b. It will make ω_m larger than γ_b as much as possible and, at the same time, make the influence from the higher FSR as little as possible. (c) The full circulation loop within the signal channel (sidebands around ω_0 , represented by the red box in the upper panel) and the idler channel (sidebands around $\omega_0 + 2\omega_m$, represented by the blue box in the lower panel). The idler channel is ignored in the idealized Hamiltonian analysis.

to connect propagating light inside the cavities, where ω is the sideband frequency in the rotating frame of ω_0 . The Fourier transform of the mechanical mode in the filter cavity reads:

$$\mathcal{F}[e^{-i\omega_{m_0}t}\hat{x}(t)] = \hat{x}(\omega - \omega_{m_0}). \quad (4.16)$$

With the ω_m blue-detuned pumping, the optomechanical interaction will couple the optical sidebands at frequency $\omega = \pm\Omega$ ($\Omega \ll \omega_{m_0}$) with the sidebands at $\omega = 2\omega_m \mp \Omega$. As mentioned in Fig. 4.1, the value of ω_m is slightly different from the mechanical resonant frequency ω_{m_0} . The difference is caused by the optical spring effect,

$$\omega_m = \omega_{m_0} + \frac{P_b\omega_0}{2m\omega_{m_0}^2c^2\tau_b}, \quad (4.17)$$

when we consider the realistic scenario beyond the resolved-sideband approximation. As illustrated in Fig. 4.5 (a)–(b), when there is optical spring, the parametric interaction will be shifted by a small frequency, causing the demanded sidebands not to be correctly coupled. As our system works near a critical point of PT symmetry [1], the effect of a rather small optical spring effect is fairly important and needs to be carefully compensated.

As illustrated in Fig. 4.5 (c), the sidebands around ω_0 are named as the signal channel, and the ones around $\omega_0 + 2\omega_m$ are named as the idler channel. We will first treat the filter cavity as an effective mirror, obtain the transformation relation for signal and idler channels, as well as mixing between the channels, and then combine it with the circulation loop of the arm cavity. As the filter cavity is pumped with frequency $\omega_0 + \omega_m$, for convenience, we temporarily use $\tilde{\omega}$ to represent the sidebands in the rotating frame of $\omega_0 + \omega_m$, where $\tilde{\omega}$ can be \tilde{a} or \tilde{b} , and $\tilde{\omega}$ is in the order of magnitude of ω_{m_0} . The input-output relation of the filter cavity can be represented as follows:

$$\begin{bmatrix} \tilde{b}_{\text{out}}(\tilde{\omega}) \\ \tilde{b}_{\text{out}}^\dagger(-\tilde{\omega}) \\ \tilde{a}_1(\tilde{\omega}) \\ \tilde{a}_1^\dagger(-\tilde{\omega}) \end{bmatrix} = \tilde{\mathbf{M}}_{\text{filter}}(\tilde{\omega}) \begin{bmatrix} \tilde{b}_{\text{in}}(\tilde{\omega}) \\ \tilde{b}_{\text{in}}^\dagger(-\tilde{\omega}) \\ \tilde{a}_2(\tilde{\omega}) \\ \tilde{a}_2^\dagger(-\tilde{\omega}) \end{bmatrix}, \quad (4.18)$$

where $\tilde{\mathbf{M}}_{\text{filter}}(\tilde{\omega})$ is determined by the optomechanical interaction and the field circulation inside the filter cavity.

Before connecting the filter cavity to the main interferometer, let's comment on the required functionality of its transfer function in the full circulation loop. Notice

that in the lossless case, the open-loop circulation in the arm cavity will result in a phase delay, without harming the amplitude. Thus, we expect the feedback gain provided by the signal channel reflection $\hat{a}_1(\Omega) \rightarrow \hat{a}_2(\Omega)$ to compensate that effect by providing the same amount of phase advance with an amplitude 1. For the phase advance, we require $4\omega_0 P_f / (m\omega_m c^2 T_{\text{ITM}}) = c/L_{\text{arm}}$ [30] and optical spring compensation to correctly amplify the demanded sidebands. For the physical parameters shown in Table 4.1, the optical spring leads to a shift of the mechanical frequency by around 77 Hz. In the actual simulation, this value will be compensated numerically to avoid any tiny discrepancy. The influence of optical spring in the signal-referred shot-noise and stability will be analyzed in the following Sections 4.3.2 and 4.3.3. The other requirement is that the amplitude of reflection should be 1, as we want the idler channel to mix with the signal channel as little as possible. The best scenario for that purpose is to set $2\omega_m$ around half FSR_b, as shown by the insert of Fig. 4.5 (b). It will make $\omega_m \gg \gamma_b$ as much as possible and, at the same time, suppress the higher FSR from amplifying the idler channel. In addition, we want the mechanical loss to be as small as possible, as the filter cavity contains a parametric process and thus the mechanical loss will ruin the reflection amplitude.

By setting $\tilde{\omega} = \mp\omega_m + \Omega$, we can extract relevant matrix components to compose the transformation matrices for the optical fields outside the filter cavity:

$$\begin{bmatrix} \hat{b}_{\text{out}}(\Omega) \\ \hat{b}_{\text{out}}^\dagger(2\omega_m - \Omega) \\ \hat{a}_1(\Omega) \\ \hat{a}_1^\dagger(2\omega_m - \Omega) \end{bmatrix} = \tilde{\mathbf{M}}_{\text{filter}}(-\omega_m + \Omega) \begin{bmatrix} \tilde{b}_{\text{in}}(\Omega) \\ \tilde{b}_{\text{in}}^\dagger(2\omega_m - \Omega) \\ \tilde{a}_2(\Omega) \\ \tilde{a}_2^\dagger(2\omega_m - \Omega) \end{bmatrix}, \quad (4.19a)$$

$$\begin{bmatrix} \hat{b}_{\text{out}}(2\omega_m + \Omega) \\ \hat{b}_{\text{out}}^\dagger(-\Omega) \\ \hat{a}_1(2\omega_m + \Omega) \\ \hat{a}_1^\dagger(-\Omega) \end{bmatrix} = \tilde{\mathbf{M}}_{\text{filter}}(\omega_m + \Omega) \begin{bmatrix} \tilde{b}_{\text{in}}(-\Omega) \\ \tilde{b}_{\text{in}}^\dagger(2\omega_m - \Omega) \\ \tilde{a}_2(-\Omega) \\ \tilde{a}_2^\dagger(2\omega_m - \Omega) \end{bmatrix}. \quad (4.19b)$$

For simplicity, we define $\tilde{\mathbf{M}}_{\mp} \equiv \tilde{\mathbf{M}}_{\text{filter}}(\mp\omega_m + \Omega)$ and thus have:

$$\mathbf{R}_{aa}(\Omega) \equiv \begin{bmatrix} \tilde{\mathbf{M}}_-^{3,3} & 0 & 0 & \tilde{\mathbf{M}}_-^{3,4} \\ 0 & \tilde{\mathbf{M}}_+^{4,4} & \tilde{\mathbf{M}}_+^{4,3} & 0 \\ 0 & \tilde{\mathbf{M}}_+^{3,4} & \tilde{\mathbf{M}}_+^{3,3} & 0 \\ \tilde{\mathbf{M}}_-^{4,3} & 0 & 0 & \tilde{\mathbf{M}}_-^{4,4} \end{bmatrix}, \quad (4.20a)$$

$$\mathbf{T}_{ab}(\Omega) \equiv \begin{bmatrix} \tilde{\mathbf{M}}_-^{3,1} & 0 & 0 & \tilde{\mathbf{M}}_-^{3,2} \\ 0 & \tilde{\mathbf{M}}_+^{4,2} & \tilde{\mathbf{M}}_+^{4,1} & 0 \\ 0 & \tilde{\mathbf{M}}_+^{3,2} & \tilde{\mathbf{M}}_+^{3,1} & 0 \\ \tilde{\mathbf{M}}_-^{4,1} & 0 & 0 & \tilde{\mathbf{M}}_-^{4,2} \end{bmatrix}, \quad (4.20b)$$

$$\mathbf{R}_{bb}(\Omega) \equiv \begin{bmatrix} \tilde{\mathbf{M}}_-^{1,1} & 0 & 0 & \tilde{\mathbf{M}}_-^{1,2} \\ 0 & \tilde{\mathbf{M}}_+^{2,2} & \tilde{\mathbf{M}}_+^{2,1} & 0 \\ 0 & \tilde{\mathbf{M}}_+^{1,2} & \tilde{\mathbf{M}}_+^{1,1} & 0 \\ \tilde{\mathbf{M}}_-^{2,1} & 0 & 0 & \tilde{\mathbf{M}}_-^{2,2} \end{bmatrix}, \quad (4.20c)$$

$$\mathbf{T}_{ba}(\Omega) \equiv \begin{bmatrix} \tilde{\mathbf{M}}_-^{1,3} & 0 & 0 & \tilde{\mathbf{M}}_-^{1,4} \\ 0 & \tilde{\mathbf{M}}_+^{2,4} & \tilde{\mathbf{M}}_+^{2,3} & 0 \\ 0 & \tilde{\mathbf{M}}_+^{1,4} & \tilde{\mathbf{M}}_+^{1,3} & 0 \\ \tilde{\mathbf{M}}_-^{2,3} & 0 & 0 & \tilde{\mathbf{M}}_-^{2,4} \end{bmatrix}, \quad (4.20d)$$

where $\mathbf{R}_{aa}(\Omega)$ represents the $\hat{a}_2 \rightarrow \hat{a}_1$ reflection, $\mathbf{T}_{ab}(\Omega)$ represents the $\hat{b}_{\text{in}} \rightarrow \hat{a}_1$ transmission, $\mathbf{R}_{bb}(\Omega)$ represents the $\hat{b}_{\text{in}} \rightarrow \hat{b}_{\text{out}}$ reflection, $\mathbf{T}_{ba}(\Omega)$ represents the $\hat{a}_2 \rightarrow \hat{b}_{\text{out}}$ transmission. Thus, the effect of filter cavity on the optical fields can be expressed as follows:

$$\begin{bmatrix} \hat{a}_1(\Omega) \\ \hat{a}_1^\dagger(-\Omega) \\ \hat{a}_1(2\omega_m + \Omega) \\ \hat{a}_1^\dagger(2\omega_m - \Omega) \end{bmatrix} = \mathbf{R}_{aa}(\Omega) \begin{bmatrix} \hat{a}_2(\Omega) \\ \hat{a}_2^\dagger(-\Omega) \\ \hat{a}_2(2\omega_m + \Omega) \\ \hat{a}_2^\dagger(2\omega_m - \Omega) \end{bmatrix} + \mathbf{T}_{ab}(\Omega) \begin{bmatrix} \hat{b}_{\text{in}}(\Omega) \\ \hat{b}_{\text{in}}^\dagger(-\Omega) \\ \hat{b}_{\text{in}}(2\omega_m + \Omega) \\ \hat{b}_{\text{in}}^\dagger(2\omega_m - \Omega) \end{bmatrix}, \quad (4.21a)$$

$$\begin{bmatrix} \hat{b}_{\text{out}}(\Omega) \\ \hat{b}_{\text{out}}^\dagger(-\Omega) \\ \hat{b}_{\text{out}}(2\omega_m + \Omega) \\ \hat{b}_{\text{out}}^\dagger(2\omega_m - \Omega) \end{bmatrix} = \mathbf{R}_{bb}(\Omega) \begin{bmatrix} \hat{b}_{\text{in}}(\Omega) \\ \hat{b}_{\text{in}}^\dagger(-\Omega) \\ \hat{b}_{\text{in}}(2\omega_m + \Omega) \\ \hat{b}_{\text{in}}^\dagger(2\omega_m - \Omega) \end{bmatrix} + \mathbf{T}_{ba}(\Omega) \begin{bmatrix} \hat{a}_2(\Omega) \\ \hat{a}_2^\dagger(-\Omega) \\ \hat{a}_2(2\omega_m + \Omega) \\ \hat{a}_2^\dagger(2\omega_m - \Omega) \end{bmatrix}. \quad (4.21b)$$

In the idealized analysis in Secion.4.2, the idler channel was ignored under resolved-sideband limit. The full analysis here will keep both signal and idler

channels. Further linking the filter cavity to the main interferometer, propagation in the arm cavity will be considered for both channels to form a closed-loop transfer function. GW strain signal will be added to the signal channel in the arm cavity and the final input-output relation takes the following form:

$$\begin{bmatrix} \hat{b}_{\text{out}}(\Omega) \\ \hat{b}_{\text{out}}^\dagger(2\omega_m - \Omega) \end{bmatrix} = \mathbf{M}(\Omega) \begin{bmatrix} \hat{b}_{\text{in}}(\Omega) \\ \hat{b}_{\text{in}}^\dagger(2\omega_m - \Omega) \end{bmatrix} + \mathbf{v}(\Omega) h(\Omega), \quad (4.22)$$

where $\mathbf{M}(\Omega)$ is a 2×2 matrix describing the transformation of the ingoing field to the outgoing field, and $\mathbf{v}(\Omega)$ is a 2×1 column vector describing the response of the outgoing field to the GW signal, with the $\mathbf{v}(\Omega)^{2,1}$ component describing the signal leading into the idler channel $\hat{b}_{\text{in}}^\dagger(2\omega_m - \Omega)$. The exact expressions for $\mathbf{M}(\Omega)$ and $\mathbf{v}(\Omega)$ are quite complicated, and in the subsection that follows, we will use the quantum noise spectral density to illustrate their frequency dependence.

4.3.2 Noise spectral density

The resulting noise spectral density from the full analysis is shown in Fig. 4.6 and Fig. 4.7.

In Fig. 4.6, the optical spring effect is shown to play an important role in modifying the sensitivity. As analyzed in Sec. 4.3.1, if left unattended, the optical spring will cause an additional resonance in the sensitivity via shifting the central frequency of signal sidebands in the filter cavity response. After compensating such a shift, the full analysis and the idealized Hamiltonian analysis produce a similar result for most of the frequencies, given the same set of parameters. However, they start to deviate at low frequencies, where the full analysis shows a higher noise spectrum.

The deviation from idealized analysis is because of the coupling to the idler channel at low frequencies, as shown in Fig. 4.7, where a larger amount of signal will leak to the idler channel than what is output in the signal channel. Thus, the idler channel has a much better sensitivity at low frequencies. We can extract the signal information contained in the idler channel either by using the heterodyne readout with the pump field at $\omega_0 + \omega_m$ as the local oscillator or using an additional at $\omega_0 + 2\omega_m$ for the homodyne readout of the idler channel. We will discuss the details about the additional homodyne readout scheme in Sec. 4.5, and show the final sensitivity by optimally combining the two readout schemes.

As we will show in Sec. 4.3.3, the parameters in Table 4.1 are within the stability regime. Therefore, we can indeed obtain sensitivity improvement without sacrificing the stability.

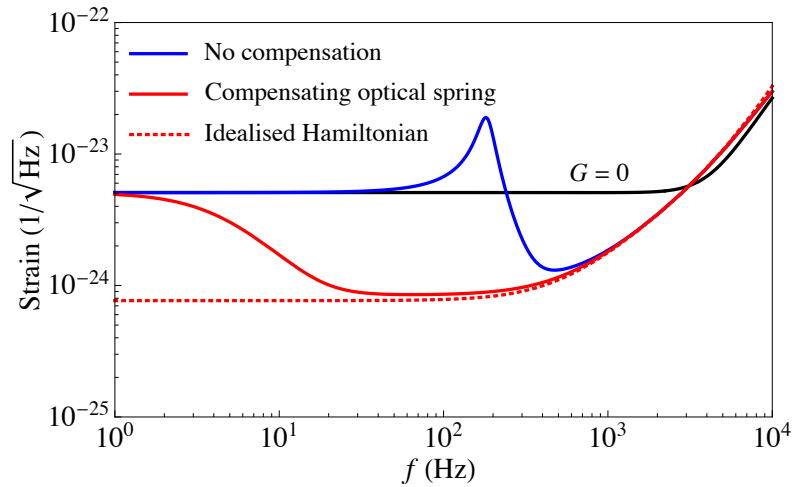


Figure 4.6: The signal-referred shot-noise spectral densities from the full analysis (red and blue) in comparison with the one obtained from idealized Hamiltonian (red dotted curve). Compensating the frequency shift of the mechanical oscillator due to the optical spring effect has a significant influence on the sensitivity.

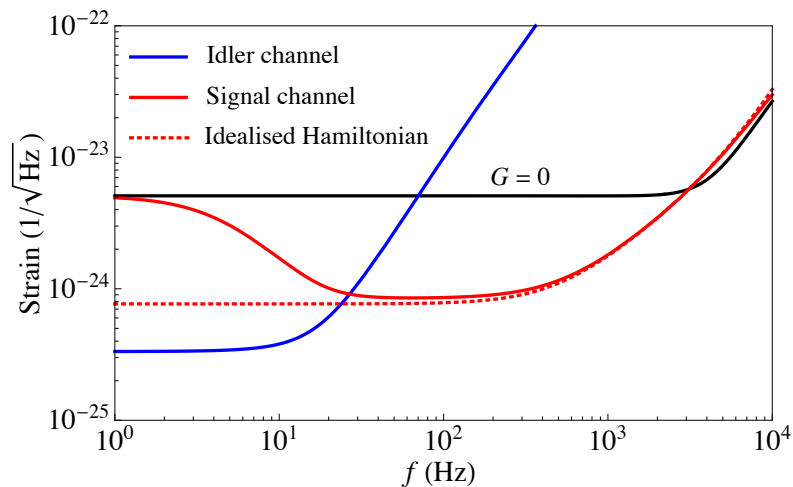


Figure 4.7: The noise spectral density for the idler channel, which can be read out by using a local oscillator at $\omega_0 + 2\omega_{m_0}$ (blue), in comparison with the signal channel (red). At low frequencies, the signal information contained in the idler channel is even more than that contained in the signal channel.

4.3.3 Stability analysis

In this section, we use the Nyquist technique [35] to analyze the system stability. The criterion is a diagrammatic approach to test the stability of a system by only using the open-loop transfer function, even with delay.

In the idealized analysis in Sec. 4.2, $G \approx \omega_s$ defines the boundary for stability. Further increasing G through increasing the pumping power of the filter cavity will destabilise the system. In the full analysis when the idler channel is also included, we have a more complicated multi-input-multi-output (MIMO) system. In the sideband picture, given the 2-dimensional open-loop transfer matrix $\mathbf{M}_{\text{OL}}(\Omega)$, the real and imaginary part of the determinant of $\mathbf{I} + \mathbf{M}_{\text{OL}}(\Omega)$, where \mathbf{I} is the 2-dimensional identity matrix, should not enclose the origin of the complex plain. This is limited to the case where $\mathbf{M}_{\text{OL}}(\Omega)$ does not contain elements that have unstable poles, and we therefore also need to be careful about the point where to extract the open-loop transfer function, even though the stability of the final closed-loop transfer function is independent of such a choice. We choose the interface near ITM as highlighted by the red dashed line on the right panel of Fig. 4.4, where the top part is the arm cavity and the bottom consists of the mechanical oscillator and SRM.

The open-loop and the closed-loop transfer matrices in our case are:

$$\mathbf{M}_{\text{OL}}(\Omega) = \mathbf{M}_{\text{opt}}(\Omega)\mathbf{M}_{\text{cav}}(\Omega), \quad \mathbf{M}_{\text{CL}}(\Omega) = (\mathbf{I} + \mathbf{M}_{\text{OL}}(\Omega))^{-1}. \quad (4.23)$$

The optomechanical transfer matrix $\mathbf{M}_{\text{opt}}(\Omega)$ is defined as:

$$\mathbf{M}_{\text{opt}}(\Omega) = e^{i\Omega\tau_{\text{SRC}}/2} \begin{bmatrix} \mathcal{T}_{\text{opt}} & \mathcal{T}_{\text{opt}} + \sqrt{R_{\text{SRM}}} \\ -\sqrt{R_{\text{SRM}}} - \mathcal{T}_{\text{opt}} & -2\sqrt{R_{\text{SRM}}} - \mathcal{T}_{\text{opt}} \end{bmatrix}, \quad (4.24)$$

where

$$\mathcal{T}_{\text{opt}} = -\sqrt{R_{\text{SRM}}} + \frac{i(1 + \sqrt{R_{\text{SRM}}})^2 g^2 \tau_{\text{SRC}} \omega_{m_0}}{2[\Omega(\Omega - 2\omega_m) + i\gamma_m(\Omega - \omega_m)]}. \quad (4.25)$$

Similarly, the passive cavity propagation matrix is:

$$\mathbf{M}_{\text{cav}}(\Omega) = \begin{bmatrix} \mathcal{T}_{\text{cav}}(\Omega) & 0 \\ 0 & \mathcal{T}_{\text{cav}}^*(2\omega_m - \Omega) \end{bmatrix}, \quad (4.26)$$

where

$$\mathcal{T}_{\text{cav}}(\Omega) = \frac{e^{i\Omega\tau_{\text{arm}}} - \sqrt{R_{\text{ITM}}}}{1 - e^{i\Omega\tau_{\text{arm}}}\sqrt{R_{\text{ITM}}}}. \quad (4.27)$$

In Fig. 4.8, we show the resulting Nyquist plot for the nominal parameters in Table 4.1. Because the mechanical frequency is not an integer number of the FSR

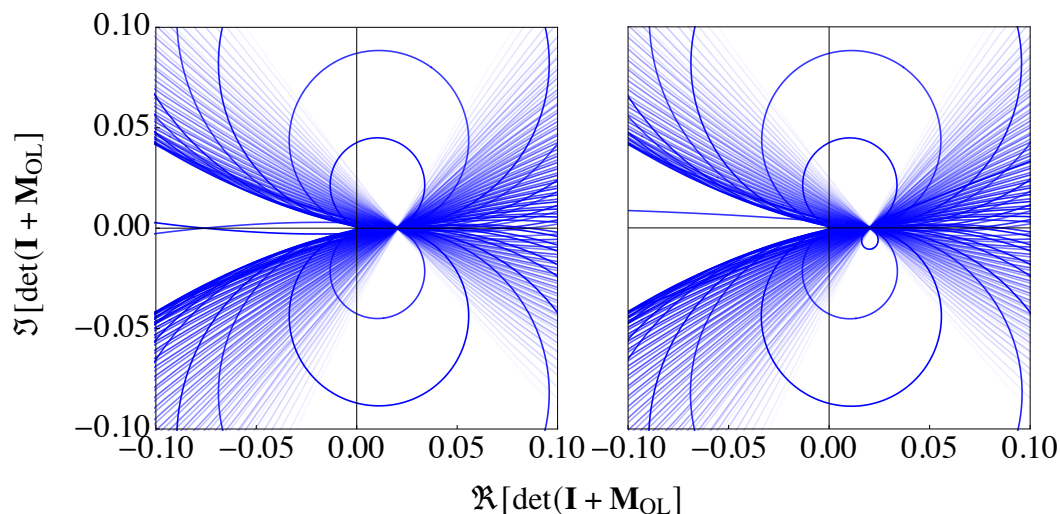


Figure 4.8: The plots for the determinant of the open-loop transfer matrix, given the nominal parameters. The left plot shows the case without compensating the optical spring, while the right one has the optical spring compensated and the contour does not enclose the origin. The opacity of the curve is intentionally made smaller when the magnitude of the frequency is large, which is to highlight the relevant low frequencies.

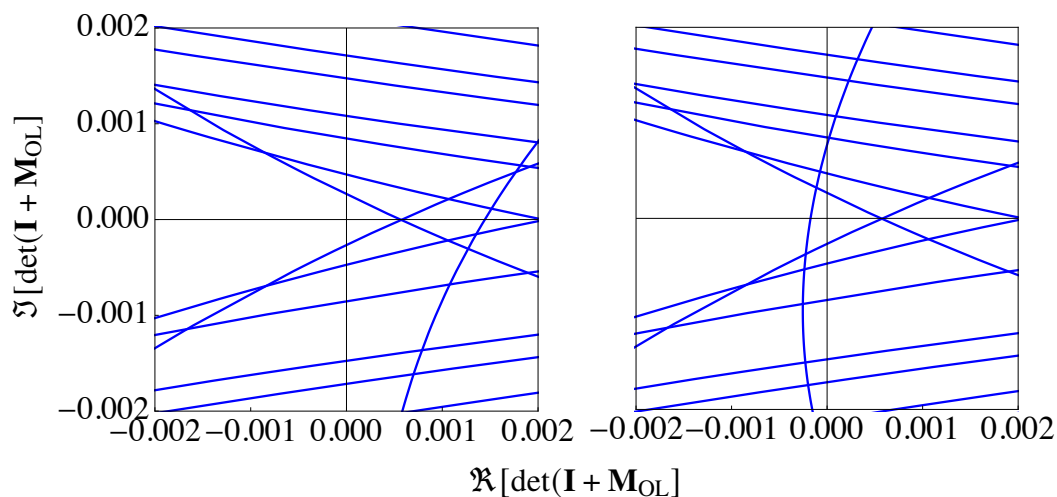


Figure 4.9: The plots for the determinant of the open-loop transfer matrix for $G = \omega_s$ (left) and $G = 1.01 \omega_s$ (right), both with the optical spring shift compensated. For clarity, we only show a tiny regime around the origin, but we have checked that only the right plot has the origin enclosed when zooming out.

of the arm cavity, the contour is quite complicated due to the phase factor $e^{2i\omega_{m_0}\tau_{\text{arm}}}$ of the idler channel. Nevertheless, we only need to check whether the origin is enclosed or not to make a firm claim on the stability, while the complex feature of the contour does not matter. It turns out that, compensating the optical spring shift not only has a significant impact on the sensitivity, as shown in Fig. 4.6, but also on the stability. As shown in the plot on the right-hand side of Fig. 4.8, with the nominal values for the parameters, the system only becomes stable after the optical spring shift is accounted for. This feature can be understood as follows: to meet the PT-symmetry condition, the parametric interaction with the mechanical mode must be achieved by the correct optical sidebands in the filter cavity; thus, only after the optical spring is correctly compensated, it is possible and meaningful to discuss the stability issue.

In Fig. 4.9, we further show the effect of the optomechanical coupling rate G on the stability, after the necessary optical spring compensation. Indeed, the system is stable when $G \leq \omega_s$, which is consistent with the idealized Hamiltonian analysis [1].

4.4 Time-domain analysis

In this section, we perform a numerical time-domain simulation to confirm the enhancement in sensitivity as derived above. The purpose of remaining in the time domain is to capture behavior that may have been lost due to approximations used in the frequency-domain analysis. It is also much easier for us to capture non-linear behavior in the time domain, as we have no need to perform Fourier transforms in this analysis. The primary limitation of this method is the relative lack of insight into the physics that we can obtain, as it is difficult to “break open” the simulation and understand the behavior of individual parts in isolation. As such, our time-domain approach is a powerful complementary tool to the analysis performed thus far and not a replacement.

We will begin by considering Eqs. (4.11a)–(4.11g). The principle of this simulation is to appropriately discretize the equations and enable the evolution of the system forward in time using the knowledge of its previous state. The mechanism through which the system steps forward and the way to recalculate relevant quantities are at the very heart of this simulation and, therefore, it is worthwhile to delve into some details.

4.4.1 Discretization of equations

The first step towards the time-domain simulation is the discretization of equations. The equations in our system can be subdivided into three distinct types. The treatment of the full system will be made clear after the functionality of each type is explored.

The first type of equation comprises all quantities that are related to others in the way of time-delay. For instance, the field quantities that propagate from one optical component to another. The general form of this type of equations reads:

$$a_2(t) = a_1(t - \tau), \quad (4.28)$$

where $\tau = L/c$ is the time delay caused by the propagation across the space of distance L , with c being the speed of light. This type of equations are discretized at time step n as

$$a_2[n] = a_1[n - n_d], \quad (4.29)$$

where n_d is time-step delay (steps in the past at which the field must be evaluated). It is given by $n_d = \tau/\Delta t$, where Δt is the simulation time increment. This type of equations encompass the forward evolution of the field quantities, whereby a field at a new simulation step can be calculated only with reference to the previous value of another field, which will have been calculated at their step.

The second type of equation comprises interactions of fields at an optical component. This treatment follows a very standard approach, where the fields at a mirror (as defined in Fig. 4.10) are given by:

$$a_2(t) = t_m a_4(t) + r_m a_1(t), \quad (4.30a)$$

$$a_3(t) = t_m a_1(t) - r_m a_4(t), \quad (4.30b)$$

where r_m and t_m are the mirror amplitude reflectivity and transmissivity respectively. The discretization of these fields is rather trivial:

$$a_2[n] = t_m a_4[n] + r_m a_1[n], \quad (4.31a)$$

$$a_3[n] = t_m a_1[n] - r_m a_4[n]. \quad (4.31b)$$

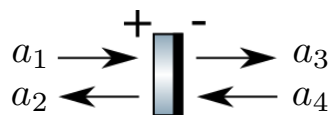


Figure 4.10: Field interactions at a mirror.

However, care must be taken in choosing the order to calculate these fields, as the field quantities are all initially unknown. The procedure for calculating these fields will be discussed later in due course.

The final consideration is the treatment of Eq. (4.12). It can be approached in many ways according to the choice of discretization for time derivative. Based on its well-studied nature [36], a “symmetric” approach is implemented:

$$\ddot{x}[n] + \gamma_m \dot{x}[n] + \omega_{m_0}^2 x[n] = \frac{F_{\text{rad}}[n]}{m}, \quad (4.32a)$$

$$\text{with } \dot{x}[n] = \frac{x[n+1] - x[n-1]}{2\Delta t}, \quad (4.32b)$$

$$\text{and } \ddot{x}[n] = \frac{x[n+1] - 2x[n] + x[n-1]}{\Delta t^2}. \quad (4.32c)$$

Note that substituting the latter two equations into Eq. (4.32a) allows for the $x[n+1]$ term to be rearranged in terms of quantities at previous time steps and, therefore, it can be used to evolve the position of the mechanical oscillator without further issue.

4.4.2 Connecting the system

After categorizing the relative equations, the next to consider is connecting the discretized equations into a consistent loop. The most challenging feature of the system is the signal-recycling structure in the optical cavities, as the signal sent “downstream” from the simulation inputs returns and combines with the upstream signal in a feedback-like structure. For a system with many cavities, the cycling of signal could become very complicated to handle.

Considering that the signal must traverse the space between optical components, which induces a time delay, it allows us to break up the system into several independent “compartments”. As the system is evolved forwards in time, when we consider fields at step n , we can rely on the values for all steps $< n$ that have already been calculated. This naturally means that all terms of the Eq. (4.28) type can be calculated immediately. To tackle the issue with Eqs. (4.30), we can treat the right-hand side quantities $a_{1,4}(t)$ as the “inputs” to the mirror, which are already available, as the “outputs” or left-hand side of Eq. (4.28). This results in a logic flow, as shown in Fig. 4.11. At the start of a new simulation step, we calculate all the “outputs” of the Eq. (4.28) type first, which give all of the “inputs” quantities of the Eq. (4.30) types. We then calculate the “outputs” of all Eq. (4.30) types, which then affect the input fields in a neighboring compartment that links the whole system together. Note that these links occur at a future time step and thus do not need to be calculated now,

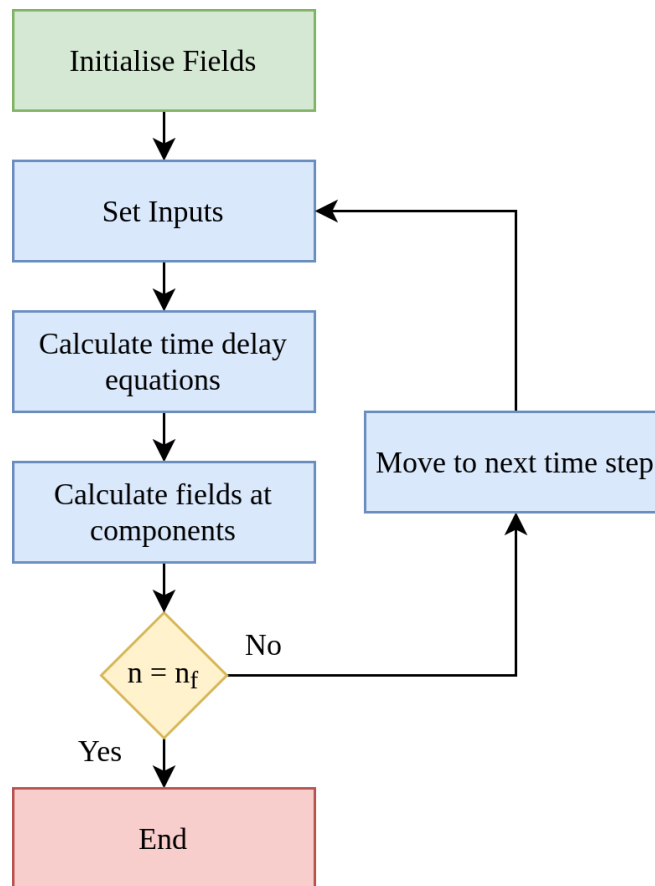


Figure 4.11: Logical flowchart of the time-domain simulation.

avoiding the trap of circular logic. This approach greatly simplifies the calculation performed in each simulation cycle. By compartmentalizing the equations in this way, we can create several independent systems with very few equations each. It is thus very easy to add extra components to the system, without the need to rewrite any existing elements in the simulation. Furthermore, the system is well set up for optimization techniques such as parallelization.

The key issue in our approach is the large number of calculations to be performed, as well as the large number of quantities that need to be stored. To suitably capture the system behavior, the time increment in simulation needs to be smaller than the shortest time-scale of the system, which in our case is the short cavity traversal time around 100 ns. Although this MHz level of sampling is far above the frequency range of interest (1 Hz - 10 kHz), it is necessary to capture the behavior of components that affect the signal response within that frequency band. This will lead to a lot of waste as we are simulating about 1000 times more data than what we are interested

in. Furthermore, we want to simulate for at least 1 second, which consists of 10 million samples, resulting in rather a lot of data for a computer to store.

A further limitation is the requirement for integer values of n_d in the discretization of Eq. (4.29). For all cavities in the system, the traversal times must be some integer multiple of Δt . To enable the free choice of cavity lengths, particularly when there are many cavities in the system, Δt may have to be even smaller than the shortest cavity traversal time. This is not a big issue in our case as cavity number can be limited to be two. All the optical components are separated by a short delay time τ_s , except for the arm cavity with a long delay time τ_a . For convenience, we can choose τ_a to be an exact multiple of τ_s , without any loss of physical insight.

4.4.3 Step-response stability analysis

The steady-state response is the most essentials in the sensitivity analysis of the system. As the simulation loop relies on past values of the system, initialization is required at some finite time from which the simulation starts. To resolve this issue, all quantities in $t < 0$ are set to be 0, which corresponds to the off state. After the simulation begins, the building-up process of the steady-state leads to an initial transient effect, which might negatively affect the response estimate. Luckily, in our simulation, this initialization takes about 0.03 s, which is sufficiently small compared to the total runtime and will not cause any problem.

Interestingly, the transient behavior is more of an opportunity than a problem. The time-domain response with custom inputs can be used to gain insight into some aspects of the system that can not be easily studied using the frequency-domain approach. One such test we can perform is to determine the stability of the system using its step response. Inserting a constant signal from $t = 0$ (step-function input) to excite the system dynamics, the resulting time-domain behavior will clearly show whether the system is stable (settling at a constant value or a steady oscillation) or unstable (growing indefinitely towards an infinite amplitude). As shown in Fig. 4.12, the position response of the mechanical oscillator in the cases with or without compensating the optical spring clearly shows the stability or instability. It further confirms the result shown in Fig. 4.8 that the system can be stabilized by optical spring compensation.

4.4.4 Numerical noise spectral density

To check the consistency with the frequency-domain approach in Sec. 4.3.2, the noise spectral density in this time-domain simulation will be determined in a two-

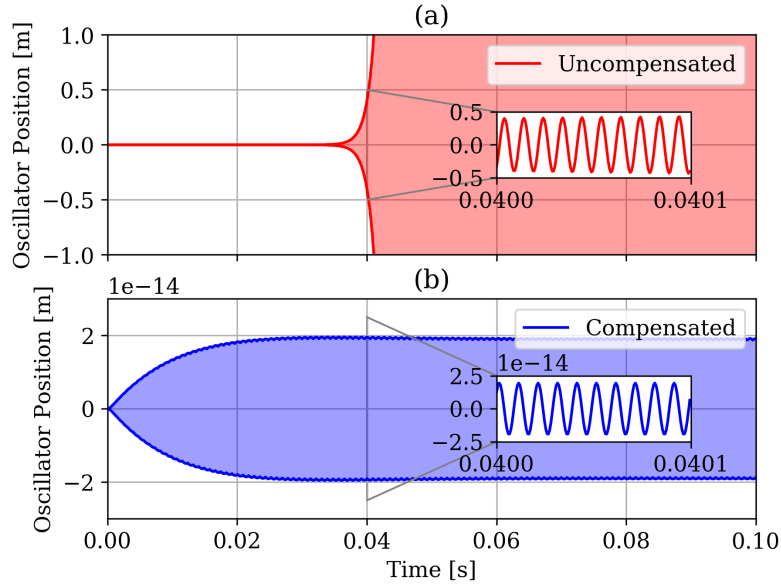


Figure 4.12: In-loop step-response of the position of the undamped mechanical oscillator. (a) When the pump field is offset by ω_{m_0} only. (b) When the pump field is further offset by compensating the optical spring. The lighter solid fill contains rapid oscillations with the dark bounding lines representing the amplitude envelope. The inserts of (a) and (b) show the zoomed-in views of two sections in the time-series, where the individual oscillations can be seen.

step approach. The noise power spectral density in the strain signal measurement is given by:

$$S_{hh}^n(\Omega) = \frac{S_{bb}^n(\Omega)}{T(\Omega)T(\Omega)^*}, \quad (4.33)$$

where $S_{bb}^n(\Omega)$ is the noise power spectral density of the appropriate quadrature of \hat{b}_{out} (see Fig. 4.4) and $T(\Omega)$ is the $h \rightarrow \hat{b}_{\text{out}}$ transfer function. The strain noise can thus be obtained through two separate simulations: one to obtain $T(\Omega)$ and another to obtain $S_{bb}^n(\Omega)$.

For a preliminary consistency check, we compare the optical transfer function $T(\Omega)$ by injecting a noiseless random signal with a constant spectral density into the channel of gravitational wave strain. By measuring the spectrum $S_{bh}(\Omega)$ of the output variable \hat{b}_{out} , the transfer function $T(\Omega)$ can be determined through the relation between cross- and power spectral density:

$$S_{bh}(\Omega) = T(\Omega)S_{hh}(\Omega). \quad (4.34)$$

Two simulations are implemented only with a difference in mechanical quality factor, as shown in Fig. 4.13, and a great agreement has been confirmed between

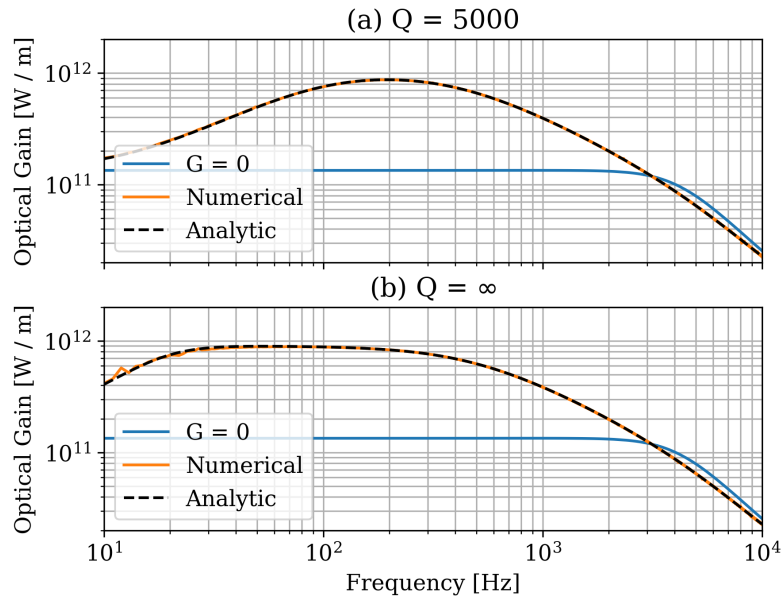


Figure 4.13: Transfer functions for optical gain with optical-spring compensated. The pump-off ($G = 0$) gain is shown in contrast to the pump-on gain for (a) a finite mechanical quality factor of 5000, and (b) an undamped oscillator. The numerical, time-domain approach shows very good agreement with the analytical, frequency-domain approach.

the numerical and analytical approaches. In Fig. 4.14 we further show the optical transfer function of the mechanically undamped system for both the signal and idler channels, which also shows good agreements.

The second simulation is implemented by injecting all relevant noises with their own spectral densities in the absence of strain signal. This provides $S_{bb}^n(\Omega)$ and, together with the optical transfer function $T(\Omega)$ obtained in the first simulation, allows us to complete the calculation of strain noise spectral density according to Eq. (4.33). The final results of the time-domain simulation are shown in Fig. 4.15, which consistently corresponds to the frequency-domain analysis in Fig. 4.7.

4.5 Optimal readout scheme

In this section, we will investigate the readout scheme to optimally blend the outputs from the signal and idler channels for achieving the best signal sensitivity. Note that the approach we apply here can in general be used for any correlated signals.

Consider a generic case with two noisy signals which measure the same observable x , \tilde{z}_1 and \tilde{z}_2 , such that $\tilde{z}_i = T_i x + \tilde{n}_i$, $i = 1, 2$, with T_i referring to the transfer function

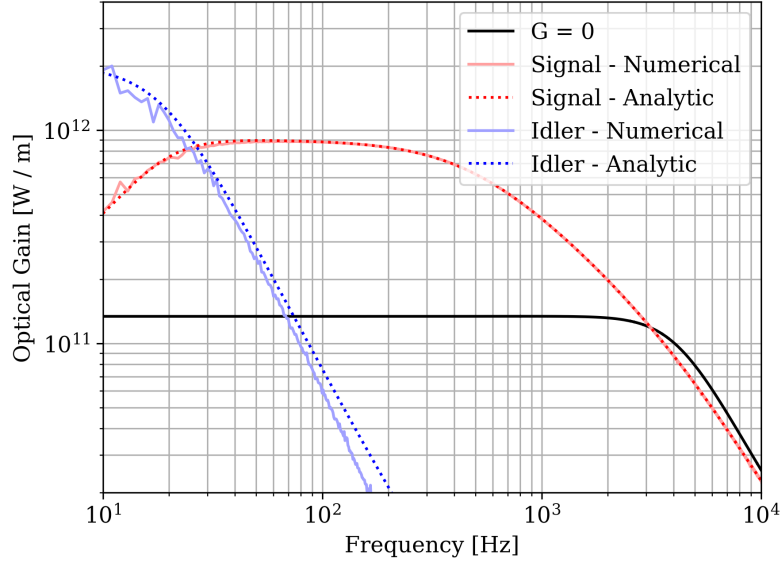


Figure 4.14: Optical gain transfer functions for the signal and idler channels in the undamped, optical-spring-compensated system.

of x to the signal, and \tilde{n}_i being the corresponding noise. These signals can be normalized such that $z_i = \tilde{z}_i/T_i = x + n_i$.

In this case x is the gravitational wave signal, where in each measurement there is differing sensitivity in different frequency bands such as that shown in Fig. 4.14. In the frequency domain representation, the normalized signals z_i , can be blended together with frequency dependent filters, $\alpha(\Omega)$ and $1 - \alpha(\Omega)$, which sum to one over the entire frequency range:

$$Z(\Omega) = \alpha(\Omega) z_1(\Omega) + (1 - \alpha(\Omega)) z_2(\Omega), \quad (4.35)$$

with total noise given by $n(\Omega) = \alpha(\Omega) n_1(\Omega) + (1 - \alpha(\Omega)) n_2(\Omega)$. The power spectrum of the total normalized noise can be represented as:

$$\begin{aligned} S_{nn}(\Omega) = & |\alpha(\Omega)|^2 S_{n_1 n_1}(\Omega) + |1 - \alpha(\Omega)|^2 S_{n_2 n_2}(\Omega) \\ & + \alpha(\Omega)(1 - \alpha^*(\Omega)) S_{n_1 n_2}(\Omega) \\ & + (1 - \alpha(\Omega))\alpha^*(\Omega) S_{n_2 n_1}(\Omega), \end{aligned} \quad (4.36)$$

with $S_{n_i n_j}(\Omega)$ being the noise spectrum of ($i = j$) or correlation between ($i \neq j$) $n_1(\Omega)$ and $n_2(\Omega)$. Minimising Eq. (4.36) with respect to the conjugate of the filter $\alpha(\Omega)$, i.e., $\frac{\partial S_{nn}(\Omega)}{\partial \alpha^*(\Omega)} = 0$, the optimal filter can be constructed for each frequency Ω independently:

$$\alpha(\Omega) = \frac{S_{n_2 n_2}(\Omega) - S_{n_2 n_1}(\Omega)}{S_{n_1 n_1}(\Omega) + S_{n_2 n_2}(\Omega) - S_{n_1 n_2}(\Omega) - S_{n_2 n_1}(\Omega)}. \quad (4.37)$$

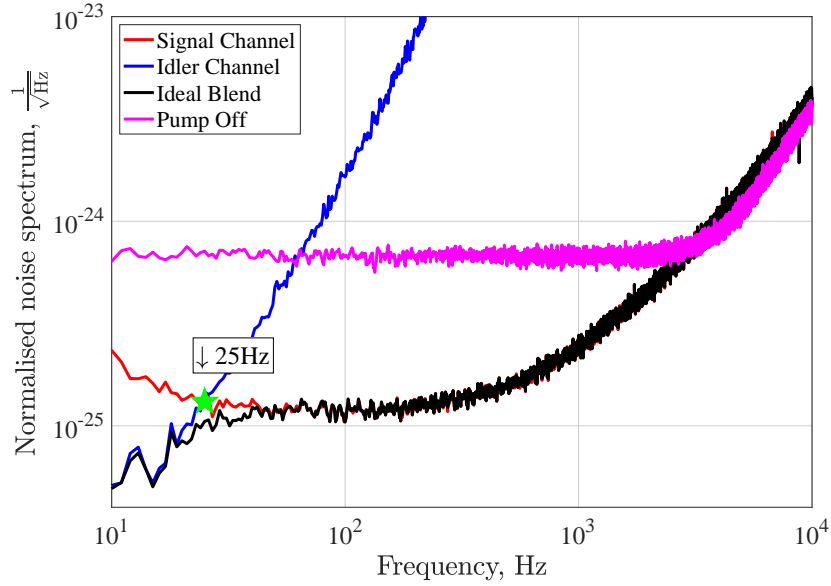


Figure 4.15: The normalized noise spectrum for the signal and idler channels. The signal channel (red) recovers the same response as the pump off case (magenta) which is limited by the bandwidth of the cavity at frequencies of a few kHz and above, which shows there is no degradation of the signal or the bandwidth of the cavity. The idler channel (blue) has greater sensitivity below 30Hz. The ideal blend (black) has greater sensitivity than both the signal and idler channels across the blend frequency range of approximately 25Hz (green star).

Applying the filters to Eq (4.35), we can obtain the the power spectrum of the total signal $Z(\Omega)$:

$$\begin{aligned}
 S_{ZZ}(\Omega) = & |\alpha(\Omega)|^2 S_{z_1 z_1}(\Omega) + |1 - \alpha(\Omega)|^2 S_{z_2 z_2}(\Omega) \\
 & + \alpha(\Omega)(1 - \alpha^*(\Omega)) S_{z_1 z_2}(\Omega) \\
 & + (1 - \alpha(\Omega))\alpha^*(\Omega) S_{z_2 z_1}(\Omega),
 \end{aligned} \tag{4.38}$$

whose noise power spectrum is the same as $S_{mn}(\Omega)$ in Eq. (4.36). When there is correlation between n_1 and n_2 , the noise across the applied high- and low-pass filters $\alpha(\Omega)$ and $1 - \alpha(\Omega)$ can be further improved. When the cross-correlation terms are zero, the final noise spectrum would be determined by the ability to create the optimal blends between two filters, such as high-order roll-offs of the filters with phase margin at the blending frequency. The advantage of this signal post-processing scheme is to reduce the stability requirement if the system is operating in a closed feedback loop.

In the simulation discussed in Sec. 4.4, the signal can be extracted from both the signal channel around ω_0 and the idler channel near $\omega_0 + 2\omega_{m_0}$. Applying the optimal

blending strategy of Eq. (4.37), the overall noise spectrum can take advantage of whichever channel with the better behavior at one frequency. As shown in Fig. 4.15, the idler channel contributes more below 25Hz, while the signal channel dominates at higher frequencies above 25Hz, and the optimal blending curve follows the better one at all frequencies.

4.6 Discussion

In this work, we analyze in detail the realization of a PT-symmetric interferometer [1] using an optomechanical filter cavity. We go beyond the idealized Hamiltonian analysis under single-mode and the resolved-sideband approximations, and consider the real physical parameters in the filter cavity setup. We prove that, after compensating the optical spring in the filter cavity, the stability and sensitivity improvement stated in the original proposal [1] remains valid in the realistic settings, even when a portion of the signal gets mixed into the idler channel.

To perform full analysis, we implement numerical simulations in both frequency-domain and time-domain. The methods' consistencies have been checked with both the signal transfer function and output noise spectrum. In the frequency-domain analysis, the system stability is confirmed using Nyquist criteria, where the Nyquist plot with the stable parameter setting does not enclose the origin. In the time-domain simulation, the stability manifests itself in the transient behavior before the system reaches its steady-state, where the stable parameter setting won't make any system quantity go to infinity.

Considering the unavoidable leakage of the signal into the idler channel in the actual setups, we further constructed the blending scheme for the output of the two channels. Applying the optimal output filter, one can take advantage of the channel with better behavior at each frequency, to obtain optimal sensitivity at all frequencies. Another scheme with an auxiliary mechanical cooling beam is under investigation, where the information in the mechanical oscillator can be read out supplemently. Together with the idler channel, they can provide more possibilities for optimized blending readout.

References

- [1] Xiang Li, Maxim Goryachev, Yiqiu Ma, Michael E. Tobar, Chunnong Zhao, Rana X Adhikari, and Yanbei Chen. Broadband sensitivity improvement via coherent quantum feedback with pt symmetry, 2020.

- [2] B. P. Abbott, R. Abbott, T. D. Abbott, M. R. Abernathy, and et. al. Observation of gravitational waves from a binary black hole merger. *Phys. Rev. Lett.*, 116:061102, Feb 2016.
- [3] B. P. Abbott, R. Abbott, T. D. Abbott, S. Abraham, and et. al. Gwtc-1: A gravitational-wave transient catalog of compact binary mergers observed by ligo and virgo during the first and second observing runs. *Phys. Rev. X*, 9:031040, Sep 2019.
- [4] R. Abbott, T. D. Abbott, S. Abraham, F. Acernese, and et. al. Gwtc-2: Compact binary coalescences observed by ligo and virgo during the first half of the third observing run, 2020.
- [5] Ioannis Kamaretsos, Mark Hannam, Sascha Husa, and B. S. Sathyaprakash. Black-hole hair loss: Learning about binary progenitors from ringdown signals. *Phys. Rev. D*, 85:024018, Jan 2012.
- [6] Ioannis Kamaretsos, Mark Hannam, and B. S. Sathyaprakash. Is black-hole ringdown a memory of its progenitor? *Phys. Rev. Lett.*, 109:141102, Oct 2012.
- [7] Andrea Taracchini, Alessandra Buonanno, Gaurav Khanna, and Scott A. Hughes. Small mass plunging into a kerr black hole: Anatomy of the inspiral-merger-ringdown waveforms. *Phys. Rev. D*, 90:084025, Oct 2014.
- [8] B. P. Abbott, R. Abbott, T. D. Abbott, M. R. Abernathy, F. Acernese, K. Ackley, C. Adams, T. Adams, P. Addesso, R. X. Adhikari, V. B. Adya, C. Affeldt, M. Agathos, K. Agatsuma, N. Aggarwal, and et al Aguiar, O. D. First targeted search for gravitational-wave bursts from core-collapse supernovae in data of first-generation laser interferometer detectors. *Phys. Rev. D*, 94:102001, Nov 2016.
- [9] Scott A. Hughes, Anuj Apte, Gaurav Khanna, and Halston Lim. Learning about black hole binaries from their ringdown spectra. *Phys. Rev. Lett.*, 123:161101, Oct 2019.
- [10] B. P. Abbott, R. Abbott, T. D. Abbott, F. Acernese, and et. al. Gw170817: Observation of gravitational waves from a binary neutron star inspiral. *Phys. Rev. Lett.*, 119:161101, Oct 2017.
- [11] Haixing Miao, Huan Yang, and Denis Martynov. Towards the design of gravitational-wave detectors for probing neutron-star physics. *Phys. Rev. D*, 98:044044, Aug 2018.
- [12] Denis Martynov, Haixing Miao, Huan Yang, Francisco Hernandez Vivanco, Eric Thrane, Rory Smith, Paul Lasky, William E. East, Rana Adhikari, Andreas Bauswein, Aidan Brooks, Yanbei Chen, Thomas Corbitt, Andreas Freise, Hartmut Grote, Yuri Levin, Chunnong Zhao, and Alberto Vecchio. Exploring the sensitivity of gravitational wave detectors to neutron star physics. *Phys. Rev. D*, 99:102004, May 2019.

- [13] Christian D Ott. The gravitational-wave signature of core-collapse supernovae. *Classical and Quantum Gravity*, 26(6):063001, feb 2009.
- [14] Kei Kotake. Multiple physical elements to determine the gravitational-wave signatures of core-collapse supernovae. *Comptes Rendus Physique*, 14(4):318 – 351, 2013. Gravitational waves / Ondes gravitationnelles.
- [15] David Radice, Viktoriya Morozova, Adam Burrows, David Vartanyan, and Hiroki Nagakura. Characterizing the gravitational wave signal from core-collapse supernovae. *The Astrophysical Journal*, 876(1):L9, apr 2019.
- [16] M Punturo, M Abernathy, F Acernese, B Allen, and et. al. The einstein telescope: a third-generation gravitational wave observatory. *Classical and Quantum Gravity*, 27(19):194002, sep 2010.
- [17] Michele Maggiore, Chris Van Den Broeck, Nicola Bartolo, and et. al. Science case for the einstein telescope. *Journal of Cosmology and Astroparticle Physics*, 2020(03):050–050, mar 2020.
- [18] David Reitze, Rana X Adhikari, Stefan Ballmer, Barry Barish, Lisa Barsotti, GariLynn Billingsley, Duncan A. Brown, Yanbei Chen, Dennis Coyne, Robert Eisenstein, Matthew Evans, Peter Fritschel, Evan D. Hall, Albert Lazzarini, Geoffrey Lovelace, Jocelyn Read, B. S. Sathyaprakash, David Shoemaker, Joshua Smith, Calum Torrie, Salvatore Vitale, Rainer Weiss, Christopher Wipf, and Michael Zucker. Cosmic explorer: The u.s. contribution to gravitational-wave astronomy beyond ligo, 2019.
- [19] B P Abbott, R Abbott, T D Abbott, M R Abernathy, and et. al. Exploring the sensitivity of next generation gravitational wave detectors. *Classical and Quantum Gravity*, 34(4):044001, jan 2017.
- [20] William DeRocco and Anson Hook. Axion interferometry. *Phys. Rev. D*, 98:035021, Aug 2018.
- [21] Ippei Obata, Tomohiro Fujita, and Yuta Michimura. Optical ring cavity search for axion dark matter. *Phys. Rev. Lett.*, 121:161301, Oct 2018.
- [22] Hongwan Liu, Brodi D. Elwood, Matthew Evans, and Jesse Thaler. Searching for axion dark matter with birefringent cavities. *Phys. Rev. D*, 100:023548, Jul 2019.
- [23] Denis Martynov and Haixing Miao. Quantum-enhanced interferometry for axion searches. *Phys. Rev. D*, 101:095034, May 2020.
- [24] H. J. Kimble, Yuri Levin, Andrey B. Matsko, Kip S. Thorne, and Sergey P. Vyatchanin. Conversion of conventional gravitational-wave interferometers into quantum nondemolition interferometers by modifying their input and/or output optics. *Phys. Rev. D*, 65:022002, Dec 2001.

- [25] Jun Mizuno. *Comparison of optical configurations for laser-interferometric gravitational-wave detectors*. PhD thesis, AEI-Hannover, MPI for Gravitational Physics, Max Planck Society, 1995.
- [26] Vladimir Braginsky and Farid Ya Khalili. *Quantum measurement*. Cambridge University Press, 1995.
- [27] Vladimir B Braginsky, Mikhail L Gorodetsky, Farid Ya Khalili, and Kip S Thorne. Energetic quantum limit in large-scale interferometers. In *AIP Conference Proceedings*, volume 523, pages 180–190. AIP, 2000.
- [28] Mankei Tsang, Howard M. Wiseman, and Carlton M. Caves. Fundamental quantum limit to waveform estimation. *Phys. Rev. Lett.*, 106:090401, Mar 2011.
- [29] Haixing Miao, Rana X Adhikari, Yiqiu Ma, Belinda Pang, and Yanbei Chen. Towards the fundamental quantum limit of linear measurements of classical signals. *Phys. Rev. Lett.*, 119:050801, Aug 2017.
- [30] Haixing Miao, Yiqiu Ma, Chunnong Zhao, and Yanbei Chen. Enhancing the bandwidth of gravitational-wave detectors with unstable optomechanical filters. *Physical review letters*, 115(21):211104, 2015.
- [31] Joe Bentley, Philip Jones, Denis Martynov, Andreas Freise, and Haixing Miao. Converting the signal-recycling cavity into an unstable optomechanical filter to enhance the detection bandwidth of gravitational-wave detectors. *Phys. Rev. D*, 99:102001, May 2019.
- [32] Yanbei Chen. Macroscopic quantum mechanics: theory and experimental concepts of optomechanics. *Journal of Physics B: Atomic, Molecular and Optical Physics*, 46(10):104001, may 2013.
- [33] Carlton M. Caves and Bonny L. Schumaker. New formalism for two-photon quantum optics. i. quadrature phases and squeezed states. *Phys. Rev. A*, 31:3068–3092, May 1985.
- [34] Bonny L. Schumaker and Carlton M. Caves. New formalism for two-photon quantum optics. ii. mathematical foundation and compact notation. *Phys. Rev. A*, 31:3093–3111, May 1985.
- [35] K.J. Åström and R.M. Murray. *Feedback Systems: An Introduction for Scientists and Engineers*. Princeton University Press, 2010.
- [36] Jan L. Cieřliński and Bogusław Ratkiewicz. On simulations of the classical harmonic oscillator equation by difference equations. *Advances in Difference Equations*, May 2006.

ATOM INTERFEROMETRY: LINEAR QUANTUM MEASUREMENT THEORY AND THE PRECISION LIMIT

The theory of linear quantum measurement has been developed for analyzing the sensitivities of experimental devices that measure extremely weak signals, such as gravitational waves. It has successfully contributed to the theoretical understanding of laser interferometer gravitational-wave detectors (used by LIGO, VIRGO, and KAGRA) and helped many important experimental upgrades. In this work, we establish a linear quantum measurement theory for another kind of measurement device — matter-wave interferometers — which has been widely discussed as an important platform for many high-precision experiments. This theory allows us to account for both atom and light fluctuations, and leads to a detailed analysis of back-action in matter-wave interferometry (action of light back onto the atoms) and its effect on dynamics and measurement noise. From this analysis, we obtain a Standard Quantum Limit (SQL) for matter-wave interferometry. A comparison between the LIGO detector and matter-wave interferometer is also given from the perspective of quantum measurement.

5.1 Introduction

The detection of gravitational waves (GWs) from merging binary black holes [1] and merging neutron star binaries [2] by an international network of gravitational-wave detectors (LIGO, VIRGO, and KAGRA) opened the era of gravitational wave astronomy (in this chapter we shall use "LIGO detector" to refer to a detector that is used by LIGO [3], VIRGO [4], and KAGRA [5]). This detection is also a milestone in the development of high-precision measurement physics, making LIGO detector the most sensitive instrument that human beings ever built. Parallel to LIGO detector where the underlying principle is the interference of the electromagnetic waves, other concepts of GW detectors have also been proposed, even before the first detection event. One particular attractive concept is the atom-interferometer GW detector, first raised by Dimopoulos et al. [6, 7] and later enriched by many further discussions [8–16]. Different from the LIGO, the physical principle under the atom-interferometer GW detector is the interference of the matter waves, rather than the light waves.

The concept of atom interferometry can be traced back to the 1930s, when Rabi demonstrated that the atoms' internal quantum states can be altered using RF Resonance [17]. In 1949, Ramsey firstly created and detected long-lived coherent superposition of internal quantum states [18]. These pioneering works pave the way for the further development of a field named *atom optics*, namely, one can manipulate coherent beams of atoms as manipulating those of light fields [19]. Atom interferometry is an art of atom optics and an important experimental platform for high-precision measurement, which is now being used for measuring earth's gravity acceleration and testing fundamental physics [20–32].

The advantage of the proposed application of atom interferometer in GW detection is mostly at low frequency (below 10 Hz), which can be understood as follows. Because the test masses are connected to the ground through a suspension system, the sensitivity of a laser interferometer GW detector is seriously contaminated at low frequencies partly through the coupling of the test masses with the seismic oscillations, although the multi-stage vibration isolation technique has been applied [12]. For space-borne optical GW detector such as Laser Interferometer Space Antenna (LISA), the test masses are also connected to the satellite platforms, thereby the random motion of the satellites will be transferred onto the test masses and contaminate the GW signal. However, for the atom interferometer, since the atoms are free-falling during the interferometry process, they are less sensitive to the seismic perturbation (or the satellite motion in the space case). The laser noise can be removed by designing the detector configuration with common mode rejection. More sophisticated designs such as implementing the large momentum transfer technique or optical cavities have been also discussed [33–37].

Typically, experimental devices such as GW detectors that targeted on measuring extremely weak signals can even be affected by quantum mechanics. The theory of quantum measurement developed from the 1960s is a framework to analyze how quantum mechanics affects the sensitivity of an experimental device [38]. The early resonant bar GW detectors and the current laser interferometer GW detectors have been extensively studied and understood using this quantum measurement theory framework [38–40]. For atom interferometry, although the effect of quantum noise has been discussed by various authors [41–44], a complete analysis under quantum measurement theory has not been discussed in the current literature. Establishing such a theory will provide important insights in understanding the atom interferometer. Here, it is useful to briefly overview such a framework, based on the

block-diagram shown in Fig. 5.1. In this framework, a quantum measurement de-

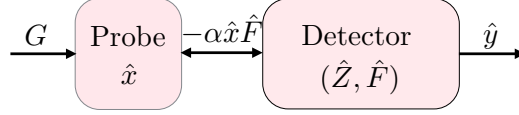


Figure 5.1: Block diagram of a linear quantum measurement device.

vice is divided into probe and detector, where the probe dynamical quantity \hat{x} is linearly coupled to G —the information to be measured. The probe and detector are coupled through linear Hamiltonian $\hat{H}_{\text{int}} = -\alpha\hat{x}\hat{F}$. The information of G will flow into the detector through probe-detector interaction and then be read out as $\hat{y}(t)$:

$$\hat{y}(t) = \hat{Z}(t) + \alpha \left[\hat{x}_{\text{zero}}(t) + x_{\text{sig}}(t) + \alpha \int_{-\infty}^t dt' \chi_m(t-t') \hat{F}(t') \right], \quad (5.1)$$

where \hat{x}_{zero} , x_{sig} , \hat{F} are the zero-point fluctuation of \hat{x} , the signal, and the back-action force, α is the coupling strength and the $\chi_m(t-t')$ is the dynamical response function of the probe. Braginsky *et al.* shows that for measuring the GW tidal force, the zero-point fluctuation of test masses does not contribute to the final sensitivity, thereby \hat{x}_{zero} can be simply ignored [45]. If \hat{Z} and \hat{F} have no correlation, the sensitivity will be limited by the so-called standard quantum limit (SQL), given by (in the frequency domain):

$$S_{xx}^{\text{SQL}}(\Omega) = 2\hbar|\chi_m(\Omega)|, \quad (5.2)$$

where Ω is the angular frequency of GWs. For advanced LIGO, the SQL is given by $S_{xx}^{\text{SQL}}(\Omega) = 2\hbar/(m\Omega^2)$, with the mass of the test mirrors denoted by m .

In this work, we set up a quantum measurement theory framework for analyzing the physics of atom interferometer, which is based on the interaction between atom cloud and two optical fields (passive and control laser). It is straightforward to extend our result to other atom interferometer configurations.

5.2 Effective Hamiltonian of an atom interferometer

In an atom-interferometer GW detector, the GW information is carried by the light field in the TT gauge, thereby the light field corresponds to the probe and the detector corresponds to the atom cloud in the above quantum measurement model. Concretely speaking, the atom cloud, as a phase meter, records the optical phase (more precisely, the phase difference between the control and passive fields as we shall see) imposed by the signal. In this section, we will establish a one-dimensional

effective Hamiltonian for analyzing this system. Real systems are three-dimensional, therefore this one-dimensional model is obtained by reducing a three-dimensional system by paraxial approximation. This Hamiltonian can be derived from first principle and the details are given in Apps. 5.8 and 5.9. In this section, we are going to show how the back-action effect manifests itself in atom interferometers.

5.2.1 Effective Hamiltonian and dynamics of an interaction kernel

The basic physical process that happens in a typical atom interferometer is a four-boson interaction, where the atomic transition between energy level $|1\rangle$ and $|2\rangle$ happens through coupling to an intermediate energy level $|3\rangle$ by control and passive fields, as shown in Fig 5.2.

The Hamiltonian describing the Raman interaction happens in an atom interferometer has the following structure:

$$\begin{aligned}\hat{H}_{\text{opt}} &= \frac{i\hbar}{2} \int_{-\infty}^{\infty} [\partial_x \hat{a}_{cx}^\dagger \hat{a}_{cx} - \partial_x \hat{a}_{px}^\dagger \hat{a}_{px}] + \text{h.c.}, \\ \hat{H}_{\text{atom}} &= \hbar\omega_A \hat{A}^\dagger \hat{A} + \hbar\omega_B \hat{B}^\dagger \hat{B}, \\ \hat{H}_{\text{int}} &= \hbar\chi (\hat{A} + \hat{A}^\dagger) (\hat{B} + \hat{B}^\dagger) (\hat{a}_c + \hat{a}_c^\dagger) (\hat{a}_p + \hat{a}_p^\dagger),\end{aligned}\tag{5.3}$$

where the \hat{H}_{opt} describes the free control light \hat{a}_c and passive light \hat{a}_p in x -space; \hat{H}_{atom} describes the whole atom clouds at two different energy levels and thereby does not depend on x ; \hat{H}_{int} describes the atom-light Raman interaction at one specific spacetime location, the derivation of such a four-field interaction Hamiltonian is shown in the Appendix. \hat{A} and \hat{B} are the effective annihilation operators for energy levels $|1\rangle$ and $|2\rangle$, respectively. Their corresponding number operators are $\hat{N}_A = \hat{A}^\dagger \hat{A}$ and $\hat{N}_B = \hat{B}^\dagger \hat{B}$, and we have the commutation relation $[\hat{A}, \hat{A}^\dagger] = 1$ (the same for

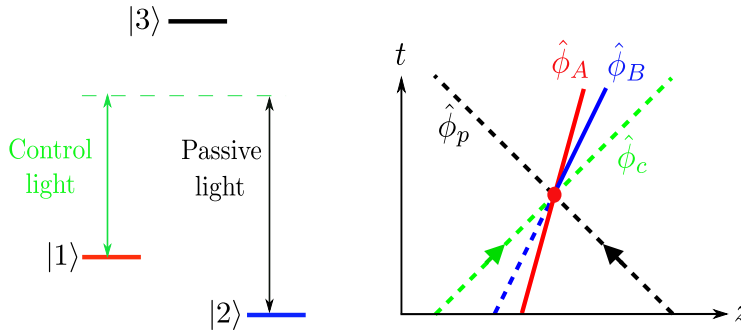


Figure 5.2: A four-boson Raman interaction kernel and its corresponding WKB trajectory. For a detailed discussion of this process and the description using field theory, see Apps. 5.8 and 5.9.

\hat{B}). For the continuous optical fields, we have $[\hat{a}_{cx}, \hat{a}_{cx'}^\dagger] = \delta(x - x')$ (the same for \hat{a}_{px}), and it is related to particle number by $\hat{N} = \int dx \hat{a}_{cx}^\dagger \hat{a}_{cx}$. The precise definition of these effective operators will be presented in Section IV.

Note that under the rotating wave approximations, only the terms satisfying $\omega_A + \omega_c = \omega_B + \omega_p$ will be kept while those non-rotating wave terms such as $\hat{A}\hat{B}\hat{a}_c^\dagger\hat{a}_p^\dagger$ etc. can be safely ignored, which leads us to a simpler form of interaction Hamiltonian:

$$\hat{H}_{\text{int}} = \hbar\chi\hat{A}^\dagger\hat{B}\hat{a}_c^\dagger\hat{a}_p + \text{h.c.}, \quad (5.4)$$

and the corresponding equations of motion for atomic clouds are given by:

$$\dot{\hat{A}} = -i\chi\hat{B}\hat{a}_c^\dagger\hat{a}_p, \quad \dot{\hat{B}} = -i\chi\hat{A}\hat{a}_c\hat{a}_p^\dagger. \quad (5.5)$$

Solving these equations perturbatively by writing the operators as: $\hat{A} = \bar{A}_A + \hat{A}_A$ and $\hat{B} = \bar{A}_B + \hat{A}_B$ (where the magnitude of $\hat{A}_{A/B}$ is small compare to the $\bar{A}_{A/B}$) leads to the zeroth-order equations:

$$\dot{\bar{A}}_A = -i\Omega\bar{A}_B e^{i\varphi}, \quad \dot{\bar{A}}_B = -i\Omega\bar{A}_A e^{-i\varphi}, \quad (5.6)$$

where $\Omega = \chi|\bar{a}_c\bar{a}_p|$ is the Rabi-frequency, and $\varphi = \varphi_c - \varphi_p$ is the phase difference between control field and passive field.

The rest terms satisfy the following equations:

$$\hat{\mathcal{L}} \begin{bmatrix} \hat{A}_A \\ \hat{A}_B \end{bmatrix} = -i\chi \begin{bmatrix} \bar{A}_B(\hat{a}_c^\dagger|\bar{a}_p|e^{-i\varphi_p} + \hat{a}_p|\bar{a}_c|e^{i\varphi_c}) \\ \bar{A}_A(\hat{a}_c|\bar{a}_p|e^{i\varphi_p} + \hat{a}_p^\dagger|\bar{a}_c|e^{-i\varphi_c}) \end{bmatrix} + \Omega\varphi_s \begin{bmatrix} \bar{A}_B e^{i\varphi} \\ -\bar{A}_A e^{-i\varphi} \end{bmatrix}, \quad (5.7)$$

in which the differential operator $\hat{\mathcal{L}}$ takes the form of:

$$\hat{\mathcal{L}} = \begin{bmatrix} \partial_t & i\Omega e^{i\varphi} \\ i\Omega e^{-i\varphi} & \partial_t \end{bmatrix}, \quad (5.8)$$

and the right-hand side of these equations describes the influence of optical fields to the evolution of atom fields. The $\varphi_s \ll \varphi$ is the signal phase carried by the optical field, and we expand it to the linear order to obtain the signal terms.

The solutions for the optical fields, to the leading order, are given by:

$$\bar{a}_{\text{cout}} = \bar{a}_{\text{cin}}, \quad \bar{a}_{\text{pout}} = \bar{a}_{\text{pin}}, \quad (5.9)$$

and the rest terms satisfy:

$$\begin{aligned} \hat{a}_{\text{cout}} &= \hat{a}_{\text{cin}} - i\chi(\bar{A}_A^*\bar{A}_B\hat{a}_p + \bar{A}_A^*\bar{a}_p\hat{A}_B + \bar{A}_B\bar{a}_p\hat{A}_A^\dagger + \bar{A}_A^*\bar{A}_B\bar{a}_p), \\ \hat{a}_{\text{pout}} &= \hat{a}_{\text{pin}} - i\chi(\bar{A}_A\bar{A}_B^*\hat{a}_c + \bar{A}_A\bar{a}_c\hat{A}_B^\dagger + \bar{A}_B^*\bar{a}_c\hat{A}_A + \bar{A}_A\bar{A}_B^*\bar{a}_c). \end{aligned} \quad (5.10)$$

The first terms in the brackets of the r.h.s. of the Eq. (5.10) are much smaller than the rest terms (the ratio $\sim \sqrt{N_a/N_L}$, where N_a and N_L are the atom number and photon number in the pulse), which can be ignored. Also note that the optical operators on the r.h.s. of the above equations are defined at the interaction point, in principle the Eq. 5.7 should be solved in the way that we substitute $\hat{a}_p = (\hat{a}_{pin} + \hat{a}_{pout})/2$ and $\hat{a}_c = (\hat{a}_{cin} + \hat{a}_{cout})/2$. However, since the atom-light interaction is weak, if we ignore the term involving high orders of χ , the r.h.s. of Eq. (5.10) can be simply written in the way that $\hat{a}_c = \hat{a}_{cin}$, $\hat{a}_p = \hat{a}_{pin}$.

Substituting Eq. (5.10) into the equations of motion for the atom field Eq. (5.7), we obtain:

$$\hat{\mathcal{L}} \begin{bmatrix} \hat{A}_A \\ \hat{A}_B \end{bmatrix} = \begin{bmatrix} \hat{F}_{flu}^A + F_{cl}^A + F_{dy}^A \\ \hat{F}_{flu}^B + F_{cl}^B + F_{dy}^B \end{bmatrix} + \Omega\varphi_s \begin{bmatrix} \bar{A}_B e^{i\varphi} \\ -\bar{A}_A e^{-i\varphi} \end{bmatrix}. \quad (5.11)$$

Here the terms on the r.h.s. can be understood as "optical force" acting on the atomic fields, explained in detail as follows:

(1) The $\hat{F}_{flu}^{A/B}$ have the form:

$$\begin{aligned} \hat{F}_{flu}^A &= -i\chi\bar{A}_B(|\bar{a}_p|e^{-i\varphi_p}\hat{a}_{cin}^\dagger + |\bar{a}_c|\hat{a}_{pin}e^{i\varphi_c}), \\ \hat{F}_{flu}^B &= -i\chi\bar{A}_A(|\bar{a}_p|e^{i\varphi_p}\hat{a}_{cin} + |\bar{a}_c|e^{-i\varphi_c}\hat{a}_{pin}^\dagger), \end{aligned} \quad (5.12)$$

which is the optical Langevin force acting on the atom fields, due to the randomness of the incoming states of optical fields.

(2) The $F_{cl}^{A/B}$ have the form:

$$\begin{aligned} F_{cl}^A &= \frac{\chi^2}{2}|\bar{A}_B|^2\bar{A}_A(|\bar{a}_p|^2 - |\bar{a}_c|^2), \\ F_{cl}^B &= \frac{\chi^2}{2}|\bar{A}_A|^2\bar{A}_B(|\bar{a}_p|^2 - |\bar{a}_c|^2), \end{aligned} \quad (5.13)$$

which describes the pondermotive force exerted by the mean optical fields on the atoms.

(3) The $F_{dy}^{A/B}$ have the form:

$$\begin{aligned} F_{dy}^A &= \frac{\chi^2}{2}(|\bar{a}_p|^2 - |\bar{a}_c|^2)(\bar{A}_A\bar{A}_B\hat{A}_B^\dagger + |A_B|^2\hat{A}_A), \\ F_{dy}^B &= \frac{\chi^2}{2}(|\bar{a}_p|^2 - |\bar{a}_c|^2)(\bar{A}_B\bar{A}_A\hat{A}_A^\dagger + |A_A|^2\hat{A}_B). \end{aligned} \quad (5.14)$$

These forces, which depend on the operators $\hat{A}_A^{(\dagger)}$, $\hat{A}_B^{(\dagger)}$ will modify the Rabi-dynamics of the atom fields.

In case of balanced passive and control fields (i.e., $|\bar{a}_p| = |\bar{a}_c| = \bar{a}_L$), these dynamical back-actions will vanish. In the following sections, we will focus on the configuration with balanced passive and control fields.

The solution of these dynamical equations can be expressed in a more convenient way by using the following basis: (1) $\hat{A}_\pm = (\hat{A}_A e^{-i\varphi/2} \pm \hat{A}_B e^{i\varphi/2})/\sqrt{2}$ for atom fields; (2) $\hat{a}_{c1} = (\hat{a}_c e^{i\varphi_c} + \hat{a}_c^\dagger e^{-i\varphi_c})/\sqrt{2}$, $\hat{a}_{p1} = (\hat{a}_p e^{-i\varphi_p} + \hat{a}_p^\dagger e^{i\varphi_p})/\sqrt{2}$, $\hat{a}_{c2} = (\hat{a}_c e^{i\varphi_c} - \hat{a}_c^\dagger e^{-i\varphi_c})/(\sqrt{2}i)$, $\hat{a}_{p2} = (\hat{a}_p e^{-i\varphi_p} - \hat{a}_p^\dagger e^{i\varphi_p})/(\sqrt{2}i)$ for optical fields; (3) the common and differential modes of incoming optical fields: $\hat{a}_{\pm\text{in}1/2} = (\hat{a}_{\text{cin}1/2} \pm \hat{a}_{\text{pin}1/2})/\sqrt{2}$. Under this basis, the equations of motion Eq. (5.7) can be transformed to:

$$(\partial_t \pm i\Omega)\hat{A}_\pm(t) = \mp\Omega\varphi_s\bar{A}_\mp(t) \mp i\chi_a[\bar{A}_\pm(t)\hat{a}_{\text{in}1} + i\bar{A}_\mp(t)\hat{a}_{\text{in}2}], \quad (5.15)$$

where $\chi_a = \chi\bar{a}_L$. Then the solution can be written as signal and noise parts, respectively. The signal part is:

$$\begin{aligned} A_{s\pm}(t) &= \mp\Omega\varphi_s \int_{t_0}^t dt' e^{\mp i\Omega(t-t')} \bar{A}_\mp(t') \\ &= \mp\varphi_s \bar{A}_\mp(0) \sin \Omega(t - t_0). \end{aligned} \quad (5.16)$$

The noise part is:

$$\hat{A}_\pm(t) = e^{\mp i\Omega t} \hat{A}_\pm(t_0) + \hat{A}_{\pm\text{opt}}(t), \quad (5.17)$$

where

$$\hat{A}_{\pm\text{opt}}(t) = \hat{A}_{\pm\text{am}}(t) + \hat{A}_{\pm\text{ph}}(t), \quad (5.18)$$

with

$$\begin{aligned} \hat{A}_{\pm\text{am}}(t) &= \mp i\chi_a \int_{t_0}^t dt' e^{\mp i\Omega(t-t')} \bar{A}_\pm(t') \hat{a}_{\text{in}1}(t'), \\ \hat{A}_{\pm\text{ph}}(t) &= \pm \chi_a \int_{t_0}^t dt' e^{\mp i\Omega(t-t')} \bar{A}_\mp(t') \hat{a}_{\text{in}2}(t'). \end{aligned} \quad (5.19)$$

Here, the $e^{\mp i\Omega(t-t')}$ is the free propagator of the atom operators \hat{A}_\pm . The $\hat{A}_{\pm\text{ph}}$ and $\hat{A}_{\pm\text{am}}$ are the quantum optical noise contribution to the atom clouds evolution, while the $\hat{A}_\pm(t_0)$ is the initial quantum fluctuation of atom field.

5.2.2 Back-action noise

For the atom interferometer systems (both for a single atom interferometer and for the GW detector configuration involving a pair of atom interferometers), there exist such situations that the same control fields connect several different interaction

kernels. For example, in Fig. 5.3, the two $\pi/2$ processes are connected by the same control field. In the GW detector configuration proposed by Dimopoulos *et al.* (see Fig. 5.4), all the interaction kernels of the two atom interferometers are connected by the control fields. In these cases, the quantum fluctuation of the first interaction kernel (e.g., denoted by a) can be carried by light field (probe) and then affects the second interaction kernel (e.g., denoted by b), and finally affects the output atom fields (detector). This would lead to a “back-action” noise, somewhat similar to the optomechanical system that the quantum fluctuation of light (detector) will be carried by the test masses (probe), and then affect the output light field (detector). Formally, to analyze such a system, we have to duplicate the Hamiltonian, and the interaction should happen at two different spacetime points:

$$H_{\text{int}} = \chi \hat{A}^{(a)\dagger} \hat{B}^{(a)} (\hat{a}_c^\dagger \hat{a}_d) |^{(a)} + \chi \hat{A}^{(b)\dagger} \hat{B}^{(b)} (\hat{a}_c^\dagger \hat{a}_d) |^{(b)}. \quad (5.20)$$

Following the same approach discussed in the last section, one can write down the equations of motion for atom clouds of the second interaction kernel in an almost identical form. The only difference is that the optical fields operators on the r.h.s. of the atom equations of motion (Eq. (5.7)) can be connected to the optical fields flying out of the atom-light interaction region of the first interaction kernel, that is:

$$\hat{a}_{\text{cin}}^{(b)} = \hat{a}_{\text{cout}}^{(a)}. \quad (5.21)$$

Substituting this relation into the Langevin force Eq. (5.12) for the second interaction kernel, and keeping only those terms, which, due to the atom fluctuations brought from the first interaction kernel, we obtain the “back-action force” acting on the atom fields of the second interaction kernel as:

$$\begin{aligned} [F_A^{(b)}]_{\text{BA}} &= \chi_a^2 \bar{A}_B^{(b)} (\bar{A}_B^{(a)*} \hat{A}_A^{(a)} + \bar{A}_A^{(a)} \hat{A}_B^{(a)\dagger}), \\ [F_B^{(b)}]_{\text{BA}} &= -\chi_a^2 \bar{A}_A^{(b)} (\bar{A}_B^{(a)} \hat{A}_A^{(a)\dagger} + \bar{A}_A^{(a)*} \hat{A}_B^{(a)}). \end{aligned} \quad (5.22)$$

In writing down these expressions, we have used the conditions of balanced control/passive lasers $|\bar{a}_p| = |\bar{a}_c| = a_L$ and the optical field strength for these two interaction kernels are identical $a_L^{(b)} = a_L^{(a)} = a_L$.

Adding these back-action force terms into the atom dynamical equations Eq. (5.11) for the second interaction kernel, integrating the equations and expressing these back-action equations in terms of \hat{A}_\pm , $\hat{a}_{1,2c/p}$, we have the back-action force contributions \hat{A}_\pm^{BA} as :

$$\hat{A}_\pm^{\text{BA}}(t) = \mp \frac{\chi_a^2}{2} \int_{t_0}^t dt' e^{\pm i\Omega(t'-t)} [\bar{A}_\pm^{(b)}(t') \hat{\mathcal{A}}(t') + \bar{A}_\mp^{(b)}(t') \hat{\mathcal{B}}(t')], \quad (5.23)$$

where

$$\begin{aligned}\hat{\mathcal{A}}(t) &= \bar{A}_+^{(a)}(t)\hat{A}_-^{(a)\dagger}(t) + \bar{A}_-^{(a)*}(t)\hat{A}_+^{(a)}(t) - \text{h.c.}, \\ \hat{\mathcal{B}}(t) &= \bar{A}_+^{(a)}(t)\hat{A}_+^{(a)\dagger}(t) - \bar{A}_-^{(a)}(t)\hat{A}_-^{(a)\dagger}(t) + \text{h.c.}\end{aligned}\quad (5.24)$$

5.3 Interferometry solution

This section will give the solution of the atom interferometer. As an example, we only show the solution of which the signal is contributed from the optical phase imprinted on the atom cloud during the atom-light interaction. This is actually the situation for the proposed atom-interferometer GW detectors. In many other important applications, the signals are carried by the atom fields themselves. For example, the atom interferometry gravity meter is based on the principle that the gravitational acceleration will affect the propagation phase of the atom fields. In an atom-interferometer GW detector, this effect is the physical origin of the gravity noise, which is an important issue that needs to be taken care for the design since the local gravitational field can not be screened. In this paper, we will not discuss these issues (and all the classical noise sources) since they are not the subject of the quantum measurement theory. For simplicity, we also do not consider the effects such as distortion of the atom cloud for simplicity, and we assume that the free propagation of atom fields is coherent.

5.3.1 Input-output relation

At the detection stage of an atom interferometer, firstly the particle numbers of A and B atom species are detected respectively, and then the signal is extracted from their difference. Since the detected quantity $\Delta\hat{N} = \hat{N}_A - \hat{N}_B$ is in the $(\hat{A}_A, \hat{A}_B)^T$ basis while the formulae of optical noise and back-action terms are more concise in the $(\hat{A}_+, \hat{A}_-)^T$ (see Eq. (5.19)), we will use the transformation matrix between these two bases, defined as:

$$\mathbb{T}(\varphi) = \frac{1}{\sqrt{2}} \begin{bmatrix} e^{i\varphi/2} & e^{i\varphi/2} \\ e^{-i\varphi/2} & -e^{-i\varphi/2} \end{bmatrix}, \quad (5.25)$$

and the transfer matrix of atom field in the $(\hat{A}_A, \hat{A}_B)^T$ basis is given by:

$$\mathbb{M}(\theta_j, \varphi_j) = \begin{bmatrix} \cos \theta_j & -i \sin \theta_j e^{i\varphi_j} \\ -i \sin \theta_j e^{-i\varphi_j} & \cos \theta_j \end{bmatrix}, \quad (5.26)$$

where $\theta_j = \Omega t_j$.

For the beam-splitting process (named as step-1), we have:

$$\begin{bmatrix} A^{(1)}(t) \\ B^{(1)}(t) \end{bmatrix} = \mathbb{M}(\theta_1, \varphi_{s1}) \begin{bmatrix} A(t_0) \\ B(t_0) \end{bmatrix}, \quad (5.27)$$

in which t_0 is the initial time of the interrogation process, and $A/B(t)$ can be decomposed into $A/B(t) = \bar{A}_{A/B}(t) + \hat{A}_{A/B}(t)$, where $\bar{A}_{A/B}(t)$ is the mean value of the atom field while $\hat{A}_{A/B}(t)$ is the perturbation around the mean value. At step-1, $\hat{A}_{A/B}(t)$ contains the quantum fluctuation of atom field and also the quantum fluctuation of light field, given as:

$$\begin{bmatrix} \hat{A}_A^{(1)}(t) \\ \hat{A}_B^{(1)}(t) \end{bmatrix} = \mathbb{M}(\theta_1, \varphi_{s1}) \begin{bmatrix} \hat{A}_A(t_0) \\ \hat{A}_B(t_0) \end{bmatrix} + \mathbb{T}(0) \begin{bmatrix} \hat{A}_{+opt}^{(1)}(t) \\ \hat{A}_{-opt}^{(1)}(t) \end{bmatrix}. \quad (5.28)$$

After the step-1, we have $\theta_1 = \pi/4$ with $t_1 = \pi/(4\Omega)$, and the $A(t)$ and $B(t)$ fields start to separate spatially. The $\pi/2$ processes for A -channel and B -channel connected by the control light happen sequentially and they should be treated individually. Let us denote the $\pi/2$ processes of the A and B channels to be the step-2a and step-2b, respectively. Clearly, the initial conditions of the step-2a and step-2b processes are $[A^{(1)}(t_1), \hat{A}_B^{(2)}]^T$ and $[\hat{A}_A^{(2)}, B^{(1)}(t_1)]^T$ respectively, where $\hat{A}_{A/B}^{(2)}$ are the field fluctuations injected at the $\pi/2$ steps, shown in Fig.5.3.

During the $\pi/2$ processes, the corresponding transfer matrices are given by:

Step-2a:

$$\begin{bmatrix} A^{(2a)}(t) \\ B^{(2a)}(t) \end{bmatrix} = \mathbb{M}(\theta_2, \varphi_{s2}) \begin{bmatrix} A^{(1)}(t_1) \\ \hat{A}_B^{(2)} \end{bmatrix} + \mathbb{T}(0) \begin{bmatrix} \hat{A}_{+opt}^{(2a)}(t) \\ \hat{A}_{-opt}^{(2a)}(t) \end{bmatrix}, \quad (5.29)$$

Step-2b:

$$\begin{bmatrix} A^{(2b)}(t) \\ B^{(2b)}(t) \end{bmatrix} = \mathbb{M}(\theta_2, \varphi_{s2}) \begin{bmatrix} \hat{A}_A^{(2)} \\ B^{(1)}(t_1) \end{bmatrix} + \mathbb{T}(0) \begin{bmatrix} \hat{A}_{+opt}^{(2b)}(t) + \hat{A}_{+BA}^{(2)}(t) \\ \hat{A}_{-opt}^{(2b)}(t) + \hat{A}_{-BA}^{(2)}(t) \end{bmatrix},$$

where the upper indices a/b denote the A/B channels, respectively. Since step-2a and step-2b are connected by the same control light, the control light after step-2a will carry atom information of step-2a and impose a "back-action" on the step-2b. Here the effect of this back-action is denoted by $\hat{A}_{\pm BA}^{(2)}(t)$, whose concrete representation can be derived from Eq. (5.23)

As shown in Fig.5.3, only one component of the output fields from step-2a/2b participates the recombination stage, while the other component is left unmeasured.

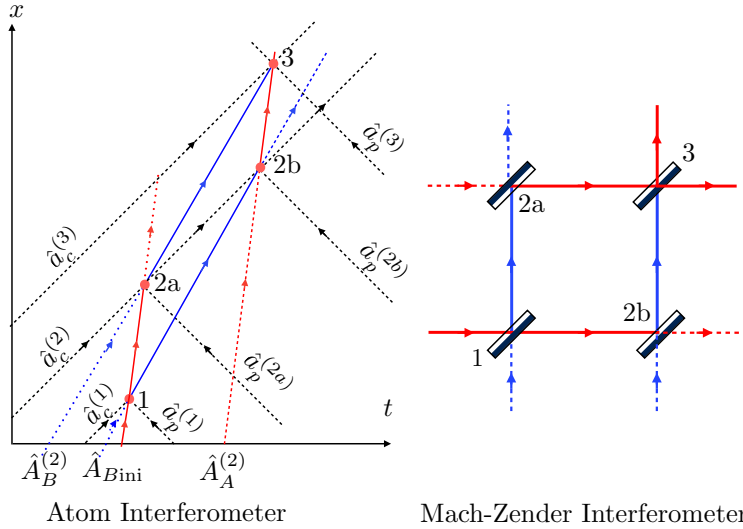


Figure 5.3: Comparison between atom interferometer and optical Mach-Zender interferometer. Left panel: space-time diagram of the $\pi/2$ processes happening in an atom interferometer. Right panel: an optical Mach-Zender interferometer. On the optical Mach-Zender interferometer, part of the quantum noise injected at 2a and 2b stages is reflected away and left unmeasured. A similar situation also happens in the atom interferometer, where part of the atom noise of $A_{A/B}$ channel injected to 2b/a interaction kernels will be reflected away and left unmeasured. However, the difference is, in the atom interferometer, the “mirrors” that reflect the matter waves are not uncorrelated as in the optical Mach-Zender interferometer. The control field that connects the interaction kernel 2a/b is the same field.

For those recombined components, we form a new input field column for the recombination stage as: $[A^{(2b)}(t_2), B^{(2a)}(t_2)]^T$, where $t_2 = \pi/(2\Omega)$.

The field’s evolution at the recombination stage now can be written as:

$$\begin{bmatrix} A^{(3)}(t) \\ B^{(3)}(t) \end{bmatrix} = \mathbb{M}(\theta_3, \frac{\pi}{2} + \varphi_{s3}) \begin{bmatrix} A^{(2b)}(t_2) \\ B^{(2a)}(t_2) \end{bmatrix} + \mathbb{T}(\frac{\pi}{2}) \begin{bmatrix} \hat{A}_{+opt}^{(3)}(t_3) \\ \hat{A}_{-opt}^{(3)}(t_3) \end{bmatrix}, \quad (5.30)$$

which completes its recombination process at $t = t_3 = \pi/(4\Omega)$. Note that this equation can be expanded perturbatively, since the signal terms containing phase φ_s and the noise terms are small compared to the expectation values. The results are given as follows:

• **Mean field.** — Expanding the output atom fields Eq. (5.30) to the zeroth order, we obtain the final mean field as:

$$\begin{bmatrix} \bar{A}_A^{(3)}(t_3) \\ \bar{A}_B^{(3)}(t_3) \end{bmatrix} = -\frac{1}{\sqrt{2}} \begin{bmatrix} e^{i\pi/4} \\ e^{-i\pi/4} \end{bmatrix} \bar{A}_A(0). \quad (5.31)$$

• **Signal field.** — Expanding the output atom fields Eq. (5.30) to the first order, we obtain the signal field as:

$$\begin{bmatrix} A_{As} \\ A_{Bs} \end{bmatrix} = \frac{1}{2} \bar{A}_A(0)^2 \begin{bmatrix} i\varphi_{s1} - (1+i)\varphi_{s2} + \varphi_{s3} \\ -i\varphi_{s1} + (1+i)\varphi_{s2} - \varphi_{s3} \end{bmatrix}. \quad (5.32)$$

• **Atom noise.** — Similarly, the noise contributed by the atom fluctuations can be written as:

$$\begin{bmatrix} \hat{A}_A^{(3)}(t_3) \\ \hat{A}_B^{(3)}(t_3) \end{bmatrix} = \underbrace{-\frac{e^{i\pi/4}}{\sqrt{2}} \begin{bmatrix} 1 & 1 \\ -i & i \end{bmatrix} \begin{bmatrix} \hat{A}_{Aini} \\ \hat{A}_{Bini} \end{bmatrix}}_{\text{atom shot noise}} \underbrace{-\frac{i\chi_a^2 \bar{A}_A^2(0)}{4\sqrt{2}\Omega} \begin{bmatrix} \hat{A}_B^{(2)} + \hat{A}_B^{(2)\dagger} \\ -\hat{A}_B^{(2)} - \hat{A}_B^{(2)\dagger} \end{bmatrix}}_{\text{back-action noise}}. \quad (5.33)$$

• **Optical noise.** — The formulae for optical noise are more complicated since they contain contributions from four different steps and the results are:

$$\begin{aligned} \hat{A}_{A/B}^{(3)}(t_3) = \frac{1}{2} [-2i\hat{A}_{+opt}^{(1)} + \hat{A}_{+opt}^{(2a)} - \hat{A}_{-opt}^{(2a)} \pm \hat{A}_{+opt}^{(2b)} + \hat{A}_{-opt}^{(2b)} \\ + (1 \pm i)(\hat{A}_{+opt}^{(3)} + \hat{A}_{-opt}^{(3)})]. \end{aligned} \quad (5.34)$$

Substituting the Eqs. (5.18) and (5.19) leads to the representation of the above formula in terms of incoming optical noise fields:

$$\begin{aligned} \hat{A}_{A/B}^{(3)}(t_3) = \frac{\chi_a \bar{A}}{2} \int_0^{\pi/2\Omega} dt' \sin 2\Omega t' [\hat{a}_{-2}^{(2a)}(t') \pm i\hat{a}_{-2}^{(2b)}(t')] \\ + e^{\pm i3\pi/4} \frac{\chi_a \bar{A}}{\sqrt{2}} \int_0^{\pi/4\Omega} dt' [\hat{a}_{+1}^{(3)}(t') + e^{2i\Omega t'} \hat{a}_{+1}^{(3)}(t')] \\ + e^{i3\pi/4} \frac{\chi_a \bar{A}}{\sqrt{2}} \int_0^{\pi/4\Omega} dt' [\hat{a}_{+1}^{(1)}(t') + ie^{2i\Omega t'} \hat{a}_{+1}^{(1)}(t')]. \end{aligned} \quad (5.35)$$

5.3.2 Standard quantum limit for a single atom interferometer

Using Eqs. (5.31)–(5.34), we can compute the particle numbers $N_A = A^\dagger A$ and $N_B = B^\dagger B$ after the recombination completes and expand to the first order of perturbation:

$$N_{A/B} \approx \frac{1}{2} \bar{A}_A^2(0) \mp \frac{1}{2} \bar{A}_A^2(0) (\varphi_{s1} - 2\varphi_{s2} + \varphi_{s3}). \quad (5.36)$$

Then the $\Delta N = N_B - N_A$, which is the atom number difference at states $|2\rangle$ and $|1\rangle$, is linearly proportional to the signal:

$$\Delta N_{\text{signal}} = -\bar{A}_A^2(0) (\varphi_{s1} - 2\varphi_{s2} + \varphi_{s3}). \quad (5.37)$$

Similar methods can be used to treat the quantum optical noise and the quantum atom noise, the latter of which is given by:

$$\Delta\hat{N}_{\text{atom}} = \underbrace{\bar{A}_A(0)(\hat{A}_{B\text{ini}} + \hat{A}_{B\text{ini}}^\dagger)}_{\text{atom shot noise}} + \underbrace{\frac{\chi_a^3 \bar{A}_A^3(0)}{2\sqrt{2}\Omega}(\hat{A}_B^{(2)} + \hat{A}_B^{(2)\dagger})}_{\text{back-action noise}}, \quad (5.38)$$

and the optical noise is given by:

$$\begin{aligned} \Delta\hat{N}_{\text{opt}} = & \frac{\bar{A}_A(0)}{\sqrt{2}} [e^{i3\pi/4} \hat{A}_{\text{opt-}}^{(1)} + e^{i\pi/4} \hat{A}_{\text{opt+}}^{(1)} - \sqrt{2} \hat{A}_{\text{opt+}}^{(3)}] \\ & + \frac{1}{\sqrt{2}} (\hat{A}_{\text{opt-}}^{(2a)} - \hat{A}_{\text{opt+}}^{(2a)} + i\hat{A}_{\text{opt-}}^{(2b)} + i\hat{A}_{\text{opt+}}^{(2b)}) + \text{h.c.} \end{aligned} \quad (5.39)$$

Now, normalizing the particle number difference ΔN by the signal coefficient, the estimator of the signal can be written as:

$$\Delta N_{\text{est}} = (\varphi_{s3} - 2\varphi_{s2} + \varphi_{s1}) + \frac{1}{\bar{A}_A^2(0)} (\Delta\hat{N}_{\text{opt}} + \Delta\hat{N}_{\text{atom}}). \quad (5.40)$$

Here, we can approximate $\varphi_{s3} - 2\varphi_{s2} + \varphi_{s1} \approx \ddot{\varphi}_s T^2$, where T is the interrogation time of the atom interferometer.

To estimate the scaling of the error contributed by these noises, we need to map the parameters in the effective Hamiltonian model to the experimental parameters. It is easy to prove that $\chi_a^2/\Omega = \chi^2 |\bar{a}_L|^2/\Omega = (\Omega a/c)/N_L$ using the relation $\chi |\bar{a}_L|^2 = \Omega$ and the fact that the photon number in the rectangular pulse is $N_L = |\bar{a}_L|^2 l_a/c$ where l_a is the width of the optical pulse. Then the scaling of the error can be estimated as:

$$\sigma_s^2 \sim \frac{N_A}{N_L^2} \left(\frac{\Omega l_a}{c} \right)^2 + \frac{2}{N_A} + \frac{1}{N_L}, \quad (5.41)$$

in which the first, second, and third terms are the orders of magnitude of the errors contributed by back-action noise, atom shot noise, and purely optical noise, respectively. Apparently the first and second terms have a trade-off when $N_a = N_L$, therefore the error has a minimum value

$$[\sigma_s^2]_{\text{mim}} \sim \frac{1}{N_L}, \quad (5.42)$$

which is actually the photon shot noise (usually $\Omega l_a/c = \pi/2$ or $\pi/4$, i.e., $\Omega l_a/c \sim 1$). This corresponds to the standard quantum limit given in Eq. (5.2).

It is important to note that this Standard Quantum Limit can only be understood *in the sense of extrapolation*. Actually when $N_a \sim N_L$, the linear approximation we used in analyzing the atom-light interaction will not be valid. The real atom interferometer does not work in this fully-nonlinear region. Therefore, for real devices, even in the most ideal situation, this Standard Quantum Limit is not as accessible as that of LIGO. It only gives a bound to the device sensitivity.

5.4 Back-action in atom interferometer pair

The back-action effect discussed in the last section, as we have mentioned, also exists for the system of a pair of atom interferometers. The detector configuration of atom interferometer pair was proposed to measure low frequency GWs. Control fields carrying the atom information of the first interferometer impose back-action on the second interferometer. The calculation follows the same logic as in the above sections, which is straightforward but a bit tedious. We only give the final results and discussions here.

The $\Delta\hat{N}_{\text{atom}}^{(\text{II})}$ for the second interferometer is given by:

$$\begin{aligned} \Delta\hat{N}_{\text{atom}}^{(\text{II})} = & \underbrace{\bar{A}_A(0)(\hat{A}_{B\text{ini}}^{(\text{II})} + \hat{A}_{B\text{ini}}^{(\text{II})\dagger})}_{\text{atom shot noise of AI}_{\text{II}}} + \underbrace{\frac{\chi_a^2 \bar{A}_A^3(0)}{2\sqrt{2}\Omega}(\hat{A}_B^{(2\text{II})} + \hat{A}_B^{(2\text{II})\dagger})}_{\text{back-action noise inside AI}_{\text{II}}} \\ & + \frac{\chi_a^2 \bar{A}_A^3(0)}{2\Omega} \left[(\hat{A}_{A\text{ini}}^{(\text{I})} + \hat{A}_{A\text{ini}}^{(\text{I})\dagger}) + i\sqrt{2}(\hat{A}_A^{(2\text{I})} - \hat{A}_A^{(2\text{I})\dagger}) \right. \\ & \left. - (\hat{A}_{B\text{ini}}^{(\text{I})} + \hat{A}_{B\text{ini}}^{(\text{I})\dagger}) + \sqrt{2}(\hat{A}_B^{(2\text{I})} + \hat{A}_B^{(2\text{I})\dagger}) \right]. \end{aligned} \quad (5.43)$$

back-action noise brought from AI_I

Here the indices (I) and (II) stand for the first (AI_I) and second (AI_{II}) interferometers. The first term in the above ΔN_{atom} is the atom shot noise of the second interferometer while the second term is the back-action noise contributed by atom fluctuations of step-2a of the second interferometer, similar to the second term in Eq. (5.38). The last term in Eq. (5.43) represents the back-action imposed by the first interferometer via control light. This result is obtained under the condition that $\bar{A}_A^{(\text{II})}(0) = \bar{A}_A^{(\text{I})}(0) = \bar{A}_A(0)$, that is, the two atom interferometers have the same atom initial states¹.

¹The original expression for the ΔN_{atom} for the second interferometer is: $\Delta\hat{N}_{\text{atom}}^{(\text{II})} = \bar{A}_A^{(\text{II})}(0)(\hat{A}_{B\text{ini}}^{(\text{II})} + \hat{A}_{B\text{ini}}^{(\text{II})\dagger}) + (\chi_a^2/2\sqrt{2}\Omega)[\bar{A}_A^{(\text{II})}(0)]^3(\hat{A}_B^{(2\text{II})} + \hat{A}_B^{(2\text{II})\dagger}) + (\chi_a^2/2\Omega)[\bar{A}_A^{(\text{II})}(0)]^2\bar{A}_A^{(\text{I})}(0)[(\hat{A}_{A\text{ini}}^{(\text{I})} + \hat{A}_{A\text{ini}}^{(\text{I})\dagger}) + i\sqrt{2}(\hat{A}_A^{(2\text{I})} - \hat{A}_A^{(2\text{I})\dagger}) - (\hat{A}_{B\text{ini}}^{(\text{I})} + \hat{A}_{B\text{ini}}^{(\text{I})\dagger}) + \sqrt{2}(\hat{A}_B^{(2\text{I})} + \hat{A}_B^{(2\text{I})\dagger})]$, where one can see the ‘‘beating’’ of atom fields of these two interferometers. The result shown in the main text is obtained simply by substituting $\bar{A}_A^{(\text{II})}(0) = \bar{A}_A^{(\text{I})}(0) = \bar{A}_A(0)$.

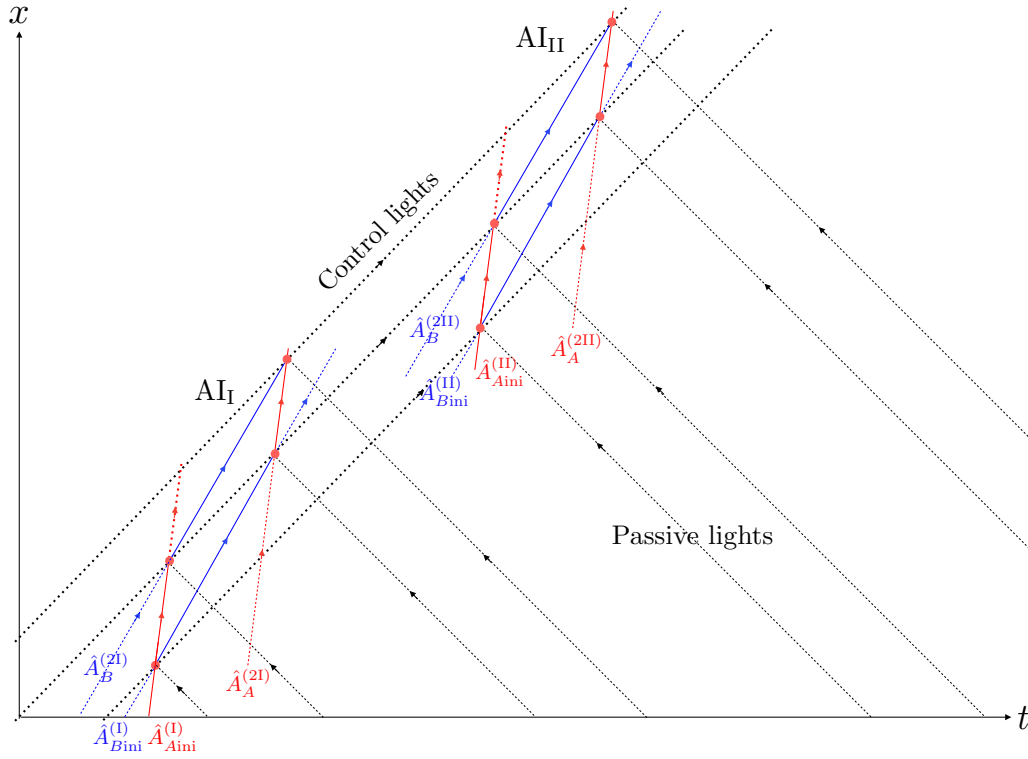


Figure 5.4: Atom interferometer gravitational wave detector configuration: this is the configuration proposed by Dimopoulos et.al. Two atom interferometers are connected by the control lights. The control fields flying out of the first atom interferometer will carry the corresponding atom information and impose a back-action noise on the second atom interferometer. The scales in this figure are for illustrative purpose and do not reflect the real situation. The distance between two interferometers in the real device is much larger than the length scale of atom interferometers themselves.

The signal field is given by:

$$\Delta N_{\text{signal}}^{(II)} = \bar{A}_A^2(0)(\varphi_{s1}^{(II)} - 2\varphi_{s2}^{(II)} + \varphi_{s3}^{(II)}). \quad (5.44)$$

Clearly, the noise terms described by Eq. (5.43) and Eq. (5.38) are correlated, since there are terms with $(\hat{A}_{Bini}^{(I)} + \hat{A}_{Bini}^{(I)\dagger})$ and $(\hat{A}_B^{(2I)} + \hat{A}_B^{(2I)\dagger})$ in Eq. (5.43). This simply means that the two interferometers are *entangled* via the coupling to the same control light fields, if the control light does not decohere strongly during its propagation between two interferometers.

The optical noise in the case of atom interferometer pair consists of the contribution of three control lights and eight passive lights, which is very cumbersome and not

very interesting in the aspect of quantum measurement theory — it simply contains the initial quantum fluctuation of the probes. We are not going to show it here.

Finally, for extracting the GW signal, we need to subtract the measurement results of the two interferometers. Suppose $\varphi_{\text{GW}i} = kx_{\text{GW}i}$ for a GW-induced optical phase modulation, then $\varphi_{\text{GW}1} - 2\varphi_{\text{GW}2} + \varphi_{\text{GW}3} \sim ka_{\text{GW}}T^2$, where $a_{\text{GW}} = \omega^2 h_{\text{GW}}L$ is the tidal acceleration (for a monochromatic gravitational wave with frequency ω and detector baseline length L) and T is the interrogation time. A more detailed calculation [6] showed that the full result (for a monochromatic GW wave with frequency ω and strain h_{GW}) is:

$$\varphi_{\text{GW}} \sim kh_{\text{GW}}L \sin^2\left(\frac{\omega T}{2}\right) \frac{\sin \omega L}{\omega} \sin \omega t, \quad (5.45)$$

in the limit of $\omega T \ll 1$ (which can be easily satisfied from low frequency GW), it reduces to the result here. For the noise part, it is easy to prove that the Eq. (5.41) and Eq. (5.42) are still the same in terms of the orders of magnitudes. It is interesting to note that, according to the general theory of linear quantum measurement, there exists a fundamental quantum limit which is the so-called quantum Cramer-Rao bound [46]. Eq. (5.42) is also the quantum Cramer-Rao bound of the atom interferometer since the signals directly couple to the optical fields (probes) in the TT gauge and the probes' fluctuations here are determined by their own initial quantum states.

5.5 Dynamics of the effective operators: A more exact treatment

The exact definition of the operators \hat{A}_A, \hat{A}_B etc, and the coupling strength χ in the effective Hamiltonian can be determined by using a field theory approach developed in the Apps. 5.8 and 5.9. This field theory approach is based on the following action:

$$S_{\text{int}} = g \int d^2x \phi_A(x) \phi_B(x) \phi_c(x) \phi_p(x), \quad (5.46)$$

where the coordinates x represents (t, z) . The relationship between g and the physical quantities describing the atom-light interaction such as the atom dipole moments, frequencies of different energy levels, etc. are given in the Appendix.

The corresponding equations of motion are given by:

$$(\partial_t + v_A \partial_z) \tilde{\phi}_A^+ = g_A \tilde{\phi}_B^+ \tilde{\phi}_p^+ \tilde{\phi}_c^-, \quad (5.47a)$$

$$(\partial_t + v_B \partial_z) \tilde{\phi}_B^+ = g_B \tilde{\phi}_A^+ \tilde{\phi}_p^- \tilde{\phi}_c^+, \quad (5.47b)$$

$$(\partial_t + \partial_z) \tilde{\phi}_c^+ = g_c \tilde{\phi}_A^- \tilde{\phi}_B^+ \tilde{\phi}_p^+, \quad (5.47c)$$

$$(\partial_t - \partial_z) \tilde{\phi}_p^+ = g_p \tilde{\phi}_A^+ \tilde{\phi}_B^- \tilde{\phi}_c^+. \quad (5.47d)$$

Here the $\tilde{\phi}_j^+$ ($j = A, B, c, p$) are the slowly varying amplitude field operators of the positive branch defined through $\hat{\phi}_j^+(x) = \tilde{\phi}_j^+(x)e^{-i\omega_{j0}(t-t_{j0})+ik_{j0}(z-z_{j0})}$, where ω_{j0} are the frequency of the free fields $\hat{\phi}_i$ and are related to the wave vector k_{j0} through $\omega_{j0}^2 = k_{j0}^2 + m_{j0}^2$ (for optical fields, the masses are zero). The $v_{A/B}$ is the WKB velocity of atom wave packet A/B and the two optical fields are propagating along the opposite directions. The coupling constants are defined as: $g_j = ig/(2\omega_{j0})$. The $\hat{\phi}_j^-$ is the corresponding negative branch field operators. As shown in detail in App. 5.10, the initial states of the mean optical fields can be treated as plane waves, and the initial states of the mean atom fields are zero and a Gaussian profile for the ϕ_B and ϕ_A , respectively. This Gaussian profile, in the spacetime-domain is given by:

$$\bar{\phi}_A = \frac{\bar{\alpha}_A \Delta_A^{1/2}}{(2\pi)^{1/4}} \exp \left[-\frac{\Delta_A^2}{4} [z - z_0 - v_a(t - t_0)]^2 \right], \quad (5.48)$$

where the $\bar{\alpha}_A$ is the coherent amplitude and the $1/\Delta_A$ is the width of the Gaussian profile.

5.5.1 Perturbative solution to the optical fields: Effective operator for atoms

Typically, in an interferometric process, the light-atom interaction time is very short compared to the free evolution time of the atom cloud, and the center-of-mass velocity of the atom cloud is very low, typically ~ 2 cm/s. Therefore to the leading order, we can treat the atom center-of-mass motion to be static during the interaction process, that is, $v_A \approx v_B \approx 0$. We also note that the spatial size of optical fields is much larger than the size of the atom cloud, therefore we can approximate the mean value of the optical fields to be almost constants during the interaction process. For this calculation, we only care about control field because it transfers noise to the next atom-light interaction kernel, while different kernels interact with different passive fields, as shown in Fig. 5.3.

These equations can be solved in a perturbative way. For the equation of motion of the control field, the formal solution of the first-order perturbation is given by:

$$\begin{aligned} \delta\phi_c^+(t+z, z) - \delta\phi_c^+(t-\epsilon, -\epsilon) = \\ g_c \int_{-\epsilon}^z dy \delta[\phi_A^-(t+y, y)\phi_B^+(t+y, y)\phi_p^+(t+y, y)], \end{aligned} \quad (5.49)$$

where the atom cloud mostly distributed in $[-\epsilon, \epsilon]$, as shown in Fig. 5.5 (we move the coordinate origin to the atom center-of-mass position). For brevity, we remove the tilde on the operators. In the following, all operators are the slowly varying

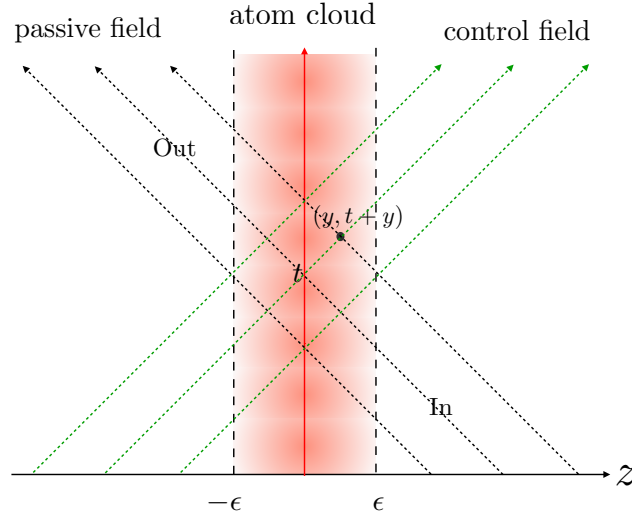


Figure 5.5: Atom-light interaction kernel. The atoms are undergoing the state swapping interaction, and during the very short interaction time (typically $\sim \mu\text{s}$), the A and B atoms do not have enough time to fly apart. Our effective atom operators Φ are defined through integration over the atomic cloud profile on the spatial direction. The discussion in the Section II will reduce the problem to be an effective model describing the interaction of the effective atom operators with the incoming light fields.

amplitude operators. Expanding the r.h.s. to the first order, we obtain:

$$\begin{aligned}
& g_c \int_{-\epsilon}^z dy \bar{\phi}_p^+ \bar{\phi}_B^+(t+y, y) \delta \phi_A^-(t+y, y) \\
& + g_c \int_{-\epsilon}^z dy \bar{\phi}_p^+ \bar{\phi}_A^-(t+y, y) \delta \phi_B^+(t+y, y) \\
& + g_c \int_{-\epsilon}^z dy \bar{\phi}_B^+(t+y, y) \bar{\phi}_A^-(t+y, y) \delta \phi_p^+(t+y, y).
\end{aligned} \tag{5.50}$$

The classical atomic fields can be written as (under the slow motion approximation):

$$\bar{\phi}_{A/B}^{+(-)}(t, y) = f_a(y) \bar{\alpha}_{A/B}^{(*)}(t), \tag{5.51}$$

where

$$f_a(y) = \frac{\Delta_a^{1/2}}{(2\pi)^{1/4}} \exp\left[-\frac{1}{4}\Delta_a^2 y^2\right]. \tag{5.52}$$

Since $y \in [-\epsilon, \epsilon]$ and $\epsilon \ll 1$, we can expand

$$\bar{\alpha}_{A/B}(t+y) \approx \bar{\alpha}_{A/B}(t) + y \dot{\bar{\alpha}}_{A/B}(t). \tag{5.53}$$

Note that $|y\dot{\bar{\alpha}}_{A/B}(t)| \sim \Omega y \bar{\alpha}_{B/A}(t)$ and $\Omega y \ll 1$, we can simplify the terms in Eq. (5.50) to be:

$$g_c \bar{\phi}_p^+ \left[\bar{\alpha}_B(t) \int_{-\epsilon}^z dy f_a(y) \delta\phi_A^-(t, y) + \bar{\alpha}_A^*(t) \int_{-\epsilon}^z f_a(y) \delta\phi_B^+(t, y) \right] + g_c \int_{-\epsilon}^z dy \bar{\alpha}_A^*(t) \bar{\alpha}_B(t) f_a^2(y) \delta\phi_p^+(t + y, y). \quad (5.54)$$

Now let us define the *effective atom operators* to be:

$$\delta\Phi_{A/B}^\pm(t) = \lim_{z \rightarrow \epsilon} \int_{-\epsilon}^z dy f_a(y) \delta\phi_{A/B}^\pm(t, y). \quad (5.55)$$

As we shall see later, these effective operators have a nice property that the commutation relation of the associated creation and annihilation operators normalizes to one. The physical interpretation of the effective operators is that it describes the whole wavepacket of the atom field. Using these effective operators, the input-output relation for a light ray passing through the atomic cloud can be written as (for the passive field, it can be calculated in the same way):

$$\begin{aligned} \delta\phi_{c\text{out}}^+(t) - \delta\phi_{c\text{in}}^+(t) &= g_c \bar{\phi}_p^+ [\bar{\alpha}_B(t) \delta\Phi_A^-(t) + \bar{\alpha}_A^*(t) \Phi_B^+(t)] \\ &\quad + g_c \bar{\alpha}_A^*(t) \bar{\alpha}_B(t) \int_{-\epsilon}^{\epsilon} dy f_a^2(y) \delta\phi_p^+(t + y, y), \\ \delta\phi_{p\text{out}}^+(t) - \delta\phi_{p\text{in}}^+(t) &= g_p \bar{\phi}_c^+ [\bar{\alpha}_B^*(t) \delta\Phi_A^+(t) + \bar{\alpha}_A(t) \Phi_B^-(t)] \\ &\quad + g_p \bar{\alpha}_A(t) \bar{\alpha}_B^*(t) \int_{-\epsilon}^{\epsilon} dy f_a^2(y) \delta\phi_p^+(t - y, y). \end{aligned} \quad (5.56)$$

The negative frequency branches simply obey the Hermitian conjugate of the above equations. The ratio between the second term and the first term on the r.h.s. of the equation is $\sim \sqrt{N_a/N_L} \ll 1$, therefore it can be safely ignored.

Furthermore, we introduce the creation and annihilation operators that correspond to those effective atom operators and also the optical operators. Remember that the operators here are related to the creation and annihilation operators as follows:

$$\delta\Phi_{A/B}^+ = \frac{\hat{A}_{A/B}(t)}{\sqrt{2\omega_a}}, \quad \delta\phi_{c/p\text{in}}^+ = \frac{\hat{a}_{c/p\text{in}}(z, t)}{\sqrt{2\omega_L}}, \quad (5.57)$$

where we take assumptions $\omega_{c0} \approx \omega_{p0} = \omega_L$ and note that $\bar{\Phi}_{A/B}^+ = \bar{\alpha}_{A/B}/(2\omega_a)$. Now we want to rewrite the equations of motion of the atom fields in a more concise way, using these creation and annihilation operators. First, let us check the dimension of the above defined creation and annihilation operators. We have

$$\hat{A}_{A/B}(t) = \int dz f_a(z) \hat{a}_{A/B}(z, t), \quad (5.58)$$

where $\hat{a}_{A/B}(z, t)$ has the standard commutation relation on one time slice t :

$$[\hat{a}_{A/B}(z, t), \hat{a}_{A/B}^\dagger(z', t)] = \delta(z - z'). \quad (5.59)$$

Using this commutation relation and the normalization condition for $f_a(z)$, it is straightforward to show that:

$$[\hat{A}_{A/B}(t), \hat{A}_{A/B}^\dagger(t)] = 1. \quad (5.60)$$

Note that \hat{A} is a dimensionless operator, while $\hat{a}_{\text{cin}}(z, t)$ has the dimension $[\text{Length}]^{-1/2}$. The gravitational wave community is more familiar with the operator satisfying $[\tilde{a}(t), \tilde{a}^\dagger(t')] = \delta(t - t')$, so it is important to note that this is an equal time commutation relation for propagating fields, and the operators here are related by $\tilde{a}_{\text{cin}}/\hat{a}_{\text{cin}} = c^{1/2}$ where c is the speed of light. In the following, we will use the \tilde{a} and replace the tilde with hat, i.e., $\tilde{a} \rightarrow \hat{a}$. Then Eqs. (5.56) can be translated to:

$$\begin{aligned} \hat{a}_{\text{cout}} - \hat{a}_{\text{ci}} &= i\chi_L e^{-i\varphi_p} [\bar{\alpha}_B(t)\hat{A}_A^\dagger + \bar{\alpha}_A^*(t)\hat{A}_B], \\ \hat{a}_{\text{pout}} - \hat{a}_{\text{pi}} &= i\chi_L e^{-i\varphi_c} [\bar{\alpha}_B^*(t)\hat{A}_A + \bar{\alpha}_A(t)\hat{A}_B^\dagger], \end{aligned} \quad (5.61)$$

where we have $\chi_L = |g_c| \bar{\phi}_L \sqrt{\omega_L/\omega_a}$ under the approximation that $\omega_c = \omega_p = \omega_L$ and $|\bar{\phi}_p^+| = |\bar{\phi}_c^+| = \bar{\phi}_L = \bar{a}_L/\sqrt{2\omega_L}$. Comparing this equation with Eq. (5.10), we know that the χ in the effective Hamiltonian has the form:

$$\chi \rightarrow -g/(2\omega_L) = g_c = g_p. \quad (5.62)$$

5.5.2 Deriving the evolution of atom fields using field theory

Using Eq. (5.55), we integrate the perturbation equations of atom fields to obtain the perturbation equations of *effective atomic operators*:

$$\begin{aligned} \partial_t \delta\Phi_A^+ + i\Omega e^{i\varphi} \delta\Phi_B^+ &= g_a \bar{\phi}_p^+ \int_{-\epsilon}^{\epsilon} dz f_a(z) \bar{\Phi}_B^+(t, z) \delta\phi_c^-(t, z) \\ &\quad + g_a \bar{\phi}_c^- \int_{-\epsilon}^{\epsilon} dz f_a(z) \bar{\Phi}_B^+(t, z) \delta\phi_p^+(t, z), \\ \partial_t \delta\Phi_B^+ + i\Omega e^{-i\varphi} \delta\Phi_A^+ &= g_a \bar{\phi}_p^- \int_{-\epsilon}^{\epsilon} dz f_a(z) \bar{\Phi}_A^+(t, z) \delta\phi_c^+(t, z) \\ &\quad + g_a \bar{\phi}_c^+ \int_{-\epsilon}^{\epsilon} dz f_a(z) \bar{\Phi}_A^+(t, z) \delta\phi_p^-(t, z). \end{aligned} \quad (5.63)$$

Now, we substitute the formal solution of $\delta\phi_{c/p}^\pm$ into the above equations, which will reveal the structure of the optical back-action on the atom fields.

Let us take the first term on the r.h.s. of the $\delta\Phi_A$ equation as an example. It has the following form after substituting $\delta\phi_c^-(t, z)$:

$$\begin{aligned} & g_a \bar{\phi}_p^+ \int_{-\epsilon}^{\epsilon} dz f_a(z) \bar{\Phi}_B^+(t, z) \delta\phi_c^-(t, z) \\ &= g_a \bar{\phi}_p^+ \alpha_B(t) \int_{-\epsilon}^{\epsilon} dz f_a^2(z) \left\{ \delta\phi_{\text{cin}}^-(t) + g_c \alpha_A(t) \alpha_B^*(t) \int_{-\epsilon}^z dy f_a^2(y) \delta\phi_p^-(y) \right. \\ & \quad \left. + g_c \bar{\phi}_p^- \int_{-\epsilon}^z dy f_a(y) [\alpha_A(t) \delta\phi_B^-(y, t) + \alpha_B^*(t) \delta\phi_A^+(y, t)] \right\}. \end{aligned} \quad (5.64)$$

Note that the $f_a(y)$ takes a Gaussian form symmetric around $y = 0$, which means that we can write:

$$\int_{-\epsilon}^{\epsilon} dz f_a^2(z) \int_{-\epsilon}^z dy f_a(y) \delta\phi_A^+(y, t) = \frac{1}{2} \delta\Phi_A^+(t), \quad (5.65)$$

where we have used the normalization condition for $f_a(z)$, and we have:

$$\begin{aligned} & g_a \bar{\phi}_p^+ \int_{-\epsilon}^{\epsilon} dz f_a(z) \bar{\Phi}_B^+(t, z) \delta\phi_c^-(t, z) \\ &= g_a \bar{\phi}_p^+ \alpha_B(t) \delta\phi_{\text{cin}}^-(t) + \frac{1}{2} |g_a g_c| |\bar{\phi}_p|^2 [\alpha_A(t) \alpha_B(t) \delta\Phi_B^-(t) + |\alpha_B(t)|^2 \delta\Phi_A^+(t)]. \end{aligned} \quad (5.66)$$

Here, we ignore the $\bar{\phi}_p^-$ term since it is much smaller than the other terms. In a similar way, we have:

$$\begin{aligned} & g_a \bar{\phi}_c^- \int_{-\epsilon}^{\epsilon} dz f_a(z) \bar{\Phi}_B^+(t, z) \delta\phi_p^+(t, z) \\ &= g_a \bar{\phi}_c^- \alpha_B(t) \delta\phi_{\text{pin}}^+(t) - \frac{1}{2} |g_a g_c| |\bar{\phi}_c|^2 [\alpha_A(t) \alpha_B(t) \delta\Phi_B^-(t) + |\alpha_B(t)|^2 \delta\Phi_A^+(t)]. \end{aligned} \quad (5.67)$$

Finally, we have the equations of motion for atom fields as:

$$\begin{aligned} \partial_t \delta\Phi_A^+ + i\Omega e^{i\varphi} \delta\Phi_B^+ &= g_a \bar{\phi}_L \alpha_B(t) [e^{-i\varphi_p} \delta\phi_{\text{cin}}^-(t) + e^{i\varphi_c} \delta\phi_{\text{pin}}^+(t)], \\ \partial_t \delta\Phi_B^+ + i\Omega e^{-i\varphi} \delta\Phi_A^+ &= g_a \bar{\phi}_L \alpha_A(t) [e^{i\varphi_p} \delta\phi_{\text{cin}}^+(t) + e^{-i\varphi_c} \delta\phi_{\text{pin}}^-(t)]. \end{aligned} \quad (5.68)$$

Then we can obtain the exact form of equations of motion for atom cloud:

$$\begin{aligned} \partial_t \hat{A}_A + i\Omega e^{i\varphi} \hat{A}_B &= i\chi_B(t) [e^{-i\varphi_p} \hat{a}_{\text{cin}}^\dagger(t) + e^{i\varphi_c} \hat{a}_{\text{pin}}(t)], \\ \partial_t \hat{A}_B + i\Omega e^{-i\varphi} \hat{A}_A &= i\chi_A(t) [e^{i\varphi_p} \hat{a}_{\text{cin}}(t) + e^{-i\varphi_c} \hat{a}_{\text{pin}}^\dagger(t)], \end{aligned} \quad (5.69)$$

where $\varphi = \varphi_c - \varphi_p$ is the phase difference between control and passive lights, and

$$\chi_{A/B}(t) = \sqrt{\frac{\omega_a}{c\omega_L}} |g_a| \bar{\phi}_L \alpha_{A/B}(t). \quad (5.70)$$

The $\alpha_{\pm}(t) = \alpha_{\pm}(0) \exp[\mp\Omega t]$ and $\chi_0 := \sqrt{\omega_a/c\omega_L} |g_a| \bar{\phi}_L$. Using the relation Eq. (5.62), we can also map Eq. (5.69) to Eq. (5.7).

5.6 Conceptual comparison with the laser interferometer GW detector

Now we can make some comparison between Laser Interferometer GW detector and atom interferometer detector from several different aspects:

- **Discrete or Continuous.** — LIGO is a detector where the optical field continuously monitors the position of the test masses, recording the continuous waveform of the gravitational wave. The continuity of such a measurement is the reason for the existence of SQL. However, the atom interferometer works differently, in a somewhat discretized way. Basically, each interrogation process records one data point of the waveform time-series, and the measurements of different data points are mutually independent. To record the waveform of the GWs, the interrogation process needs to be repeated many times. For each data point, the measurement is continuous, with the time scale equal to the interrogation time scale of the matter-wave interferometry. Therefore, the quantum limit discussed here is the limitations to the data point recorded by each individual interrogation process.

- **Measurement quantity.** — Gravitational wave information is carried in the curvature perturbation $\Psi \sim \ddot{h}$, which corresponds to the acceleration of the test masses. For LIGO, we have the equation of motion for the test masses as $m\ddot{x} \sim m\Psi \sim mL\ddot{h}$, where m and L are effective mass of the test masses motion and the baseline length of the interferometer, respectively. The light field will directly carry the information of test mass displacement, and thus the interferometer is a displacement sensor. However, for an atom interferometer, each interrogation process directly records the acceleration as shown in Eq. (5.44), therefore, an atom interferometer is an acceleration sensor.

- **Test mass quantization.** — As we have shown in Eq. (5.1), test mass quantization will generally have an impact on the measurement result. LIGO's measurement result will be in principle affected by the test mass quantization if we directly apply Eq. (5.1). However, if we do the post-data processing to extract the curvature perturbation (acceleration) information, we are targeted on $x(2\Delta t) - 2x(\Delta t) + x(0)$. Using the free mass evolution equation $\hat{x}(t) = Lh(t) + \hat{p}_0 t/m + \hat{x}_0$, it is easy to prove that all the information about the initial test mass quantum state will be eliminated when we extract the acceleration information. This important result has been obtained by Braginsky et al. [45] The key for the elimination of test mass quantization effect is the fact that the differential motion of the test masses of the two arms is a single degree of freedom during the entire detection process. However, for atom interferometer (Dimopulous configuration), four different pairs of laser

beams are needed to complete one interrogation period and they belong to different degrees of freedom. Therefore, the probe quantization effect can not be removed in the same way as LIGO, that is why we need to consider the quantum fluctuation of light field (or the probe in a more general sense) in discussing the sensitivity of the atom interferometer.

• **Back-action.** — In LIGO, the back-action is contributed by the radiation pressure force acting on the test mass. In the atom interferometer, the back-action comes from the atom noise carried by the control fields linking two atom interferometers. In LIGO, the back-action can not only be a noise source, but also can change the dynamical behavior of the system in certain parameter regions. For example, if the resonant frequency of the interferometer does not match the carrier laser frequency, which can be done through tuning the signal recycling cavity, the dynamics of the test mass and optical field will change and create an optical rigidity for the test mass. In atom interferometer, the state transition dynamics (Rabi rate) of the atom cloud can also be changed by the interaction between optical and atomic fields, if there is an intensity unbalance between the control and passive fields, as we have shown in detail in Section 5.2.1 and Section 5.5.2.

The above discussion qualitatively compares the physics of atom-interferometer GW detector with the LIGO detector. It is also worth to comment the similarity between atom-interferometer GW detector with the LISA detector. Unlike the Michelson-type LIGO detector, the LISA detector is actually a transponder system where pairs of test masses are connected by optical links and the optical phase changes due to the gravitational waves are recorded with local interferometry setups around each test mass. Atom interferometers also match with this picture, where two atom clouds are connected by an optical link and the phase change of this optical link is recorded. In LISA, only the optical sensing noise is worthy of consideration and the quantum back-action is extremely weak since the optical power received on each satellite is of picowatts. Zero-point fluctuation of the test masses on LISA can be eliminated since it is also a displacement sensor. For a detailed study for the comparison between atom-interferometer GW detector with LISA detector, see Refs. [10, 47].

5.7 Discussion

In this chapter, the matter-wave interferometry, in particular the example of a one-dimensional model of atom interferometer, is carefully added onto the jigsaw

puzzle of the linear quantum measurement theory. Previous studies on the atom interferometry [7, 48], although quite complete and careful, mostly worked in the Schrödinger picture and did not speak in the language of quantum measurement theory. Establishing such a theory for matter-wave interferometry can help the LIGO community clearly understand the physics of atom-interferometer GW detectors. Our result demonstrates in detail how the light-atom interaction affects the dynamical and noise behavior of the atom clouds and gives the input-output relation for the linear response of this device. Concretely, we clarify how the concepts of detector shot noise, probe's zero-point fluctuation, back-action noise, and dynamical back-action manifest themselves in the atom interferometry. Similar to LIGO case, we also obtain the formula for the Standard Quantum Limit in the atom interferometry.

The configuration raised by Dimopoulos *et al.* is the most original one proposed for detecting GWs. Other configurations were also raised [9, 11, 37], in particular, the so called single-photon atom interferometer, where the interferometric process happens via transition of Rabi oscillation of two-level atoms rather than Raman transition [9]. The advantage of this configuration is that the optical noise (zero-point fluctuations of probe) can be removed in the ideal one-dimensional case through common mode rejection. In order to increase the fringe visibility of the atom interferometer, the distinguishability of the atom cloud trajectory should be increased which means we need a larger momentum transfer [33–35]. The formalism developed in this paper can be extended to these configurations also. Moreover, the concept of optical-cavity-assisted atom interferometry was also discussed and experimentally tested [36, 37]; using our formalism to study these configurations will be a future work.

The analysis in this work is targeted on revealing the physical principle. Therefore we focus on the simplest case where we ignore the classical noise sources and optical losses that would more seriously affect the sensitivity of atom interferometry. One typical example is: The back-action noise carried by the control fields that propagate from one interferometer to the other will not contribute to the sensitivity in the current design of atom-interferometer GW detector. The reasons are the following: (1) The real three-dimensional atom-light interactions happen in a point-scattering way that the cross-sectional area of the light field is much larger than that of the atom field. Therefore such a scattering itself is very lossy thereby noisy. (2) For detecting GWs, these two interferometers must be separated in a relatively large distance so that the atom clouds of the second interferometer will only interact with

a small patch of the large wavefront propagated from the first interferometer. The diffraction loss will erase most of the information of the atom cloud of the first interferometer carried by the light field. Here, we want to emphasize that the loss of back-action noise here does not imply that the current atom-interferometer designs are perfect, quite contrary, it implies that current designs are too lossy to have the back-action issue. It is probably insightful to study the method to mitigate these issues in the future. General understanding tells us that the capability of any type of interferometric experimental platform is determined by the coherence of every physical step in the device, and the goal for reaching a better sensitivity is practically realized by mitigating all the issues that decohere the waves in the interferometer. To mitigate the first issue mentioned above, we have to design the system so that we have a mode-matched atom-light interaction and thereby a more coherent scattering of light by atom cloud, which is very difficult under the current technology; while to mitigate the second issue, one way is to place the two atom interferometers in some optical-cavity-assisted structures. This idea has been proposed for the MIGA (Matter-wave laser Interferometric Gravitation Antenna) project [37]. Analyzing the quantum noise for such a device will be a future extension of this work.

5.8 Appendix: Field formalism for atom interferometer

Usually, the light-atom interaction happens in a Λ -level system with lower energy levels $|1\rangle, |2\rangle$ which are the hyperfine structures and a higher energy level $|3\rangle$, as shown in Fig. 5.2. The atomic system is interacting with optical field which is off-resonant with respect to the energy gap of $|1\rangle - |3\rangle$ and $|2\rangle - |3\rangle$. The dynamics of this system can be reduced to an effective $|1\rangle - |2\rangle$ dynamics by adiabatically eliminating the energy level $|3\rangle$. Moreover, the atom states $|1\rangle$ and $|2\rangle$ are also associated with different linear center-of-mass momentum. The non-relativistic Hamiltonian of such a system, in a single-particle formalism, can be written as:

$$\hat{H} = -\frac{\nabla_i^2}{2m} + \sum_i \hbar\omega_i |i\rangle\langle i| + E_c(x)d_{13}|1\rangle\langle 3| + E_p(x)d_{23}|2\rangle\langle 3| + \text{h.c.}, \quad (5.71)$$

where m is the inertia mass of the atom with center-of-mass momentum $p_i = -i\hbar\nabla_i$, ω_i corresponds to the energy of the internal electron state and d_{ij} describes the dipole moment of the electron and it is convenient to define them as real numbers. The summation is over all three energy levels. Since the $|1\rangle - |2\rangle$ transition is forbidden, therefore $d_{12} = 0$. For extension to the multi-particle system and furthermore establishing a field-theoretic approach, we need to do *second quantization* [49].

5.8.1 Free fields

For doing second quantization, we need to first distinguish the group of non-interacting identical particles, or equivalently, free theory. Tracing out the internal energy levels for the non-interaction single particle Hamiltonian, we have:

$$\hat{H}_i = \hbar\omega_i - \frac{\nabla_i^2}{2m}, \quad (5.72)$$

Assuming that there are N - identical particles in group i , we have a multi-particle Hamiltonian as:

$$\hat{\mathcal{H}}_i = \sum_a^N \left[\hbar\omega_i - \frac{\nabla_{ai}^2}{2m} \right], \quad (5.73)$$

where a is the index of particles, and ∇_{ai} only act on the coordinate of a -th particle belong to group i .

Following the standard method of doing second quantization, and choosing the orthonormal eigenfunctions of particles to be their momentum eigenstates, we have:

$$\hat{\mathcal{H}}_i = \int \frac{d^3p}{(2\pi)^3} \left(\hbar\omega_i + m + \frac{p^2}{2m} \right) \hat{a}_p^\dagger \hat{a}_p, \quad (5.74)$$

where the rest mass term is also included here. Apparently, this is a non-relativistic Hamiltonian. The full relativistic form is:

$$\hat{\mathcal{H}}_i = \int \frac{d^3p}{(2\pi)^3} \left(\sqrt{m_i^2 + p^2} \right) \hat{a}_p^\dagger \hat{a}_p, \quad (5.75)$$

where $m_i = m + \hbar\omega_i$ with the physical meaning that the internal electron-nuclei interaction energy also contributes to the ‘‘rest mass’’ of the atom. It is clear that such a Hamiltonian can be derived from a canonically quantized Klein-Gordon field with the action:

$$S_i = \int d^4x \left(\frac{1}{2} \partial_\mu \phi_i \partial^\mu \phi_i + m_i^2 \phi_i^2 \right). \quad (5.76)$$

Since we are now discussing a one-dimensional mode of atom interferometers, we will apply the para-axial approximation in order to reduce the above 3+1 action to a 1+1 action by integrating out the transversal components.

The relationship between 1+1 fields and the 3+1 fields is given as follows. The plane wave expansion of the fields is:

$$\phi_{3+1}(x) = \int \frac{dk_z}{(2\pi)(2\omega)} e^{-i\omega t + ik_z z} \int \frac{d^2k_\perp}{(2\pi)^2} e^{i\vec{k}_\perp \cdot \vec{x}_\perp} \hat{a}_k + c.c. \quad (5.77)$$

We thus have the dimensional relation: $[a_k] = [m]^{3/2} [\text{Hz}]^{1/2}$. While for 1+1 fields, we have:

$$\phi_{1+1}(x) = \int \frac{dk_z}{(2\pi)(2\omega)} e^{-i\omega t + ik_z z} a_{k_z} + c.c., \quad (5.78)$$

where $[a_{k_z}] = [m]^{1/2} [\text{Hz}]^{1/2}$. Denoting the cross-sectional area of field beams as A , we then integrate out the transversal components and define:

$$a_{k_z} \equiv \int \frac{d^2 k_{\perp}}{(2\pi)^2} a_k e^{i\vec{k}_{\perp} \vec{x}_{\perp}} \sqrt{A}, \quad (5.79)$$

so that

$$\begin{aligned} \phi_{3+1}(x) &= \int \frac{dk_z}{(2\pi)(2\omega)\sqrt{A}} e^{-i\omega t + ik_z z} a_{k_z} + c.c. \\ &= \frac{1}{\sqrt{A}} \phi_{1+1}(x). \end{aligned} \quad (5.80)$$

The 3+1 form for electromagnetic field can be written as:

$$\hat{E}_{c/p} = \int \frac{d^3 k}{(2\pi)^3} \sqrt{\frac{\hbar\omega_k}{\epsilon_0}} \hat{a}_k^{c/p} e^{-i(\omega_k t - kx)} + \text{h.c.}, \quad (5.81)$$

and following the same approach, one can show that it can be effectively described by a 1+1 scalar field under paraxial approximation:

$$E_{c/p}(z, t) = \sqrt{2\omega_{c/p}} \sqrt{\frac{\hbar\omega_{c/p}}{\epsilon_0 A}} \phi_{c/p}(z, t). \quad (5.82)$$

5.8.2 Interacting fields

In a similar way, we can do second quantization to the interaction Hamiltonian as follows:

$$\hat{H}_{p'p}^{ij} = \int d^3 x_a \psi_{p'}^*(x_a) e^{iE_{p'}^j t} \hat{E}_{c/p}(x_a) d_{ij} \psi_p(x_a) e^{-iE_p^i t}, \quad (5.83)$$

where $E_p^i = m_i + p^2/(2m_i)$, and $\psi_p(x_a)$ is the momentum eigenfunctions of atoms in the coordinate representation. Using box normalization condition, we have $\psi_p(x_a) = \exp(-i\vec{p}\vec{x}_a)/\sqrt{V_a}$. Substituting the second quantization form of the electromagnetic field:

$$\hat{E}_{c/p} = \int \frac{d^3 k}{(2\pi)^3} \sqrt{\frac{\hbar\omega_k}{\epsilon_0}} \hat{a}_k^{c/p} e^{-i(\omega_k t - kx)} + \text{h.c.}, \quad (5.84)$$

leads to:

$$\begin{aligned} \hat{H}_{p'p}^{ij} &= d_{ij} \hat{a}_{p'}^{j\dagger} \hat{a}_p^i \int \frac{d^3 x_a d^3 k}{(2\pi)^3} \psi_{p'}^*(x_a) \psi_p(x_a) e^{-ikz_a} e^{i(E_{p'} - E_p - \omega_k)t} \hat{a}_k^{c/p} \\ &+ (\hat{a}_k \rightarrow \hat{a}_k^\dagger, k \rightarrow -k, \omega \rightarrow -\omega) + \text{h.c.} \end{aligned} \quad (5.85)$$

Performing the integral on x_a , we have:

$$\hat{H}_{p'p}^{ij} = \sqrt{\frac{\hbar\omega_0}{\epsilon_0 V_a^2}} \frac{d_{ij}}{(2\pi)^3} e^{i(E_{p'}^j - E_p^i - \omega_{p'-p})t} \hat{a}_{p'}^{j\dagger} \hat{a}_p^i \hat{a}_{p-p'}^{c/p}, \quad (5.86)$$

+ (non rotating wave terms) + h.c..

The energy difference in the exponential can be written as:

$$m_i + \frac{p^2}{2m_i} + \omega_{c/p} - \left(m_j + \frac{(p+k_c)^2}{2m_j} \right), \quad (5.87)$$

which clearly describes the energy transfer of the photon-absorption process. In practice, the non rotating-wave terms can be safely ignored. The total interaction Hamiltonian will be:

$$H = \sum_{p,p'} H_{p,p'}, \quad (5.88)$$

where p, p' are discretized momenta. In the continuous case, we have:

$$H = \int \frac{d^3 p}{(2\pi)^3} \frac{d^3 p'}{(2\pi)^3} \sqrt{\frac{\hbar\omega_0}{\epsilon_0}} \frac{d_{ij}}{(2\pi)^3} \hat{a}_{p'}^{j\dagger} \hat{a}_p^i \hat{a}_{p-p'}^{c/p} e^{i(E_{p'}^j - E_p^i - \omega_{p'-p})t} + \text{h.c.}, \quad (5.89)$$

where for the atomic operators: $\hat{a}_p \rightarrow \sqrt{V_a} \hat{a}_p$ (note that the dimension changes correspondingly).

This Hamiltonian can be derived from the following interaction action:

$$S_{\text{int}}^{\text{full}} = g \int d^4 x \phi_A(x) \phi_3(x) \phi_{c/p}(x), \quad (5.90)$$

where:

$$g = \sqrt{\frac{\hbar\omega_0}{\epsilon_0}} \frac{d_{ij}}{(2\pi)^9} (2\omega_A)^{1/2} (2\omega_c)^{1/2} (2\omega_{c/p})^{1/2}. \quad (5.91)$$

Reducing it to 1+1 D case, the g will change as:

$$g = \sqrt{\frac{\hbar\omega_0}{\epsilon_0 A}} \frac{d_{ij}}{(2\pi)^9} (2\omega_A)^{1/2} (2\omega_c)^{1/2} (2\omega_{c/p})^{1/2}, \quad (5.92)$$

and we have an 1+1 interaction action:

$$S = g_{13} \int dz dt \phi_A \phi_3 \phi_c + g_{23} \int dz dt \phi_B \phi_3 \phi_p. \quad (5.93)$$

5.8.3 Effective interaction

The above full interaction Hamiltonian can be further reduced to an effective Hamiltonian describing the transition between energy levels $|1\rangle - |2\rangle$ by integrating out the $\phi_3(x)$ field, which can be done by solving the Heisenberg equation of motions for the field $\hat{\phi}_3(x)$ (under canonical quantization).

The Heisenberg equation of motion for $\hat{\phi}_3(x)$ corresponds to the above action is:

$$(\square + m_3^2)\hat{\phi}_3 = g_{13}\hat{\phi}_A\hat{\phi}_c + g_{23}\hat{\phi}_B\hat{\phi}_p. \quad (5.94)$$

Written in the rotating frame of ω_{30} and k_{30} (they are the Compton frequency and Compton wave vector for the atoms on level $|3\rangle$), we have:

$$\hat{\phi}_3(x) = \tilde{\phi}_3(x)e^{-i\omega_{30}t + ik_{30}z} + \text{h.c.}, \quad (5.95)$$

and the equations of motion for $\tilde{\phi}_3$ is given approximately by:

$$(\partial_t + v\partial_z)\tilde{\phi}_3(x) = \frac{ig_{13}}{2\omega_{30}}\tilde{\phi}_c\tilde{\phi}_Ae^{i\Delta\omega_{3A}t - i\Delta k_{3A}z} + \frac{ig_{23}}{2\omega_{30}}\tilde{\phi}_p\tilde{\phi}_Be^{i\Delta\omega_{3B}t - i\Delta k_{3B}z}, \quad (5.96)$$

where we have already ignored the non-rotating-wave terms, which oscillates at frequencies $\omega_{30} \pm \omega_{c/p0} \mp \omega_{A/B0}$ or $\omega_{30} + \omega_{c/p0} + \omega_{A/B0}$. The $\Delta\omega_{3A/B}$, $\Delta k_{3A/B}$ are defined as:

$$\begin{aligned} \Delta\omega_{3A/B} &= \omega_{30} - \omega_{c/p} - \omega_{A/B0} \approx \omega_{3A/3B} - \omega_{c/p0} + v_{A/B}(k_{30} - k_{A/B0}), \\ \Delta k_{3A/B} &= k_{30} - k_{c/p} - k_{A/B0}, \end{aligned} \quad (5.97)$$

where $\omega_{3A/B}$ are the energy level difference between $|3\rangle$ and $|1\rangle, |2\rangle$. In ideal case, we assume that the phase matching is satisfied $\Delta k_{3A/B} = 0$. We also define $\Delta\omega_0 := \omega_{3A} - \omega_c = \omega_{3B} - \omega_p$ and if we further choose $\tilde{\phi}_3$ to work in the rotating frame of $\Delta\omega_0$, the equation becomes:

$$\Delta\omega_0\bar{\phi}_3(x) + (\partial_t + v\partial_z)\bar{\phi}_3(x) = \frac{g_{13}}{2\omega_{30}}\tilde{\phi}_c\tilde{\phi}_Ae^{iv_Ak_c t} + \frac{g_{23}}{2\omega_{30}}\tilde{\phi}_p\tilde{\phi}_Be^{iv_Bk_p t}. \quad (5.98)$$

Under the adiabatic approximation that the typical time scale of varying $\bar{\phi}_3(x)$ is much smaller than $1/\Delta\omega_0$, the dynamics of $\bar{\phi}_3(x)$ is solved by the right-hand side of the equation above:

$$\bar{\phi}_3(x) \approx \frac{g_{13}}{2\Delta\omega_0\omega_{30}}\tilde{\phi}_c\tilde{\phi}_Ae^{iv_Ak_c t} + \frac{g_{23}}{2\Delta\omega_0\omega_{30}}\tilde{\phi}_p\tilde{\phi}_Be^{iv_Bk_p t}, \quad (5.99)$$

while the positive frequency branch of $\hat{\phi}_3(x)$ can be recovered by changing to the original frame: $\bar{\phi}_3(x)\exp[i\Delta\omega_0 t - i\omega_{30} t + ik_{30}z]$. Substituting $\hat{\phi}_3(x)$ back into the

interaction Hamiltonian Eq. (5.93), we have:

$$\begin{aligned}
\hat{\mathcal{H}}_{\text{int}} &= \hat{\mathcal{H}}_{\text{int}}^{\text{Stark}} + \hat{\mathcal{H}}_{\text{int}}^{\text{AB}}, \quad \text{with} \\
\hat{\mathcal{H}}_{\text{int}}^{\text{Stark}} &= \frac{g_{13}^2}{2\Delta\omega_0\omega_{30}} \int dz \hat{\phi}_A(x) \hat{\phi}_c(x) \hat{\phi}_c(x) \hat{\phi}_A(x) \\
&\quad + \frac{g_{23}^2}{2\Delta\omega_0\omega_{30}} \int dz \hat{\phi}_B(x) \hat{\phi}_p(x) \hat{\phi}_p(x) \hat{\phi}_B(x), \\
\hat{\mathcal{H}}_{\text{int}}^{\text{Raman}} &= 2 \times \frac{g_{13}g_{23}}{2\Delta\omega_0\omega_{30}} \int dz \hat{\phi}_A(x) \hat{\phi}_c(x) \hat{\phi}_p(x) \hat{\phi}_B(x).
\end{aligned} \tag{5.100}$$

Here, the $\hat{\mathcal{H}}_{\text{int}}^{\text{Stark}}$ corresponds to the AC Stark shift of the mass of the atom fields, which is typically very small compared to the internal energy and rest mass thereby negligible². The $\hat{\mathcal{H}}_{\text{int}}^{\text{Raman}}$ term is the one we are interested in, i.e., describing the Raman transition between $|1\rangle$ and $|2\rangle$ induced by control and passive fields. This term can also correspond to an effective four-scalar field interaction action:

$$S_{\text{int}} = g \int d^2x \phi_A(x) \phi_B(x) \phi_c(x) \phi_p(x), \tag{5.101}$$

where g represents the coupling coefficient in $\hat{\mathcal{H}}_{\text{int}}^{\text{Raman}}$.

5.9 Appendix: Field quantization

5.9.1 Definition of field operators

As discussed above, The one-dimensional light-atom interaction model can be described by the following interaction action as:

$$S_{\text{int}} = g \int d^2x \phi_A(x) \phi_B(x) \phi_c(x) \phi_p(x), \tag{5.102}$$

where $x = (t, z)$. These free scalar fields, after *canonical quantization* can be expanded as:

$$\hat{\phi}_j^{(0)}(x) = \int \frac{dk_j}{2\pi 2\omega_j} \left[\hat{a}(k_j) e^{-i\omega_j(t-t_{j0}) + ik_j(z-z_{j0})} + \text{h.c.} \right], \tag{5.103}$$

where the $\hat{a}(k_j)$ is an annihilation operator which is covariant under Lorentz transformation and $j = A, B, c, p$. The ω_j and k_j are related by dispersion relation $\omega_j^2 = k_j^2 + m_j^2$, while for optical fields $m_j = 0$. The t_{j0}, z_{j0} determine the phase reference point.

²The mass correction due to AC Stark shift is position-dependent here, which is not surprising since the light-atom interaction happens in a local region of space-time.

When we introduce the interaction, the Heisenberg operators will be modified, according to:

$$\hat{O}(t, z) = \hat{U}_I^\dagger(-\infty, t) \hat{O}^{(0)}(t, z) \hat{U}_I(-\infty, 0), \quad (5.104)$$

where $\hat{O}^{(0)}(t, z)$ and $\hat{O}(t, z)$ are the operators whose evolution are governed by the free and full Hamiltonian, respectively. The $\hat{U}_I(t_1, t_2)$ is the evolution operator in the interaction picture. Therefore, in the interaction case, one can have a full field operator given by:

$$\hat{\phi}_j(x) = \int \frac{dk_j}{2\pi 2\omega_j} [\hat{A}(k_j, t) e^{-i\omega_j(t-t_{j0}) + ik_j(z-z_{j0})} + \text{h.c.}], \quad (5.105)$$

where $\hat{A}(k_j, t) = \hat{U}_I^\dagger(0, t) \hat{A}(k_j, 0) \hat{U}_I(0, t)$.

Since all these fields have a WKB trajectory in real experiment, they can take a scale-separated form as:

$$\hat{\phi}_j(x) = \tilde{\phi}_j(x) e^{-i\omega_{j0}(t-t_{j0}) + ik_{j0}(z-z_{j0})} + \text{h.c.}, \quad (5.106)$$

where the exponents describe the fast-oscillating part of the field and the tilde operators describe the slowly varying amplitudes. Using the above definition, one can obtain the relation between the \hat{A} and $\tilde{\phi}$ operators as:

$$\tilde{\phi}_j(t, z) = \int \frac{dk_A}{2\pi 2\omega_j} [\hat{A}(t, k_j) e^{-i(\omega_j - \omega_{j0})(t-t_{j0}) + i(k_j - k_{j0})(z-z_{j0})} + \text{h.c.}]. \quad (5.107)$$

Also note that the transformation $\hat{U}(0, t)$, as an unitary transformation, will not affect the commutation relation, therefore we have:

$$[\hat{A}_j(t, k), \hat{A}_j^\dagger(t, k')] = 2\omega_j \delta(k - k'). \quad (5.108)$$

It is worth noting that in the spatial domain, the \hat{A} and the $\tilde{\phi}$ is related by (take A-field as an example):

$$\tilde{\phi}^{(+)}(x) = \hat{A}(t, z - z_A^t) / (2\omega_{A0}), \quad (5.109)$$

where $z - z_A^t$ ($z_A^t = z_A(t_0) + v_A(t - t_0)$) comes from the propagation and the first t -argument comes from the perturbation due to the 4-scalar interaction.

5.9.2 Quantum states of fields

In the experimental setup, the control/passive field can be well approximated to have a rectangular profile, and the state of, e.g., the control field is given by:

$$|\psi_c\rangle = \exp \left[\int \frac{dk_c}{2\omega_c} \left(\alpha_c(k_c) \hat{a}_c^\dagger(k_c) - \text{h.c.} \right) \right] |0\rangle_c, \quad (5.110)$$

where

$$\alpha_c(k_c) = \bar{\alpha}_c \frac{\sin \pi a \delta k}{\sqrt{a} \pi \delta k}, \quad \delta k = k_c - k_{c0}, \quad (5.111)$$

and $2\pi a$ is the width of this rectangular wave and $\bar{\alpha}_c$ is the coherent amplitude.

It is easy to show the ϕ waveform:

$$\begin{aligned} \bar{\phi}^{(+)} &= \int \frac{dk}{2\pi} \left(\frac{1}{2\omega} \right) \bar{\alpha}_c \frac{\sin \pi a \delta k}{\sqrt{a} \pi \delta k} e^{i(k_0 + \delta k)(x - t - x_0 + t_0)} \\ &\approx \frac{\bar{\alpha}_c}{2\omega_0} \text{Rect}_a [x - t - x_0 + t_0] e^{ik_0(x - t - x_0 + t_0)}. \end{aligned} \quad (5.112)$$

Since the typical atom width is much smaller than the light pulse width, it can be approximated as almost a plane wave in the atom-light interaction region by $\lim_{a \rightarrow \infty} a \text{sinc}(\pi a x) = \delta(x)$.

The initial state of atomic cloud is a Gaussian profile, given as:

$$|\psi_A\rangle = \exp \left[\int \frac{dk_A}{2\omega_A} \left(\alpha_A(k_A) \hat{a}_A^\dagger(k_A) - \text{h.c.} \right) \right] |0\rangle_A, \quad (5.113)$$

with

$$\alpha_A(k_A) = \frac{\bar{\alpha}_A}{(2\pi)^{1/4} \Delta_A^{1/2}} \exp \left[-\frac{(k_A - k_{A0})^2}{4\Delta_A^2} \right], \quad (5.114)$$

while the B -field is a vacuum initially. Here the $\bar{\alpha}_A$ is the atom coherent amplitude, Δ_A is its width in the k -domain.

5.9.3 Equations of motion: Structures

Following the standard canonical quantization scheme, we have the Heisenberg equations of motion for the atomic and optical field as:

$$\begin{aligned} (\square + m_A^2) \hat{\phi}_A &= g \hat{\phi}_B \hat{\phi}_c \hat{\phi}_p, & \square \hat{\phi}_c &= g \hat{\phi}_A \hat{\phi}_B \hat{\phi}_p \\ (\square + m_B^2) \hat{\phi}_B &= g \hat{\phi}_A \hat{\phi}_c \hat{\phi}_p, & \square \hat{\phi}_p &= g \hat{\phi}_A \hat{\phi}_B \hat{\phi}_c, \end{aligned} \quad (5.115)$$

where $\square = \partial_t^2 - \nabla^2$ (in 1-dimensional case here, $\square = \partial_t^2 - \partial_z^2$). These equations have the same form as their classical counterparts, this is because different $\hat{\phi}_j$ belongs to different Hilbert space and their operators are commute with each other. Substituting Eq. (5.106), we have the approximated equations for the slowly varying operator's positive frequency part (we take $c = 1$ and their Hermitian conjugates are ignored

for brevity):

$$\begin{aligned}
(\partial_t + v_A \partial_z) \tilde{\phi}_A^+ &= g_A \tilde{\phi}_B^+ \tilde{\phi}_p^+ \tilde{\phi}_c^-, \\
(\partial_t + v_B \partial_z) \tilde{\phi}_B^+ &= g_B \tilde{\phi}_A^+ \tilde{\phi}_p^- \tilde{\phi}_c^+, \\
(\partial_t + \partial_z) \tilde{\phi}_c^+ &= g_c \tilde{\phi}_A^- \tilde{\phi}_B^+ \tilde{\phi}_p^-, \\
(\partial_t - \partial_z) \tilde{\phi}_p^+ &= g_p \tilde{\phi}_A^+ \tilde{\phi}_B^- \tilde{\phi}_c^+.
\end{aligned} \tag{5.116}$$

Here, $v_{A/B}$ the WKB velocity of atom wave packet A/B and the two optical fields are propagating along the opposite directions. The coupling constants are defined as: $g_j = ig/(2\omega_{j0})$, where $j = A, B, c, p$. In deriving the above equations of motion, we take the leading non-relativistic approximation so that $v_{A/B} \approx k_{A/B}/m_{A/B}$ and we also use the rotating wave approximation, namely, we only keep those terms satisfying:

$$k_{p0} - k_{c0} = k_{A0} - k_{B0}, \quad \omega_{c0} - \omega_{p0} = \omega_{B0} - \omega_{A0}. \tag{5.117}$$

These conditions, under non-relativistic approximation and $m_B \approx m_A$, have the clear physical meaning of relativistic Doppler effect:

$$\omega_{c0} - \omega_{p0} \approx v(k_{A0} - k_{B0}), \tag{5.118}$$

where $v \approx v_A \approx v_B$ is the approximate speed of atom. The Hermitian conjugation of these equations can also be easily obtained. In the following, we are going to solve these equation in a perturbative way.

5.10 Appendix: Mean field solutions

Typically, in an interferometric process, the light-atom interaction time is very short compared to the free evolution time of the atom cloud, and the center-of-mass velocity of the atom cloud is very low, typically ~ 2 cm/s. Therefore to the leading order, we can treat the atom's center-of-mass motion to be static during the interaction process, that is, $v_A \approx v_B \approx 0$. We also note that the spatial size of optical fields are much larger than the size of the atom cloud, therefore we can approximate the mean value of the optical fields to be almost constants during the interaction process.

The zeroth-order of the equations of motion is simple:

$$\begin{aligned}
\partial_t \bar{\phi}_A^+ &= (g_A \bar{\phi}_p^+ \bar{\phi}_c^-) \bar{\phi}_B^+, & (\partial_t + \partial_z) \bar{\phi}_c^+ &= 0, \\
\partial_t \bar{\phi}_B^+ &= (g_B \bar{\phi}_p^- \bar{\phi}_c^+) \bar{\phi}_A^+, & (\partial_t - \partial_z) \bar{\phi}_p^+ &= 0.
\end{aligned} \tag{5.119}$$

We ignore the r.h.s. of the equation for the optical field because the photon number is much larger than the atom number. Since $\bar{\phi}_p$ and $\bar{\phi}_c$ are almost constant, therefore

we can rewrite the zeroth-order atom equations to be:

$$\partial_t \bar{\phi}_A^+ = -i\Omega e^{i\varphi_{pc}} \bar{\phi}_B^+, \quad \partial_t \bar{\phi}_B^+ = -i\Omega e^{-i\varphi_{pc}} \bar{\phi}_A^+, \quad (5.120)$$

where φ_{pc} is the phase difference between the control field and passive field, Ω is the Ramsey frequency. Here, we make use of the approximation $g_A = g_B := g_a$ thereby $\Omega = |g_a \bar{\phi}_p \bar{\phi}_c|$. The full solution of this equation is:

$$\begin{aligned} \bar{\phi}_A^+(t) &= \bar{\phi}_A^+(0) \cos \Omega t - i \bar{\phi}_B^+(0) e^{i\varphi_{cp}} \sin \Omega t, \\ \bar{\phi}_B^+(t) &= \bar{\phi}_B^+(0) \cos \Omega t - i \bar{\phi}_A^+(0) e^{-i\varphi_{cp}} \sin \Omega t. \end{aligned} \quad (5.121)$$

The gravitational wave signal will be carried by the φ_{cp} . Clearly, this is where the matrix $\mathbb{M}(\theta, \varphi)$ in the main text comes from.

References

- [1] LIGO Scientific Collaboration and Virgo Collaboration. Observation of gravitational waves from a binary black hole merger. *Phys. Rev. Lett*, 116:061102, Feb. 2016.
- [2] LIGO Scientific Collaboration and Virgo Collaboration. Gw170817: Observation of gravitational waves from a binary neutron star inspiral. *Phys. Rev. Lett*, 119:161101, Oct 2017.
- [3] Gregory M Harry and the LIGO Scientific Collaboration. Advanced ligo: the next generation of gravitational wave detectors. *Classical and Quantum Gravity*, 27:084006, 2010.
- [4] Virgo Collaboration. Advanced virgo: a second-generation interferometric gravitational wave detector. *Classical and Quantum Gravity*, 32:024001, 2015.
- [5] KAGRA Collaboration. Kagra: 2.5 generation interferometric gravitational wave detector. *Nature Astronomy*, 3:35–40, Jan 2019.
- [6] S. Dimopoulos, P. W. Graham, J. M. Hogan, M. A. Kasevich, and S. Rajendran. Gravitational wave detection with atom interferometry. *Physics Letter B*, 678:37–40, jul 2009.
- [7] Savas Dimopoulos, Peter W. Graham, Jason M. Hogan, Mark A. Kasevich, and Surjeet Rajendran. Atomic gravitational wave interferometric sensor. *Phys. Rev. D*, 78:122002, Dec 2008.
- [8] G M Tino and F Vetrano. Is it possible to detect gravitational waves with atom interferometers? *Classical and Quantum Gravity*, 24(9):2167–2178, apr 2007.

- [9] N. Yu and M. Tinto. Gravitational wave detection with single-laser atom interferometers. *Gen. Rel. Grav.*, 43:1943–1952, jul 2011.
- [10] P. L. Bender. Limitations of atom interferometry for gravitational wave observations in space. *Gen. Relativ. Gravit.*, 44(711), Nov 2012.
- [11] Peter W. Graham, Jason M. Hogan, Mark A. Kasevich, and Surjeet Rajendran. New method for gravitational wave detection with atomic sensors. *Phys. Rev. Lett.*, 110:171102, apr 2013.
- [12] Jan Harms, Bram J. J. Slagmolen, Rana X. Adhikari, M. Coleman Miller, Matthew Evans, Yanbei Chen, Holger Mueller, and Masaki Ando. Low-frequency terrestrial gravitational-wave detectors. *Phys. Rev. D*, 88:122003, Dec 2013.
- [13] Remi Geiger. Future gravitational wave detectors based on atom interferometry. In Gerard Auger and Eric Plagnol, editors, *An Overview of Gravitational Waves: Theory, Sources and Detection*, pages 285–313. World Scientific, 2017.
- [14] Peter W. Graham and Sunghoon Jung. Localizing gravitational wave sources with single-baseline atom interferometers. *Phys. Rev. D*, 97:024052, Jan 2018.
- [15] J. Junca, A. Bertoldi, D. O. Sabulsky, G. Lefevre, X. Zou, J.-B. Decitre, R. Geiger, A. Landragin, S. Gaffet, P. Bouyer, and B. Canuel. Characterizing earth gravity field fluctuations with the miga antenna for future gravitational wave detectors. *Phys. Rev. D*, 99:104026, may 2019.
- [16] Ming-Sheng Zhan, Jin Wang, Wei-Tou Ni, Dong-Feng Gao, Gang Wang, Ling-Xiang He, Run-Bing Li, Lin Zhou, Xi Chen, Jia-Qi Zhong, Biao Tang, Zhan-Wei Yao, Lei Zhu, Zong-Yuan Xiong, Si-Bin Lu, Geng-Hua Yu, Qun-Feng Cheng, Min Liu, Yu-Rong Liang, Peng Xu, Xiao-Dong He, Min Ke, Zheng Tan, and Jun Luo. ZAIGA: Zhaoshan Long-baseline Atom Interferometer Gravitation Antenna. *arXiv e-prints*, page arXiv:1903.09288, Mar 2019.
- [17] I. I. Rabi, J. R. Zacharias, S. Millman, and P. Kusch. A new method of measuring nuclear magnetic moment. *Phys. Rev.*, 53:318–318, Feb. 1938.
- [18] Norman F. Ramsey. A molecular beam resonance method with separated oscillating fields. *Phys. Rev.*, 78:695–699, Jun 1950.
- [19] Alexander D. Cronin, Jorg Schmiedmayer, and David E. Pritchard. Optics and interferometry with atoms and molecules. *Rev. Mod. Phys.*, 81:1051–1129, Jul 2009.
- [20] Savas Dimopoulos, Peter W. Graham, Jason M. Hogan, and Mark A. Kasevich. Testing general relativity with atom interferometry. *Phys. Rev. Lett.*, 98:111102, Mar 2007.

- [21] Holger Mueller, Sheng-vey Chiow, Sven Herrmann, Steven Chu, and Keng-Yeow Chung. Atom-interferometry tests of the isotropy of post-newtonian gravity. *Phys. Rev. Lett.*, 100:031101, Jan 2008.
- [22] Asimina Arvanitaki, Savas Dimopoulos, Andrew A. Geraci, Jason Hogan, and Mark Kasevich. How to test atom and neutron neutrality with atom interferometry. *Phys. Rev. Lett.*, 100:120407, Mar 2008.
- [23] Savas Dimopoulos, Peter W. Graham, Jason M. Hogan, and Mark A. Kasevich. General relativistic effects in atom interferometry. *Phys. Rev. D*, 78:042003, Aug 2008.
- [24] Keng-Yeow Chung, Sheng-Wey Chiow, Sven Herrmann, Steven Chu, and Holger Mueller. Atom interferometry tests of local lorentz invariance in gravity and electrodynamics. *Phys. Rev. D*, 80:016002, Jul 2009.
- [25] Rym Bouchendira, Pierre Clade, Saida Guellati-Khelifa, Francois Nez, and Francois Biraben. New determination of the fine structure constant and test of the quantum electrodynamics. *Phys. Rev. Lett*, 106:080801, Feb. 2011.
- [26] Michael A. Hohensee, Steven Chu, Achim Peters, and Holger Mueller. Equivalence principle and gravitational redshift. *Phys. Rev. Lett*, 106:151102, Apr 2011.
- [27] Zhong-Kun Hu, Bu-Liang Sun, Xiao-Chun Duan, Min-Kang Zhou, Le-Le Chen, Su Zhan, Qiao-Zhen Zhang, and Jun Luo. Demonstration of an ultrahigh-sensitivity atom-interferometry absolute gravimeter. *Phys. Rev. A*, 88:043610, Oct 2013.
- [28] G. Rosi, F. Sorrentino, L. Cacciapuoti, M. Prevedelli, and G. M. Tino. Precision measurement of the newtonian gravitational constant using cold atoms. *Nature*, 510:518 EP –, 06 2014.
- [29] P. Hamilton, M. Jaffe, P. Haslinger, Q. Simmons, H. Müller, and J. Khoury. Atom-interferometry constraints on dark energy. *Science*, 349:849–851, 2015.
- [30] Xiao-Chun Duan, Xiao-Bing Deng, Min-Kang Zhou, Ke Zhang, Wen-Jie Xu, Feng Xiong, Yao-Yao Xu, Cheng-Gang Shao, Jun Luo, and Zhong-Kun Hu. Test of the universality of free fall with atoms in different spin orientations. *Phys. Rev. Lett*, 117:023001, Jul 2016.
- [31] Benjamin Elder, Justin Khoury, Philipp Haslinger, Matt Jaffe, Holger Müller, and Paul Hamilton. Chameleon dark energy and atom interferometry. *Phys. Rev. D*, 94:044051, Aug 2016.
- [32] R. Parker, C. Yu, W. Zhong, J. Kwan, B. Estey, and H. Muller. Measurement of the fine structure constant as a test of the standard model. *Science*, 360:191–195, 2018.

- [33] Holger Mueller, Sheng-wei Chiow, Quan Long, Sven Herrmann, and Steven Chu. Atom interferometry with up to 24-photon-momentum-transfer beam splitters. *Phys. Rev. Lett.*, 100:180405, May 2008.
- [34] Pierre Clade, Saidada Guellati-Khelifa, Francois Nez, and Francois Biraben. Large momentum beam splitter using bloch oscillations. *Phys. Rev. Lett.*, 102:240402, Jun 2009.
- [35] Onur Hosten, Nils J. Engelsen, Rajiv Krishnakumar, and Mark A. Kasevich. Measurement noise 100 times lower than the quantum-projection limit using entangled atoms. *Nature*, 529:505 EP –, 01 2016.
- [36] Paul Hamilton, Matt Jaffe, Justin M. Brown, Lothar Maisenbacher, Brian Estey, and Holger Mueller. Atom interferometry in an optical cavity. *Phys. Rev. Lett.*, 114:100405, Mar 2015.
- [37] B. Canuel, A. Bertoldi, L. Amand, E. Pozzo di Borgo, T. Chantrait, C. Danquigny, M. Dovale Álvarez, B. Fang, A. Freise, R. Geiger, J. Gillot, S. Henry, J. Hinderer, D. Holleville, J. Junca, G. Lefèvre, M. Merzougui, N. Mielec, T. Monfret, S. Pelisson, M. Prevedelli, S. Reynaud, I. Riou, Y. Rogister, S. Rosat, E. Cormier, A. Landragin, W. Chaibi, S. Gaffet, and P. Bouyer. Exploring gravity with the miga large scale atom interferometer. *Scientific Reports*, 8(1):14064, 2018.
- [38] V. B. Braginsky, F. Y. Khalili, and K. S. Thorne. *Quantum Measurement*. Cambridge University Press, sep 1992.
- [39] H. J. Kimble, Yuri Levin, Andrey B. Matsko, Kip S. Thorne, and Sergey P. Vyatchanin. Conversion of conventional gravitational-wave interferometers into quantum nondemolition interferometers by modifying their input and/or output optics. *Phys. Rev. D*, 65:022002, Dec 2001.
- [40] Alessandra Buonanno and Yanbei Chen. Signal recycled laser-interferometer gravitational-wave detectors as optical springs. *Phys. Rev. D*, 65:042001, Jan 2002.
- [41] W. M. Itano, J. C. Bergquist, J. J. Bollinger, J. M. Gilligan, D. J. Heinzen, F. L. Moore, M. G. Raizen, and D. J. Wineland. Quantum projection noise: Population fluctuations in two-level systems. *Phys. Rev. A*, 47:3554–3570, May 1993.
- [42] J. Jacobson, G. Bjork, and Y. Yamamoto. Quantum limit for the atom-light interferometer. *Applied Physics B: Lasers and Optics*, 60:187–191, feb 1995.
- [43] Jonathan P. Dowling. Correlated input-port, matter-wave interferometer: Quantum-noise limits to the atom-laser gyroscope. *Phys. Rev. A*, 57:4736–4746, jun 1998.

- [44] Marlan O. Scully and Jonathan P. Dowling. Quantum-noise limits to matter-wave interferometry. *Phys. Rev. A*, 48:3186–3190, Oct 1993.
- [45] Vladimir B. Braginsky, Mikhail L. Gorodetsky, Farid Ya. Khalili, Andrey B. Matsko, Kip S. Thorne, and Sergey P. Vyatchanin. Noise in gravitational-wave detectors and other classical-force measurements is not influenced by test-mass quantization. *Phys. Rev. D*, 67:082001, Apr 2003.
- [46] Haixing Miao, Rana X Adhikari, Yiqiu Ma, Belinda Pang, and Yanbei Chen. Towards the fundamental quantum limit of linear measurements of classical signals. *Phys. Rev. Lett.*, 119:050801, Aug 2017.
- [47] John G. Baker and J. I. Thorpe. Comparison of atom interferometers and light interferometers as space-based gravitational wave detectors. *Phys. Rev. Lett.*, 108:211101, may 2012.
- [48] Christian J. Bordé. Theoretical tools for atom optics and interferometry. *Comptes Rendus de l'Académie des Sciences - Series IV - Physics*, 2(2):509–530, 2001.
- [49] L. D. Landau and E. M. Lifshitz. *Quantum mechanics, Course of Theoretical Physics*. Oxford: Pergamon Press, 1965.

Chapter 6

HIGH-PRECISION MODELING FOR GRAVITATIONAL WAVES OF BBH REMNANTS

The gravitational radiation from the ringdown of a binary black hole merger is described by the solution of the Teukolsky equation, which predicts both the temporal dependence and the angular distribution of the emission. Many studies have explored the temporal feature of the ringdown wave through black hole spectroscopy. In this work, we further study the spatial distribution, by introducing a global fitting procedure over both temporal and spatial dependences, to propose a more complete test of General Relativity. We show that spin-weighted spheroidal harmonics are the better representation of the ringdown angular emission patterns compared to spin-weighted spherical harmonics. The differences are distinguishable in numerical relativity waveforms. We also study the correlation between progenitor binary properties and the excitation of quasinormal modes, including higher-order angular modes, overtones, prograde and retrograde modes. Specifically, we show that the excitation of retrograde modes is dominant when the remnant spin is anti-aligned with the binary orbital angular momentum. This study seeks to provide an analytical strategy and inspire the future development of ringdown tests using real gravitational wave events.

6.1 Introduction

The gravitational waves emitted at the final stage of a binary black hole (BBH) merger — the ringdown stage, consist of a series of quasinormal modes (QNMs) [1–5]. QNMs are solutions to the homogeneous Teukolsky equation [6–9], i.e., the linearized Einstein’s equations in the background of a Kerr black hole [10–14]. The foundation for doing so follows models that describe stellar collapses [10–13] — the strong-field region “falls down” toward the future horizon of the final black hole, revealing a spacetime region in which perturbations satisfy the homogeneous Teukolsky equation with ingoing condition near the horizon and outgoing condition near infinity.

The homogeneous Teukolsky equation not only predicts the *temporal* dependence of the ringdown waves, in terms of their *complex* spectra, but also their *spatial* distributions, in terms of angular emission patterns. There have been many studies

on black hole ringdown spectroscopy involving multiple angular frequencies by modeling it as the superposition of exponentially damped sinusoids [15–20], or using other methods of frequency extraction [21, 22]. Recently, it has been shown that the inclusion of overtones [4, 23] can improve the fitting of numerical relativity (NR) waveforms and lead to better estimation of ringdown model parameters [20, 24, 25], because of the better characterization of the post-merger signal from an earlier time.

Many phenomenological fitting studies based on NR waveforms have been done [26–28], while most previous works only focused on the ringdown temporal properties. Our study further includes spatial dependence on different models, explicitly. Specifically, when the final spin is not aligned with the initial orbital angular momentum, the spatial properties for retrograde excitations [29–32] have not been carefully studied. As the temporal-spatial consistency check of ringdown emission can provide a more complete test of General Relativity [33–36], exploring such a problem defines the theme of this work.

In gravitational wave observations, the prospective searches for ringdown waveforms [37, 38] would enable the test of the spatial-temporal features. With the rapidly increasing number of binary coalescences observed [39–42] by ground-based detectors like Advanced LIGO [43] and Advanced Virgo [44], events with detectable higher-order modes [45–47] are observed, e.g., GW190412 [48] and GW190814 [49]. The detectability of higher-order modes not only impacts the parameter estimation [18, 19, 36, 50–52], but can be used to study angular emission as well. Currently, in the ringdown stage, a high signal-to-noise ratio (SNR) is difficult to achieve due to the lack of post-merger cycles and the degraded detector sensitivity at high frequency range. However, the sensitivity of the proposed next-generation detectors, including Einstein Telescope [53, 54], Cosmic Explorer [55, 56], and NEMO [57], will be significantly improved [58], especially at the high frequencies, opening more possibilities in the BBH post-merger studies [25]. Although a single event could provide limited information about angular dependence, combining multiple events and extracting angular-dependent features will become possible with the expected large number of events in the future. That calls for strategic studies of temporal-spatial emission patterns before more events with high ringdown SNR are observed.

In this work, we study ringdown gravitational waves and show that the spin-weighted spheroidal harmonics are essential in the faithful representation of the *temporal-spatial* ringdown emission pattern [59], further confirming that the Teukol-

sky equation describes the ringdown dynamics. We fit the NR simulated strain data of merging binaries with different parameters provided in the Simulating eXtreme Spacetimes (SXS) Collaboration catalog [60], without adding simulated noise. The exclusion of nonlinear gravitational wave memory effects in SXS waveforms [61] provides an ideal test bed for the linear perturbation theory. We infer the final black hole spin and mass via parameter estimation [62, 63], as in the usual temporal-only fitting. Our results show that when the spatial distribution is considered in addition to the spectrum, more information could be extracted from the ringdown stage, which would benefit the determination of the progenitor BBH properties and their formation channels [64, 65]. Along this procedure, we describe various features of the temporal-spatial emission pattern; in particular, we illustrate the physical meaning of the two complex amplitudes of each QNM. We also study the cases where retrograde modes [29–32, 66] are excited when the initial spin of the primary progenitor black hole is large and anti-aligned with the orbital angular momentum [64, 67], and thus the remnant spin is left anti-aligned with the binary orbital angular momentum.

The structure of this chapter is organized as follows. In Sec. 6.2, we review the QNM decomposition model under the spin-weighted spheroidal harmonic basis and the spin-weighted spherical harmonic basis, respectively. In Sec. 6.3, we present the temporal-spatial fitting strategy used in this work for memory-free NR waveforms. In Secs. 6.4–6.5, we describe the fitting results for waveforms of a benchmark binary and several nonspinning binaries with different mass ratios, and discuss the distinguishability of the two decomposition models and the contributions of higher-order modes and overtones. Then, in Sec. 6.6, we investigate the excitation of retrograde modes when the remnant spin is anti-aligned with the binary orbital angular momentum. Finally, in Sec. 6.7, we summarize and further discuss our results.

6.2 Ringdown models

In this section, we define the coordinate frames used to describe outgoing waves near infinity, carry out QNM decomposition in two types of bases, describe the temporal and spatial dependences of the QNMs, and discuss the excitations of prograde and retrograde modes.

In this work, the discussion is restricted to non-precessing binaries, for which we establish two coordinate systems: the “orbital frame” adapted to the binary

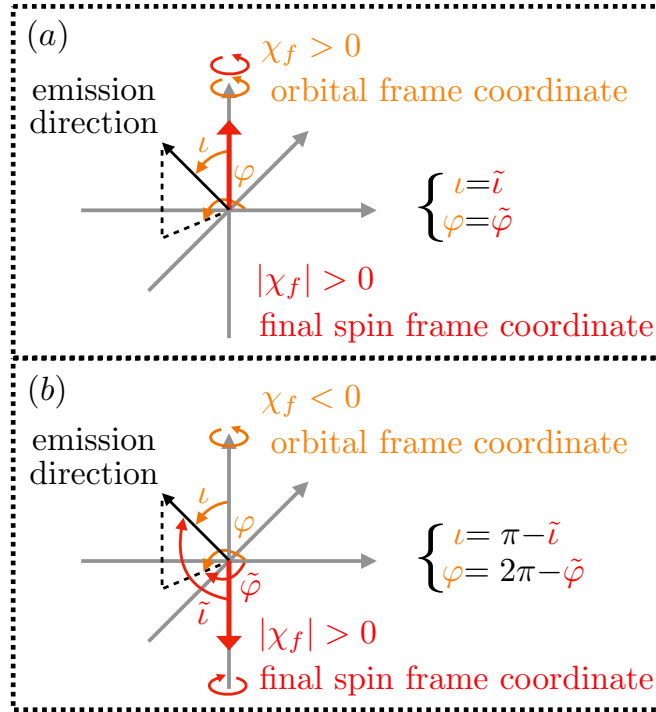


Figure 6.1: Convention of coordinate continuation from positive to negative values of the final spin χ_f . (a) Spin-aligned case ($\chi_f > 0$): when the final spin is aligned with the orbital angular momentum, the final spin frame coincides with the orbital frame, with $\iota = \tilde{\iota}$ and $\varphi = \tilde{\varphi}$. (b) Spin-anti-aligned case ($\chi_f < 0$): when the final spin is anti-aligned with the orbital angular momentum, we have $\iota = \pi - \tilde{\iota}$ and $\varphi = 2\pi - \tilde{\varphi}$.

orbital angular momentum, and the “final spin frame” adapted to the remnant spin angular momentum. In the final spin frame, we decompose the temporal and angular distribution of gravitational waves into a sum over QNMs. This analytical decomposition will be *fitted* to the waveforms from NR simulations.

6.2.1 Coordinate frames

For the majority of BBH events detected so far, the inspiral stage often contributes most of the SNR [35, 36, 40, 42]. The most natural coordinate system to describe non-precessing binaries has its \hat{z} axis aligned with the direction of the orbital angular momentum. We refer to this as the *orbital frame* and use (ι, φ) to label the polar (inclination) and azimuthal angles, respectively. In particular, waveforms of non-precessing binaries from the SXS catalog adopt the orbital frame. On the other hand, QNM decomposition is most easily performed by taking the \hat{z} axis along the spin direction of the remnant black hole. We shall refer to this as the *final spin frame*

and use $(\tilde{\iota}, \tilde{\varphi})$ for its polar (inclination) and azimuthal angles.

The transformation between the orbital frame and the final spin frame in two specific cases is illustrated in Fig. 6.1: (a) When the final spin of the remnant black hole is aligned with the orbital angular momentum (spin-aligned case) [28], the two frames coincide, i.e., $\iota = \tilde{\iota}$, $\varphi = \tilde{\varphi}$. (b) When the final spin is anti-aligned with the orbital angular momentum (spin-anti-aligned case), we have $\iota = \pi - \tilde{\iota}$ and $\varphi = 2\pi - \tilde{\varphi}$. With such coordinate transformation, the parameter space of χ_f is constructed to be continuous across zero, thus linking the cases of aligned and anti-aligned remnant spins. For more general cases of spin misaligned with the orbital angular momentum, the orbital angular momentum precesses in time, and is neither aligned nor anti-aligned with the final spin — this is left for future studies.

For consistency with the SXS data structure and most of the literature, we adopt the orbital frame when describing the final remnant spin χ_f , with $\chi_f < 0$ corresponding to the spin-anti-aligned case, and use $|\chi_f|$ to denote the spin magnitude. For simplicity, we use the symbol $\vec{\Omega} \equiv (\iota, \varphi)$ to represent coordinates in the orbital frame.

6.2.2 QNM decomposition models

Let us now perform QNM decomposition of outgoing gravitational waves near infinity in the final spin frame. From a start time t_0 , the complex-valued ringdown waveform can be written as [1, 5, 7, 8, 68]:

$$\begin{aligned}
 & h^{(S)}(\tilde{\iota}, \tilde{\varphi}, t) \\
 & = (h_+ - i h_\times)^{(S)}(\tilde{\iota}, \tilde{\varphi}, t) \\
 & = \frac{M_f}{r} \sum_{l=2}^{l_{\max}} \sum_{m=-l}^{m=l} \sum_{n=0}^{n_{\max}} [B_{lmn}^{(S+)} e^{-i\omega_{lmn}(t-t_0)} {}_{-2}S_{lmn}(\gamma_{lmn}, \tilde{\iota}, \tilde{\varphi}) + \\
 & \quad B_{lmn}^{(S-)} e^{i\omega_{lmn}^*(t-t_0)} {}_{-2}S_{lmn}^*(\gamma_{lmn}, \pi - \tilde{\iota}, \tilde{\varphi})], \quad (6.1)
 \end{aligned}$$

where h_+ and h_\times are the plus- and cross- polarization components, respectively, r is the distance from the source binary to the detector on Earth. The QNMs summed over here are labeled by three integers: the angular indices (l, m) with $l = 2, 3, \dots$ and $|m| \leq l$, and the overtone index $n = 0, 1, \dots$. Here we have only carried out the summations up to finite maximal values of the angular quantum number l_{\max} and the overtone number n_{\max} . The real and imaginary parts of each ω_{lmn} correspond to the (angular) frequency and decay rate of the QNM; the entire spectrum $\{\omega_{lmn}\}$ is exclusively determined by the remnant black hole's mass M_f and dimensionless

spin χ_f — the only two parameters that characterize a stationary uncharged black hole, according to the no-hair theorem [25, 34, 69–73]. The angular functions ${}_{-2}S_{lmn}$ in Eq. (6.1) are the spin-weighted *spheroidal* harmonics, with dimensionless *spheroidicity parameter* γ_{lmn} given by [8]:

$$\gamma_{lmn} = \chi_f M_f \omega_{lmn}. \quad (6.2)$$

The dependence of the angular function on γ_{lmn} can be attributed to the deformation of bounded photon orbits due to a Kerr black hole's spin.

In practice, on the other hand, the ringdown waveform is often *approximated* by an expansion of decaying sinusoids with angular dependence given by spin-weighted *spherical* harmonics $\{{}_{-2}Y_{lm}\}$:

$$\begin{aligned} h^{(Y)}(\tilde{t}, \tilde{\varphi}, t) &= (h_+ - i h_\times)^{(Y)}(\tilde{t}, \tilde{\varphi}, t) \\ &= \frac{M_f}{r} \sum_{l=2}^{l_{\max}} \sum_{m=-l}^{m=l} \sum_{n=0}^{n_{\max}} [B_{lmn}^{(Y+)} e^{-i\omega_{lmn}(t-t_0)} {}_{-2}Y_{lm}(\tilde{t}, \tilde{\varphi}) + \\ &\quad B_{lmn}^{(Y-)} e^{i\omega_{lmn}^*(t-t_0)} {}_{-2}Y_{lm}^*(\pi - \tilde{t}, \tilde{\varphi})]. \end{aligned} \quad (6.3)$$

For simplicity, we refer to the decompositions in Eqs. (6.1) and (6.3) as *S* model and *Y* model, respectively. The mode mixing between the two bases depends on the spheroidicity γ_{lmn} [8, 26, 68, 74]:

$$\begin{aligned} {}_{-2}S_{lmn}(\gamma_{lmn}, \tilde{t}, \tilde{\varphi}) &= {}_{-2}Y_{lm}(\tilde{t}, \tilde{\varphi}) + \gamma_{lmn} \sum_{l' \neq l} c_{l'l m} {}_{-2}Y_{l'm}(\tilde{t}, \tilde{\varphi}) \\ &\quad + \mathcal{O}(\gamma_{lmn})^2, \end{aligned} \quad (6.4)$$

where $c_{l'l m}$ are the mixing coefficients between spin-weighted spheroidal harmonics and spin-weighted spherical harmonics with different l' and l but the same m index. To test the angular emission patterns of remnant black holes, we compare the two models and check which one is more consistent with the QNM expansions.

For the convenience of readers, the notation and terminology specifically defined and used in this chapter are listed in Table 6.1. It is worth pointing out that the conventions for writing the QNM expansion in Eq. (6.1) are not all consistent in the existing literature, e.g., Refs [5, 26, 68]. We will briefly comment on them in Sec. 6.2.5 and summarize in Table 6.2.

Table 6.1: Notations and terminology used in this chapter.

Notation	Definition and description
S	The QNM decomposition in spin-weighted spheroidal harmonics, defined in Eq. (6.1), often labeled in superscripts.
Y	The QNM decomposition in spin-weighted spherical harmonics, defined in Eq. (6.3), often labeled in superscripts.
t_{offset}	The offset of starting time from the peak of $\sum_{lm} h_{lm}(t) ^2$ (t_{peak}), defined in Eq. (6.6); it serves as the control hyperparameter in fitting.
$\chi^2[h, g_{\text{opt}}^{(S/Y)}]$	The optimal distance over the searched (M_f, χ_f) parameter space, defined in Eq. (6.43), shortened as χ^2 in the figures.
t_{trans}	Transition time, the value of t_{offset} after which the optimal distance converges to a stable level, defined in Sec. 6.4.2.
χ_{min}^2	Minimum distance, the converged value of the optimal distance after the transition time, defined in Sec. 6.4.2.
$ \Delta M_f/M_f , \Delta \chi_f/\chi_f $	Relative errors, the quantities used to characterize the accuracy of the estimated parameters, defined in Eqs. (6.17).

6.2.3 Temporal and spatial dependences of the modes

The physical meanings of the parameters and terms in Eqs. (6.1) and (6.3) are explained as follows:

Time dependence. — Each ω_{lmn} represents one complex frequency of the QNMs with index lmn , with the imaginary part being the decay rate. Among the QNMs, the $m > 0$ modes are *prograde*, while the $m < 0$ terms are *retrograde*. In this work, we obtain ω_{lmn} numerically using the `qnm` python package [75]. As we vary χ_f , the trajectories of a selected set of ω_{lmn} appear as branches in the complex plane in Fig. 6.2. Real parts of prograde-mode frequencies (solid curves) increase with the spin magnitude $|\chi_f|$, while those of the retrograde-mode frequencies (dotted curves) decrease with $|\chi_f|$. Moreover, the decay rate increases with increasing overtone number n , as shown in the upper ($n = 0$) and lower ($n = 1$) parts of Fig. 6.2. Higher overtones play more important roles in the earlier stage of the

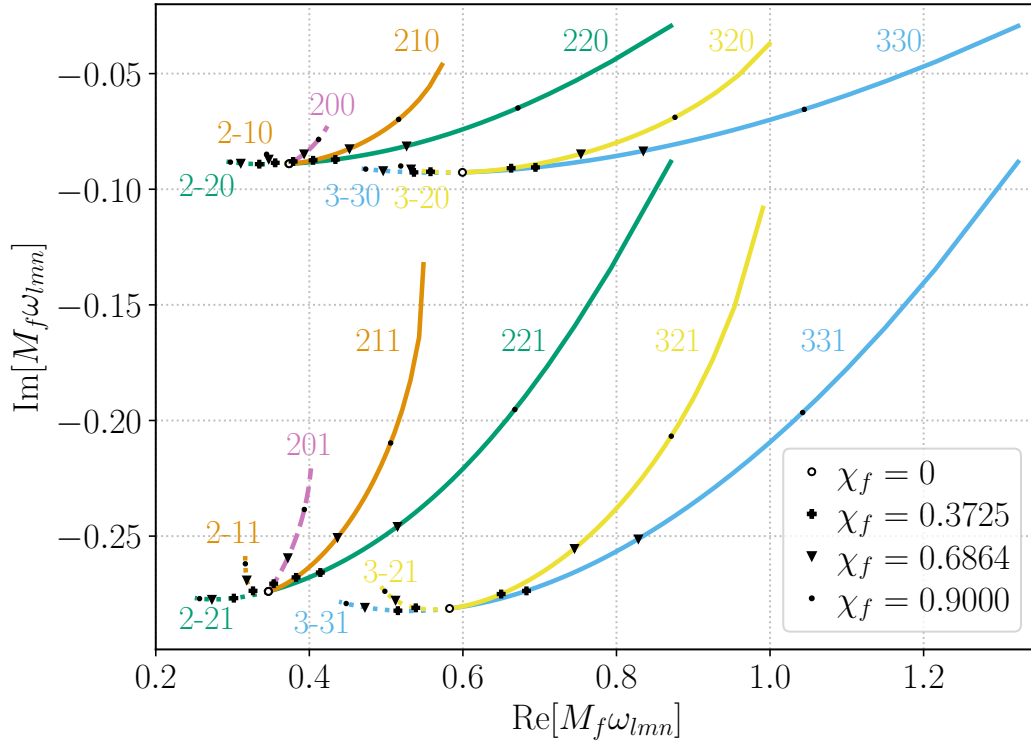


Figure 6.2: Examples of complex QNM frequencies for $\chi_f \in [0, 0.99]$ (similar to Fig. 6 in Ref. [68]). The horizontal axis represents the frequency (the real part) and the vertical axis represents the decay rate (the imaginary part). The solid, dashed, and dotted curves stand for prograde modes ($m > 0$), $m = 0$ modes and retrograde modes ($m < 0$), respectively. Each curve is labeled by its lmn indices, starting with the frequency value of $\chi_f = 0$ and ending at the frequency value of $\chi_f = 0.99$. When $\chi_f = 0$, QNM frequencies with the same l index coincide, as indicated by the black circles. We mark the frequencies corresponding to $\chi_f = 0.3725$ (N9; see waveform label in Table 6.3), $\chi_f = 0.6864$ (N1) and $\chi_f = 0.9$ (the example in Fig. 6.3) by plus, inverted triangle, and dot markers, respectively. For the modes with the same lm indices, the ones with overtone $n = 1$ (lower curves) have larger decay rates than the ones with $n = 0$ (upper curves).

ringdown [4, 23–25].

Spatial dependence. — For prograde (retrograde) modes with indices $m > 0$ ($m < 0$), the $\{B_{lmn}^{(S+)} {}_{-2}S_{lmn}(\gamma_{lmn}, \tilde{\iota}, \tilde{\varphi})\}$, $\{B_{lmn}^{(Y+)} {}_{-2}Y_{lm}(\tilde{\iota}, \tilde{\varphi})\}$ terms describe the emission mainly towards the north (south) hemisphere, while the $\{B_{lmn}^{(S-)} {}_{-2}S_{lmn}^*(\gamma_{lmn}, \pi - \tilde{\iota}, \tilde{\varphi})\}$, $\{B_{lmn}^{(Y-)} {}_{-2}Y_{lm}^*(\pi - \tilde{\iota}, \tilde{\varphi})\}$ ones describe the emission mainly towards the south (north) hemisphere. The coefficients $B_{lmn}^{(S\pm/Y\pm)}$ are the corresponding excitations of the lmn mode and are governed by the merging dynamics of the progenitor binary. The temporal and spatial features of different terms are summarized in Table 6.2.

	[a]	[b]	[c]	[d]
Temporal-spatial profile	$e^{-i\omega_{220}t} {}_{-2}S_{220}(\gamma_{220}, \tilde{t}, \tilde{\varphi})$	$e^{i\omega_{220}^*t} {}_{-2}S_{220}^*(\gamma_{220}, \pi - \tilde{t}, \tilde{\varphi})$	$e^{-i\omega_{2-20}t} {}_{-2}S_{2-20}(\gamma_{2-20}, \tilde{t}, \tilde{\varphi})$	$e^{i\omega_{2-20}^*t} {}_{-2}S_{2-20}^*(\gamma_{2-20}, \pi - \tilde{t}, \tilde{\varphi})$
Amplitude in Eq. (6.1)	$B_{220}^{(+)}$	$B_{220}^{(-)}$	$B_{2-20}^{(+)}$	$B_{2-20}^{(-)}$
Right-/Left-handed (R/L)	R	L	R	L
Prograde/Retrograde	Prograde	Prograde	Retrograde	Retrograde
Emission direction (in final spin frame)	North	South	South	North
Angular eigenfunction (standard form)	${}_{-2}S_{220}(\gamma_{220}, \tilde{t}, \tilde{\varphi})$	${}_{-2}S_{2-20}(-\gamma_{220}^*, \tilde{t}, \tilde{\varphi})$	${}_{-2}S_{2-20}(\gamma_{2-20}, \tilde{t}, \tilde{\varphi})$	${}_{-2}S_{220}(-\gamma_{2-20}^*, \tilde{t}, \tilde{\varphi})$
Amplitude in [68] ¹ (2006)	\mathcal{A}_{220}	\mathcal{A}'_{220} (mirror mode of [a])	\mathcal{A}_{2-20}	\mathcal{A}'_{2-20} (mirror mode of [c])
Terminology in [26] (2014)	Regular mode	Regular mode	Mirror mode of [b]	Mirror mode of [a]
Amplitude in [30, 32] (2019)	\mathcal{A}_{220}	\mathcal{A}'_{220}	\mathcal{A}_{2-20}	\mathcal{A}'_{2-20}
Amplitude in [36] (2021)	\mathcal{A}_{220}	\mathcal{A}_{2-20}	(not included)	(not included)
Amplitude in [5] (2021)	$C_{[1]220}$	$C_{[1]2-20}$	$C_{[-1]220}$	$C_{[-1]2-20}$
Amplitude in [76] (2021)	C_{220}	C'_{2-20} (mirror mode of [c])	C_{2-20}	C'_{220} (mirror mode of [a])
Amplitude in [77, 78] (2021)	C_{220}	C_{2-20}	C'_{2-20} (mirror mode of [b])	C'_{220} (mirror mode of [a])

Table 6.2: Conventions and notations for writing the QNM expansion, taking $(l, m, n) = (2, \pm 2, 0)$ for example.

¹Ref. [68] denotes GW strain tensor as $h_+ + i h_\times$, thus we include a sign change in angular frequency when comparing the convention in [68] with other papers.

6.2.4 Excitations of prograde and retrograde modes

Let us now discuss the features of prograde and retrograde modes, and how they should be excited in a merging binary. In Fig. 6.3, we illustrate the polarization contents of each ringdown mode by plotting in 2D graphs the $(h_+(t), h_\times(t))$ observed from the north ($\iota = 0, \varphi = 0$) and south ($\iota = \pi, \varphi = 0$) poles in the orbital frame, for $t \in [0, 100M_f]$. For illustration purposes, we choose $\chi_f = 0.9, l = 2$, and $m = \pm 2$ in the plot. We assign the same, arbitrarily chosen starting amplitude for all the modes, $(h_+(0), h_\times(0)) = (0.63, 0)$. Since the modes oscillate and decay over time, each mode traces a trajectory that spirals toward the center as time passes.

Here we emphasize that plotting $h_+(t)$ along the x direction and $h_\times(t)$ along the y direction in the graph (instead of the opposite) illustrates the way that the polarization patterns rotate: if a binary along with its emission pattern rotates about the (ι, φ) emission direction by an angle, say ζ , following right-hand rule, the complex strain value $h = h_+ - ih_\times$ will become $e^{-2i\zeta}h = e^{-2i\zeta}(h_+ - ih_\times)$ and the pattern of $(h_+(t), h_\times(t))$ in the plot will rotate by 2ζ counterclockwise.

Spin-aligned case. — In the left panels (a) of Fig. 6.3, we study the spin-aligned case, with $\chi_f > 0$. At the north pole ($\iota = 0$, upper left panel), we observe that the $B_{m>0}^{(+)}$ (blue solid curve) and $B_{m<0}^{(-)}$ (orange dashed curve) terms correspond to the counterclockwise and clockwise trajectories in the (h_+, h_\times) plane, respectively. It is important to note that the other two terms, with amplitudes $B_{m>0}^{(-)}$ and $B_{m<0}^{(+)}$, vanish at the north pole due to the properties of spin-weighted spheroidal harmonics. The counterclockwise (clockwise) trajectory corresponds to the positive (negative) value of the real part in the QNM frequency of the $B_{m>0}^{(+)}$ ($B_{m<0}^{(-)}$) term. In this case, the spin of the black hole is counterclockwise, therefore $B_{m>0}^{(+)}$ ($B_{m<0}^{(-)}$) corresponds to a prograde (retrograde) pattern of polarization rotation. One can also see that the prograde $B_{m>0}^{(+)}$ mode spirals decay “slower” toward the center than the retrograde $B_{m<0}^{(-)}$ mode (the blue solid curve reaches the gray dotted circle at $t = 10M_f$ while the orange dashed curve reaches it before $t = 10M_f$), because the prograde mode has a higher quality factor (the ratio between absolute values of real and imaginary parts of the QNM frequency).

At the south pole ($\iota = \pi$, lower left panel), again according to properties of the spin-weighted spheroidal harmonics, we only observe the $B_{m>0}^{(-)}$ (solid orange curve) and $B_{m<0}^{(+)}$ (dashed blue curve) terms, which represent the prograde and retrograde modes, respectively. In comparison with the view from the north pole, the prograde (retrograde) mode now spirals clockwise (counterclockwise). This is consistent

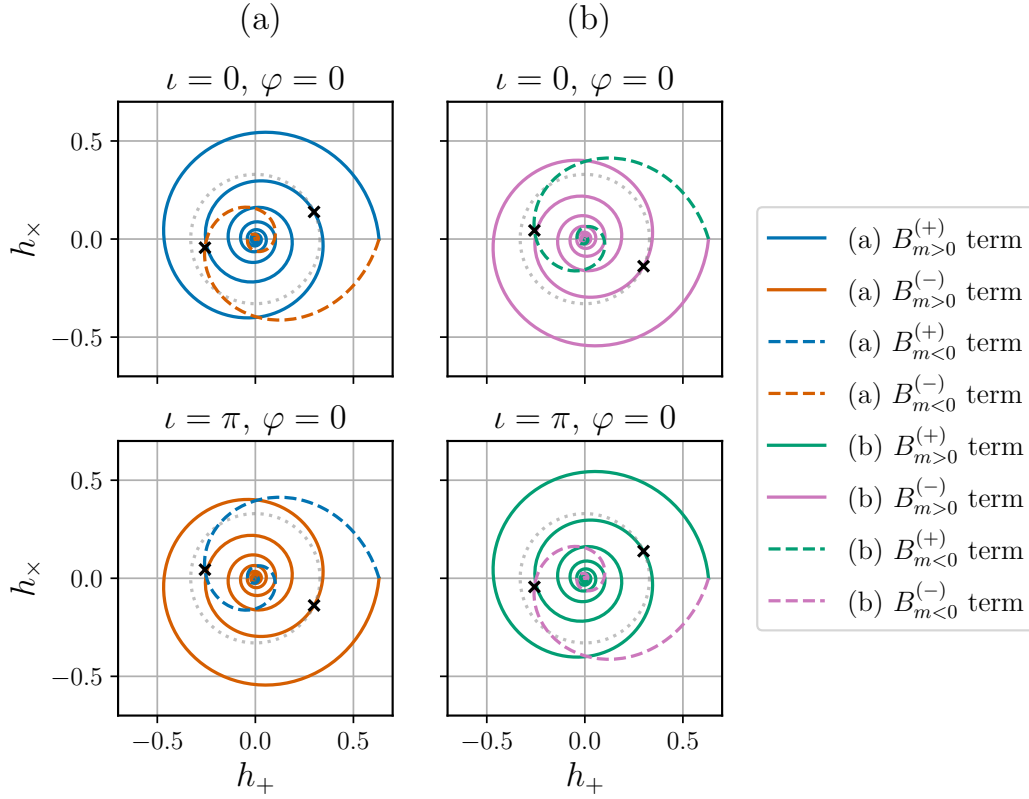


Figure 6.3: Polarization contents ($h_+(t)$, $h_\times(t)$) of the template ringdown waveform indexed with $(l, m) = (2, 2), (2, -2)$, observed from the north pole ($\iota = 0, \varphi = 0$) and south pole ($\iota = \pi, \varphi = 0$) in the orbital frame for (a) spin-aligned ($\chi_f = 0.9$) and (b) spin-anti-aligned ($\chi_f = -0.9$) cases. Each parametric curve starts at $t = 0$ from $(h_+, h_\times) = (0.63, 0)$ and evolves as a spiral over $t \in [0, 100M_f]$. The “ \times ” marker indicates the strain at $t = 10M_f$ and the gray dotted circle indicates the strain magnitude of prograde mode at that moment for reference. The $B_{m>0}$ and $B_{m<0}$ terms represent the prograde and retrograde QNMs excitation, respectively. For $B_{m>0}$ ($B_{m<0}$), the “(+)” superscript stands for the emission in the same (opposite) direction as the spin. For (a) spin-aligned case, the $B_{m>0}^{(+)}$ and $B_{m<0}^{(-)}$ terms represent the emission towards the north pole direction; for (b) spin-anti-aligned case, the $B_{m>0}^{(-)}$ and $B_{m<0}^{(+)}$ terms represent the emission towards the north pole direction. In either case, the $B_{m>0}^{(+)}$ and $B_{m<0}^{(-)}$ terms represent the emission towards the remnant spin direction.

with the fact that the black hole rotates clockwise when viewed from the south pole. Mathematically, the signs of the real parts of the eigenfrequencies are flipped, while the imaginary parts remain unchanged.

Spin-anti-aligned case. — In the right panels (b) of Fig. 6.3, we study the spin-anti-aligned case, with $\chi_f < 0$. We still follow an expansion in the final spin frame $(\tilde{\iota}, \tilde{\varphi})$

using Eq. (6.1) with dimensionless spin equal to $|\chi_f|$, but now need to carry out the transformation ($\iota = \pi - \tilde{\iota}$, $\varphi = 2\pi - \tilde{\varphi}$) to obtain the complex strain h in the orbital frame. Because of this transformation, at the north pole ($\iota = 0$, upper right panel), we observe the $B_{m>0}^{(-)}$ (solid magenta curve) and $B_{m<0}^{(+)}$ (dashed green curve) modes. They still correspond to prograde and retrograde modes, respectively, although now the prograde (retrograde) mode has its frequency with a negative real part and a spiral pattern that goes clockwise (counterclockwise). These are consistent with the fact that the spin direction of the black hole is clockwise viewed from the north pole.

At the south pole ($\iota = \pi$, lower right panel), we observe the $B_{m>0}^{(+)}$ (solid green curve) and $B_{m<0}^{(-)}$ (dashed magenta curve) modes, which correspond to prograde and retrograde modes, respectively. The black hole spins counterclockwise when viewed from the south.

It is worth pointing out that both the remnant spin direction and the excitation of prograde or retrograde mode are determined by the binary dynamics. They are related to each other because the polarization patterns of the inspiral wave would transition smoothly to the ringdown modes. During the inspiral stage, the orbital motion of the binary appears counterclockwise (clockwise) when viewed from the north (south) pole. When the progenitor black holes are nonspinning, the remnant spin is contributed solely from the orbital angular momentum and thus aligned with the orbital angular momentum. Therefore, we anticipate the prograde modes to be more strongly excited. On the other hand, when the initial spin is anti-aligned with the orbital angular momentum, there would be competition between the spin and orbital angular momentum during the merger. The left-over stronger contribution will determine the direction of remnant spin, as well as the excitation of prograde or retrograde modes. Specifically, when the contribution from the negative individual spin is larger, the remnant black hole is left with a spin-anti-aligned with the orbital angular momentum, and we anticipate stronger excitations for retrograde modes.

6.2.5 QNM conventions

Before moving on to the following discussion, we briefly comment on the conventions for writing the QNM expansion in Eq. (6.1) or (6.3) in this chapter and in other literature. The QNM expansion consists of four parts corresponding to the combinations of two frequencies (ω_{lmn} and $-\omega_{lmn}^*$), as well as the prograde and retrograde modes.

In our convention, we first add up the terms with conjugate frequencies explicitly,

and then sum up prograde (the expressions with positive m 's) and retrograde modes (with negative m 's) over all the lmn indices through the summation signs. The convention and summation order in Ref. [5] are similar to ours. In Eq. (1) of [5], the $p = 1$ terms represent the prograde modes (our $m > 0$ terms), and $p = -1$ terms represent the retrograde modes (our $m < 0$ terms). When the retrograde modes are not considered, the Eq. (3) of Ref. [5] is equivalent to our $m \geq 0$ terms in Eq. (6.1), with $(-1)^l$ absorbed into the $B_{lmn}^{(S-)}$ coefficients to be determined.

In an alternative convention, one can sum up the terms with the same sign of frequencies first. Specifically, the terminology of “mirror mode” was first mentioned in [68] to describe the feature that half of the QNM frequencies are “degenerate in modulus of the frequency and damping time,” as shown in Fig. 6 of [68]. Later in Ref. [26], the terminology “mirror modes” was used to refer to the retrograde modes with a different frequency sign from the corresponding prograde modes; while in Ref. [76], it was used to refer to all terms with negative frequencies. In recent work presented in [77, 78], the same terminology “mirror modes” is used to describe the retrograde modes that emit to the same direction as the considered prograde modes (Fig. 1 of Ref. [77]), while the remaining terms with the conjugate frequencies are taken into account by symmetry. Since there is no consistent definition of mirror modes yet, we choose not to use such terminology and, instead, define and describe the prograde and retrograde modes, as well as the terms with conjugate frequencies explicitly. We summarize the conventions and notations for writing the QNM expansion in some existing literature in Table 6.2. More details are given in App. 6.8.

6.2.6 Beyond linear ringdowns

We finally point out that in addition to QNMs, the gravitational waveform after the merger phase also contains power-law tails [79] and gravitational wave memory [80–82]. Power-law tails arise from the long-range nature of the black hole’s gravitational potential. This contribution decay with time, following a power law, and is generally believed to be negligible for binary black hole coalescence.

Gravitational wave memory originally refers to the change in spacetime geometry at future null infinity before and after the passage of a transient gravitational wave. Linear memory refers to changes that can be related to the initial and final momentum distributions of the gravitational wave source [80], while non-linear memory is induced by the non-linearity of the Einstein’s equations [81]; it can be further

interpreted as arising from the gravity effect caused by the energy and momentum of the gravitons [82]. For compact binaries, the memory waveform also refers to a non-oscillatory component of the total waveform that starts off at zero and gradually reaches the final value equal to the gravitational wave memory [83]. Memory waveform can be computed from those waveforms obtained from perturbation theory that do not account for the memory effect [84, 85].

Recent numerical simulations have also been able to decompose the full waveform at null infinity into a memory piece and a memory-free piece [86]. It is also shown that the previous SXS waveforms (including those approximated by the NR surrogate models) correspond to the memory-free piece. In this study, we use the memory-free waveforms, and show that they can be decomposed into QNMs, in terms of both the temporal and spatial distributions. The memory waveform, on the other hand, *cannot* be decomposed into QNMs.

6.3 Fit memory-free NR waveforms with QNM expansions

We now develop a strategy to use QNM expansions (6.1) and (6.3) to *fit* memory-free NR waveforms. In our strategy, we do not focus on one wave-emission direction, or one particular (l, m) mode, but rather consider the joint temporal and spatial (angular) dependence of the ringdown gravitational waves. More specifically, for each binary, and its ringdown waveform starting from a particular time t_0 , we find the optimal set of parameters (M_f, χ_f) and coefficients $\{B_{lmn}^{(S\pm/Y\pm)}\}$ with which the expansion in Eqs. (6.1) or (6.3) best describes the $h(\vec{\Omega}, t)$ obtained from numerical relativity. From this approach, we are able to determine whether the S or the Y model is the more faithful representation of the ringdown gravitational waves.

6.3.1 Target waveforms and templates

In this study, our (memory-free) *target waveform* $h(\vec{\Omega}, t)$ is obtained from the SXS catalog, which provides h in terms of the expansion in spin-weighted spherical harmonics:

$$h(\vec{\Omega}, t) = \sum_{lm} {}_{-2}Y_{lm}(\vec{\Omega}) h_{lm}(t). \quad (6.5)$$

For each binary, we denote the time at which $\sum_{lm} |h_{lm}(t)|^2$ is maximum by t_{peak} . We then use *templates* in the forms of QNM expansion, either Eq. (6.1) or Eq. (6.3), to approximate the target waveform during $t \in [t_0, +\infty)^1$. Here t_0 is a starting time

¹Practically, for all value of t_0 , we consider the waveform till $t_{\text{peak}} + 100M$ when it essentially damps to 0.

not far from t_{peak} , with an offset

$$t_{\text{offset}} = t_0 - t_{\text{peak}}. \quad (6.6)$$

In order to evaluate the quality of the fit, we first define a temporal-spatial inner product of the target waveform $h(\vec{\Omega}, t)$ and the template waveform $g(\vec{\Omega}, t)$ by doing a double integral over both time and angular coordinates:

$$\langle g | h \rangle = \int d^2\vec{\Omega} \int_{t_0}^{+\infty} dt \left[g^*(\vec{\Omega}, t) h(\vec{\Omega}, t) \right]. \quad (6.7)$$

We can then characterize the distance between $h(\vec{\Omega}, t)$ and $g(\vec{\Omega}, t)$ using

$$\chi^2[h, g] = \frac{\langle h - g | h - g \rangle}{\langle h | h \rangle}. \quad (6.8)$$

For each binary configuration, the distance χ^2 depends on the starting time t_0 of ringdown fit, the mass and dimensionless spin (M_f, χ_f) of the remnant black hole, the set of QNM modes summed over (including whether we use the S or the Y model), and their complex amplitudes $\{B_{lmn}^{(\pm)}\}$. The parameters (M_f, χ_f) are intrinsic and need to be optimized numerically, the mode amplitudes $\{B_{lmn}^{(\pm)}\}$ can be optimized analytically, while the starting time t_0 works as the hyperparameter that controls the fitting.

6.3.2 Strategy for minimizing χ^2 over $\{B_{lmn}^{(\pm)}\}$

As it turns out, minimization of χ^2 over $\{B_{lmn}^{(\pm)}\}$ can be carried out analytically, because χ^2 can be viewed as squared distance between h and a linear subspace spanned by the spin-weighted harmonic basis by varying coefficients/coordinates $\{B_{lmn}^{(\pm)}\}$.

Let us do this explicitly for the S model, and the procedure for the Y model can be obtained by simply switching S to Y . Let us first define the following quantities for inner products:

$$K_{lmn}^{(\sigma)} = \int d^2\vec{\Omega} \int_{t_0}^{+\infty} dt g_{lmn}^{(\sigma)*}(\vec{\Omega}, t) h(\vec{\Omega}, t), \quad (6.9)$$

$$G_{lmn, l'm'n'}^{(\sigma, \sigma')} = \int d^2\vec{\Omega} \int_{t_0}^{+\infty} dt g_{lmn}^{(\sigma)*}(\vec{\Omega}, t) g_{l'm'n'}^{(\sigma')}(\vec{\Omega}, t). \quad (6.10)$$

Here $\sigma = \pm$, and we further define

$$g_{lmn}^{(+)}(\vec{\Omega}, t) = e^{-i\omega_{lmn}(t-t_0)} {}_{-2}S_{lmn}(\gamma_{lmn}, \tilde{l}, \tilde{\varphi}), \quad (6.11)$$

$$g_{lmn}^{(-)}(\vec{\Omega}, t) = e^{i\omega_{lmn}^*(t-t_0)} {}_{-2}S_{lmn}^*(\gamma_{lmn}, \pi - \tilde{l}, \tilde{\varphi}). \quad (6.12)$$

Note that $(\tilde{\iota}, \tilde{\varphi})$ need to be converted to (ι, φ) depending on whether we have spin-aligned or spin-anti-aligned binaries. We can now view $B_{lmn}^{(\sigma)}$ and $K_{lmn}^{(\sigma)}$ as the components of column vectors \vec{B} and \vec{K} , and $G_{lmn,l'm'n'}^{(\sigma,\sigma')}$ as those of a Hermitian matrix \mathbb{G} . The inner product in Eq. (6.7) can thus be written as:

$$\langle g|h \rangle = \vec{B}^\dagger \vec{K}, \quad \langle g|g \rangle = \vec{B}^\dagger \mathbb{G} \vec{B}. \quad (6.13)$$

This leads to the least-squares value of distance

$$\chi_{1-s}^2 = 1 - \frac{\vec{K}^\dagger \mathbb{G} \vec{K}}{\langle h|h \rangle}, \quad (6.14)$$

which is achieved when the coefficients satisfy

$$\vec{B} = \mathbb{G}^{-1} \vec{K}. \quad (6.15)$$

We then search the 2D parameter space of (M_f, χ_f) to find the best estimates of $(M_{f,\text{est}}, \chi_{f,\text{est}})$ that yield the optimal distance $\chi^2[h, g_{\text{opt}}^{(S/Y)}]$ for S and Y models, respectively. Details of the numerical implementation can be found in App. 6.10.

6.4 Fitting the benchmark GW150921-like binary

In this section and the following Sec. 6.5, we focus on spin-aligned binaries, for which the spin of the remnant black hole is in the same direction as the binary orbital angular momentum. For both the S and Y models of QNM expansion, starting from different times (described by the hyperparameter t_{offset}), we compare the optimal distance $\chi^2[h, g_{\text{opt}}^{(S/Y)}]$ (χ^2 for short in the plot labels) and the corresponding $(M_{f,\text{est}}, \chi_{f,\text{est}})$, when different groups of angular (l, m) modes and overtones are included. We demonstrate that, as expected, the S model describes the NR waveforms better than the Y model. We carry out this study firstly for a ‘‘benchmark binary’’ waveform, G0 (with parameters similar to the first GW event GW150914 [60, 87, 88]), and then nine non-spinning binaries with mass ratio q ranging from 1 to 6, as listed in Table 6.3.

In Sec. 6.4.1, we introduce our strategy for choosing which angular (l, m) modes to include in the QNM expansion. In Sec. 6.4.2, we present the fitting results for the benchmark binary waveform G0.

¹All SXS waveforms [60] used in this work have the ID type ‘‘BBH_SKS’’, and the levels listed are the maximum available ones.

²The initial values are taken at the reference time after junk radiation [89]. At an accuracy level of 10^{-4} , the spin components in \hat{x} and \hat{y} directions are zero for all the primary, secondary, and remnant black holes listed here.

³For simplicity, in the main text we use χ_f to represent $(\vec{\chi}_f)_z$.

Table 6.3: SXS BBH waveforms used in Secs. 6.4–6.5.

Label	SXS ID/Lev ¹	q_{ref}^2	$(\vec{\chi}_{\text{ref},1})_z^2$	$(\vec{\chi}_{\text{ref},2})_z^2$	χ_{eff}	$(\vec{\chi}_f)_z^{2,3}$
G0	0305/Lev6	1.221	0.3300	-0.4399	-0.0166	0.6921
N1	1154/Lev3	1.000	0.0000	0.0000	0.0000	0.6864
N2	1143/Lev3	1.250	-0.0001	0.0000	-0.0001	0.6795
N3	0593/Lev3	1.500	0.0000	0.0001	0.0001	0.6641
N4	1354/Lev3	1.832	-0.0002	0.0001	-0.0001	0.6377
N5	1166/Lev3	2.000	0.0000	0.0000	0.0000	0.6234
N6	2265/Lev3	3.000	0.0000	0.0000	0.0000	0.5406
N7	1906/Lev3	4.000	0.0001	-0.0001	0.0000	0.4718
N8	0187/Lev3	5.039	0.0000	0.0000	0.0000	0.4148
N9	0181/Lev4	6.000	0.0000	0.0000	0.0000	0.3725

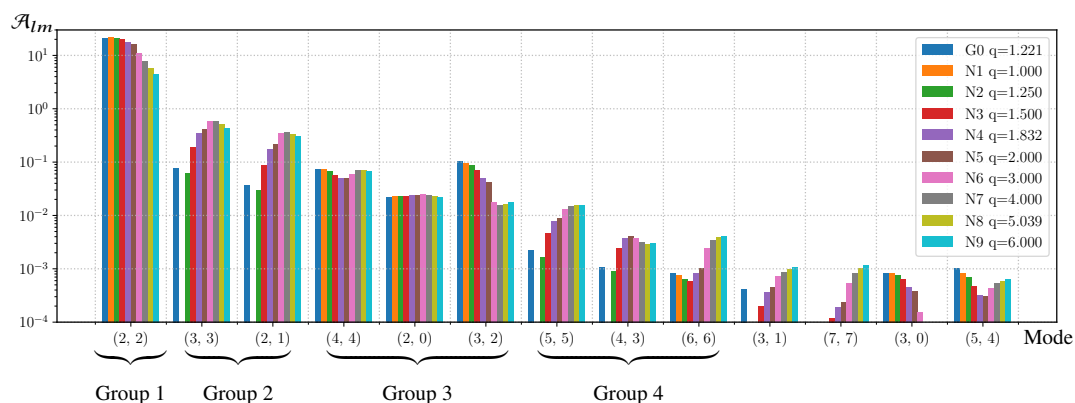


Figure 6.4: The relative importance \mathcal{A}_{lm} , defined in Eq. (6.16) as the strain component in spin-weighted spherical mode (l, m) squared and integrated from t_{peak} to $t_{\text{peak}} + 100M$. Groups 1–4 of the (l, m) modes are defined according to their relative importance in the QNM expansion, and are added to the fitting models in order. See details in Sec. 6.4.1.

6.4.1 Strategy for choosing angular modes

Even though the quadrupole $(l, m) = (2, 2)$ mode is the dominant component of the inspiral, merger, and ringdown waves, gravitational wave detectors at present and in the future are capable of detecting higher multipole modes that are also excited [45]. This capability is the foundation for this study. The NR waveforms from the SXS catalog include all (l, m) modes up to $l_{\text{max}} = 8$ [60]. However, incorporating too many modes in the QNM expansion will eventually lead to overfitting and numerical noise. We need a strategy to include the appropriate angular modes, which should be based on: (i) the strength of excitation of the modes, and (ii) the accuracy of the NR waveforms, and the sensitivity of our detectors.

Let us now address (i) above, while (ii) will be discussed at the end of Sec. 6.4.2.

To investigate the excitation strength of each (l, m) mode, we can rank them in terms of their *relative importance* for the QNM expansion:

$$\mathcal{A}_{lm} = \int_{t_{\text{peak}}}^{t_{\text{peak}}+100M} dt |h_{lm}(t)|^2. \quad (6.16)$$

For G0 and N1–N9 binaries, we plot their \mathcal{A}_{lm} as vertical bars in Fig. 6.4. According to the order of magnitude of \mathcal{A}_{lm} for all q 's, the (l, m) modes can be qualitatively categorized into four groups:

Group 1: (2, 2),

Group 2: (3, 3), (2, 1),

Group 3: (4, 4), (2, 0), (3, 2),

Group 4: (5, 5), (4, 3), (6, 6).

In our studies, instead of testing each of the individual modes, we add modes to our QNM expansion by groups, from Group 1 to Group 4 sequentially. The contribution of each group can thus be quantified by comparing the fitting results before and after adding that group.

Before moving on to the fitting, let us comment that the magnitude of the \mathcal{A}_{lm} 's can be traced qualitatively to the excitation of the corresponding (l, m) mode during the inspiral stage. The initial magnitudes of (l, m) modes are determined by (a) their post-Newtonian order, i.e., higher (l, m) modes are generally weaker, and (b) the suppression due to symmetry, i.e., the $(l, m) = (3, 3), (2, 1), (5, 5), (4, 3)$ modes are prohibited for equal mass ratio binaries (e.g., N1). As \mathcal{A}_{lm} is an integral over time, the ranking of each \mathcal{A}_{lm} is determined jointly by the initial magnitude and the decay rate of that specific mode.

6.4.2 Fittings results for the benchmark binary G0

In this section, we discuss the fitting results for the benchmark binary G0. This binary waveform is used to verify the fitting algorithm described in Sec. 6.3, as it has the best numerical precision in the SXS catalog to date [60, 87, 88]. We first investigate the distinguishability of the S and Y models and the contributions of higher-order angular modes and overtones. We then comment on the fitting error by comparing the results obtained using waveforms at different numerical resolution levels.

To characterize the accuracy of $(M_{f,\text{est}}, \chi_{f,\text{est}})$, we define the relative errors as

follows:

$$|\Delta M_f/M_f| \equiv |(M_{f,\text{est}} - M_{f,\text{true}})/M_{f,\text{true}}|, \quad (6.17a)$$

$$|\Delta \chi_f/\chi_f| \equiv |(\chi_{f,\text{est}} - \chi_{f,\text{true}})/\chi_{f,\text{true}}|, \quad (6.17b)$$

where the true values ($M_{f,\text{true}}, \chi_{f,\text{true}}$) are taken from the SXS metadata. In Fig. 6.5, for both the S and Y models, we show results of the optimal distance $\chi^2[h, g_{\text{opt}}^{(S/Y)}]$ and the relative estimation errors. The results obtained using the S and Y models are presented by blue solid and orange dotted curves, respectively. All results are shown with respect to t_{offset} defined in Eq. (6.6). Each row represents the fitting with the same (l, m) modes but different numbers of overtones. Different rows display the results with different groups of (l, m) modes.

Let us first discuss the influence of varying the hyperparameter t_0 , or equivalently, t_{offset} . As shown in each panel of Fig. 6.5, with the increasing t_{offset} , $\chi^2[h, g_{\text{opt}}^{(S/Y)}]$ decreases and converges to a stable level after some specific value of t_{offset} , which looks like a “flat tail” in the plot. We define that specific t_{offset} as *transition time* (t_{trans}), and the converged value of distance as *minimum distance* (χ_{min}^2). More discussion about t_{trans} and χ_{min}^2 can be found at the end of Sec. 6.5. Practically, we define t_{trans} as the time when 30% of the maximum slope in logarithmic scale of the fitting distance with respect to t_{offset} is reached. For the S model, in each χ^2 block, t_{trans} is marked by a vertical line and χ_{min}^2 by a horizontal line, both in translucent blue. The accuracies of $M_{f,\text{est}}$ and $\chi_{f,\text{est}}$ (shown in blocks below each χ^2 block) oscillate, while in general the levels of accuracy agree with the evolution of χ^2 with respect to t_{offset} , i.e., the relative errors decrease significantly before t_{trans} and slightly oscillate around a stable level after that. Despite the oscillation, after t_{trans} , the relative errors are generally bounded by some specific small error level (similar to the reaching of χ_{min}^2 in the χ^2 plot). As the t_{trans} values generally agree between χ^2 and the accuracies of $(M_{f,\text{est}}, \chi_{f,\text{est}})$, we simply refer to the optimal distance when comparing the fitting results in the following discussions.

We then discuss the contribution of different (l, m) angular modes. The ranking of each \mathcal{A}_{lm} (Fig. 6.4) indicates its significance in the fitting. The contribution of higher-order angular modes can be observed by comparing among different rows in Fig. 6.5. Specifically, the four panels in the first column show the results of fitting with different (l, m) mode groups, with the fundamental $n = 0$ overtones only. From top to bottom, the χ_{min}^2 values for the S and Y models are listed in Table 6.4. The χ_{min}^2 values for the S model are consistently smaller than those for the Y model.

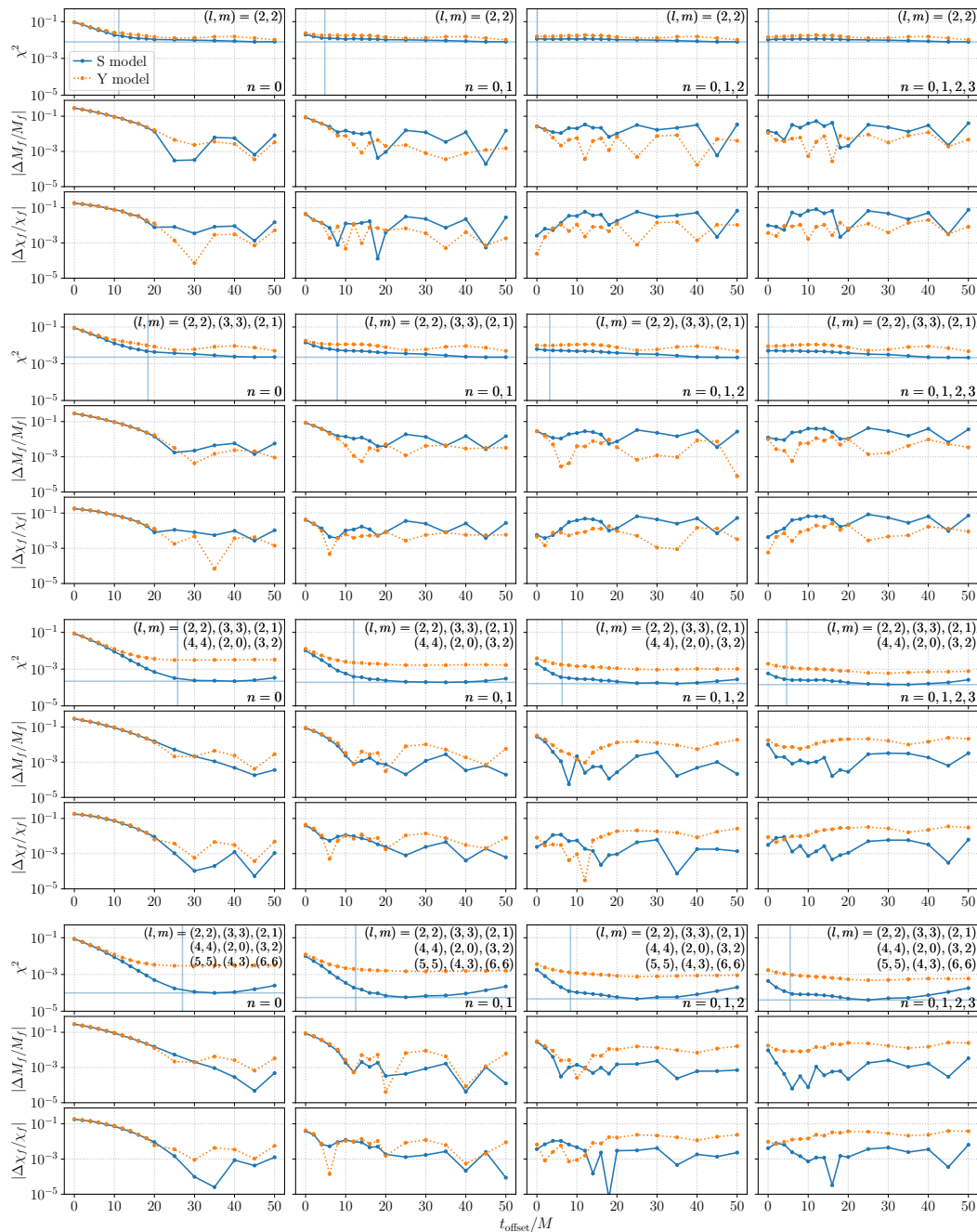


Figure 6.5: Fitting results for the benchmark binary G0. Each three closely laid blocks show the optimal distance χ^2 and the relative error in estimated (M_f, χ_f) , with respect to t_{offset}/M . The solid blue and dotted orange curves correspond to the S and Y models, respectively. Different rows, from top to bottom, correspond to adding (l, m) modes sequentially in groups, as specified in the upper right corner of each χ^2 block. Within each row, different columns, from left to right, correspond to adding overtones for the same set of (l, m) modes, as specified in the lower right corner of each χ^2 block.

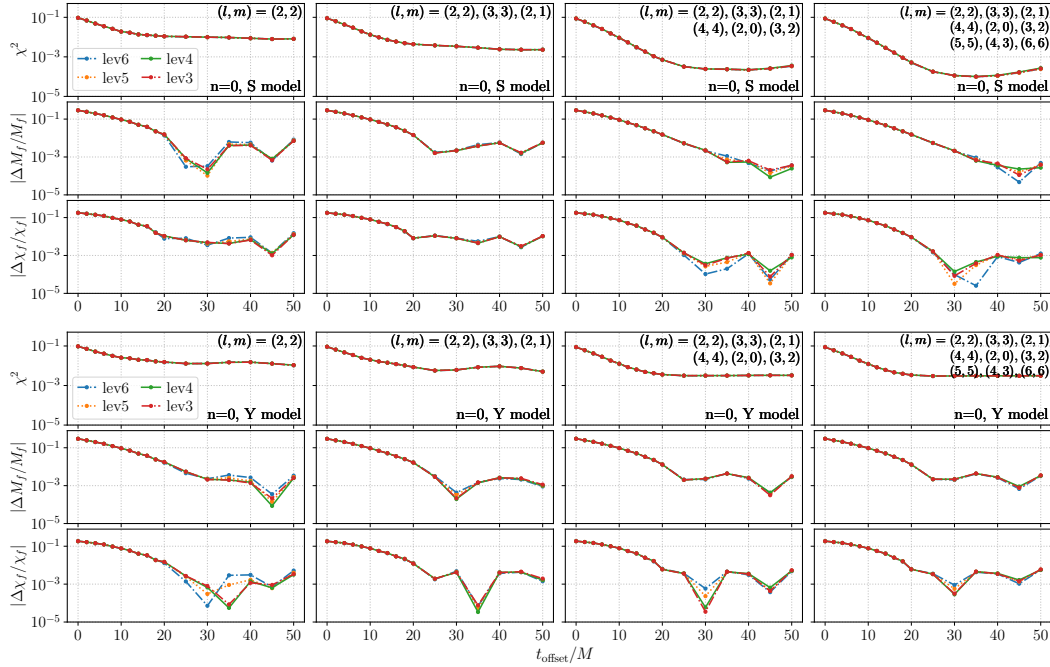


Figure 6.6: Fitting results for G0 using SXS data with different numerical levels (presented in different colors). The first and second rows correspond to fitting with the S and Y models, respectively. Within each row, the columns, from left to right, correspond to adding (l, m) modes sequentially in groups. In this comparison, the models only contain the $n = 0$ fundamental modes without including overtones.

In the case of using the S model, adding Group 3, $(l, m) = (4, 4), (2, 0), (3, 2)$, improves the results most significantly. It reduces χ_{\min}^2 from $\sim 10^{-3}$ to $\sim 10^{-4}$ and the relative estimation error from $\sim 10^{-2}$ to $\sim 10^{-3}$. On the contrary, no order of magnitude improvement is seen when using the Y model by adding (l, m) groups, as the Y model is not accurate enough such that the errors due to missing higher-order modes are smaller compared to the errors caused by the inaccuracy of the Y model itself. As shown in Fig. 6.4, for binary G0, $(l, m) = (3, 2)$ in Group 3 and $(3, 3)$ in Group 2 are the subdominant modes except for the leading mode $(2, 2)$ in Group 1; while Group 4 is the least important group among 1–4. Accordingly, in Fig. 6.5, we can see that including Groups 2 and 3 leads to significant improvement while including Group 4 does not.

On the other hand, the effect of overtones can be observed by comparing different columns within each row. It is shown that adding overtones can bring t_{trans} to an earlier time; the more overtones added, the earlier t_{trans} becomes. This effect can be explained by referring to Fig. 6.2: the higher-order overtones have larger decay

rates and usually play roles at the time closer to t_{peak} . By including overtones, the ringdown model is more accurate at an earlier time after the merger and thus χ_{min}^2 can be achieved with a smaller t_{offset} .

The distinguishability between the S and Y models is influenced jointly by (l, m) modes and overtones. With the same modes included, the S model can always yield smaller χ_{min}^2 than the Y model. Moreover, the improvement in χ_{min}^2 of using S compared to Y is more significant when more (l, m) modes are added, and when more overtones are included. This is illustrated by Eq. (6.4): there is a certain difference between S and Y bases for each given lmn mode. Specifically, in the S model, different overtones of the (l, m) mode have different angular distributions, while they share the same distribution in the Y model. Therefore, adding more (l, m) modes and overtones enlarges the difference between two models. Additionally, by adding higher-order overtones, χ_{min}^2 generally does not change, because higher-order overtones are damped before t_{trans} and have negligible contribution to the converged level of distance. In terms of the relative errors in $(M_{f,\text{est}}, \chi_{f,\text{est}})$, the advantage of using the S model only becomes obvious when adding modes up to Group 3. This will be further discussed in Sec. 6.5 with other nonspinning binaries N1–N9.

Before the extensive comparison of binaries with various mass ratios in the next section, we first comment on possible sources of fitting errors that could potentially impact the conclusion of model distinguishability. In this study, no simulated noise has been added. Thus, apart from the limitation of the model itself, the fitting errors mostly come from numerical noises in the NR waveforms. The SXS waveforms are provided at several numerical resolution levels labeled as Lev1, Lev2, Lev3, etc. For the same binary, a higher level has higher resolution; while between different binaries, level numbers are not necessarily meaningful [60]. The uncertainties in χ_{min}^2 and $(M_{f,\text{est}}, \chi_{f,\text{est}})$ are supposed to be bounded by the difference between the results obtained from the numerical level used in Table 6.3 and the adjacent lower level [60]. For the results in Fig. 6.5, we used the highest available numerical level of G0, Lev6, as listed in Table 6.3. We now compare them with the results

Table 6.4: The values of χ_{min}^2 when fitting G0 with different (l, m) modes ($n = 0$ only).

Model	Group 1	Group 1,2	Group 1–3	Group 1–4
S	7.9×10^{-3}	2.3×10^{-3}	2.2×10^{-4}	9.9×10^{-5}
Y	1.0×10^{-2}	5.1×10^{-3}	3.1×10^{-3}	3.0×10^{-3}

obtained from lower levels, Lev5–Lev3. If the difference between using the S and Y models at Lev6 is clearly larger than the difference of results obtained among different levels, we are able to state that the two models are distinguishable. In Fig. 6.6, we plot the results obtained from different levels, with different (l, m) groups ($n = 0$ only). It is shown that the χ^2 values obtained at different levels are not distinguishable by eye, and are definitely smaller than the S/Y difference shown in Fig. 6.5. Thus, the conclusion that the S model can be distinguished from the Y model and is a more faithful representation of the NR waveform is not impacted by the numerical errors. Note that not all SXS waveforms have such a good numerical precision in the ringdown part for the purpose of this study, probably due to memory residuals in the chosen Bondi-Metzner-Sachs (BMS) frame [90]. To avoid this impact, we select the SXS waveforms that can produce consistent results from different numerical levels. See App. 6.12 for more details. When the ringdown waveform has significantly decayed, if the model is sufficiently accurate with Group 3 and Group 4 included, subtle ringdown residuals due to the choice of frame in the numerical data will manifest as slightly increased χ^2 values for $40 \lesssim t_{\text{offset}} \lesssim 50$ (see Fig. 6.5 and App. 6.11). Potentially, subtractions of the late ringdown residuals [24] could help improve the fitting in the range of $40 \lesssim t_{\text{offset}} \lesssim 50$. We do not conduct such subtraction because it is not well motivated, and the small impact from the residuals [91] does not quantitatively change the resulting transition time and minimum distance in our analysis. Recent studies show that using the Cauchy-characteristic extraction (CCE) and mapping to the super-rest frame would be a proper approach to obtain the memory-free waveform [90, 91].

6.5 Nonspinning binaries with different mass ratios

In Sec. 6.4.2, we have verified the fitting algorithm with the benchmark binary G0. To study the contributions of (l, m) modes and overtones in binaries with various mass ratios [25], we apply the same method to a series of nonspinning binary waveforms N1–N9 with mass ratios ranging from 1 to 6, as listed in Table 6.3. In this section, we demonstrate that more modes are needed in order to achieve the same level of χ_{min}^2 with larger mass ratios, as the higher-order modes are more strongly excited in larger mass-ratio binaries. We summarize the results in two plots grouped by (l, m) groups and numbers of overtones: Fig. 6.7 shows the comparison between the S and Y models in terms of χ_{min}^2 ; Fig. 6.8 displays t_{trans} for the S model when different modes and overtones are included. Detailed fitting results in the same format as those of G0 in Fig. 6.5 are presented in App. 6.11.

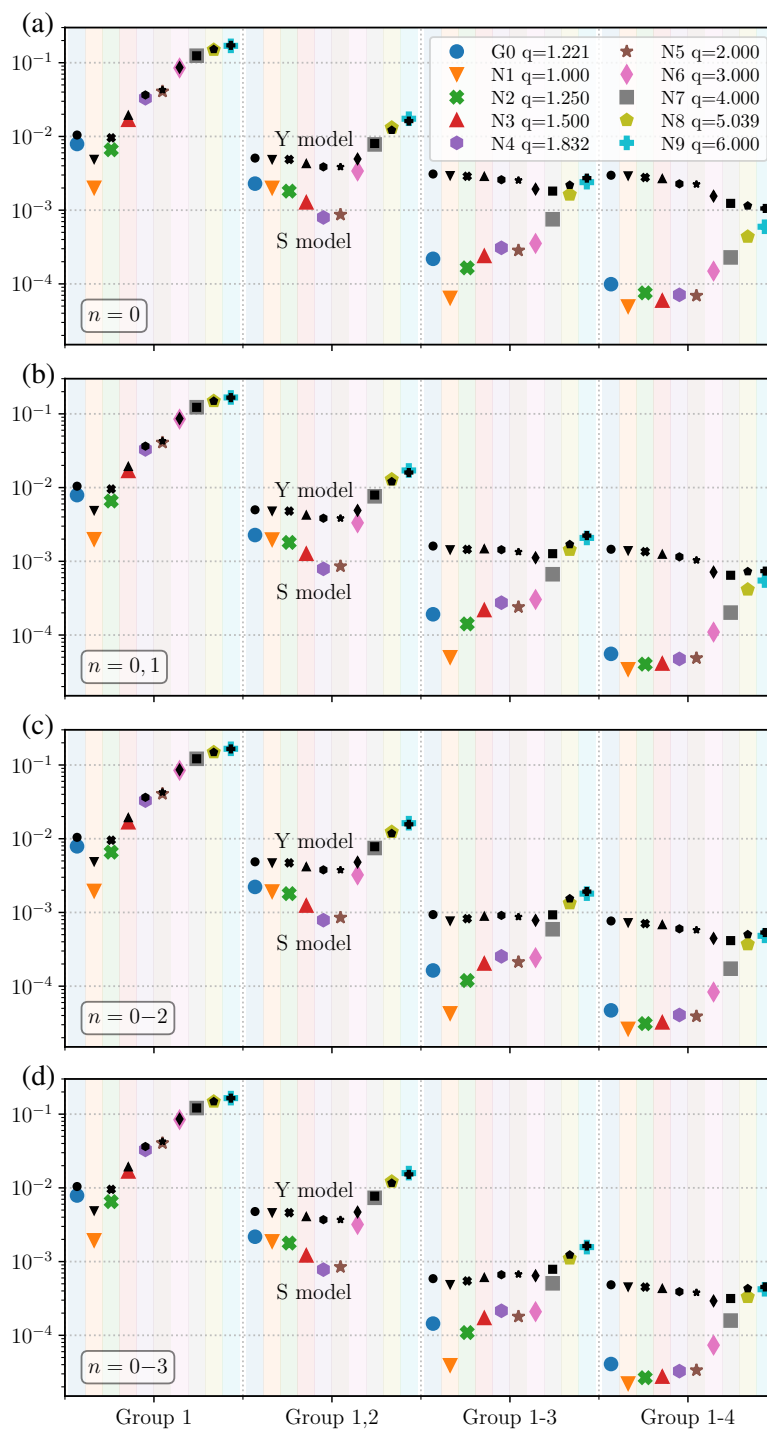


Figure 6.7: The minimum distance χ^2_{\min} obtained for binaries G0 and N1–N9 when (a) $n = 0$, (b) $n = 0, 1$, (c) $n = 0, 1, 2$, and (d) $n = 0, 1, 2, 3$ are considered. The horizontal axes are arranged by (l, m) groups. Within each group, results for different waveforms are shown by markers in different shapes, as indicated by the legend in (a). For each binary waveform, the big colored and the small black markers indicate χ^2_{\min} obtained using the S and Y models, respectively.

In Fig. 6.7, for both the S and Y models, χ_{\min}^2 decreases when more (l, m) modes are added. For a binary with larger q , more significant improvement is seen when adding more (l, m) modes. In the case of the S model, χ_{\min}^2 for binary N1 ($q = 1$) decreases from 2×10^{-3} (Group 1) to 7×10^{-5} (Group 1–4), with the accuracy level improved by a factor of ~ 30 ; for binary N9 ($q = 6$), an improvement by a factor of ~ 280 is achieved from Group 1 to Group 1–4. As indicated in Fig. 6.4, higher angular modes are more strongly excited in binaries with larger mass ratios and thus play a more important role in the QNM expansion. On the other hand, to reach an accuracy of $\chi_{\min}^2 < 0.01$ in the S model, the fundamental $(2, 2)$ mode is enough for $q < 1.25$; while (l, m) modes up to Group 2 are needed for $1.25 < q < 4$ binaries and Group 1–3 are needed for $q > 5$. Comparing panels (a)–(d) in Fig. 6.7, we see that adding more overtones does not result in any order-of-magnitude improvement to χ_{\min}^2 . That is because higher-order overtones decay faster and thus only influence the ringdown waveform at an earlier time while having negligible impact on the converged χ_{\min}^2 after t_{trans} .

Comparing results of different binaries in Fig. 6.7, the differences between S and Y are the most and least significant for the $q = 1$ and $q = 6$ binaries, respectively. Taking the last column of groups (Groups 1–4) in panel (a) for example, for binary N1 ($q = 1$), we have $\chi_{\min}^2 = 7 \times 10^{-5}$ and 3×10^{-3} for the S and Y models, respectively, with a factor of ~ 40 improvement in accuracy by using S versus Y ; while for binary N9 ($q = 6$), the accuracy is only a factor of ~ 1.8 better by using S ($\chi_{\min}^2 = 6.0 \times 10^{-4}$ for S and 1×10^{-3} for Y). This is because the distinction between the S and Y bases depends on the spheroidicities, as shown in Eq. (6.4), which are proportional to $|\chi_f|$, M_f , and ω_{lmn} 's. Meanwhile, when the progenitor black holes are nonspinning, $|\chi_f|$ decreases as q increases, e.g., $\chi_f = 0.6864$ for N1 and $\chi_f = 0.3725$ for N9.

Even though the S model results in better χ_{\min}^2 than the Y model, it is not always the case for the estimated parameters $M_{f,\text{est}}$ and $\chi_{f,\text{est}}$. The features of relative errors defined in Eq. (6.17) are summarized below, with detailed results presented in App. 6.11:

- For G0, N1–N4: Before adding (l, m) Group 3, Y model behaves better; S turns better after adding Group 3.
- For N5: There is no clear S/Y distinction when including only Group 1; Y behaves better after adding Group 2; S behaves better after adding Group 3.

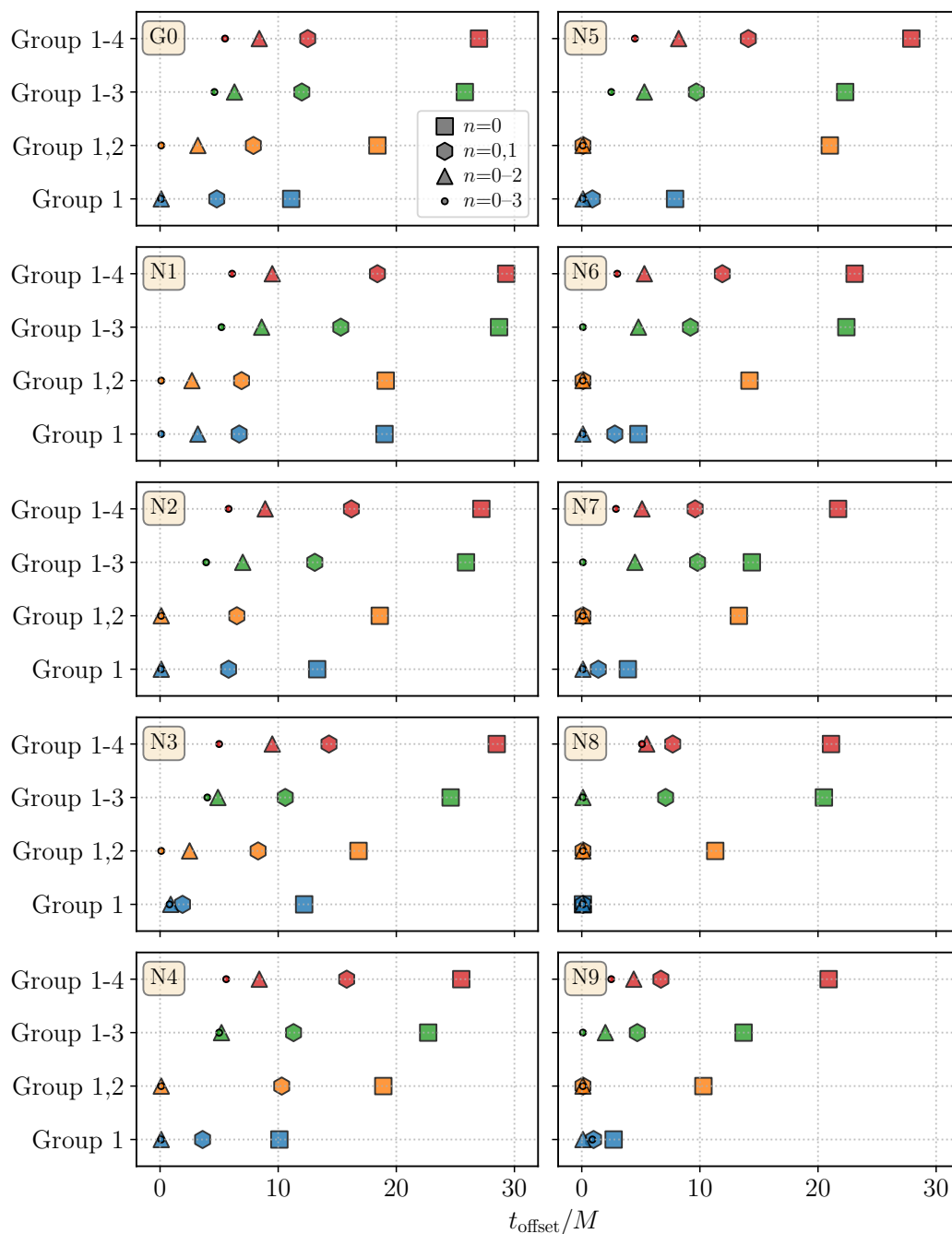


Figure 6.8: The S model transition time t_{trans} for binaries G0 and N1–N9. Each panel corresponds to a specific binary, labeled in the upper left corner. The horizontal axis is t_{offset}/M , and the discretized vertical axis specifies the (l, m) groups. Markers in different shapes indicate different numbers of overtones included, shown in the legend in the top left panel.

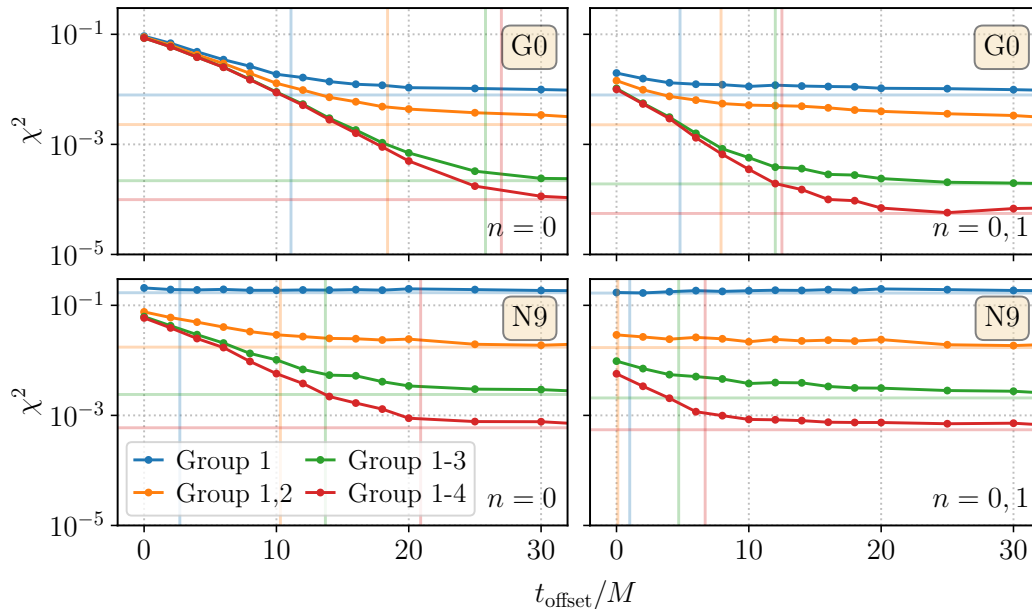


Figure 6.9: Example S model distances χ^2 for binaries G0 and N9, with respect to t_{offset} . The left and right columns are for $n = 0$ and $n = 0, 1$, respectively. Curves with different colors stand for different (l, m) Groups, as shown in the legend. The translucent vertical and horizontal lines indicate t_{trans} and χ^2_{min} , respectively.

- For N6: Y behaves better before adding Group 3; there is no distinction after adding Group 3 but not Group 4; S behaves better after adding Group 4.
- For N7: Y behaves better before adding Group 3; there is no distinction after adding Group 3.
- For N8–N9: Y behaves better before adding Group 4; there is no distinction after adding Group 4.

From the observations above, we notice that when not including enough (l, m) modes, S model is not necessarily better than Y model in estimating parameters of the remnant black hole. It indicates that the more accurate S model with spin-weighted spheroidal harmonics are more impacted by the missing (l, m) modes, while the less accurate Y model with orthogonal spin-weighted spherical harmonics is less impacted. For binaries with larger q , more (l, m) modes have non-negligible contributions to the ringdown waveform, and thus are all required for a precise characterization when using the S model. Once those (l, m) modes are included, the S model is consistently better than the Y model in both χ^2_{min} and the accuracy of $(M_{f,\text{est}}, \chi_{f,\text{est}})$.

Based on the discussion above, we conclude that the spin-weighted spheroidal harmonics (S model) is indeed the better representation of gravitational wave ring-down signals compared to the spin-weighted spherical harmonics (Y model), and that the difference is distinguishable in NR waveforms.

Let us comment on the temporal behavior of fitting with different (l, m) modes and overtones. Now we only consider the S model as we have demonstrated that the S model is a better representation. In Fig. 6.8, we summarize t_{trans} for binaries G0 and N1–N9, and further in Fig. 6.9, we show the details of χ^2 with respect to t_{offset} for two example binaries, G0 and N9. Essentially, the transition time t_{trans} happens when the missing overtones have mostly decayed in the NR waveform, with χ^2 reaching the minimum distance χ_{min}^2 determined by the precision that the model can achieve. Adding overtones brings forward t_{trans} , while adding (l, m) modes postpones t_{trans} — when the model becomes more accurate, the achievable χ_{min}^2 is smaller and thus takes more time to arrive. In other words, when the model template includes more (l, m) modes, more overtones are needed accordingly to reach the transition at a similar time. Similarly, mass ratios also influence the transition time as a result of different achievable χ_{min}^2 levels. As shown in Fig. 6.8, with the same sets of modes included in the template, t_{trans} generally occurs earlier when q is larger, because the achievable χ_{min}^2 is relatively larger.

In this section, we have discussed the S/Y model distinguishability and contribution of higher-order (l, m) modes and overtones. In the next section, we will further consider the situations when the progenitor binaries have spins along the $-\hat{z}$ direction that leads to anti-aligned spins in remnant black holes.

6.6 Spinning binaries and retrograde excitation

For nonspinning binaries, only the orbital angular momentum contributes to the remnant spin. While in general cases, the spin angular momentum of each individual progenitor black hole also leaves imprints in the ringdown waveform. Specifically, when the spins of the progenitor black holes are anti-aligned with the orbital angular momentum [64, 67, 92] and are large enough, retrograde modes could be excited in the remnant black hole. Retrograde excitations have been studied in the case of extreme mass ratio inspirals [29–32] using black hole perturbation theory [7]. Features of the ringdown waveforms have also been numerically studied in superkick BBH systems with equal mass [93], while not many studies have been done in the intermediate mass ratio inspirals [94, 95].

Table 6.5: SXS BBH waveforms used in Sec. 6.6.

Label ¹	SXS ID/Lev	q_{ref}	$(\vec{\chi}_{\text{ref},1})_z$	$(\vec{\chi}_{\text{ref},2})_z$	χ_{eff}	$(\vec{\chi}_f)_z$
A0	0188/Lev3	7.187	0.0000	0.0000	0.0000	0.3306
A1	1424/Lev3	6.464	-0.6566	-0.7991	-0.6757	-0.0929
A2	1435/Lev3	6.589	-0.7893	0.0673	-0.6764	-0.1828
A3	1422/Lev3	7.953	-0.8001	-0.4588	-0.7620	-0.2721

To study the retrograde excitations, we apply the fitting method described above to three binaries, A1–A3, with $\chi_f < 0$ ($|\chi_f|$ increases from A1 to A3), as listed in Table 6.5. A nonspinning binary A0 with $\chi_f > 0$ is included for comparison purposes. The orbital angular momentum and the spin angular momentum of the primary black hole, when in opposite directions, will cancel out to some extent in the merger stage [67, 92]. Because of that, retrograde QNMs, excited when the anti-aligned spin dominates, have smaller frequencies compared with the corresponding prograde modes. During the merger, the inspiral polarization pattern transitions smoothly to the dominating prograde or retrograde ringdown modes for remnant spin $\chi_f > 0$ and $\chi_f < 0$, respectively. This will be discussed in more details as discussed in Sec. 6.2.4.

In this section, we describe the fitting strategy, again, based on the relative importance of different modes in these waveforms (A0–A3) and implement the fitting with both prograde and retrograde modes included, or with prograde modes only. We then analyze the results and discuss the features of QNM frequencies and

¹Omit the same notes as in Table 6.3.

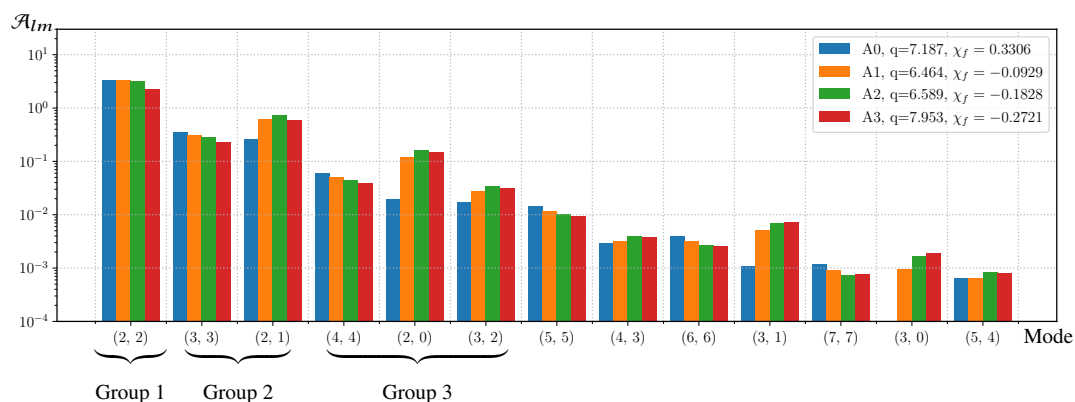


Figure 6.10: The relative importance \mathcal{A}_{lm} of binaries A0–A3. The definitions of Group 1–3 follow those in Fig. 6.4. Considering the computing cost with retrograde modes added, we only include (l, m) modes up to Group 3 in Sec. 6.6.

polarization patterns in the spin-anti-aligned case.

The relative importance \mathcal{A}_{lm} (defined in Eq. (6.16)) of binaries A0–A3 are plotted in Fig. 6.10. We follow the convention in Fig. 6.1 to extend the parameter space of the orbital frame spin χ_f to include negative values. In Secs. 6.4–6.5 we have demonstrated that the S model is more accurate compared to the Y model. In this section, we focus on the fitting using the S model. We follow the grouping and ranking of (l, m) modes discussed in Sec. 6.4.1. Given that the fitting including retrograde modes is more computationally expensive (the number of modes doubled) and that the main purpose here is to study the retrograde modes, we directly compare the results between including only the prograde modes up to Group 3, i.e., $(l, m) = (2, 2), (3, 3), (2, 1), (4, 4), (2, 0), (3, 2)$, and the results including the corresponding retrograde modes $(l, m) = (2, -2), (3, -3), (2, -1), (4, -4), (3, -2)$ as well. To confirm the contribution of overtones, we implement two sets of fittings with $n = 0$ and $n = 0, 1$ for each of the two scenarios above. Also, since χ_{\min}^2 will be stabilized at some given level after t_{trans} , we carry out the fitting up to $t_{\text{offset}} = 35M$ in this section.

The polarization patterns for A0–A3 have similar features at different emission directions, as shown in Fig. 6.11 — they all look counterclockwise when viewed from the north side ($\iota < \pi/2$) and clockwise when viewed from the south side ($\iota > \pi/2$). Combined with Fig. 6.3, we can see that the dominant excitations are either characterized by $B_{m>0}^{(S\pm)}$ for spin-aligned binaries, or by $B_{m<0}^{(S\pm)}$ for spin-anti-aligned binaries. Thus the dominant QMNs should be prograde modes for A0 but retrograde modes for A1–A3.

Another feature we expect to see when comparing the fitting results with and without the retrograde modes is associated with $|\chi_f|$. As shown in Fig. 6.2, the QNM frequencies of the retrograde modes correspond to the dotted curves, extending towards lower frequencies when $|\chi_f|$ increases from the points with $\chi_f = 0$, while the curves of prograde modes extend towards higher frequencies when $|\chi_f|$ increases. For larger $|\chi_f|$, the frequencies of a prograde mode and the corresponding retrograde mode become more separated in the spectrum. Thus the difference in fittings with and without the retrograde modes becomes more distinct.

The fitting results are shown in Fig. 6.12, where (a) and (b) correspond to the cases with overtones $n = 0$ and $n = 0, 1$, respectively. When showing $\chi_{f,\text{est}}$, we no longer use the relative error defined in Eq. (6.17), as it is not a good measure when the true value is small and comparable to the level of oscillation, e.g., A1 has

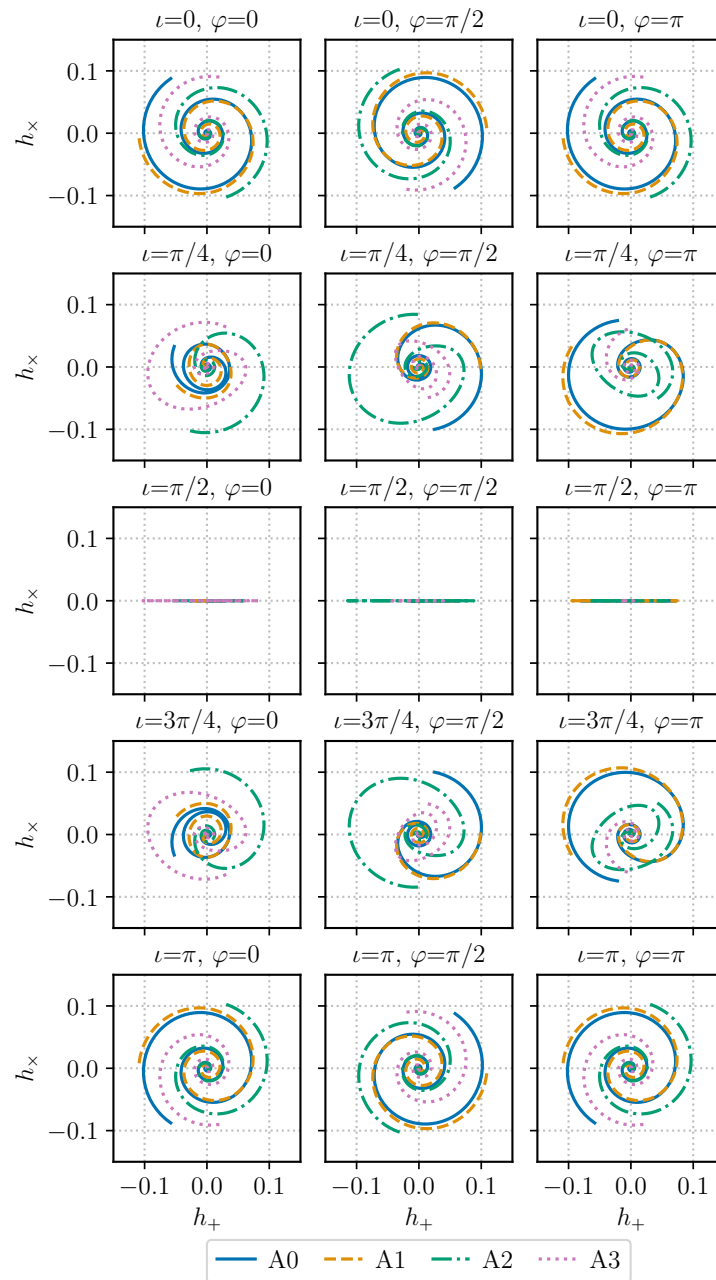


Figure 6.11: Polarization contents $(h_+(t), h_x(t))$ of the ringdown waveform of binaries A0–A3, with $t = 0$ starting at their own t_{peak} . The plotting convention follows that of Fig. 6.3.

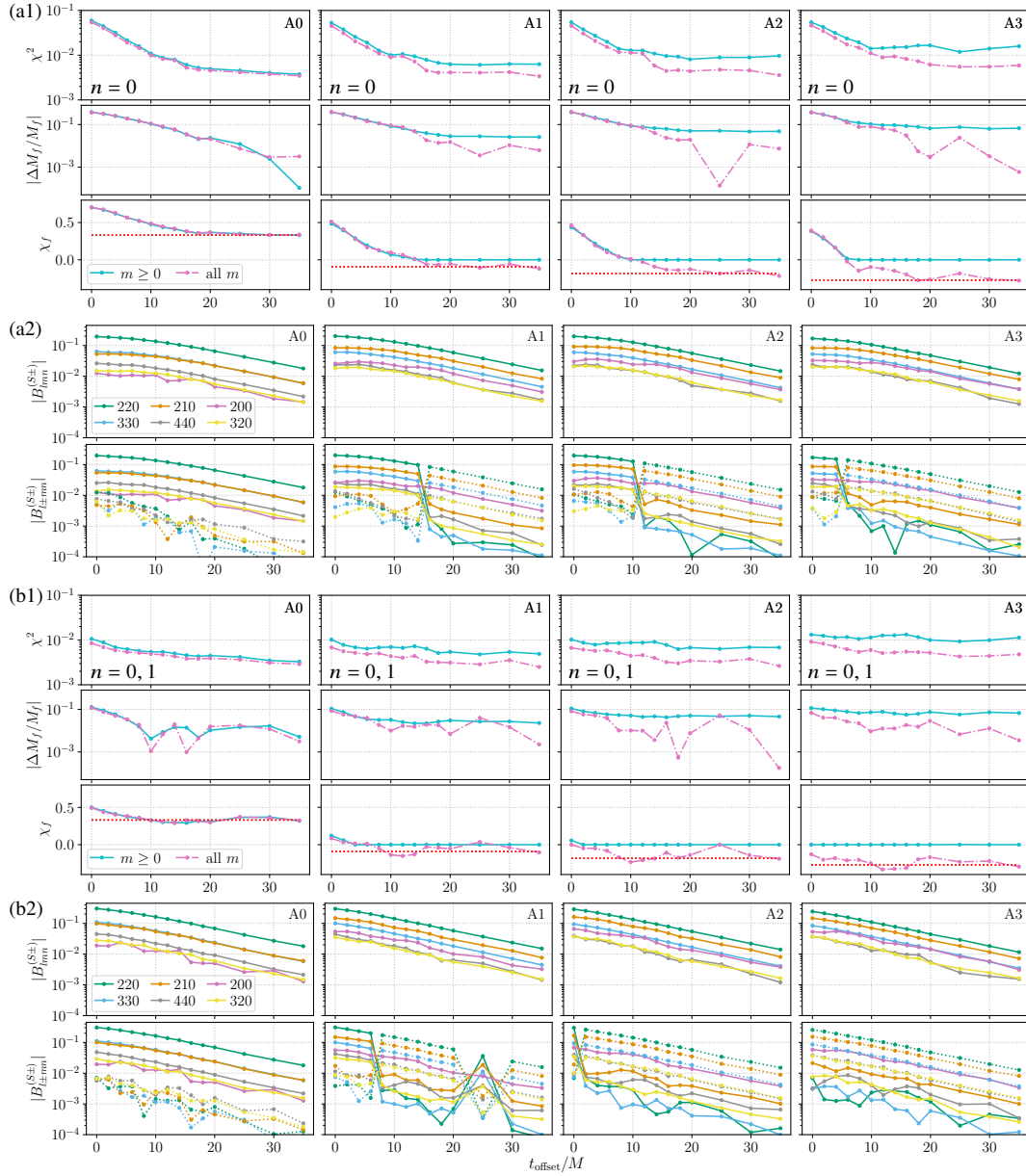


Figure 6.12: Fitting results for binaries A0–A3 using the S model with (a) only the fundamental modes $n = 0$ and (b) overtones $n = 0, 1$. For each binary (in each column), (a1) and (b1) show the optimal distance χ^2 , the relative error in $M_{f,\text{est}}$, and $\chi_{f,\text{est}}$; (a2) and (b2) show the magnitudes of the optimal coefficients. In (a1) and (b1), the solid cyan and dot-dashed magenta curves correspond to the results without and with retrograde modes included, respectively. The dotted red line in each χ_f block indicates the $\chi_{f,\text{true}}$. In (a2) and (b2), the upper and lower blocks show optimal coefficients when fitting without and with retrograde modes included, respectively. The solid and dotted curves correspond to prograde and retrograde modes, respectively. Note that $B_{lmn}^{(S+)}$ and $B_{lmn}^{(S-)}$ with the same lmn indices are roughly conjugate to each other (in the spin-aligned or spin-anti-aligned cases). For brevity, we only plot their absolute values.

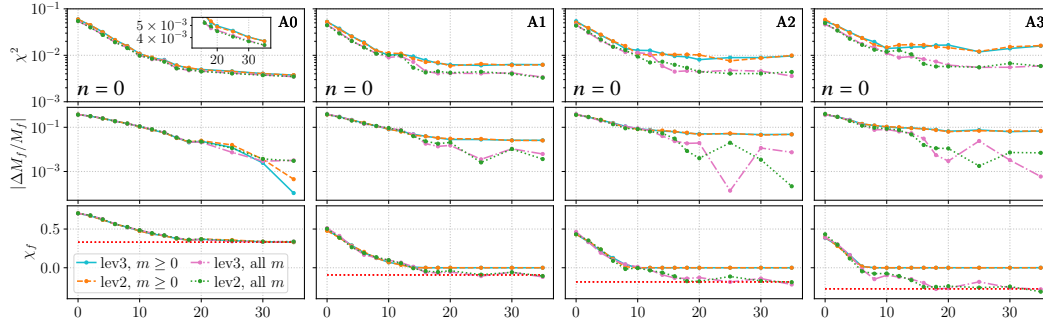


Figure 6.13: Fitting results for the binary waveforms A0–A3 using SXS data with different numerical levels. The S model used for fitting only contains the fundamental $n = 0$ modes. Plot settings are the same as Fig. 6.6. The inset in the χ^2 block of the first column shows the results in a zoomed-in range.

$\chi_{f,\text{true}} = -0.0929$, while $\chi_{f,\text{est}}$ oscillates up to ~ 0.1 . Instead, we directly compare $\chi_{f,\text{est}}$ to $\chi_{f,\text{true}}$ (the dotted red lines in Fig. 6.12).

In Fig. 6.12, the difference between excluding and including retrograde modes becomes more significant from left (A0) to right (A3). Taking the $n = 0$ case for example, we list the χ_{\min}^2 values in Table 6.6. For the nonspinning binary A0, the ratio between the χ_{\min}^2 values obtained with models including and excluding retrograde modes is close to unity, i.e., the difference is small. For binaries A1–A3, including retrograde modes largely improves the fitting accuracy and the improvement becomes more significant when $|\chi_f|$ is larger. Again, we estimate the fitting error by comparing the results obtained from different numerical resolution levels. As shown in Fig. 6.13, for all binaries A0–A3, the difference of results obtained between Lev3 and Lev2 is much smaller compared to the difference between using models including and excluding retrograde modes. Thus the results are not impacted by the numerical errors in the waveforms.

In terms of $M_{f,\text{est}}$ and $\chi_{f,\text{est}}$, when adding the retrograde modes for A0, there

Table 6.6: The values of χ_{\min}^2 when fitting with prograde modes only (P), versus fitting with both prograde and retrograde modes (PR) (all modes fundamental $n = 0$). The last row lists the ratio between the χ_{\min}^2 values obtained with and without including retrograde modes.

Model	A0	A1	A2	A3
P	0.0037	0.0063	0.0090	0.0130
PR	0.0035	0.0041	0.0046	0.0055
Ratio (PR/P)	0.93	0.65	0.51	0.42

is little difference in the fitting results. While for A1–A3, including retrograde modes improves the accuracy of $M_{f,\text{est}}$ and $\chi_{f,\text{est}}$ a lot. Specifically, in the cases of $\chi_{f,\text{true}} < 0$ when retrograde modes are not included, the algorithm tends to find a lower spin value but does not go below $\chi_f = 0$, even though we allow negative χ_f values in the fitting in both cases. This is because the prograde modes for $\chi_f < 0$ cannot satisfy the polarization patterns of the NR waveforms shown in Fig. 6.11.

The magnitudes of the optimal coefficients $B_{lmn}^{(S\pm)}$ and $B_{l\pm mn}^{(S\pm)}$ are also plotted in Fig. 6.12, characterizing the contribution of each mode. In (a2) and (b2), it is shown that adding retrograde modes barely influences the prograde mode coefficients (solid curves) at all discrete t_{offset} values for A0 (first column), and the prograde mode coefficients are consistently larger than the coefficients of the corresponding retrograde modes (dotted curves) by order(s) of magnitude. While for A1–A3, the retrograde modes appear to be dominant (with larger coefficients) when they are included in the fitting. In the case of A3 with $n = 0, 1$, as shown in the last column of (b2), the retrograde mode coefficients are dominant at all t_{offset} values. In other cases, the retrograde mode coefficients are larger at some t_{offset} values but switch to be smaller at other t_{offset} 's — and such a switch always happens when $\chi_{f,\text{est}}$ flips its sign. That is understandable from the polarization patterns of the data waveform, and the following two facts: (1) The prograde modes dominate for $\chi_f > 0$ while retrograde modes dominate for $\chi_f < 0$; (2) The dominating modes in both cases have similar polarization patterns and frequencies, and thus can generate similar waveforms. At earlier times, the incorrect results with dominant prograde modes are caused by the lack of overtones that have non-negligible contributions before t_{trans} , and thus the model is not accurate enough to represent the waveform, and more specifically, the correct frequencies. The switch happens at an earlier time for binaries with a larger mass ratio (A3). For A1, there is another switch at $t_{\text{offset}} = 25M$ as shown in the second column of (b2). This could be caused by numerical errors or the random jumps in the (M_f, χ_f) parameter space — when $|\chi_{f,\text{true}}|$ has such a small value of 0.0929, the estimates can easily oscillate around zero.

The results and analysis in this section are all consistent with our expectations discussed in Sec. 6.2.4. An interesting follow-up study is to map the progenitor black hole properties to the ringdown QNM excitations. We leave it to future work.

6.7 Discussion

In this work, using results from numerical simulations, we verified predictions of black-hole perturbation theory for gravitational waves emitted by remnant black holes of binary mergers. In particular, we simultaneously fitted the temporal and spatial dependences of the NR ringdown waveforms to models of QNM expansion. Comparing between the spin-weighted spheroidal harmonics (S model) and the spin-weighted spherical harmonics (Y model), we have demonstrated that the S model, as predicted by the Teukolsky equation, is the more faithful representation of the ringdown waveform. The combination of temporal and spatial behaviors allowed a more comprehensive study of the linearized Einstein's equations in the background of a Kerr black hole and complemented existing black hole spectroscopy studies.

With spatial dependence included, we reinforced conclusions in previous studies of black-hole spectroscopy about higher-order (l, m) modes and overtones. When the progenitor binary has asymmetric masses, higher-order angular modes are required to accurately represent the ringdown waveform. For nonspinning binaries, the necessity of taking into account the higher-order modes depends on the mass ratio and the resulting remnant spin magnitude. The $(l, m) = (2, 2)$ fundamental mode is enough to achieve an accuracy above 99% (i.e., $\chi_{\min}^2 < 0.01$) when modeling the ringdown with the S model for $q < 1.25$, while for $1.25 < q < 4$ and $q > 5$, about three and six modes are needed, respectively, to achieve that level of accuracy (with changes subject to the grouping strategy, see Sec. 6.4.1). On the other hand, adding overtones improves the accuracy of the model at an earlier time of the ringdown. For binaries with higher mass ratios, when more (l, m) modes are included, more overtones are needed accordingly to accurately represent the early stage ringdown waveform. The fact that overtones can improve the QNM expansion when both temporal and angular patterns are matched to numerical waveforms, and the fact that the S model works better than the Y model, provide stronger evidence that overtones are truly excited, and that such an improvement is not due to overfitting.

During the transition from inspiral to ringdown, the magnitudes, spatial dependence, and polarization patterns of the gravitational waves during the inspiral stage are transferred to the ringdown stage. Our study confirmed this transfer. The magnitudes of the initial excitation of the (l, m) ringdown QNMs are determined by the leading post-Newtonian order of the mode during inspiral, with possible suppression due to symmetry. The polarization content of the mode (i.e., left- versus right-hand) is determined by the direction of the orbital angular momentum of the

binary. The remnant spin direction and the excitation of prograde or retrograde mode are determined by the binary dynamics. When the remnant spin is aligned (anti-aligned) with the orbital angular momentum, the prograde (retrograde) modes are dominant. Including the retrograde modes is necessary to build an accurate model of the ringdown waveform in the spin-anti-aligned case. The more general cases with the remnant spin misaligned with the orbital angular momentum will be left to future work.

Under the sensitivity of the currently working detectors, higher-order angular modes, overtones, or retrograde modes generally do not play an important role in the detection or parameter estimation for most of the events. However, events with high signal-to-noise ratios (especially the high signal-to-noise ringdown) are expected to be observed regularly with the next generation detectors [58]. Features discussed in this work will be important for future studies of the source properties.

Finally, this work also provided a theoretical and analytical foundation for developing strategies for testing the temporal-spatial emission patterns of the ringdown. Even though, practically, each binary is only observed from one particular wave-emission direction, angular emission pattern can be reconstructed by collecting multiple events.

6.8 Appendix: QNM expansion conventions

Solutions to the Teukolsky equation can be written in the form of:

$$\psi(t, r, \tilde{t}, \tilde{\varphi}) = e^{-i\omega_{lmn}t} R_{lmn}(r) S_{lmn}(\tilde{t}) e^{im\tilde{\varphi}}. \quad (6.18)$$

Here (l, m) are the angular quantum numbers, n is the overtone number, and $R_{lmn}(r)$ is the radial function. To avoid confusion, we continue using the notations defined in the main text, i.e., the coordinates in the final spin frame $(\tilde{t}, \tilde{\varphi})$ here and the remnant black hole parameters (a_f, M_f) , although the solutions to the Teukolsky equation apply to all Kerr black holes.

As it turns out, for each overtone number n , there is a family of modes with $\text{Re}(\omega_{lmn}) > 0$ and another family with $\text{Re}(\omega_{lmn}) < 0$. They correspond to modes with polarization patterns that either rotate counterclockwise or clockwise, when the wave comes toward the observer directly face-on. We denote $\text{Re}(\omega_{lmn}^R) > 0$ as right-handed (R) and $\text{Re}(\omega_{lmn}^L) < 0$ as left-handed (L). At $r \rightarrow +\infty$, for both

families, we can write:

$$\psi_{lmn}^R(t, r \rightarrow +\infty, \tilde{t}, \tilde{\varphi}) \sim e^{-i\omega_{lmn}^R(t-r^*)} r^{-1} S_{lmn}^R(\tilde{t}) e^{im\tilde{\varphi}}, \quad (6.19)$$

$$\psi_{lmn}^L(t, r \rightarrow +\infty, \tilde{t}, \tilde{\varphi}) \sim e^{-i\omega_{lmn}^L(t-r^*)} r^{-1} S_{lmn}^L(\tilde{t}) e^{im\tilde{\varphi}}, \quad (6.20)$$

where r^* is the tortoise coordinate [9].

Note that ω_{lmn}^R corresponds to the usual tabulated values of QNM frequencies, so we write

$$\omega_{lmn}^R = \omega_{lmn}. \quad (6.21)$$

Here $m > 0$ are prograde, and $m < 0$ are retrograde modes. We also have

$$S_{lmn}^R(\tilde{t}) e^{im\tilde{\varphi}} = -2S_{lmn}(\chi_f M_f \omega_{lmn}, \tilde{t}, \tilde{\varphi}). \quad (6.22)$$

The frequencies and the angular mode functions of the L and R modes are related, and we wish to make this relation explicit. We notice that if $\psi(t, r, \tilde{t}, \tilde{\varphi})$ is an outgoing solution to the Teukolsky equation, then $\psi^*(t, r, \pi - \tilde{t}, \tilde{\varphi})$ is also an outgoing solution, with $*$ denoting the complex conjugate. In this way, $\psi_{lmn}^{R*}(t, r, \pi - \tilde{t}, \tilde{\varphi})$ is also a QNM, with

$$\psi_{lmn}^{R*}(t, r, \pi - \tilde{t}, \tilde{\varphi}) = e^{i\omega_{lmn}^*(t-r^*)} r^{-1} {}_{-2}S_{lmn}^*(\chi_f M_f \omega_{lmn}, \pi - \tilde{t}, \tilde{\varphi}). \quad (6.23)$$

We can further write [9]

$${}_{-2}S_{lmn}^*(\chi_f M_f \omega_{lmn}, \pi - \tilde{t}, \tilde{\varphi}) = {}_{-2}S_{lmn}^*(\chi_f M_f \omega_{lmn}, \pi - \tilde{t}) e^{-im\tilde{\varphi}} \quad (6.24)$$

$$= {}_{-2}S_{lmn}(\chi_f M_f \omega_{lmn}^*, \pi - \tilde{t}) e^{-im\tilde{\varphi}} \quad (6.25)$$

$$= (-1)^l {}_{-2}S_{l-mn}(-\chi_f M_f \omega_{lmn}^*, \tilde{t}) e^{-im\tilde{\varphi}}, \quad (6.26)$$

leading to

$$\psi_{lmn}^{R*}(t, r, \pi - \tilde{t}, \tilde{\varphi}) = (-1)^l e^{i\omega_{lmn}^*(t-r^*)} r^{-1} {}_{-2}S_{l-mn}(-\chi_f M_f \omega_{lmn}^*, \tilde{t}, \tilde{\varphi}). \quad (6.27)$$

By comparing Eqs. (6.27) and (6.20) and replacing m with $-m$, we can see that

$$\omega_{lmn}^L = -\omega_{l-mn}^*, \quad \psi_{lmn}^L(t, r, \tilde{t}, \tilde{\varphi}) = (-1)^l \psi_{l-mn}^{R*}(t, r, \pi - \tilde{t}, \tilde{\varphi}). \quad (6.28)$$

Using the symmetry above, we can expand the QNM in two different ways. To avoid confusion, we intend to write out all arguments explicitly. The first way is

to group in terms of (l, m) spin-weighted spherical harmonics (see Table 6.2 for corresponding notations [a][b][c][d]):

$$h(t, r, \tilde{t}, \tilde{\varphi}) \sim \sum_{l=2}^{l_{\max}} \sum_{m=-l}^l \sum_{n=0}^{n_{\max}} \left[A_{lmn}^R \psi_{lmn}^R(t, r, \tilde{t}, \tilde{\varphi}) + A_{lmn}^L \psi_{lmn}^L(t, r, \tilde{t}, \tilde{\varphi}) \right] \quad (6.29a)$$

$$= \frac{M_f}{r} \sum_{l=2}^{l_{\max}} \sum_{m=-l}^l \sum_{n=0}^{n_{\max}} \left[A_{lmn}^R e^{-i\omega_{lmn}^R(t-r^*)} S_{lmn}^R(\tilde{t}) e^{im\tilde{\varphi}} \right. \\ \left. + A_{lmn}^L (-1)^l \psi_{l-mn}^{R*}(t, r, \pi - \tilde{t}, \tilde{\varphi}) \right] \quad (6.29b)$$

$$= \frac{M_f}{r} \sum_{l=2}^{l_{\max}} \sum_{m=-l}^l \sum_{n=0}^{n_{\max}} \left[\underbrace{A_{lmn}^R e^{-i\omega_{lmn}^R(t-r^*)} {}_{-2}S_{lmn}(\chi_f M_f \omega_{lmn}, \tilde{t}, \tilde{\varphi})}_{[a] \text{ for } m>0; [c] \text{ for } m<0;} \right. \\ \left. + \underbrace{A_{lmn}^L e^{i\omega_{l-mn}^*(t-r^*)} {}_{-2}S_{lmn}(-\chi_f M_f \omega_{l-mn}^*, \tilde{t}, \tilde{\varphi})}_{[d] \text{ for } m>0; [b] \text{ for } m<0.} \right]. \quad (6.29c)$$

In this way, A_{lmn}^R and A_{lmn}^L correspond to the excited modes with different absolute oscillation frequencies and decay rates; there is one prograde and one retrograde mode in each lmn group. The two terms have different polarization patterns (R and L), but the same emission direction: for $m > 0$, both terms emit toward the north, while for $m < 0$, both terms emit toward the south.

Alternatively, switching m and $-m$ for the A_{lmn}^L term in Eq. (6.29c), we can regroup the summation as follows:

$$h(t, r, \tilde{t}, \tilde{\varphi}) = \frac{M_f}{r} \sum_{l=2}^{l_{\max}} \sum_{m=-l}^l \sum_{n=0}^{n_{\max}} \left[A_{lmn}^R e^{-i\omega_{lmn}^R(t-r^*)} {}_{-2}S_{lmn}(\chi_f M_f \omega_{lmn}, \tilde{t}, \tilde{\varphi}) \right. \\ \left. + A_{l-mn}^L e^{i\omega_{l-mn}^*(t-r^*)} {}_{-2}S_{l-mn}(-\chi_f M_f \omega_{l-mn}^*, \tilde{t}, \tilde{\varphi}) \right] \quad (6.30a)$$

$$= \frac{M_f}{r} \sum_{l=2}^{l_{\max}} \sum_{m=-l}^l \sum_{n=0}^{n_{\max}} \left[A_{lmn}^R e^{-i\omega_{lmn}^R(t-r^*)} {}_{-2}S_{lmn}(\chi_f M_f \omega_{lmn}, \tilde{t}, \tilde{\varphi}) \right. \\ \left. + A_{l-mn}^L e^{i\omega_{l-mn}^*(t-r^*)} (-1)^l {}_{-2}S_{l-mn}^*(\chi_f M_f \omega_{l-mn}, \pi - \tilde{t}, \tilde{\varphi}) \right] \quad (6.30b)$$

$$= \frac{M_f}{r} \sum_{l=2}^{l_{\max}} \sum_{m=-l}^l \sum_{n=0}^{n_{\max}} \left[\underbrace{A_{lmn}^{(+)} e^{-i\omega_{lmn}^R(t-r^*)} {}_{-2}S_{lmn}(\chi_f M_f \omega_{lmn}, \tilde{t}, \tilde{\varphi})}_{[a] \text{ for } m>0; [c] \text{ for } m<0;} \right. \\ \left. + \underbrace{A_{lmn}^{(-)} e^{i\omega_{l-mn}^*(t-r^*)} {}_{-2}S_{l-mn}^*(\chi_f M_f \omega_{l-mn}, \pi - \tilde{t}, \tilde{\varphi})}_{[b] \text{ for } m>0; [d] \text{ for } m<0.} \right]. \quad (6.30c)$$

Here we have defined

$$A_{lmn}^{(+)} = A_{lmn}^R, \quad A_{lmn}^{(-)} = (-1)^l A_{l-mn}^L. \quad (6.31)$$

In this way of grouping, $A_{lmn}^{(+)}$ and $A_{lmn}^{(-)}$ correspond to the excited modes with different angular emission patterns (in terms of both polarization and direction), but the same absolute oscillation frequency and decay rates. Prograde and retrograde modes are not mixed into the same lmn group. Eq. (6.30c) has the same form as we defined in the main text Eq. (6.1). We believe this is more convenient, since modes in the same group tends to be either both excited or both not excited. For example, the entire retrograde groups can be ignored in many situations, as is done in e.g., Ref. [36].

6.9 Appendix: Limitation of single-direction fittings

Here we briefly comment on the limitation of single-direction fittings, which is one of the motivations of implementing a temporal-spatial fitting strategy in this work. In brief, the S/Y models cannot be distinguished using the signal of a single event without prior information about QNM excitations.

The excitation amplitudes $\{B_{lmn}^{(S\pm/Y\pm)}\}$ are governed by progenitor binary dynamics, and the emission strength varies with the spherical coordinate $\vec{\Omega}$, especially the inclination angle ι [58]. The waveform observed from a single direction cannot reveal angular distribution in the source frame, and thus we can only fit the waveform with a single-direction model:

$$h^{\text{SD}}(t) = \frac{M_f}{r} \sum_{l=2}^{l_{\max}} \sum_{m=-l}^{m=l} \sum_{n=0}^{n_{\max}} \left[C_{lmn}^{(+)} e^{-i\omega_{lmn}t} + C_{lmn}^{(-)} e^{i\omega_{lmn}^*t} \right], \quad (6.32)$$

with $\{C_{lmn}^{(\pm)}\}$ being the relative amplitudes of different frequency components. While we do find that single-direction fitting is capable of finding the dominant frequency components, the relative amplitudes $\{C_{lmn}^{(\pm)}\}$ do not help in the S/Y model selection unless the binary inclination is known from the inspiral stage. Taking the spin-aligned case for an example, the $\{C_{lmn}^{(\pm)}\}$ are related to $\{B_{lmn}^{(S\pm/Y\pm)}\}$ via:

$$C_{lmn}^{(+)} = B_{lmn}^{(S+)} {}_{-2}S_{lmn}(\gamma_{lmn}, \tilde{\iota}, \tilde{\varphi}), \quad B_{lmn}^{(Y+)} {}_{-2}Y_{lm}(\iota, \varphi), \quad (6.33a)$$

$$C_{lmn}^{(-)} = B_{lmn}^{(S-)} {}_{-2}S_{lmn}^*(\gamma_{lmn}, \pi - \tilde{\iota}, \tilde{\varphi}), \quad B_{lmn}^{(Y-)} {}_{-2}Y_{lm}^*(\pi - \tilde{\iota}, \tilde{\varphi}), \quad (6.33b)$$

for the S/Y models, respectively. However, in practice, the inclination angle ι is usually not well constrained, even from the full inspiral-merger-ringdown waveform fitting. Thus, the S and Y models are not distinguishable from a single event.

In addition, due to the parameter degeneracy in single-direction fitting, it is likely that different (M_f, χ_f) values with different dominant QNMs could result

in the same set of dominant frequencies. Thus, for non-face-on emission or more complicated binaries with precession and/or misaligned spin [45, 76], the lack of spatial information might lead to incorrect estimation of the source parameters. This degeneracy could in principle be broken if we know the relative amplitude of each QNM *a priori*, and we can, in turn, use the relative amplitudes of different frequency components to estimate the inclination angle.

6.10 Appendix: Numerical implementation for optimizing $\{B_{lmn}^{(\pm)}\}$

In the fitting, the NR ringdown waveform is treated as data, $h(\vec{\Omega}, t)$. The template waveform $g^{(S/Y)}(\vec{\Omega}, t)$ is built from Eq. (6.1) and Eq. (6.3) for the S and Y models, respectively, with excitation coefficients $\{B_{lmn}^{(S\pm/Y\pm)}\}$ to be determined. In numerical realization, we use discretized representation to express temporal-spatial functions and their inner products. We define a $N_t \times N_\Omega$ matrix \mathbb{M}_h to represent the temporal-spatial function $h(\vec{\Omega}, t)$, where N_t is the number of discretized time steps and N_Ω is the number of spatial points that include reasonably sampled ι and φ values:

$$\mathbb{M}_h = \begin{pmatrix} \bar{h}(\vec{\Omega}_1, t_1) & \bar{h}(\vec{\Omega}_1, t_2) & \dots & \bar{h}(\vec{\Omega}_1, t_{N_t}) \\ \bar{h}(\vec{\Omega}_2, t_1) & \bar{h}(\vec{\Omega}_2, t_2) & \dots & \bar{h}(\vec{\Omega}_2, t_{N_t}) \\ \dots & \dots & \dots & \dots \\ \bar{h}(\vec{\Omega}_{N_\Omega}, t_1) & \bar{h}(\vec{\Omega}_{N_\Omega}, t_2) & \dots & \bar{h}(\vec{\Omega}_{N_\Omega}, t_{N_t}) \end{pmatrix}. \quad (6.34)$$

In the matrix (6.34), $\bar{h}(\vec{\Omega}_i, t_j) \equiv \sqrt{\sin \iota_i} h(\vec{\Omega}_i, t_j)$ is the strain value at a specific spatial point $\vec{\Omega}_i = (\iota_i, \varphi_i)$ and a specific time step t_j , weighted by $\sqrt{\sin \iota_i}$, the square root of the Jacobian for a unit sphere. This weight factor is introduced because we are going to represent the temporal-spatial inner product (Eq. (6.7)) using the vector product in Eq. (6.36), and want to have the Jacobian $\sin \iota_i$ shared equally by the data and template waveforms. We further express the matrix in a $1 \times N_t N_\Omega$ row vector:

$$\vec{\mathbb{V}}_h = \left(\bar{h}(\vec{\Omega}_1, t_1), \dots, \bar{h}(\vec{\Omega}_1, t_{N_t}), \bar{h}(\vec{\Omega}_2, t_1), \dots \right. \\ \left. \dots, \bar{h}(\vec{\Omega}_{N_\Omega-1}, t_{N_t}), \bar{h}(\vec{\Omega}_{N_\Omega}, t_1), \dots, \bar{h}(\vec{\Omega}_{N_\Omega}, t_{N_t}) \right). \quad (6.35)$$

For the template waveform $g(\vec{\Omega}, t)$, using the similar matrix and vector representations as (6.34) and (6.35), the temporal-spatial inner product in Eq. (6.7) can be represented by the vector product as follows (c.f. Eq.(6.13)):

$$\langle g | h \rangle = \vec{\mathbb{V}}_h \vec{\mathbb{V}}_g^\dagger. \quad (6.36)$$

With a given set of parameters (M_f, χ_f) , each lmn mode contributes to two $1 \times N_t N_\Omega(M_f, \chi_f)$ vectors $\vec{\mathbb{V}}_{lmn}^{(S\pm/Y\pm)}(M_f, \chi_f)$, for S/Y model respectively. Combined

with coefficients $B_{lmn}^{(S\pm/Y\pm)}$, we can construct the discretized template waveform $g^{(S/Y)}(\vec{\Omega}, t; M_f, \chi_f)$ in the (6.35) vector form:

$$\vec{V}_g^{(S/Y)}(M_f, \chi_f) = \sum_{lmn} \left(B_{lmn}^{(S+/Y+)} \vec{V}_{lmn}^{(S+/Y+)}(M_f, \chi_f) + B_{lmn}^{(S-/Y-)} \vec{V}_{lmn}^{(S-/Y-)}(M_f, \chi_f) \right). \quad (6.37)$$

Considering the \pm components, there are $2N_{lmn}$ modes in total. We form a large matrix for these $2N_{lmn}$ modes:

$$\mathcal{M}_g^{(S/Y)}(M_f, \chi_f) = \begin{pmatrix} \vec{V}_{(lmn)_1}^{(S+/Y+)}(M_f, \chi_f) \\ \dots \\ \vec{V}_{(lmn)N_{lmn}}^{(S+/Y+)}(M_f, \chi_f) \\ \vec{V}_{(lmn)_1}^{(S-/Y-)}(M_f, \chi_f) \\ \dots \\ \vec{V}_{(lmn)N_{lmn}}^{(S-/Y-)}(M_f, \chi_f) \end{pmatrix}, \quad (6.38)$$

and assemble the matrix with the coefficient vector,

$$\vec{B}^{(S/Y)} = \left(B_{(lmn)_1}^{(S+/Y+)}, \dots, B_{(lmn)N_{lmn}}^{(S+/Y+)}, B_{(lmn)_1}^{(S-/Y-)}, \dots, B_{(lmn)N_{lmn}}^{(S-/Y-)} \right), \quad (6.39)$$

such that the discretized template waveform (6.37) can be expressed as:

$$\vec{V}_g^{(S/Y)}(M_f, \chi_f) = \vec{B}^{(S/Y)} \mathcal{M}_g^{(S/Y)}(M_f, \chi_f). \quad (6.40)$$

The fitting procedure is as follows: For each set of remnant parameters (M_f, χ_f) , we obtain the QNM frequencies $\{\omega_{lmn}\}$ using the `qnm` package [75] and compose the template waveform (6.38) for S and Y models, separately. We then apply multi-variable linear regression [96] to determine the least-squares excitation coefficients $B_{lmn}^{(S\pm/Y\pm)}$ (c.f. Eq. (6.15)):

$$\vec{B}_{1-s}^{(S/Y)}(M_f, \chi_f) = [\vec{V}_h \mathcal{M}_g^{(S/Y)\dagger}(M_f, \chi_f)] [\mathcal{M}_g^{(S/Y)}(M_f, \chi_f) \mathcal{M}_g^{(S/Y)\dagger}(M_f, \chi_f)]^{-1}, \quad (6.41)$$

such that the distance between the data waveform \vec{V}_h and the template waveform $\vec{V}_{g,1-s}^{(S/Y)}(M_f, \chi_f) = \vec{B}_{1-s}^{(S/Y)}(M_f, \chi_f) \mathcal{M}_g^{(S/Y)}(M_f, \chi_f)$ is minimized (c.f. Eq. (6.14)):

$$\chi^2[h, g_{1-s}^{(S/Y)}(M_f, \chi_f)] = \frac{[\vec{V}_h - \vec{V}_{g,1-s}^{(S/Y)}(M_f, \chi_f)] [\vec{V}_h - \vec{V}_{g,1-s}^{(S/Y)}(M_f, \chi_f)]^\dagger}{\vec{V}_h \vec{V}_h^\dagger}. \quad (6.42)$$

Note that Eqs. (6.37)–(6.42) are defined under values of M_f and χ_f . Then we carry out a search in the 2D parameter space of (M_f, χ_f) to find the minimum point of

$\chi^2[h, g_{1-s}^{(S/Y)}(M_f, \chi_f)]$ and define it as the optimal distance:

$$\chi^2[h, g_{\text{opt}}^{(S/Y)}] \equiv \min_{(M_f, \chi_f)} \chi^2[h, g_{1-s}^{(S/Y)}(M_f, \chi_f)]. \quad (6.43)$$

The mass and spin that yield this optimal distance are denoted by $(M_{f,\text{est}}, \chi_{f,\text{est}})$ (for S and Y models separately). The corresponding excitation coefficients (6.41) computed with $(M_{f,\text{est}}, \chi_{f,\text{est}})$ are the optimal coefficients and are labeled as $\vec{B}_{\text{opt}}^{(S/Y)}$. Comparing results between the S and Y models, the one that yields a smaller optimal distance demonstrates a better fit.

6.11 Appendix: Full fitting results for N1–N9

The full fitting results for N1–N9 are shown in Figs. 6.14–6.22, plotted in the same way as Fig. 6.5.

6.12 Appendix: Numerical error in SXS waveforms

In the main text, we use the highest numerical resolution levels available for each chosen binary, as listed in Tables 6.3 and 6.5. In this appendix, we show the results of the lower SXS numerical resolution levels for binaries N1–N9. Figs. 6.23–6.25 are plotted in a similar way as Fig. 6.6 for both the S and Y models. It shows that all the differences from various numerical levels are clearly smaller than the difference from using different fitting models (S versus Y , or including different lmn modes). Therefore, our conclusions in Sec. 6.5 are not impacted by numerical errors of the waveforms.

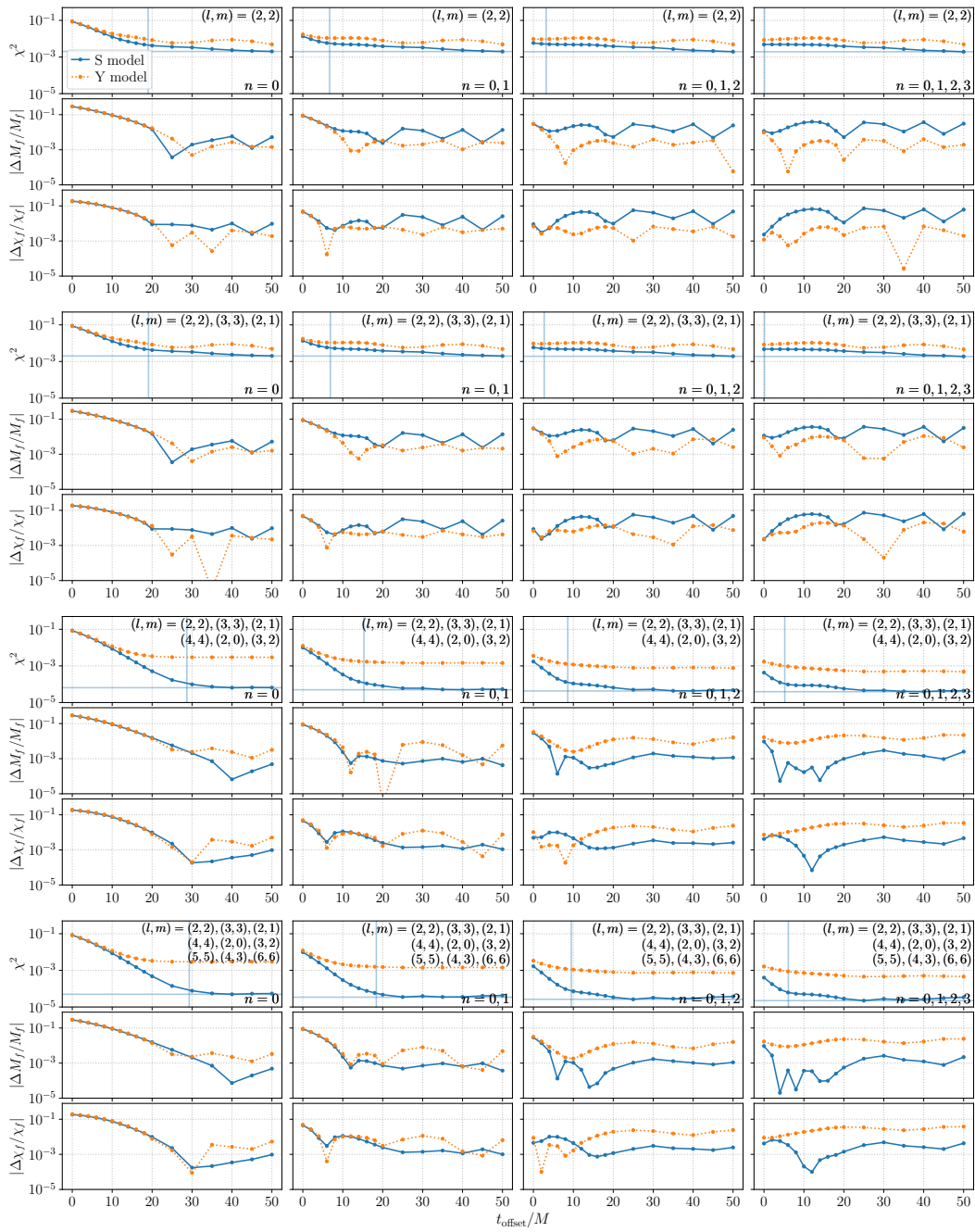


Figure 6.14: Fitting results for binary waveform N1. Plot settings are the same as Fig. 6.5.

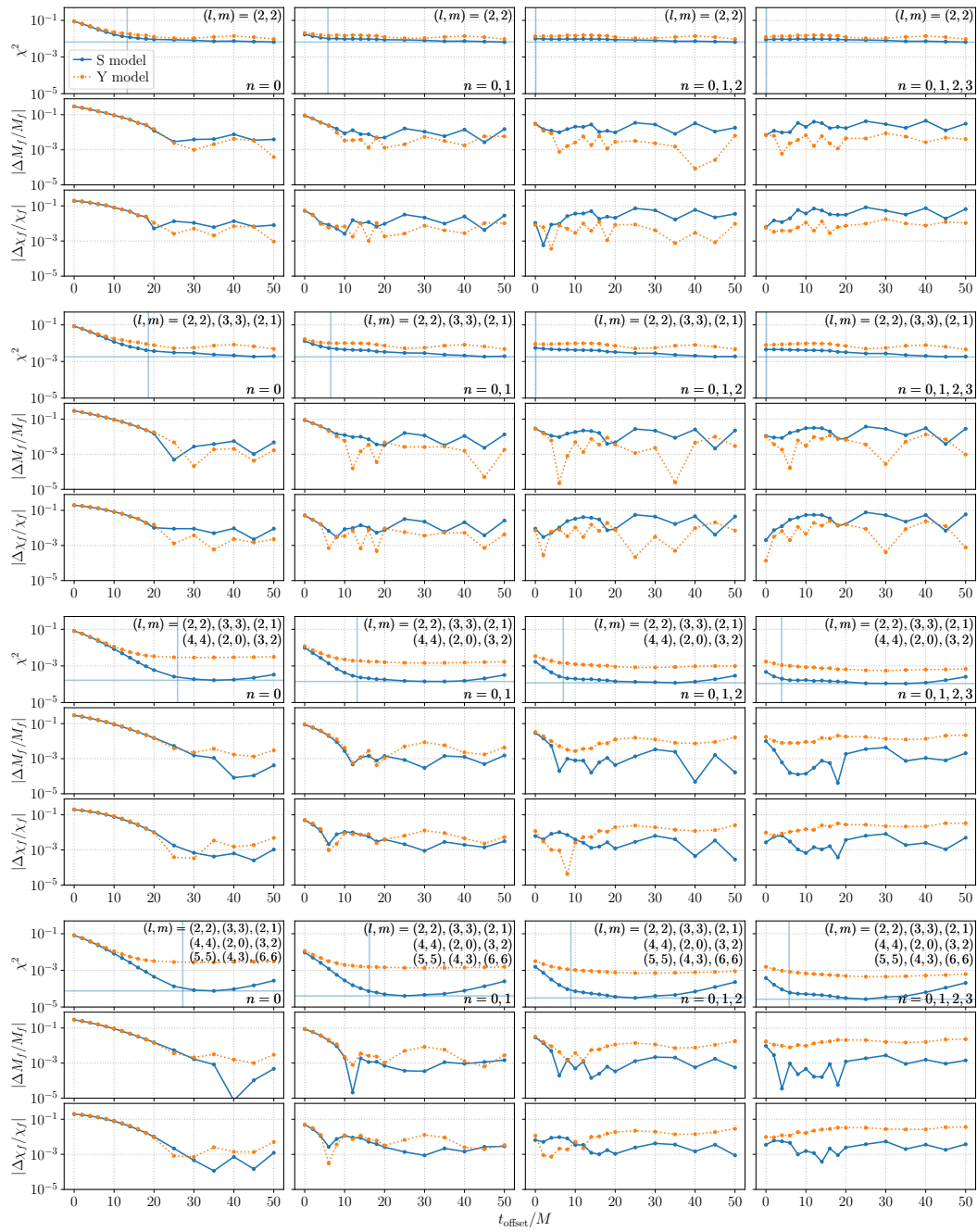


Figure 6.15: Fitting results for binary waveform N2. Plot settings are the same as Fig. 6.5.

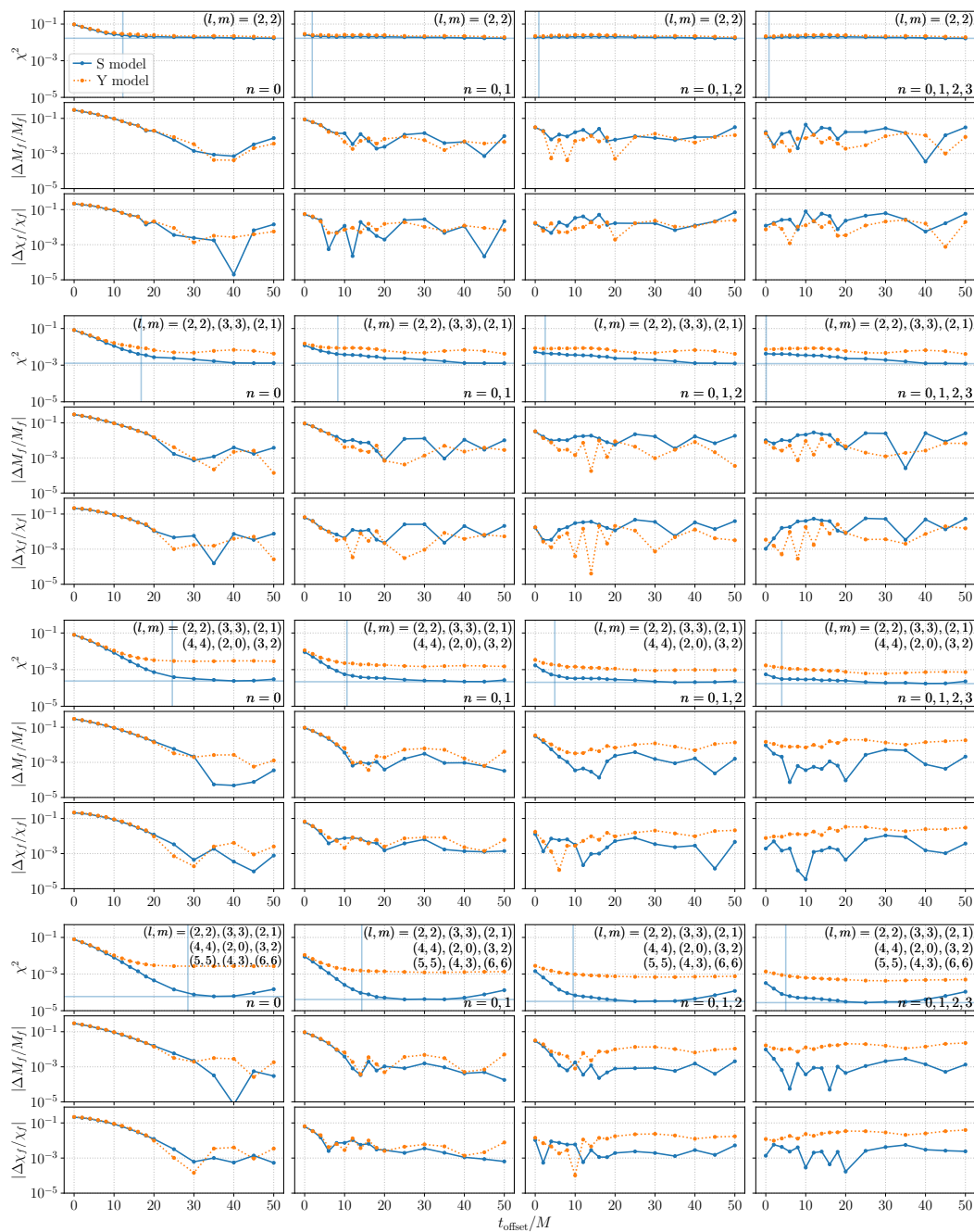


Figure 6.16: Fitting results for binary waveform N3. Plot settings are the same as Fig. 6.5.

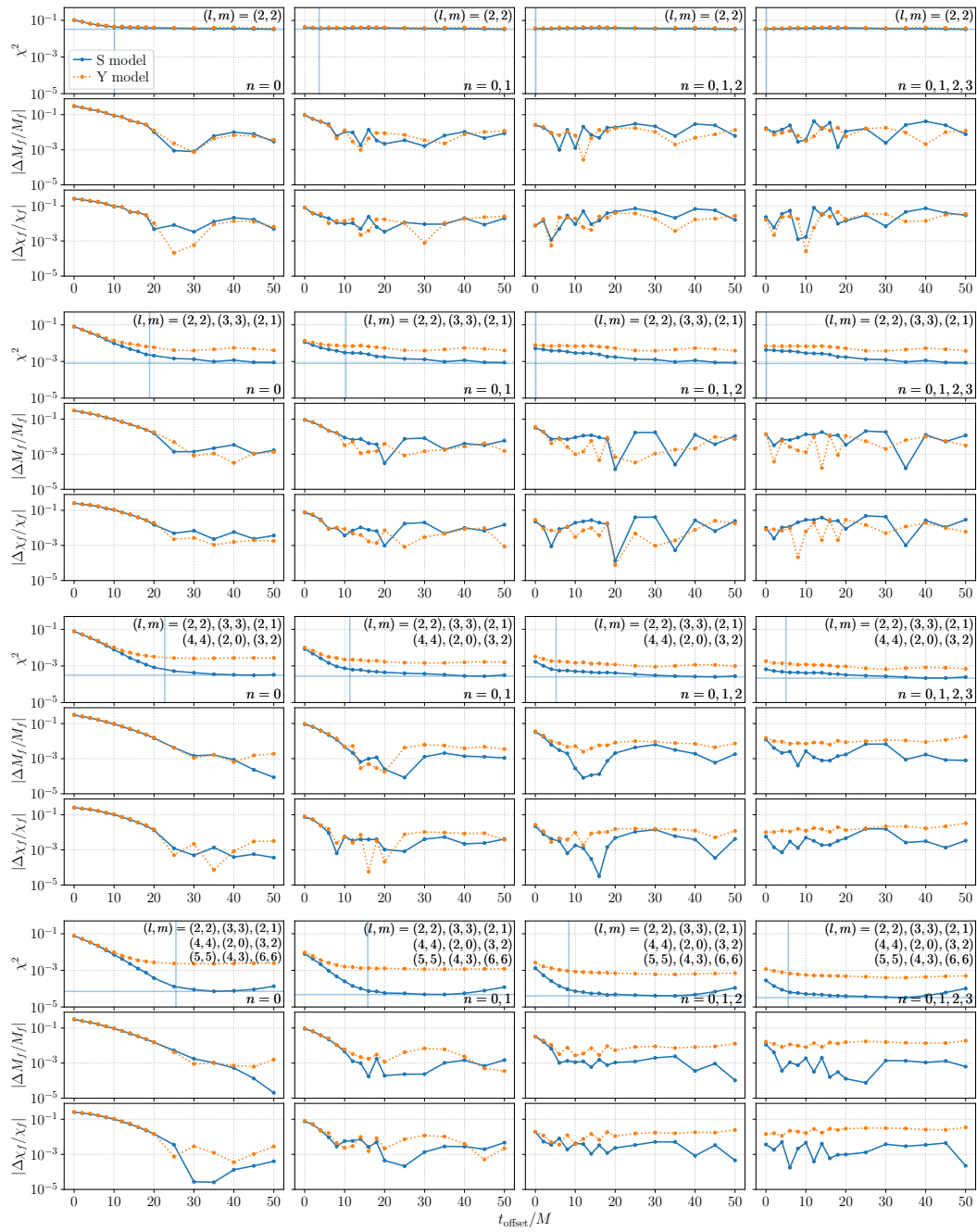


Figure 6.17: Fitting results for binary waveform N4. Plot settings are the same as Fig. 6.5.

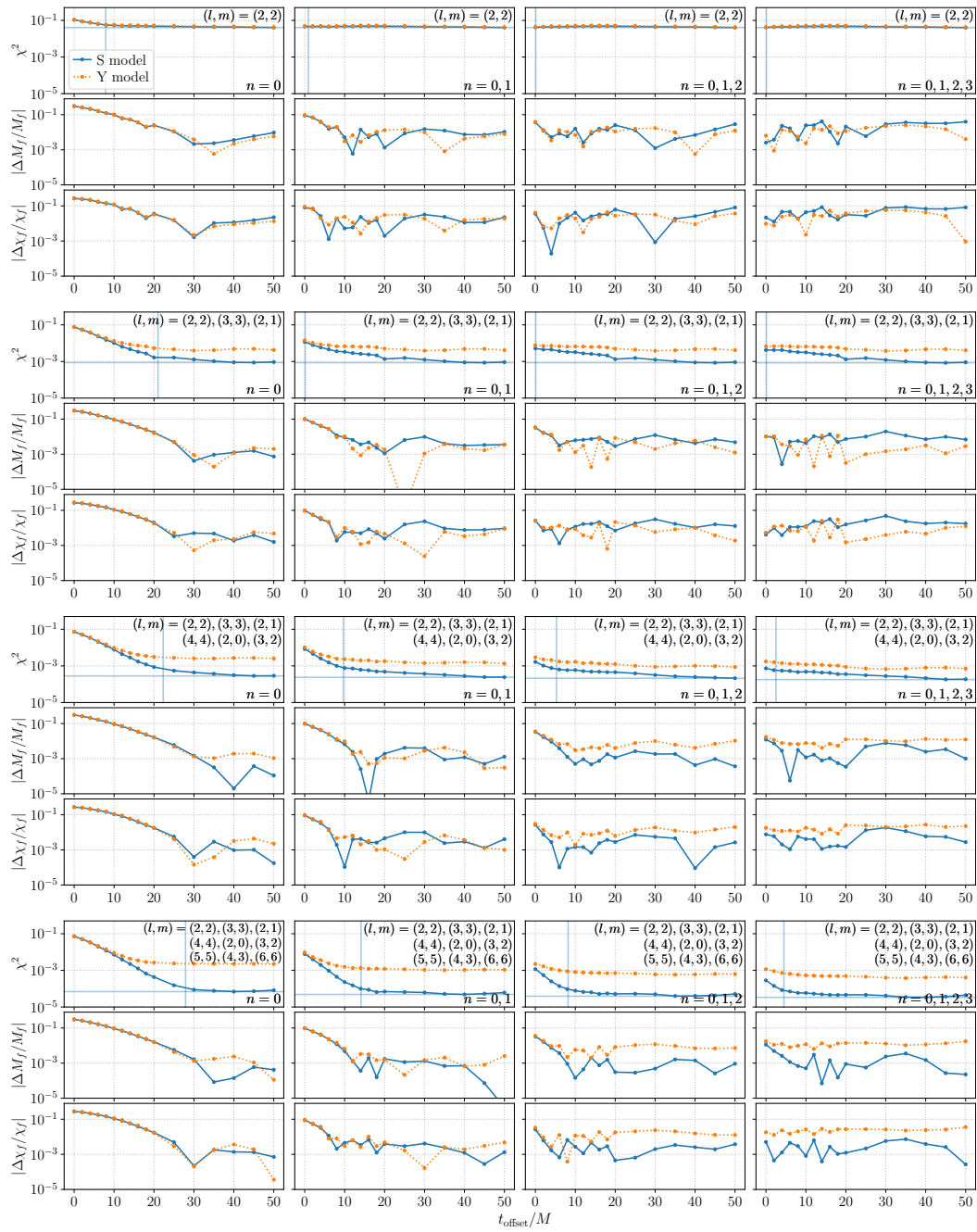


Figure 6.18: Fitting results for binary waveform N5. Plot settings are the same as Fig. 6.5.

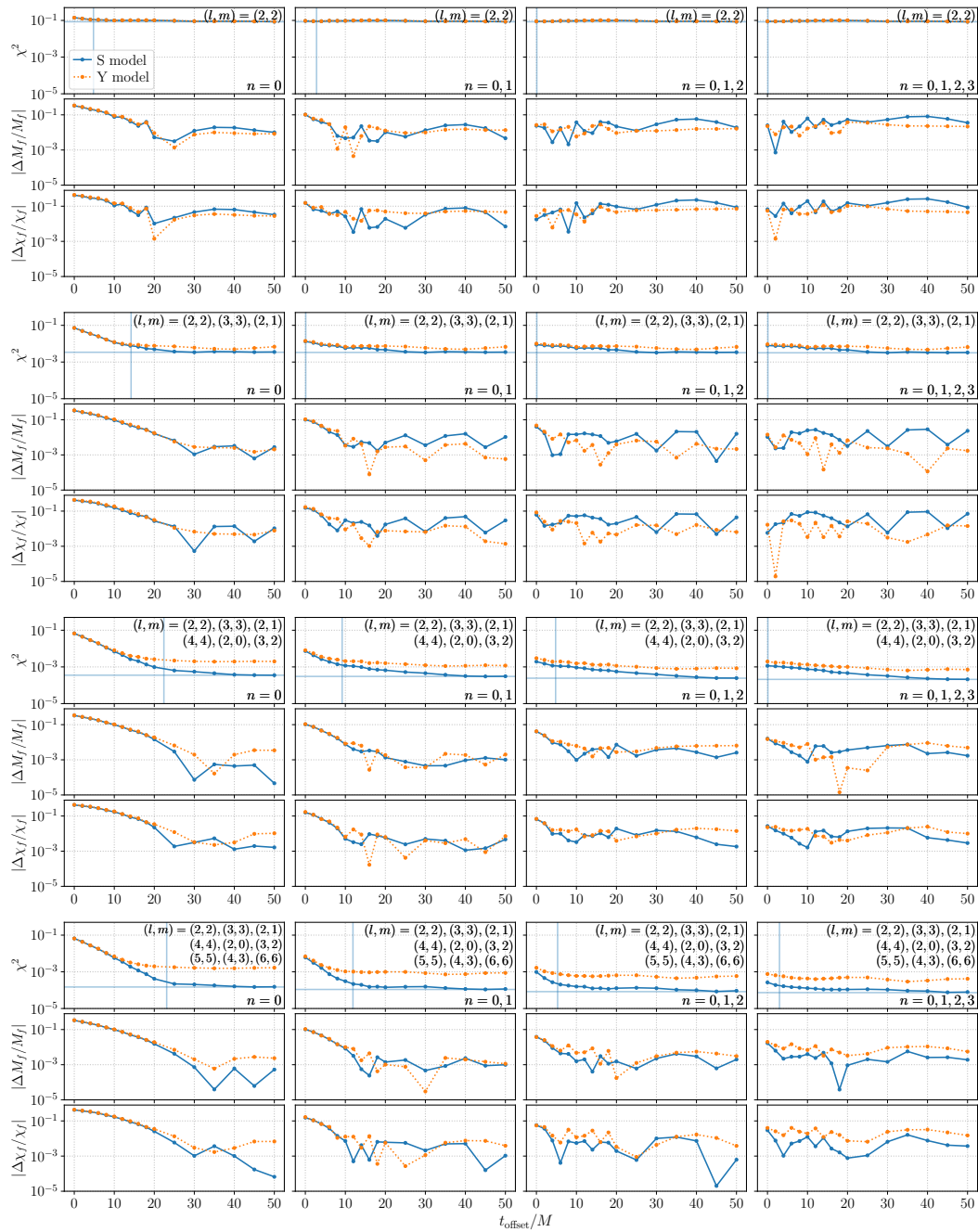


Figure 6.19: Fitting results for binary waveform N6. Plot settings are the same as Fig. 6.5.

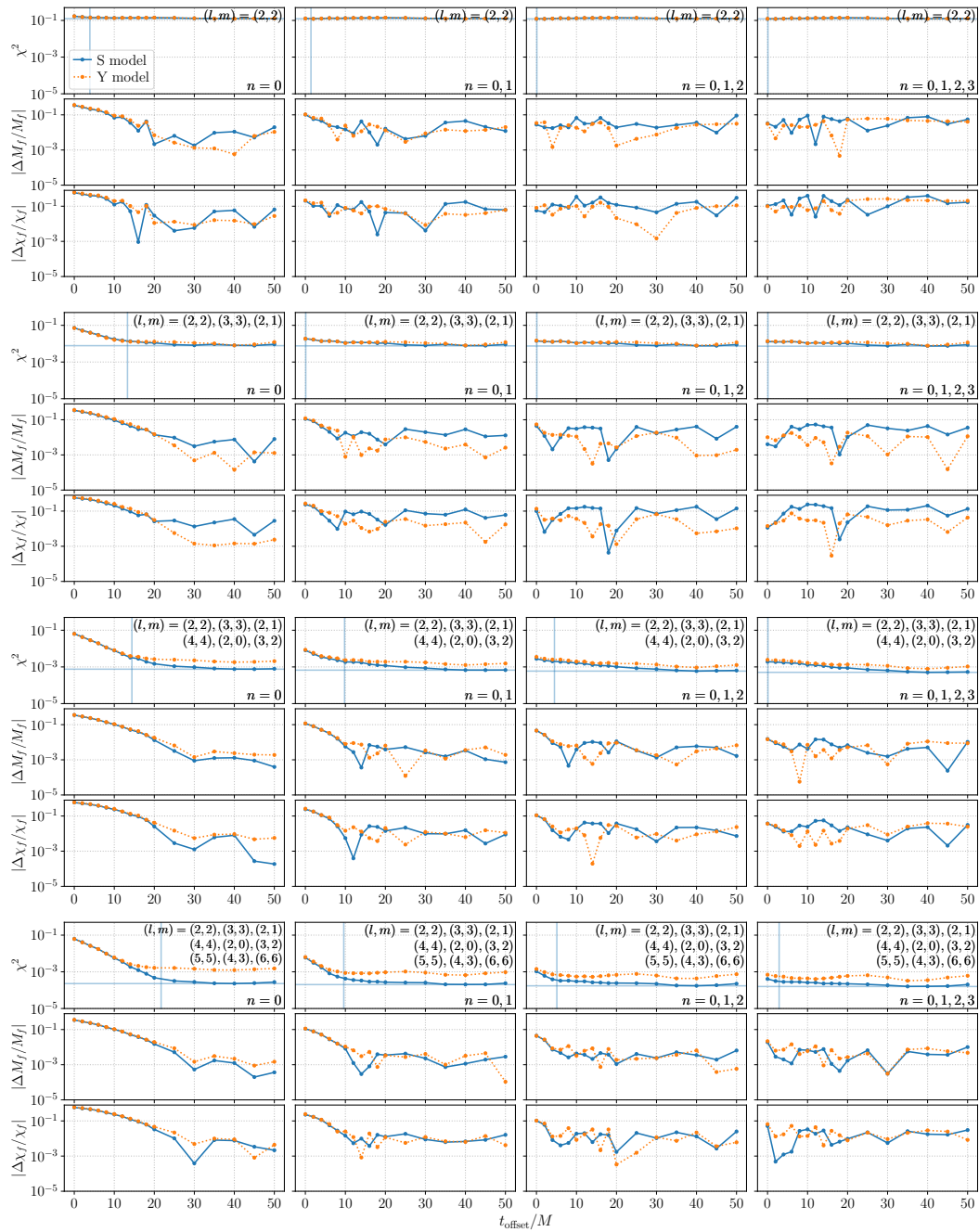


Figure 6.20: Fitting results for binary waveform N7. Plot settings are the same as Fig. 6.5.

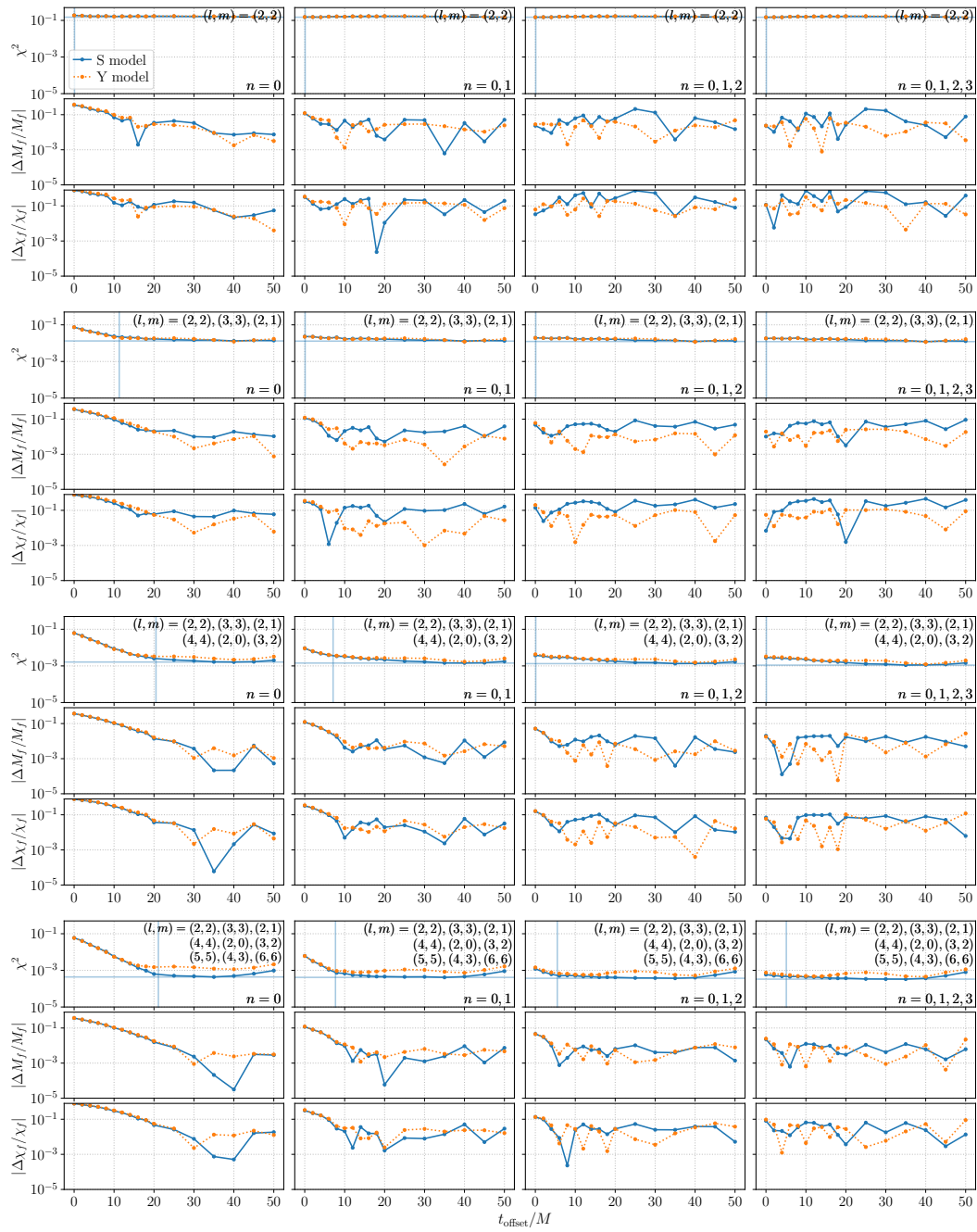


Figure 6.21: Fitting results for binary waveform N8. Plot settings are the same as Fig. 6.5.

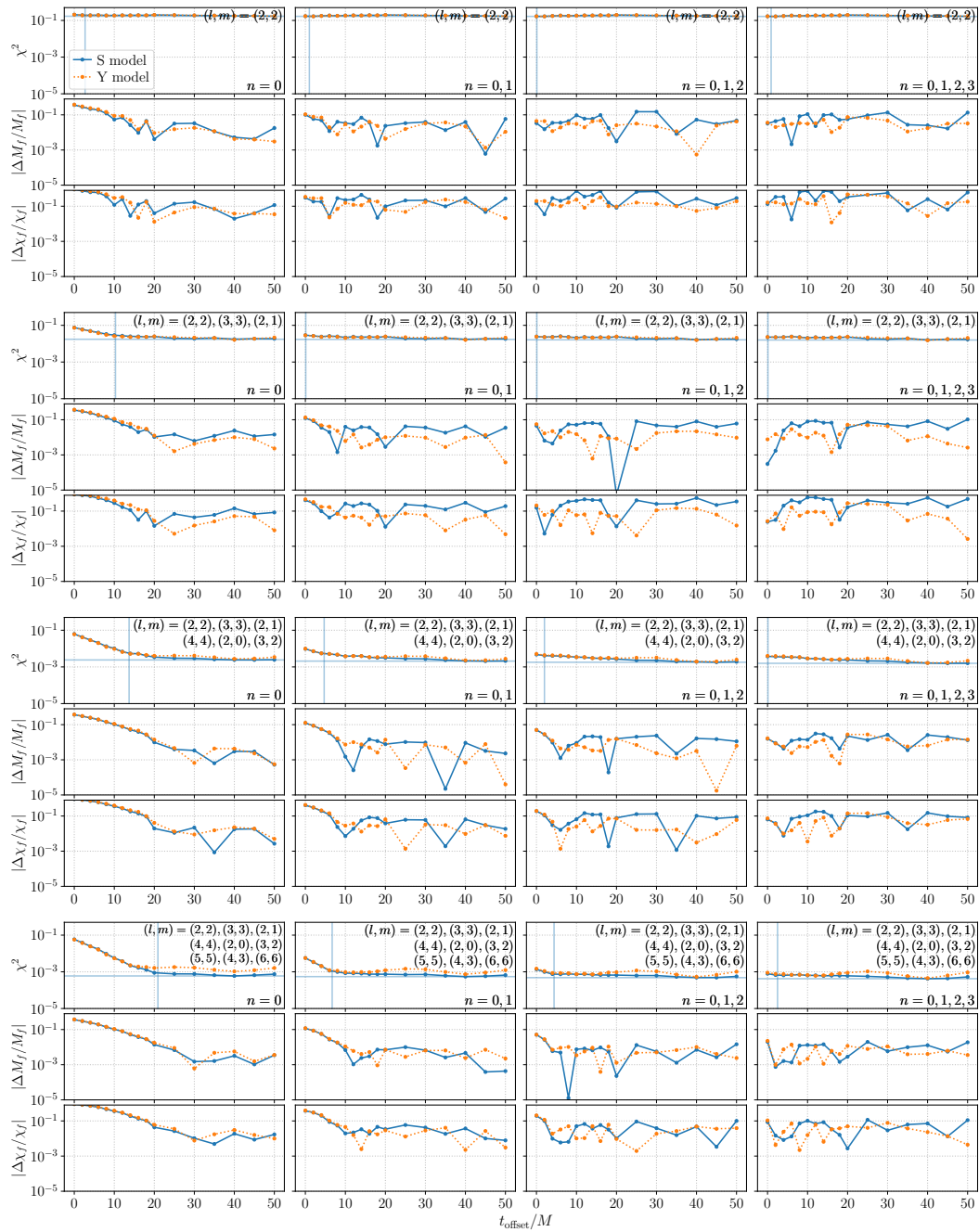


Figure 6.22: Fitting results for binary waveform N9. Plot settings are the same as Fig. 6.5.

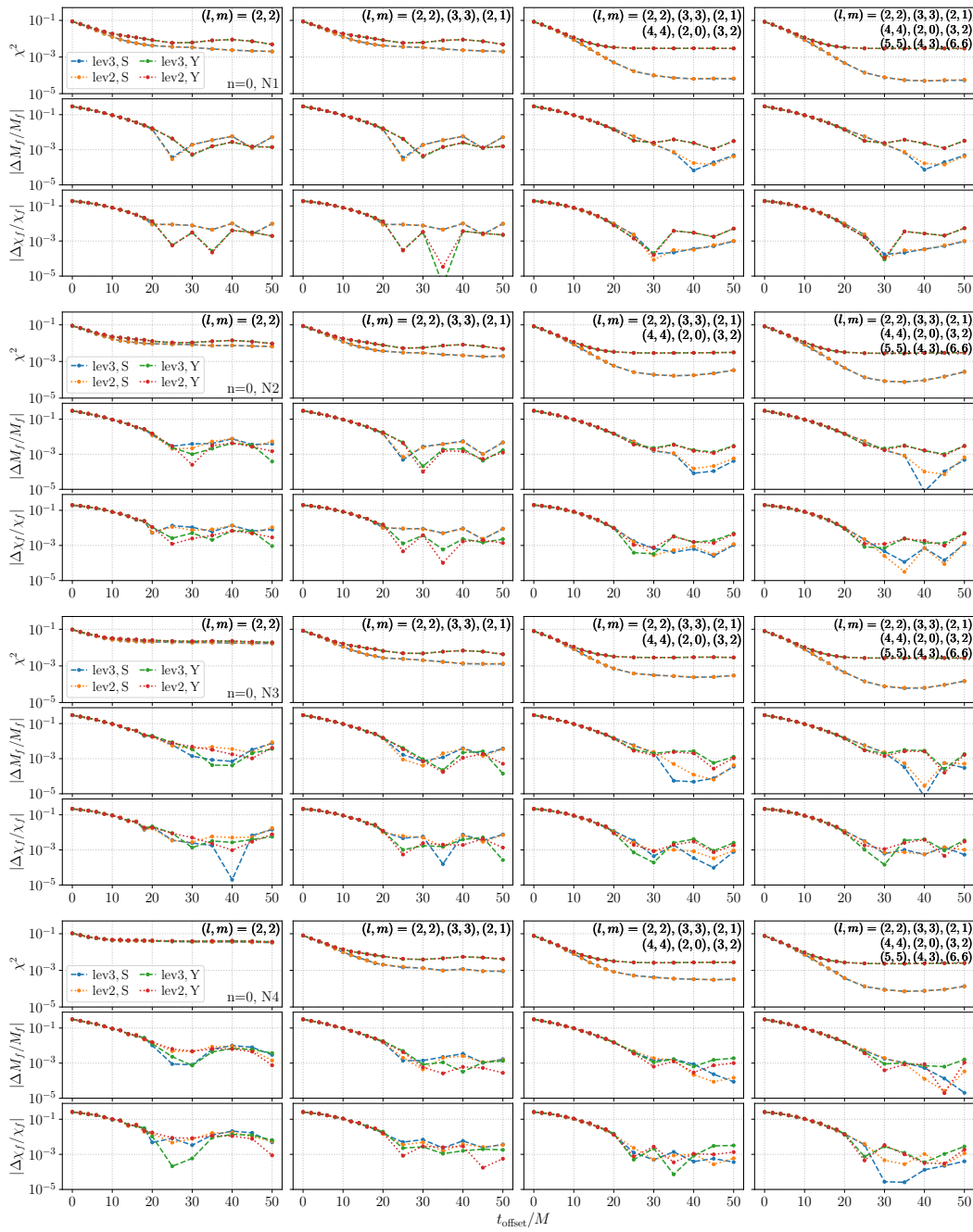


Figure 6.23: Fitting results for N1–N4 using SXS data with different numerical levels. Plot settings are the same as Fig. 6.6.

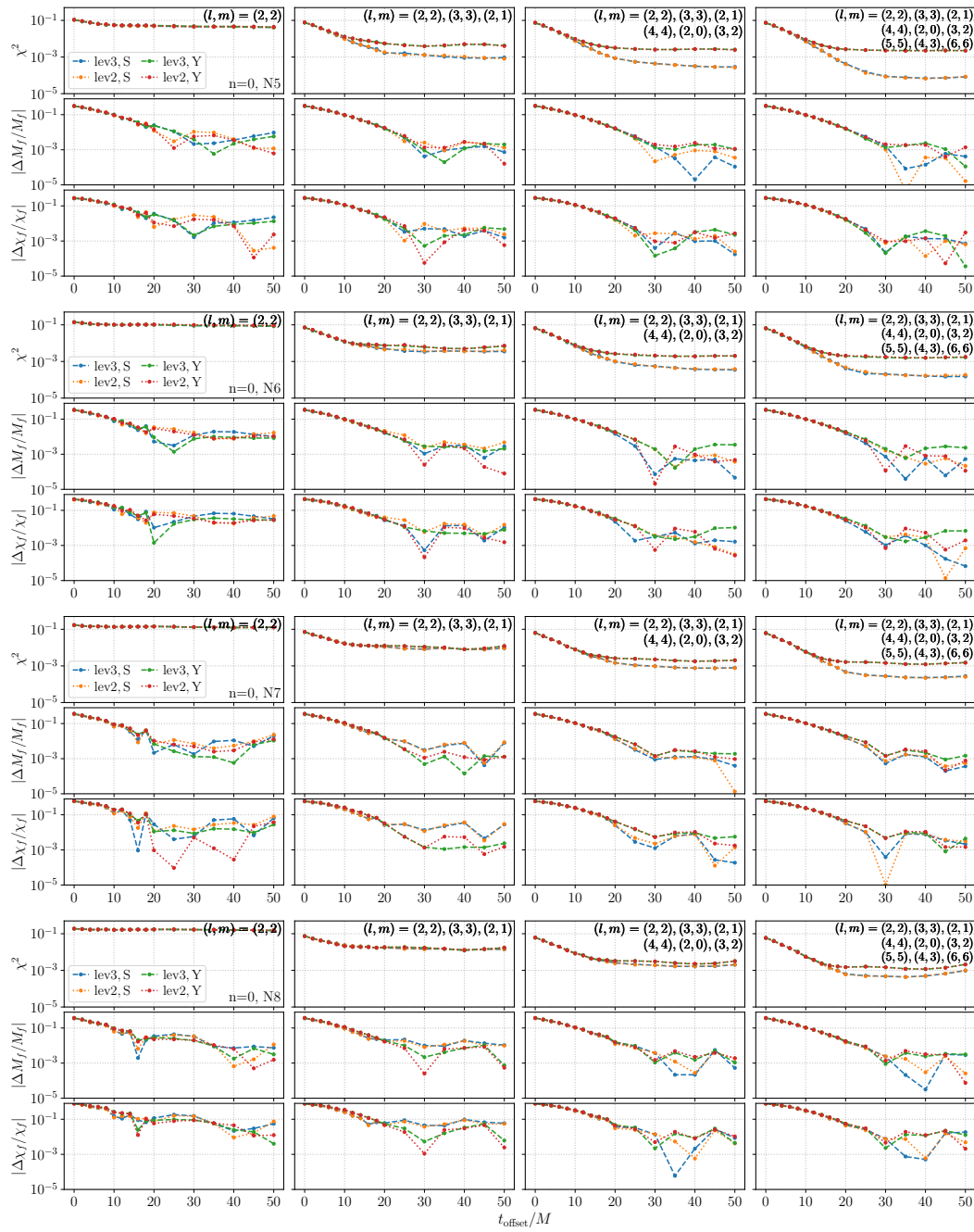


Figure 6.24: Fitting results for N5–N8 using SXS data with different numerical levels. Plot settings are the same as Fig. 6.6.

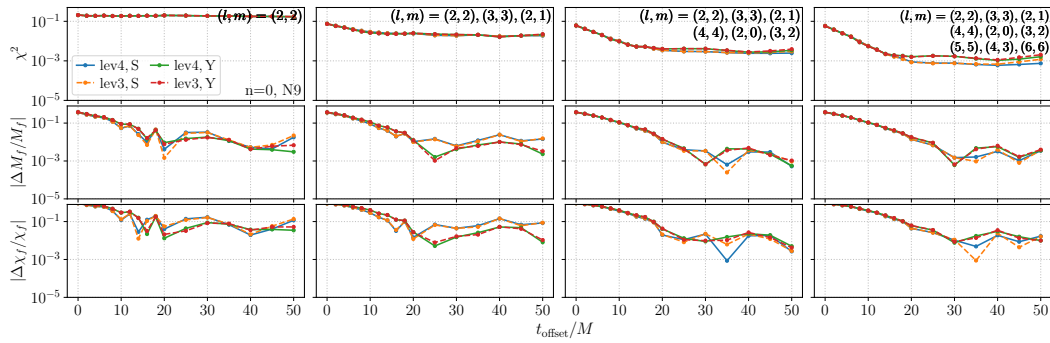


Figure 6.25: Fitting results for N9 using SXS data with different numerical levels. Plot settings are the same as Fig. 6.6.

References

- [1] E. W. Leaver. An Analytic representation for the quasi normal modes of Kerr black holes. *Proc. Roy. Soc. Lond. A*, 402:285–298, 1985.
- [2] Kostas D. Kokkotas and Bernd G. Schmidt. Quasinormal modes of stars and black holes. *Living Rev. Rel.*, 2:2, 1999.
- [3] Hans-Peter Nollert. TOPICAL REVIEW: Quasinormal modes: the characteristic ‘sound’ of black holes and neutron stars. *Class. Quant. Grav.*, 16:R159–R216, 1999.
- [4] Emanuele Berti, Vitor Cardoso, and Andrei O. Starinets. Quasinormal modes of black holes and black branes. *Class. Quant. Grav.*, 26:163001, 2009.
- [5] Maximiliano Isi and Will M. Farr. Analyzing black-hole ringdowns, 7 2021.
- [6] Saul A. Teukolsky. Rotating black holes: Separable wave equations for gravitational and electromagnetic perturbations. *Phys. Rev. Lett.*, 29:1114–1118, Oct 1972.
- [7] Saul A. Teukolsky. Perturbations of a Rotating Black Hole. I. Fundamental Equations for Gravitational, Electromagnetic, and Neutrino-Field Perturbations. *Astrophys. J.*, 185:635–648, October 1973.
- [8] William H. Press and Saul A. Teukolsky. Perturbations of a Rotating Black Hole. II. Dynamical Stability of the Kerr Metric. *Astrophys. J.*, 185:649–674, October 1973.
- [9] Gregory B. Cook and Maxim Zaltskiy. Gravitational perturbations of the Kerr geometry: High-accuracy study. *Phys. Rev. D*, 90(12):124021, 2014.
- [10] Richard H. Price. Nonspherical Perturbations of Relativistic Gravitational Collapse. I. Scalar and Gravitational Perturbations. *Phys. Rev. D*, 5:2419–2438, May 1972.

- [11] Richard H. Price. Nonspherical Perturbations of Relativistic Gravitational Collapse. II. Integer-Spin, Zero-Rest-Mass Fields. *Phys. Rev. D*, 5:2439–2454, May 1972.
- [12] C. T. Cunningham, R. H. Price, and V. Moncrief. Radiation from collapsing relativistic stars. I - Linearized odd-parity radiation. *Astrophys. J.*, 224:643, 1978.
- [13] C. T. Cunningham, R. H. Price, and V. Moncrief. Radiation from collapsing relativistic stars. II. Linearized even-parity radiation. *Astrophys. J.*, 230:870–892, 1979.
- [14] Saul A Teukolsky. The kerr metric. *Classical and Quantum Gravity*, 32(12):124006, jun 2015.
- [15] Thibault Damour and Alessandro Nagar. New analytic representation of the ringdown waveform of coalescing spinning black hole binaries. *Phys. Rev. D*, 90:024054, Jul 2014.
- [16] B. P. Abbott et al. Tests of general relativity with GW150914. *Phys. Rev. Lett.*, 116(22):221101, 2016. [Erratum: <https://journals.aps.org/prl/abstract/10.1103/PhysRevLett.121.129902> *Phys. Rev. Lett.* 121, 129902 (2018)].
- [17] Walter Del Pozzo and Alessandro Nagar. Analytic family of post-merger template waveforms. *Phys. Rev. D*, 95:124034, Jun 2017.
- [18] Richard Brito, Alessandra Buonanno, and Vivien Raymond. Black-hole spectroscopy by making full use of gravitational-wave modeling. *Phys. Rev. D*, 98:084038, Oct 2018.
- [19] Gregorio Carullo, Walter Del Pozzo, and John Veitch. Observational Black Hole Spectroscopy: A time-domain multimode analysis of GW150914. *Phys. Rev. D*, 99(12):123029, 2019. [Erratum: <https://link.aps.org/doi/10.1103/PhysRevD.100.089903> *Phys. Rev. D* 100, 089903 (2019)].
- [20] Gregory B. Cook. Aspects of multimode Kerr ringdown fitting. *Phys. Rev. D*, 102:024027, Jul 2020.
- [21] Emanuele Berti, Vitor Cardoso, Jose A. Gonzalez, and Ulrich Sperhake. Mining information from binary black hole mergers: A Comparison of estimation methods for complex exponentials in noise. *Phys. Rev. D*, 75:124017, 2007.
- [22] Hiroyuki Nakano, Tatsuya Narikawa, Ken-ichi Oohara, Kazuki Sakai, Hisaki Shinkai, Hirotaka Takahashi, Takahiro Tanaka, Nami Uchikata, Shun Yamamoto, and Takahiro S. Yamamoto. Comparison of various methods to extract ringdown frequency from gravitational wave data. *Phys. Rev. D*, 99(12):124032, 2019.

- [23] Emanuele Berti and Vitor Cardoso. Quasinormal ringing of Kerr black holes. I. The Excitation factors. *Phys. Rev. D*, 74:104020, 2006.
- [24] Matthew Giesler, Maximiliano Isi, Mark A. Scheel, and Saul A. Teukolsky. Black hole ringdown: The importance of overtones. *Phys. Rev. X*, 9:041060, Dec 2019.
- [25] Xisco Jiménez Forteza, Swetha Bhagwat, Paolo Pani, and Valeria Ferrari. Spectroscopy of binary black hole ringdown using overtones and angular modes. *Phys. Rev. D*, 102:044053, Aug 2020.
- [26] Lionel London, Deirdre Shoemaker, and James Healy. Modeling ringdown: Beyond the fundamental quasinormal modes. *Phys. Rev. D*, 90(12):124032, 2014. [Erratum: *Phys.Rev.D* 94, 069902 (2016)].
- [27] Xisco Jiménez-Forteza, David Keitel, Sascha Husa, Mark Hannam, Sebastian Khan, and Michael Pürrer. Hierarchical data-driven approach to fitting numerical relativity data for nonprecessing binary black holes with an application to final spin and radiated energy. *Phys. Rev. D*, 95(6):064024, 2017.
- [28] L. T. London. Modeling ringdown. II. Aligned-spin binary black holes, implications for data analysis and fundamental theory. *Phys. Rev. D*, 102(8):084052, 2020.
- [29] Andrea Taracchini, Alessandra Buonanno, Gaurav Khanna, and Scott A. Hughes. Small mass plunging into a Kerr black hole: Anatomy of the inspiral-merger-ringdown waveforms. *Phys. Rev. D*, 90:084025, Oct 2014.
- [30] Scott A. Hughes, Anuj Apte, Gaurav Khanna, and Halston Lim. Learning about black hole binaries from their ringdown spectra. *Phys. Rev. Lett.*, 123:161101, Oct 2019.
- [31] Anuj Apte and Scott A. Hughes. Exciting black hole modes via misaligned coalescences: I. Inspiral, transition, and plunge trajectories using a generalized Ori-Thorne procedure. *Phys. Rev. D*, 100(8):084031, 2019.
- [32] Halston Lim, Gaurav Khanna, Anuj Apte, and Scott A. Hughes. Exciting black hole modes via misaligned coalescences: II. The mode content of late-time coalescence waveforms. *Phys. Rev. D*, 100(8):084032, 2019.
- [33] Vitor Cardoso and Leonardo Gualtieri. Testing the black hole ‘no-hair’ hypothesis. *Class. Quant. Grav.*, 33(17):174001, 2016.
- [34] Maximiliano Isi, Matthew Giesler, Will M. Farr, Mark A. Scheel, and Saul A. Teukolsky. Testing the no-hair theorem with GW150914. *Phys. Rev. Lett.*, 123:111102, Sep 2019.
- [35] B. P. Abbott et al. Tests of General Relativity with the Binary Black Hole Signals from the LIGO-Virgo Catalog GWTC-1. *Phys. Rev. D*, 100(10):104036, 2019.

- [36] R. Abbott et al. Tests of General Relativity with Binary Black Holes from the second LIGO-Virgo Gravitational-Wave Transient Catalog, 10 2020.
- [37] Emanuele Berti, Jaime Cardoso, Vitor Cardoso, and Marco Cavaglia. Matched-filtering and parameter estimation of ringdown waveforms. *Phys. Rev. D*, 76:104044, 2007.
- [38] Andrea Maselli, Kostas Kokkotas, and Pablo Laguna. Observing binary black hole ringdowns by advanced gravitational wave detectors. *Phys. Rev. D*, 95(10):104026, 2017.
- [39] B. P. Abbott et al. Binary Black Hole Mergers in the first Advanced LIGO Observing Run. *Phys. Rev. X*, 6(4):041015, 2016. [Erratum: <https://journals.aps.org/prx/abstract/10.1103/PhysRevX.8.039903> *Phys. Rev. X* 8, 039903 (2018)].
- [40] B. P. Abbott et al. GWTC-1: A Gravitational-Wave Transient Catalog of Compact Binary Mergers Observed by LIGO and Virgo during the First and Second Observing Runs. *Phys. Rev. X*, 9(3):031040, 2019.
- [41] Tejaswi Venumadhav, Barak Zackay, Javier Roulet, Liang Dai, and Matias Zaldarriaga. New binary black hole mergers in the second observing run of advanced ligo and advanced virgo. *Phys. Rev. D*, 101:083030, Apr 2020.
- [42] R. Abbott et al. GWTC-2: Compact Binary Coalescences Observed by LIGO and Virgo During the First Half of the Third Observing Run, 10 2021.
- [43] J. Aasi et al. Advanced LIGO. *Class. Quant. Grav.*, 32:074001, 2015.
- [44] F. Acernese et al. Advanced Virgo: a second-generation interferometric gravitational wave detector. *Class. Quant. Grav.*, 32(2):024001, 2015.
- [45] James Healy, Pablo Laguna, Larne Pekowsky, and Deirdre Shoemaker. Template Mode Hierarchies for Binary Black Hole Mergers. *Phys. Rev. D*, 88(2):024034, 2013.
- [46] Larne Pekowsky, James Healy, Deirdre Shoemaker, and Pablo Laguna. Impact of higher-order modes on the detection of binary black hole coalescences. *Phys. Rev. D*, 87(8):084008, 2013.
- [47] Cameron Mills and Stephen Fairhurst. Measuring gravitational-wave higher-order multipoles. *Phys. Rev. D*, 103:024042, Jan 2021.
- [48] R. Abbott et al. GW190412: Observation of a Binary-Black-Hole Coalescence with Asymmetric Masses. *Phys. Rev. D*, 102(4):043015, 2020.
- [49] R. Abbott et al. GW190814: Gravitational Waves from the Coalescence of a 23 Solar Mass Black Hole with a 2.6 Solar Mass Compact Object. *Astrophys. J. Lett.*, 896(2):L44, 2020.

- [50] Roberto Cotesta, Alessandra Buonanno, Alejandro Bohé, Andrea Taracchini, Ian Hinder, and Serguei Ossokine. Enriching the symphony of gravitational waves from binary black holes by tuning higher harmonics. *Phys. Rev. D*, 98:084028, Oct 2018.
- [51] Ethan Payne, Colm Talbot, and Eric Thrane. Higher order gravitational-wave modes with likelihood reweighting. *Phys. Rev. D*, 100:123017, Dec 2019.
- [52] Jacob Lange, Richard O’Shaughnessy, and Monica Rizzo. Rapid and accurate parameter inference for coalescing, precessing compact binaries, 2018.
- [53] M. Punturo et al. The Einstein Telescope: A third-generation gravitational wave observatory. *Class. Quant. Grav.*, 27:194002, 2010.
- [54] Michele Maggiore et al. Science Case for the Einstein Telescope. *JCAP*, 03:050, 2020.
- [55] David Reitze et al. Cosmic Explorer: The U.S. Contribution to Gravitational-Wave Astronomy beyond LIGO. *Bull. Am. Astron. Soc.*, 51(7):035, 2019.
- [56] Evan D. Hall et al. Gravitational-wave physics with Cosmic Explorer: limits to low-frequency sensitivity, 12 2020.
- [57] K. Ackley et al. Neutron Star Extreme Matter Observatory: A kilohertz-band gravitational-wave detector in the global network. *Publ. Astron. Soc. Austral.*, 37:e047, 2020.
- [58] Divyajyoti, Preet Baxi, Chandra Kant Mishra, and K. G. Arun. Detectability of gravitational higher order modes in the 3G era, 3 2021.
- [59] Emanuele Berti, Vitor Cardoso, and Marc Casals. Eigenvalues and eigenfunctions of spin-weighted spheroidal harmonics in four and higher dimensions. *Phys. Rev. D*, 73:024013, 2006. [Erratum: <https://link.aps.org/doi/10.1103/PhysRevD.73.109902> *Phys. Rev. D* 73, 109902 (2006)].
- [60] Michael Boyle et al. The SXS Collaboration catalog of binary black hole simulations. *Class. Quant. Grav.*, 36(19):195006, 2019.
- [61] Keefe Mitman et al. Adding gravitational memory to waveform catalogs using BMS balance laws. *Phys. Rev. D*, 103(2):024031, 2021.
- [62] Wolfgang Tichy and Pedro Marronetti. The Final mass and spin of black hole mergers. *Phys. Rev. D*, 78:081501, 2008.
- [63] Luciano Rezzolla, Enrico Barausse, Ernst Nils Dorband, Denis Pollney, Christian Reisswig, Jennifer Seiler, and Sascha Husa. Final spin from the coalescence of two black holes. *Phys. Rev. D*, 78:044002, Aug 2008.

- [64] Carl L. Rodriguez, Michael Zevin, Chris Pankow, Vasilliki Kalogera, and Frederic A. Rasio. Illuminating Black Hole Binary Formation Channels with Spins in Advanced LIGO. *Astrophys. J. Lett.*, 832(1):L2, 2016.
- [65] Davide Gerosa, Emanuele Berti, Richard O’Shaughnessy, Krzysztof Belczynski, Michael Kesden, Daniel Wysocki, and Wojciech Gladysz. Spin orientations of merging black holes formed from the evolution of stellar binaries. *Phys. Rev. D*, 98:084036, Oct 2018.
- [66] Gaurav Khanna and Richard H. Price. Black Hole Ringing, Quasinormal Modes, and Light Rings. *Phys. Rev. D*, 95(8):081501, 2017.
- [67] Emanuele Berti and Marta Volonteri. Cosmological black hole spin evolution by mergers and accretion. *Astrophys. J.*, 684:822–828, 2008.
- [68] Emanuele Berti, Vitor Cardoso, and Clifford M. Will. Gravitational-wave spectroscopy of massive black holes with the space interferometer LISA. *Phys. Rev. D*, 73:064030, Mar 2006.
- [69] Werner Israel. Event horizons in static vacuum space-times. *Phys. Rev.*, 164:1776–1779, 1967.
- [70] S. W. Hawking. Black holes in general relativity. *Commun. Math. Phys.*, 25:152–166, 1972.
- [71] B. Carter. Axisymmetric Black Hole Has Only Two Degrees of Freedom. *Phys. Rev. Lett.*, 26:331–333, 1971.
- [72] Norman Gürlebeck. No-hair theorem for black holes in astrophysical environments. *Phys. Rev. Lett.*, 114:151102, Apr 2015.
- [73] Gregorio Carullo et al. Empirical tests of the black hole no-hair conjecture using gravitational-wave observations. *Phys. Rev. D*, 98(10):104020, 2018.
- [74] Emanuele Berti and Antoine Klein. Mixing of spherical and spheroidal modes in perturbed Kerr black holes. *Phys. Rev. D*, 90(6):064012, 2014.
- [75] Leo C. Stein. qnm: A Python package for calculating Kerr quasinormal modes, separation constants, and spherical-spheroidal mixing coefficients. *J. Open Source Softw.*, 4(42):1683, 2019.
- [76] Eliot Finch and Christopher J. Moore. Modelling the ringdown from precessing black hole binaries, 2021.
- [77] Arnab Dhani. Importance of mirror modes in binary black hole ringdown waveform. *Phys. Rev. D*, 103(10):104048, 2021.
- [78] Arnab Dhani and B. S. Sathyaprakash. Overtones, mirror modes, and mode-mixing in binary black hole mergers, 7 2021.

- [79] E. S. C. Ching, P. T. Leung, W. M. Suen, and K. Young. Late time tail of wave propagation on curved space-time. *Phys. Rev. Lett.*, 74:2414–2417, 1995.
- [80] Vladimir B Braginsky and Kip S Thorne. Gravitational-wave bursts with memory and experimental prospects. *Nature*, 327(6118):123–125, 1987.
- [81] D. Christodoulou. Nonlinear nature of gravitation and gravitational wave experiments. *Phys. Rev. Lett.*, 67:1486–1489, 1991.
- [82] Kip S. Thorne. Gravitational-wave bursts with memory: The Christodoulou effect. *Phys. Rev. D*, 45(2):520–524, 1992.
- [83] Colm Talbot, Eric Thrane, Paul D. Lasky, and Fuhui Lin. Gravitational-wave memory: Waveforms and phenomenology. *Phys. Rev. D*, 98:064031, Sep 2018.
- [84] Luc Blanchet and Thibault Damour. Hereditary effects in gravitational radiation. *Phys. Rev. D*, 46:4304–4319, 1992.
- [85] Marc Favata. The gravitational-wave memory effect. *Classical and Quantum Gravity*, 27(8):084036, apr 2010.
- [86] Keefe Mitman, Jordan Moxon, Mark A. Scheel, Saul A. Teukolsky, Michael Boyle, Nils Deppe, Lawrence E. Kidder, and William Throwe. Computation of displacement and spin gravitational memory in numerical relativity. *Phys. Rev. D*, 102(10):104007, 2020.
- [87] B. P. Abbott et al. Properties of the Binary Black Hole Merger GW150914. *Phys. Rev. Lett.*, 116(24):241102, 2016.
- [88] Geoffrey Lovelace et al. Modeling the source of GW150914 with targeted numerical-relativity simulations. *Class. Quant. Grav.*, 33(24):244002, 2016.
- [89] Geoffrey Lovelace. Reducing spurious gravitational radiation in binary-black-hole simulations by using conformally curved initial data. *Class. Quant. Grav.*, 26:114002, 2009.
- [90] Keefe Mitman et al. Fixing the BMS frame of numerical relativity waveforms. *Phys. Rev. D*, 104(2):024051, 2021.
- [91] Lorena Magaña Zertuche et al. High Precision Ringdown Modeling: Multi-mode Fits and BMS Frames. 10 2021.
- [92] Manuela Campanelli, C. O. Lousto, and Y. Zlochower. Spinning-black-hole binaries: The orbital hang up. *Phys. Rev. D*, 74:041501, 2006.
- [93] Sizheng Ma, Matthew Giesler, Vijay Varma, Mark A. Scheel, and Yanbei Chen. Universal features of gravitational waves emitted by superkick binary black hole systems, 7 2021.

- [94] Ilya Mandel, Duncan A. Brown, Jonathan R. Gair, and M. Coleman Miller. Rates and Characteristics of Intermediate-Mass-Ratio Inspirals Detectable by Advanced LIGO. *Astrophys. J.*, 681:1431–1447, 2008.
- [95] Eliu Antonio Huerta. *Source modelling of extreme and intermediate mass ratio inspirals*. PhD thesis, Cambridge U., Inst. of Astron., 2011.
- [96] David A Freedman. *Statistical models: theory and practice*. cambridge university press, 2009.